

# REPRODUCED COPY

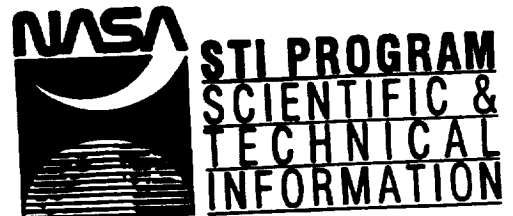
(NASA-CR-118610-Vol-1) PRIMARY G  
AND N SYSTEM LUNAR ORBIT  
OPERATIONS, VOLUME 1 (MIT) 258 p

N95-70301

Unclas

29/13 0030483

*Produced by the*  
NASA Center for AeroSpace Information  
800 Elkridge Landing Road  
Linthicum Heights, MD 21090-2934  
(301) 621-0390



FACILITY FORM 042

(ACCESSION NUMBER)	258	(THRU)	1945-76301
(PAGES)		(CODE)	
(NASA CR OR TMX OR AD NUMBER)		(CATEGORY)	21



ORIGINAL PAGE IS  
OF POOR QUALITY

*Nasa CR-118610*  
*Vol. I of II*

# APOLLO

## GUIDANCE AND NAVIGATION

Approved: *Milton B. Trageser* Date: *7/1*  
Milton B. Trageser, Director  
Apollo Guidance and Navigation Program

Approved: *Roger B. Woodbury* Date: *8/1*  
Roger B. Woodbury, Deputy Director  
Instrumentation Laboratory

MASSACHUSETTS INSTITUTE OF TECHNOLOGY

R-446

(Unclassified)

PRIMARY G&N SYSTEM  
LUNAR ORBIT OPERATIONS

(Vol. I of II) Edited by

Norman E. Sears

April 1964

LIBRARY COPY

SEP 4 1964

LEWIS LIBRARY, NASA  
CLEVELAND, OHIO

# INSTRUMENTATION LABORATORY

CAMBRIDGE 39, MASSACHUSETTS

COPY # 71 OF 225 COPIES  
THIS DOCUMENT CONTAINS 762 PAGES

ORIGINAL PAGE IS  
OF POOR QUALITY

## ACKNOWLEDGMENT

This report was prepared under DSR Project 55-191, sponsored by the Manned Spacecraft Center of the National Aeronautics and Space Administration through Contract NAS 9-153.

The following Space Guidance Analysis group personnel contributed to the preparation of this report.

D. S. Baker  
R. D. Brown  
G. W. Cherry  
P. G. Felleman  
R. D. Goss  
E. S. Muller - Raytheon Resident Engineer  
R. J. Phaneuf  
N. E. Sears  
R. L. White  
J. B. Young

The publication of this report does not constitute approval by the National Aeronautics and Space Administration of the findings or the conclusions contained therein. It is published only for the exchange and stimulation of ideas.

VOLUMES I AND II

PRIMARY G&N SYSTEM LUNAR ORBIT OPERATIONS

ABSTRACT

This report summarizes the primary G&N system operation and performance during the lunar orbit phases of the Apollo lunar landing mission. The lunar orbit phases include orbit navigation, descent, landing, surface operations, launch and ascent, rendezvous and LEM aborts. These phases are primarily concerned with the LEM primary G&N operation, but CSM operations of orbit navigation, LEM back-up guidance capability, and LEM retrieval are included. Each lunar orbit phase is described with respect to:

- 1) Primary G&N system objectives and operating modes.
- 2) Current guidance equations.
- 3) Typical trajectories.
- 4) Primary G&N performance and error analysis.

A general description and performance specification is included for the basic units of the primary G&N system.

Edited by

Norman E. Sears

April 1964

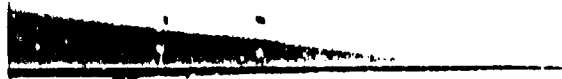


# TABLE OF CONTENTS

## VOLUME I OF II

<u>Chapter</u>		<u>Page</u>
1	PRIMARY GUIDANCE & NAVIGATION SYSTEM	
	DESCRIPTION AND OBJECTIVES . . . . .	1
1.1	Introduction . . . . .	1
1.2	LEM Primary Guidance and Navigation System . . . . .	6
1.2.1	General Comment and LEM Installation . . . . .	6
1.2.2	Inertial Measurement Unit . . . . .	9
1.2.3	LEM Guidance Computer. . . . .	15
1.2.4	Display and Controls . . . . .	23
1.2.5	Coupling Data Unit . . . . .	27
1.2.6	Power Servo Assembly . . . . .	29
1.2.7	Alignment Optical Telescope . . . . .	31
1.2.8	Rendezvous Radar. . . . .	34
1.2.9	Landing Radar. . . . .	36
1.3	IMU Alignment. . . . .	42
1.3.1	General Comment. . . . .	42
1.3.2	Coarse Alignment. . . . .	43
1.3.3	Fine Alignment . . . . .	46
2	LUNAR ORBIT NAVIGATION PHASE . . . . .	51
2.1	General Objectives . . . . .	51
2.2	Navigation Concept and G&N System Operation . . . . .	54
2.3	Orbit Navigation Models and G&N Performance . . . . .	61
2.4	Landing Site Determination . . . . .	79

TABLE OF CONTENTS (Cont)

<u>Chapter</u>	<u>Page</u>
2.5 Lunar Terrain and Gravity Effects . . . . .	84
2.5.1 Lunar Landmark Bias Effects . . . . .	84
2.5.2 Lunar Gravity Bias Effects . . . . .	86
2.5.3 Lunar Landmark Mapping Accuracy Effects . . . . .	87
2.6 CSM Operations after LEM Descent . . . . .	88
3 DESCENT ORBIT PHASE . . . . .	91
3.1 Genral Description . . . . .	91
3.2 Equal Period Descent Orbit . . . . .	92
3.2.1 General Description . . . . .	92
3.2.2 Guidance and Steering Equations . . . . .	93
3.2.2.1 $\underline{V}_G \times \dot{\underline{V}}_G$ Steering Concept . . . . .	93
3.2.2.2 $\underline{W} \times \underline{V}$ Steering Concept . . . . .	96
3.2.2.3 Equivalent Orbit Guidance . . . . .	99
3.2.2.4 Aim Point Guidance . . . . .	101
3.2.3 Descent Injection Maneuver. . . . .	105
3.2.4 Aborts During Descent Injection . . . . .	114
3.3 Hohmann Descent Orbit . . . . .	116
3.3.1 General Description . . . . .	116
3.3.2 Guidance and Steering Equations . . . . .	116
3.3.2.1 Hohmann Descent Guidance. . . . .	116
3.3.2.2 Aim Point Guidance for Hohmann Type Descents. . . . .	118
3.3.3 Descent Injection Maneuvers . . . . .	120

## TABLE OF CONTENTS (Cont)

<u>Chapter</u>	<u>Page</u>
3.4 Injection Timing Determination . . . . .	126
3.5 Noncoplanar Descent and Landing Conditions .	131
3.6 Descent Phase G&N Operations . . . . .	135
3.7 G&N Performance for Equal Period Descents .	138
3.8 G&N Performance for Hohmann Descents . .	143
4 POWERED LANDING MANEUVER . . . . .	149
4.1 General Description . . . . .	149
4.2 Lunar Landing Steering Equations . . . . .	150
4.2.1 General Comments . . . . .	151
4.2.2 Derivation of Landing Maneuver Guidance Equations . . . . .	162
4.2.3 Guidance Equation Summary . . . . .	169
4.2.4 Determination of T or T <sub>go</sub> . . . . .	174
4.2.5 Engine Ignition Algorithm . . . . .	181
4.3 Landing Maneuvers from Hohmann Descents .	187
4.4 Primary G&N System Operation and Performance . . . . .	198
4.4.1 G&N System Performance for Landing Maneuvers from Hohmann Descents . .	198
4.4.2 G&N System Operation . . . . .	207
4.4.3 Landing Radar Operation . . . . .	207
4.4.4 Landing Site Display . . . . .	215

TABLE OF CONTENTS (Cont)

<u>Chapter</u>	<u>Page</u>
4.5	Landing Maneuvers from Equal Period Descents 220
4.5.1	Typical Landing Maneuver Trajectories 220
4.5.2	G&N System Performance . . . . . 220
4.5.3	Landing Radar Operations . . . . . 235
4.5.4	Lunar Surface Transponder Landing . 241
4.6	Hover and Touchdown Phase . . . . . 243
<hr/>	
ME II OF II 5	SURFACE AND PRELAUNCH OPERATIONS . . . . 251
5.1	General Objectives . . . . . 251
5.2	Primary G&N Operations . . . . . 252
5.3	LEM-CSM Tracking Operations . . . . . 253
5.3.1	CSM Tracking Operation . . . . . 254
5.3.2	LEM Tracking Operation. . . . . 258
5.4	Launch Aim Point and Timing Determination . 261
6	LAUNCH AND POWERED ASCENT PHASE . . . . 277
6.1	Primary G&N System Objectives . . . . . 277
6.2	Powered Ascent Guidance Equations . . . . . 279
6.2.1	General . . . . . 279
6.2.2	Derivation of E Guidance Equations . . 284
6.2.3	The Determination of T . . . . . 294
6.2.4	Controlling the Injection Velocity Vector Without Controlling the Injection Altitude 304
6.2.5	Powered Ascent-to-Intercept Guidance. 306
6.2.6	Burnout Position Prediction . . . . . 308
6.2.7	Control of Spacecraft Burnout Attitude 311
6.3	Typical Powered Ascent Trajectories . . . . 313
6.4	Effects of Delayed Launch Time . . . . . 319
6.5	G&N System Performance . . . . . 325

TABLE OF CONTENTS (Cont)

<u>Chapter</u>		<u>Page</u>
7	RENDEZVOUS PHASE . . . . .	331
7.1	Rendezvous Phase Description and Objectives . . . . .	331
7.2	Rendezvous Guidance Equations . . . . .	336
7.2.1	General Comments . . . . .	336
7.2.2	Rendezvous Navigation Computation . . . . .	340
7.2.3	Rendezvous Statistical Computation . . . . .	348
7.2.4	Velocity Correction Computation and Decision . . . . .	353
7.2.4.1	Midcourse Velocity Correction . . . . .	353
7.2.4.2	Terminal Rendezvous Velocity Correction . . . . .	357
7.3	Rendezvous Statistical Parameter Study . . . . .	364
7.4	Typical Long Range Rendezvous Trajectories and Primary G&N Performance . . . . .	377
7.4.1	Primary G&N Operation . . . . .	377
7.4.2	Simulation Results . . . . .	378
7.4.3	Current Ascent Trajectories . . . . .	394
7.5	Midcourse Velocity Correction Logic . . . . .	399
7.5.1	General Comment . . . . .	399
7.5.2	Disadvantages of SVC Logic . . . . .	400
7.5.3	Fixed Time Velocity Correction Concept . . . . .	404
7.5.4	Summary . . . . .	411
7.6	Terminal Rendezvous Phase . . . . .	411
7.6.1	G&N Operation . . . . .	411
7.6.2	Terminal Rendezvous Maneuvers . . . . .	414

TABLE OF CONTENTS (Cont)

<u>Chapter</u>		<u>Page</u>
	7. 6. 3 Docking and Operation Prior to Transearth Injection . . . . .	422
	7. 7 CSM Monitoring Operation . . . . .	422
8	PRIMARY G&N CONTROLLED ABORT MANEUVERS . . . . .	423
	8. 1 General Description . . . . .	423
	8. 2 Aborts Prior to the Landing Maneuver . . . . .	424
	8. 3 Aborts During Landing Maneuvers from Hohmann Descents . . . . .	427
	8. 3. 1 Typical Powered Abort Maneuvers . . . . .	427
	8. 3. 2 Aim Point Determination for Abort Trajectories. . . . .	431
	8. 3. 3 Primary G&N Performance . . . . .	438
	8. 4 Aborts During Landing Maneuvers from Equal Period Descents . . . . .	443
	8. 4. 1 Typical Powered Abort Maneuvers. . . . .	443
	8. 4. 2 Primary G&N Performance . . . . .	445
	8. 5 Rendezvous Trajectories from Aborted Landings . . . . .	451
9	CSM RETRIEVAL AND LEM BACK-UP OPERATIONS . . . . .	457
	9. 1 Objectives . . . . .	457
	9. 2 CSM Back-up Guidance Operation for LEM . . . . .	457
	9. 2. 1 General Comments. . . . .	457
	9. 2. 2 Emergency Launch from the Lunar Surface Under LEM Back-up Guidance Control. . . . .	459

## TABLE OF CONTENTS (Cont)

<u>Chapter</u>	<u>Page</u>
9.2.3 CSM Primary G&N System for LEM	
Aborts . . . . .	464
9.2.3.1 Aborts from Landing Maneuvers with the LEM Back-up G&N System . . . . .	467
9.2.3.2 Ascent from the Lunar Surface with the LEM Back-up G&N System . . . . .	470
9.3 CSM Retrieval Operations . . . . .	472
9.3.1 General. . . . .	472
9.3.2 Retrieval after Normal LEM Ascents . . . . .	472
9.3.3 Retrieval after LEM Abort Cases . . . . .	481
9.3.3.1 LEM Aborts Prior to the Powered Landing Maneuver . . . . .	481
9.3.3.2 LEM Direct Aborts During Landing Maneuver . . . . .	485
9.3.3.3 CSM Retrieval of the LEM in a Parking Orbit . . . . .	485
9.4 CSM Operations after Retrieval . . . . .	489
Appendix A . . . . .	491
Appendix B . . . . .	495
Appendix C . . . . .	499
References . . . . .	503



## VOLUME I OF II

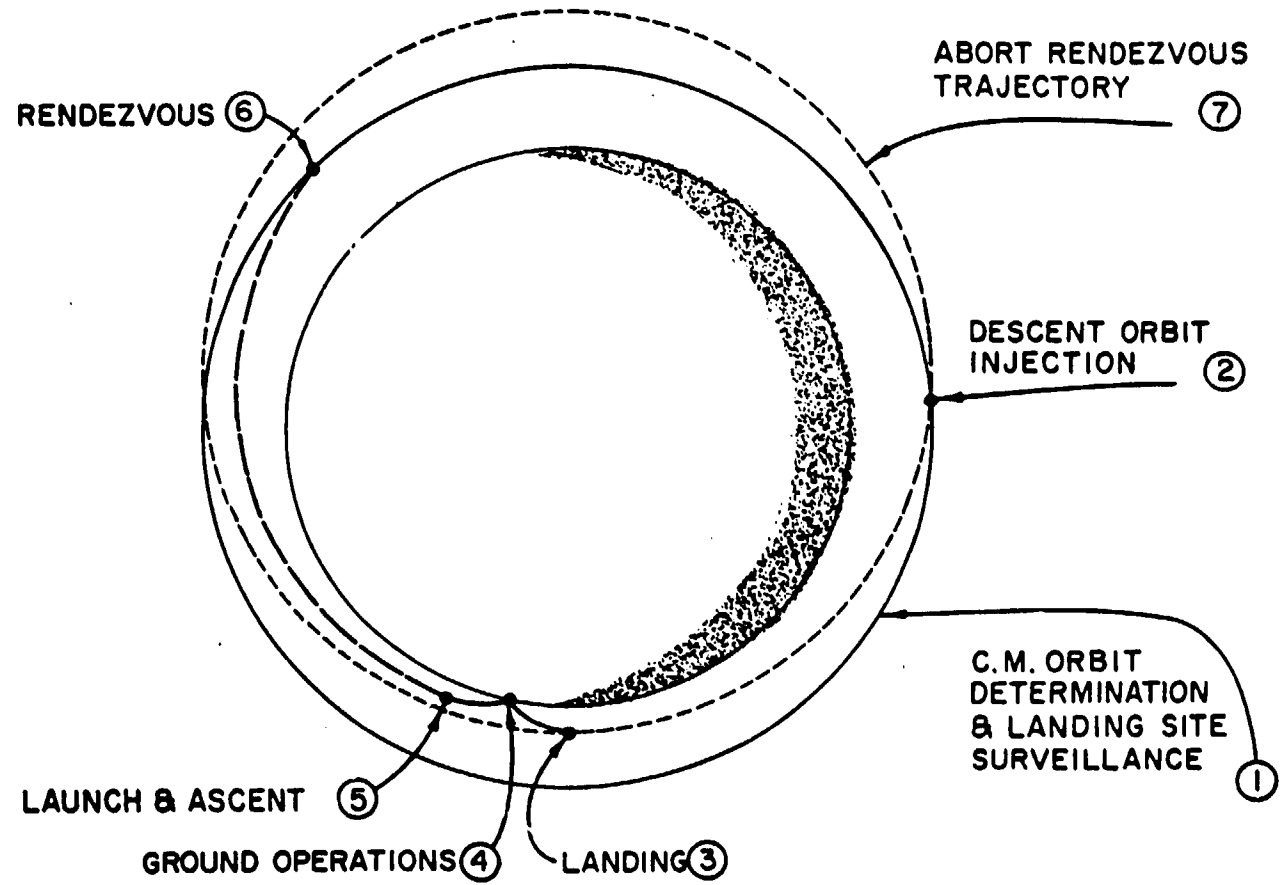
### CHAPTER I

#### PRIMARY GUIDANCE AND NAVIGATION SYSTEM DESCRIPTION AND OBJECTIVES

##### 1.1 Introduction

The purpose of this report is to present a description of the primary guidance and navigation (G&N) system with its operating modes and performance for the lunar orbit phases of the Apollo lunar landing mission. The lunar orbit phases of this mission are defined in this report as those after the lunar orbit insertion maneuver, and prior to transearth injection. The lunar orbit phases are illustrated in Fig. 1.1, and include lunar orbit navigation through descent injection, landing, ascent and rendezvous. Abort conditions in which the primary G&N system controls the abort maneuvers and trajectories are also included. The lunar orbit mission phases are primarily concerned with the Lunar Excursion Module (LEM) primary G&N system operation. The Command Service Modules (CSM) G&N operation for the lunar orbit navigation phase is included, since it establishes the initial data inputs for the LEM G&N system. Knowledge of the CSM orbital ephemeris is also an important parameter used in the LEM launch and rendezvous phases. The CSM maintains this orbit navigation mode of operation along with a monitoring function throughout the LEM phases of the nominal landing mission. The CSM primary G&N system operation for orbit navigation, LEM back-up guidance capability, and active retrieval and rendezvous are included in this report.

The primary method of reporting analytical results for the primary G&N system performance during the lunar orbit phases has been through oral presentations made at MSC Navigation and



2

Fig. 1.1 Lunar operation phases.

Guidance Systems Meetings. These meetings have been called by NASA at average intervals of six to eight weeks over the past 18 months. This report is a summary of the G&N system lunar orbit operations and the majority of the figures included in this report are copies of vu-graphs that were used in presentations at these meetings. These figures have been revised or updated where necessary to reflect the current primary G&N system configuration and operation.

The main objective of this report is to present a review of the current LEM primary G&N system units and their operation. Each phase of the mission illustrated in Fig. 1.1 is described individually to cover the following items:

1. Primary G&N system operation and objectives.
2. Guidance equations currently considered.
3. Typical trajectories.
4. G&N system performance and instrument error analysis.

The primary G&N operating modes for normal mission phases are described in detail. Monitoring and back-up operations involving the primary G&N system are also generally described.

The guidance equations presented for each mission phase are those that will be used in system simulations currently planned or in progress. It is expected that the general concept and form of these equations will be maintained, unless changes are required due to vehicle attitude and propulsion system dynamics. Minor changes are expected when the guidance equations are programmed for simulations involving AGC or LGC units in order to minimize fixed storage and computation time requirements.

The trajectories presented in this report are typical of those resulting from primary G&N system control. These trajectories are not optimum in the sense of  $\Delta V$  requirements.

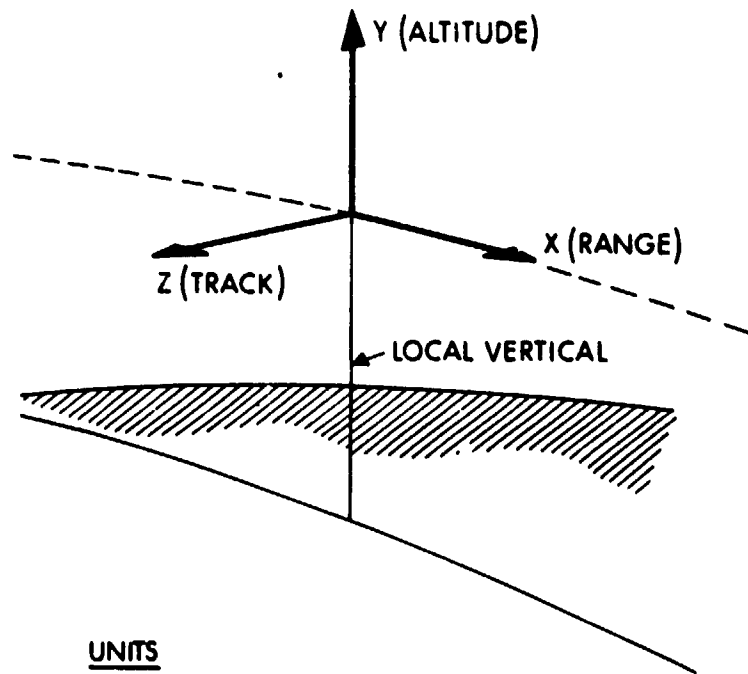
The design of the primary G&N system attempted to limit  $\Delta V$  requirements near the theoretical optimum for the various mission requirements imposed in each phase, but no attempt was made to achieve exact optimum  $\Delta V$  conditions in any single phase. Two types of LEM descent trajectories are presented in this report. These are the equal period descent (Fig. 1.1), and the Hohmann type descent. Both of these descent trajectories affect the powered landing maneuver and abort conditions during the landing maneuver. Each type of descent trajectory is considered in the chapters describing these phases. All detailed trajectories presented in this report are in the local vertical coordinate system illustrated in Fig. 1.2. The X (range) axis is horizontal in the direction of travel, Y (altitude) is along the local geometrical vertical, and Z (track) is normal to the trajectory plane. The units used throughout this report are those listed in Fig. 1.2. The LEM vehicle axes shown in Fig. 1.2 which are frequently referred to, should not be confused with the trajectory coordinate system described above.

The primary G&N system error analysis or uncertainties presented for each phase are due to instrument errors in the G&N system, combined with appropriate initial condition uncertainties. The trajectory uncertainties due to guidance equation approximations are generally one order of magnitude less than the instrument uncertainties, and are not considered in the results presented.

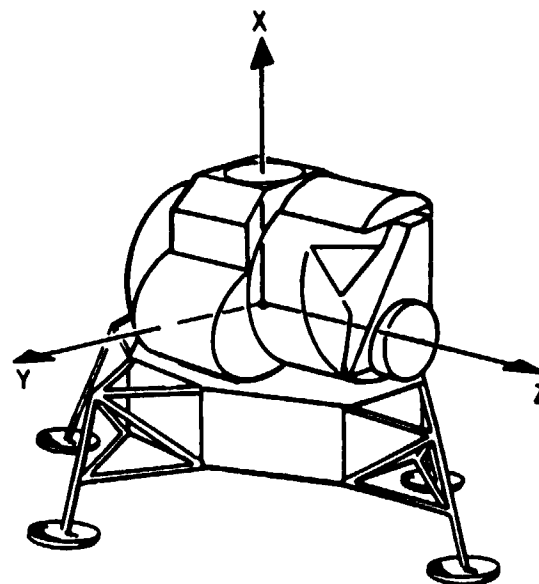
The LEM primary G&N system has an overall design objective of achieving a lunar landing circular error probability (CEP) of 3000 feet for landing sites not marked by surface radar transponders or beacons. A 100 foot landing CEP is the design objective for landing sites marked by a lunar surface transponder.

A review of the primary G&N system of each basic unit is described in the following section, along with the tentative G&N system installation in the LEM.

TRAJECTORY DEVIATION COORDINATES



LEM VEHICLE COORDINATES



UNITS

DISTANCES : ft OR N.M.

VELOCITY : fps

ANGLE : DEGREES OR m.r.

Fig. 1.2 Coordinate systems.

## 1.2 LEM Primary Guidance and Navigation System.

### 1.2.1 General Comments and LEM Installation.

The primary G&N system of the LEM consists of the basic units shown on the right of Fig. 1.3. Grumman Aircraft Engineering Corporation is the contractor for the rendezvous and landing radars. The other G&N units listed are being designed and developed by the MIT Instrumentation Laboratory with associate contractors: AC Spark Plug, Sperry Gyroscope Company, Raytheon Company and the Kollsman Instrument Corporation. Some of the LEM characteristics assumed in the analytical portion of this report are listed on the left table of Fig. 1.3.

The current estimated weights of the various units of the LEM primary G&N system (Ref. 1.1) are summarized in Fig. 1.4. This weight summary does not include the rendezvous and landing radars.

Some of the basic units in the LEM G&N system are identical to those in the CSM G&N system. The significant differences between the two systems are the following:

- a) The CSM will have two computers identical to the one in the LEM except for fixed programming, installation and external covers.
- b) The LEM will use a landing radar which is not required in the other vehicle.
- c) Optical sightings in the LEM will be made with a non-articulating telescope (AOT), as compared to the sextant (SXT) and scanning telescope (SCT) in the CSM.
- d) To aid the astronaut in monitoring and allow changes in the landing site during the powered landing phase, a window reticle or landing display system will be used in the LEM. The operation of this device is described in Section 4.4.4.

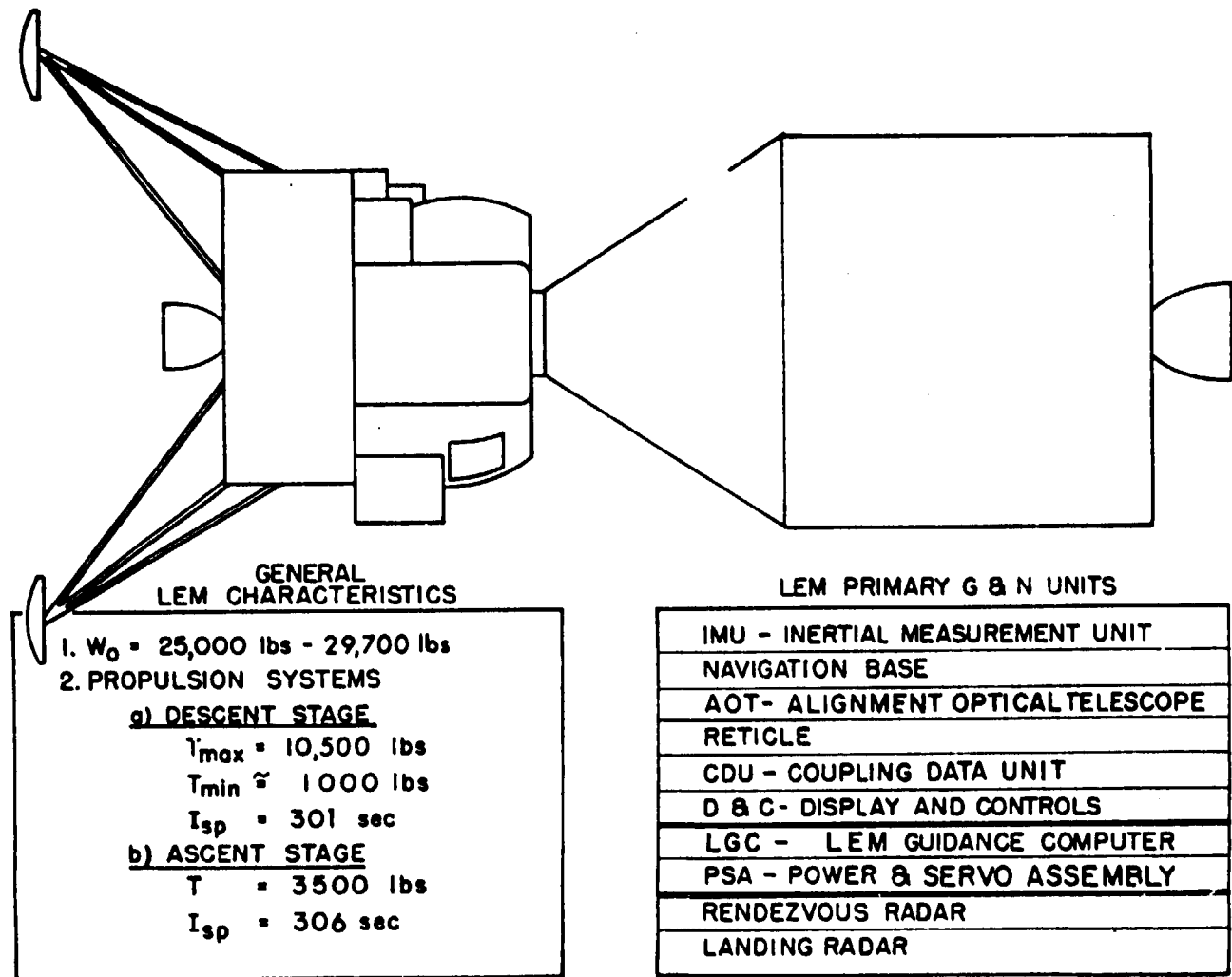


Fig. 1.3 LEM primary guidance and navigation units.

		POUNDS AT 1g
(IMU) INERTIAL MEASUREMENT UNIT	-----	42.0
(LGC) LEM GUIDANCE COMPUTER	-----	41.5
(PSA) POWER AND SERVO ASSEMBLY	-----	24.8
(CDU) COUPLING DATA UNITS	-----	15.0
		<u>123.3</u>
	BARE GUIDANCE SYSTEM	-----
(AOT) ALIGNMENT OPTICAL TELESCOPE	-----	24.5
NAV BASE	-----	0.0
(D&C) DISPLAYS AND CONTROLS		
LGC	-----	19.5
OTHERS	-----	15.0
CABLE	-----	10.0
(RETICLE) EYE REGISTER DEVICE AND TWO DIGIT READOUT	-----	7.0
		<u>199.3</u>
	BASIC SYSTEM	-----
COVERS	-----	6.7
BOOK OF PROCEDURES, ETC.	-----	2.0
		<u>208.0</u>
	TOTAL	-----

Fig. 1.4 LEM G&N weight summary.

[REDACTED]

Development of the CSM primary G&N system may be chronologically divided into two types of hardware called Blocks I and II. Block I designates the earlier hardware, which will be involved in unmanned CSM flights or manned flights of limited duration. Block II includes the later hardware with certain improvements, which will be used in all manned flights of significant duration. Those G&N units in the LEM which are identical to those in the CSM will be of the Block II type.

The primary G&N system in the CSM will not be described in this report, since sufficient literature exists on this system (Refs. 1.2 through 1.9).

A tentative installation of the LEM primary G&N units is shown in Fig. 1.5. The astronaut is shown at the center position between the two windows where the AOT is operated. The landing radar, which is on the descent stage, is not shown.

#### 1.2.2 Inertial Measurement Unit.

The inertial measurement units are identical in the CSM and LEM installations, and are the primary inertial sensing devices on both vehicles. Their three major functions are to:

- 1) Measure changes in spacecraft attitude
- 2) Measure spacecraft velocity changes due to thrust
- 3) Assist in generating steering commands.

To accomplish these functions, the IMU provides an inertial reference consisting of a stable member (see Fig. 1.6) gimbaled in three degrees of freedom and stabilized by three size 25 inertial reference integrating gyros (25 IRIG's). The IRIG's have an angular momentum of  $450,00 \text{ gm/cm}^2/\text{sec}$ . These are floated integrating gyroscopes, and are geometrically positioned with respect to the case by the flotation fluid and a magnetic suspension system (ducosyn). Float angles relative to the gyro case are transmitted by a microsyn signal generator. Fine alignment of the IMU is accomplished by sending pulses to the microsyn torque generators in the gyros.

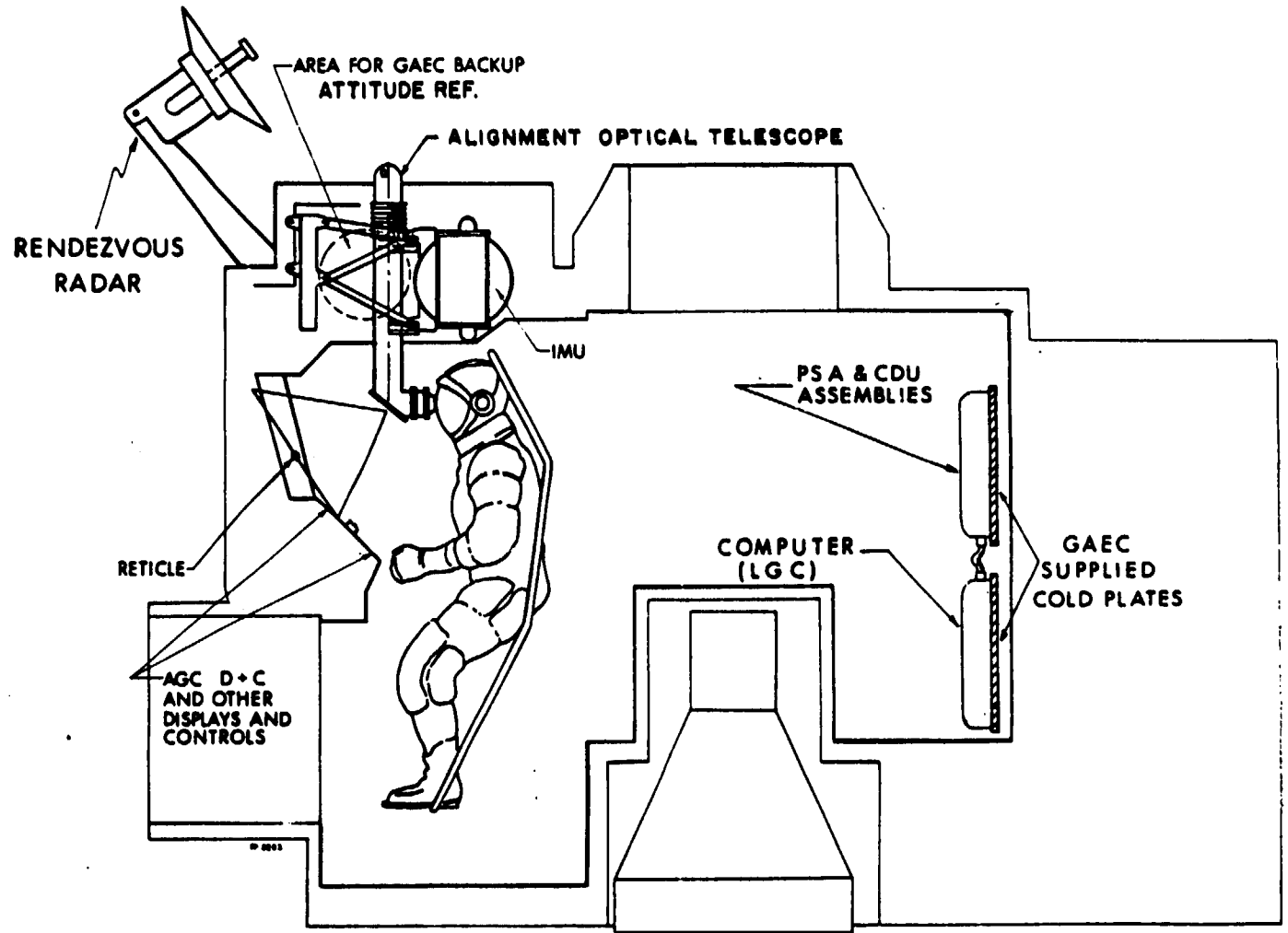


Fig. 1.5 LEM primarily G&N installation.

Fig. 1-6



The middle and outer gimbals and gimbal case are spherical in form. The 12.5 inch diameter gimbal case shown in Fig. 1.7 contains integral coolant passages and provides hermetic sealing of the unit. The location of the IMU in the LEM is shown in Fig. 1.5 and is installed so that the outer gimbal axis is parallel to the X-axis of the LEM (see Fig. 1.2). When the IMU is caged, the middle and inner gimbal axes coincide with the Z and Y axes of the LEM, respectively. This installation was chosen so that gimbal lock could normally be avoided during the LEM mission phases. Gimbal lock occurs when the IMU outer and inner gimbal axes coincide or fall within 10 degrees of each other due to some combination of LEM attitude maneuvers. The procedure for gimbal lock avoidance in the LEM is discussed in Ref 1.10.

The IMU in the LEM will be mounted on a common navigation base or structure with the alignment optical telescope. The manner in which the IMU and optics are mounted on the navigation base in the CSM, is shown in Fig. 1.8.

Each time the IMU is energized, the stable member must be aligned with respect to a predetermined reference by sighting the optical instruments on stars. If the IMU is operated over a prolonged period of time, realignment may be necessary since the gyros, which maintain the space referenced stable member, may drift and cause error in trajectory calculations. The method of IMU alignment in the two spacecraft differs mainly in the optical instruments used for star sightings. The procedure for IMU alignment in the LEM is described in Section 1.3.

Once the IMU is energized and aligned, any rotational motion of the spacecraft will be about the gimbaled stable member, which remains fixed with respect to inertial space. Resolvers, mounted on the gimbal axes, act as angular sensing devices and

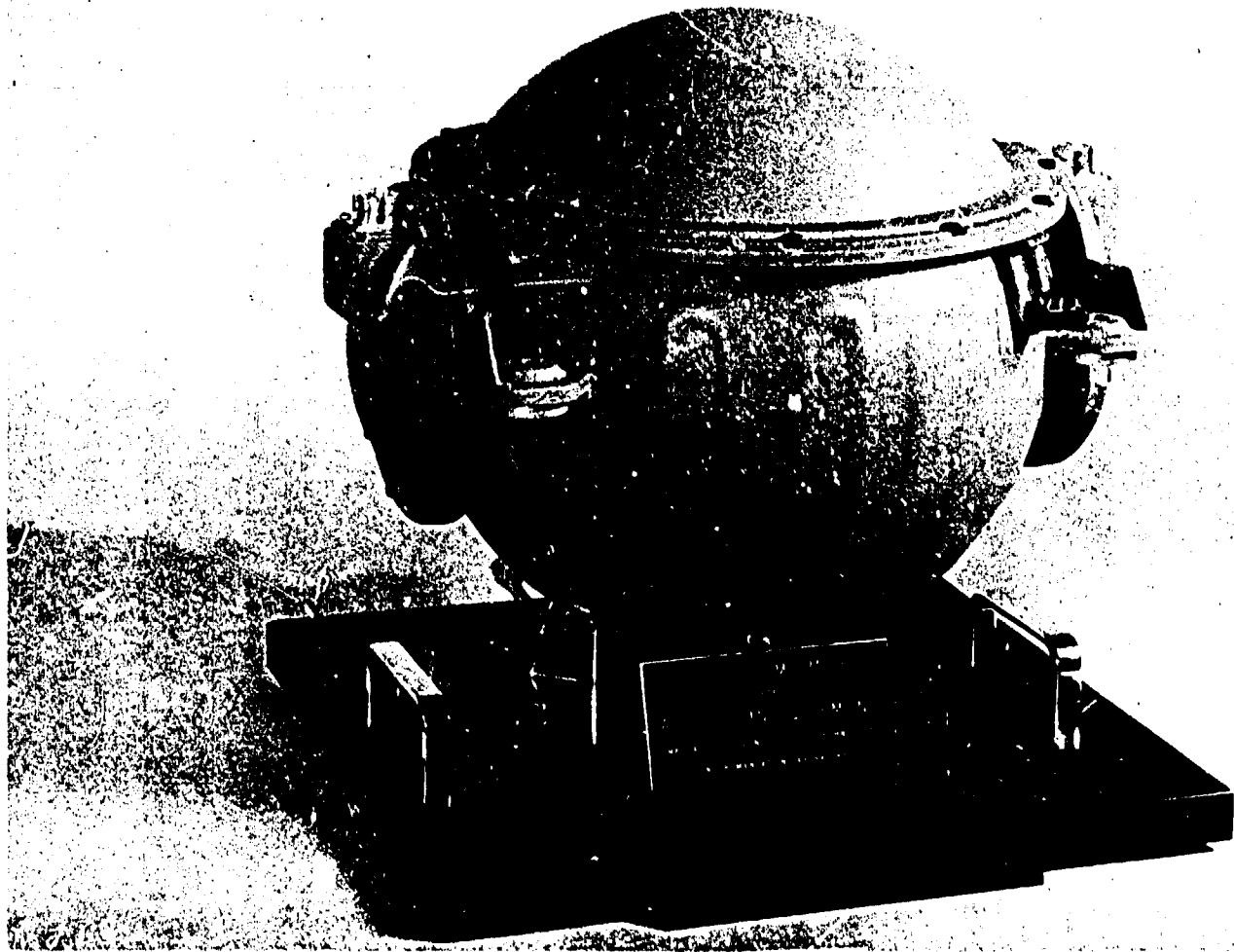
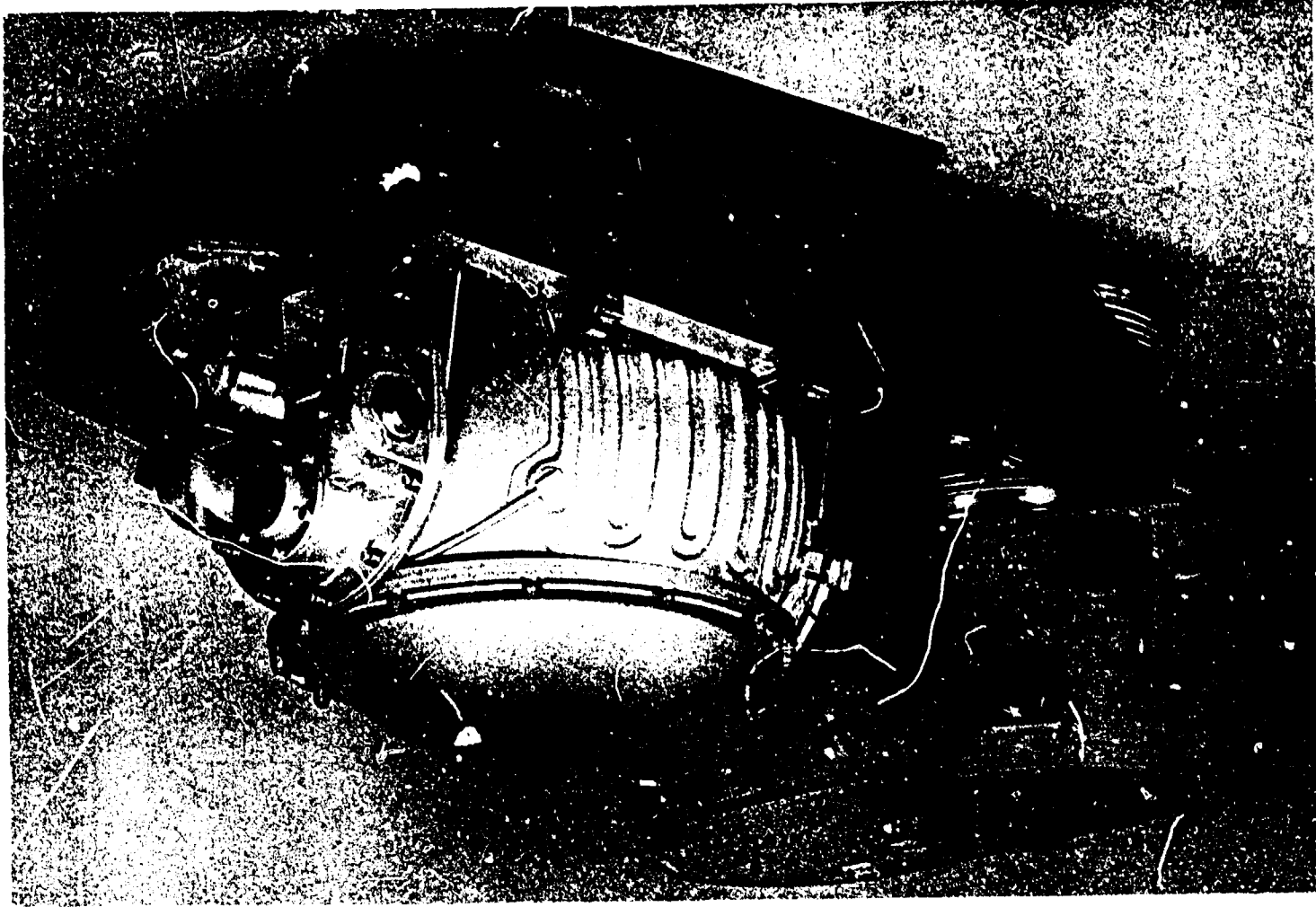


Fig. 1-7

Fig. 1-8 IMU and optics mounted on the navigation base.



measure the attitudes of the spacecraft with respect to the stable member. These angular measurements are sent to the LEM guidance computer (LGC) through the coupling data units (CDUs).

Acceleration of the spacecraft along three mutually perpendicular axes is sensed by three size 16 pulse integrating pendulums (16 PIP's) mounted on the stable member. The PIP's in conjunction with their associated electronics provide velocity increments of the acceleration to the LGC. The PIP's are geometrically stabilized with respect to the case by the flotation fluid and the magnetic suspension (ducosyn). Like the gyros, they contain a microsyn signal generator and torque generator.

The IMU modes of operation can be initiated manually by the astronaut, automatically by the LGC, or by astronaut selection of computer program via the computer keyboard. The status or mode of operation is displayed on the display and control panels and supplied to the computer.

The IMU instrument performance uncertainties presently being used in all LEM primary G&N system analyses are listed in Table 1.1, and represent the expected performance in the lunar environment.

### 1.2.3 LEM Guidance Computer

The primary G&N guidance computers (Refs. 1.6 through 1.9) installed on the CSM (AGC) and LEM (LGC) are identical basic units differing only in fixed programming, installation, and external covers. Two complete and active computers, each having the same functions, will be used in the CSM installation. A single complete guidance computer having the same functions as one of the computers in the CSM will be installed in the LEM. The LEM guidance computer is presently located in the aft equipment bay (Fig. 1.5). A Block I mock-up of two CSM computers, consisting of four trays, is shown in Fig. 1.9. A pictorial of the LGC is shown in Fig. 1.10.

TABLE 1.1  
 IMU CHARACTERISTICS  
 (One Sigma Values)

1.	Accel. Input Axis Non-Orthogonality	0.1 mr
2.	Accelerometer Errors	
	Bias	0.2 cm/sec <sup>2</sup>
	Scale Factor Error	100 ppm
	Accel. Sens. S. F Error	10 ppm/g
3.	Gyro Errors	
	Bias Drift	10 meru
	Accel. Sens. Drift	10 meru/g
	Accel. Squared Sens. Drift	1 meru/g <sup>2</sup>

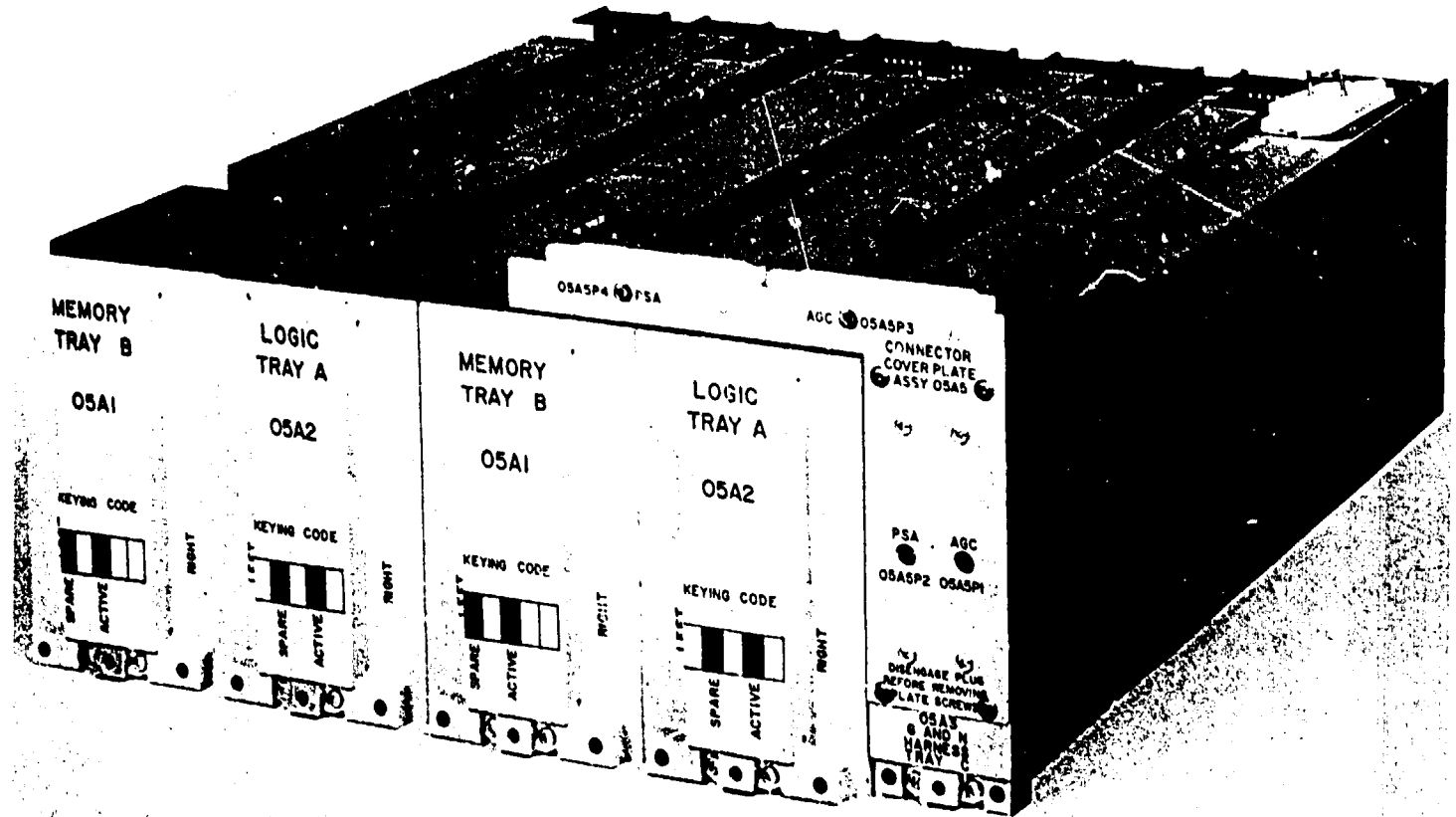


Fig. 1-9 Block I mock-up of two CSM computers.

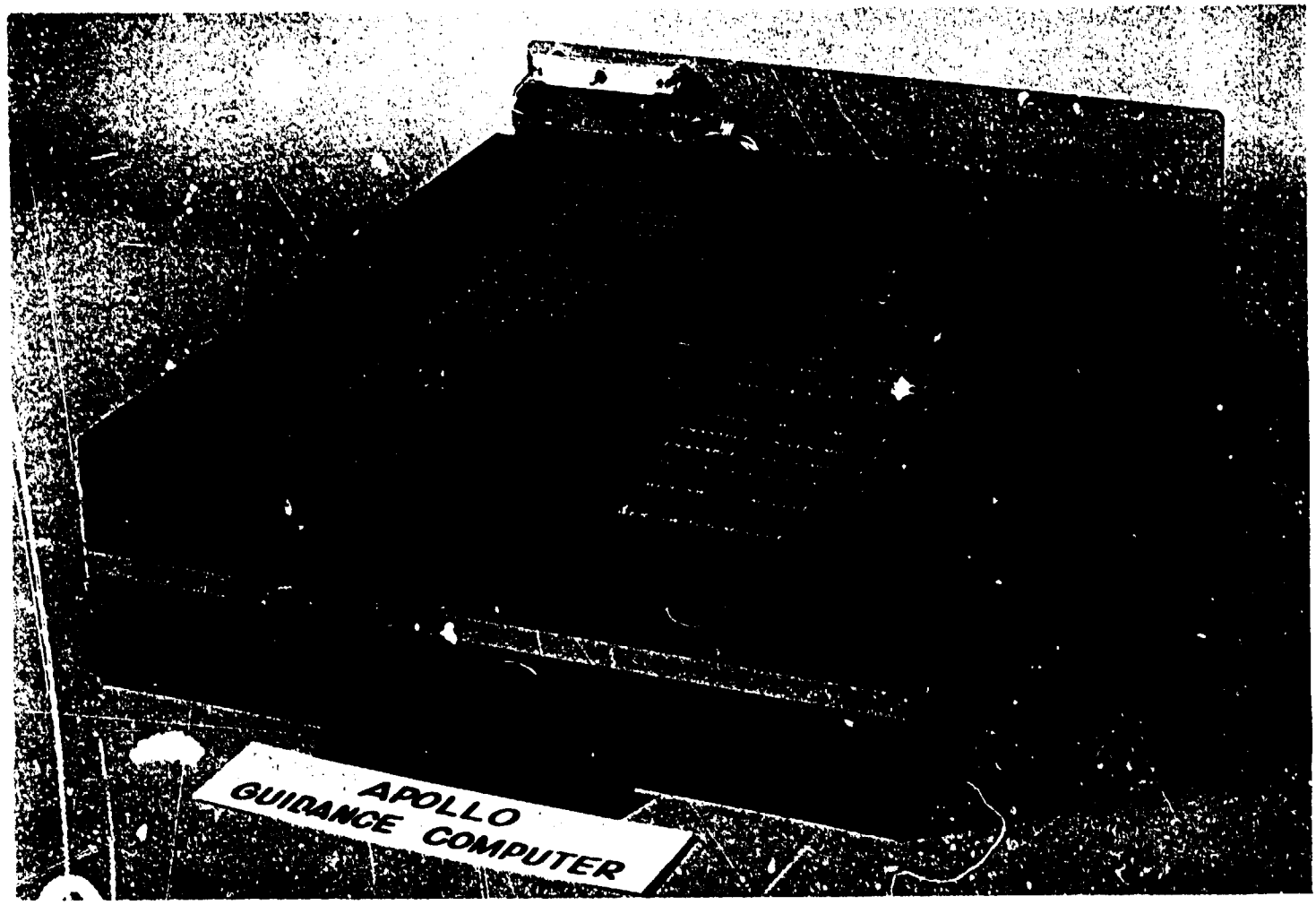


Fig. 1-10

The LGC is the control and processing center of the LEM primary G&N system. It processes data and issues discrete control signals, both for the G&N system and the other spacecraft systems. The LGC is a control computer with many features of a general purpose computer. As a control computer, it aligns the IMU and issues commands to the spacecraft. As a general purpose computer, the LGC solves the guidance and navigation problems. In addition, the LGC monitors the operation of the G&N system.

The LGC stores data pertinent to the flight profile that the spacecraft must assume in order to complete its mission. This data, consisting of position, velocity, and trajectory information, is used by the LGC to solve the guidance and steering equations. The LGC determines the required magnitude and direction of vehicle thrust to achieve the desired mission objectives of each mission phase. The LGC issues both steering and engine throttling commands to the LEM stabilization and control system. The IMU accelerometers sense velocity changes and supply them to the LGC for calculating the total vehicle velocity vector. By means of the Coupling Data Units (CDUs), the LGC is able to drive and read the gimbal angles of the IMU.

In the CSM, the AGC is able to drive and read the shaft and trunnion angles of the optics (sextant and scanning telescope) by means of two optics CDUs. There is no electrical interface between the computer and the alignment optical telescope (AOT) in the LEM installation.

In the CSM, the rendezvous radar angle tracking servos can be slaved to the shaft and trunnion servos of the optics and vice versa. The AGC, therefore, is capable of pointing and commanding an angular search pattern for the radar. When the radar has locked onto the target, the AGC can obtain the radar gimbal angles by having the optics follow the radar. In the LEM, there is no optical interface between the rendezvous radar and the

LGC, however, the LGC will be able to drive and read the radar gimbal angles by means of two radar CDUs.

In both spacecraft, the computer receives range, range rate and various discrete signals directly from the rendezvous radar which indicate that radar power is on, angle lock-on has been achieved, etc. The LGC in the LEM receives the altitude, three components of doppler velocity, and discrete signals from the landing radar similar to those for the rendezvous radar. A more complete description of the interface between the computer and the radar systems is given in Sections 1.2.5, 1.2.8 and 1.2.9.

The uplink word from the spacecraft telemetry system originates in ground based stations and is supplied to the LGC. This word provides ground based operators with a computer control capability similar to that available with the Display & Controls (D&C).

Data specifically selected by program functions is used to compose downlink words, which are supplied to the spacecraft telemetry system for transmission to ground based stations.

The LGC is an automatic, digital computer with parallel internal transfer and a large fixed rope core memory for guidance programs. It has an additional erasable ferrite core memory sufficient to meet the operational requirements of all mission phases.

Some of the general characteristics of the LGC are listed in Table 1.2. The LGC uses the one's complement binary number system in its data manipulations. In this system, the negative binary number is the complement of the corresponding positive binary number. The LGC can only perform the addition operation. To subtract, it must add the complement of the subtrahend. Multiplication is performed by successive additions and shifting. Division is performed by successive additions of

TABLE 1.2  
TENTATIVE LGC CHARACTERISTICS

<u>WORD LENGTH:</u> 16 Bits (15 B's + Parity)	
<u>NUMBER SYSTEM</u> One's Complement, with Overflow Correction	
<u>MEMORY CYCLE TIME</u> (MCT)	11.7 $\mu$ sec
<u>WIRED-IN MEMORY</u> (CORE ROPE)	24,576 Words
<u>ERASABLE MEMORY</u> (Coincident Current Ferrite)	1024 Words
<u>NORMAL ORDER CODE</u>	11 Instructions
<u>INVOLUNTARY INSTRUCTIONS</u> (Interrupt Increment, Load, Start)	8 Instructions
<u>INTERRUPT OPTIONS</u>	5 Options
<u>ADD INSTRUCTION TIME</u>	23 $\mu$ sec
<u>MULTIPLY</u> (Excluding Index)	93.6 $\mu$ sec

TABLE 1.2 (Cont)  
TENTATIVE LGC CHARACTERISTICS

<u>DOUBLE PRECISION ADD SUBROUTINE</u> $(X + x) + (Y + y) = (Z + z)$	234 $\mu$ sec
<u>DOUBLE PRECISION MULTIPLY</u> <u>SUBROUTINE</u>	971.1 $\mu$ sec
<u>COUNTER INCREMENTING</u>	11.7 $\mu$ sec
<u>NUMBER OF COUNTERS</u> (Input)	20 Counters
<u>DISCRETE INPUT REGISTERS</u>	4
<u>DISCRETE OUTPUTS REGISTERS</u>	5
<u>PULSED OUTPUTS UNDER PROGRAM</u> <u>CONTROL</u>	25
<u>PULSED OUTPUTS NOT UNDER PROGRAM</u> <u>CONTROL</u> (Timing Signals for S/C And G&N)	16
<u>TELEMETRY:</u>  Signal Processing for Both Up Telemetry (or Pace Digital Command System) and Down Telemetry	

complements and shifting. The basic word length of the LGC is 15 bits, plus a parity bit for parity check. Routines are available for double and triple precision. The logical manipulations within the LGC are implemented using micrologic NOR elements.

The oscillator for the LGC is the frequency standard for all of the G&N and spacecraft systems. It is a 2.048 megacycle, crystal-controlled, transistor oscillator with an oven for thermal regulation. The computer uses, as its clock signals, four phases of the 1.024 mc square wave obtained from a binary division of the oscillator output. One more binary division produces the 512 kc signal, which serves as a synchronizing signal to the spacecraft systems clock. Further frequency division provides timing signals for the operation and synchronization of the electro-mechanical parts of the guidance system and for other sequential control processes with which the computer is concerned.

The LGC has two modes of operation. In the idle mode, the LGC simply keeps track of time and consumes about 10 watts, whereas, in the normal mode, the power consumption will be about 100 watts.

#### 1.2.4 Display and Controls

The purpose of the display and controls (D&C) is to provide the astronaut with an indication of various conditions within the G&N system, and to permit him to instigate and control various functions. Information on the D&C of the CSM may be obtained in Refs. 1.2, 1.3, and 1.5.

A possible G&N display and control configuration in the LEM is shown in Fig. 1.11. At the top of the figure is the alignment optical telescope (AOT) with its controls for viewing position and reticle rotation and visual readout of the reticle rotation angle. Immediately below the AOT is the main display area which will contain displays and controls for the primary G&N system. The G&N displays indicated in Fig. 1.11 are only

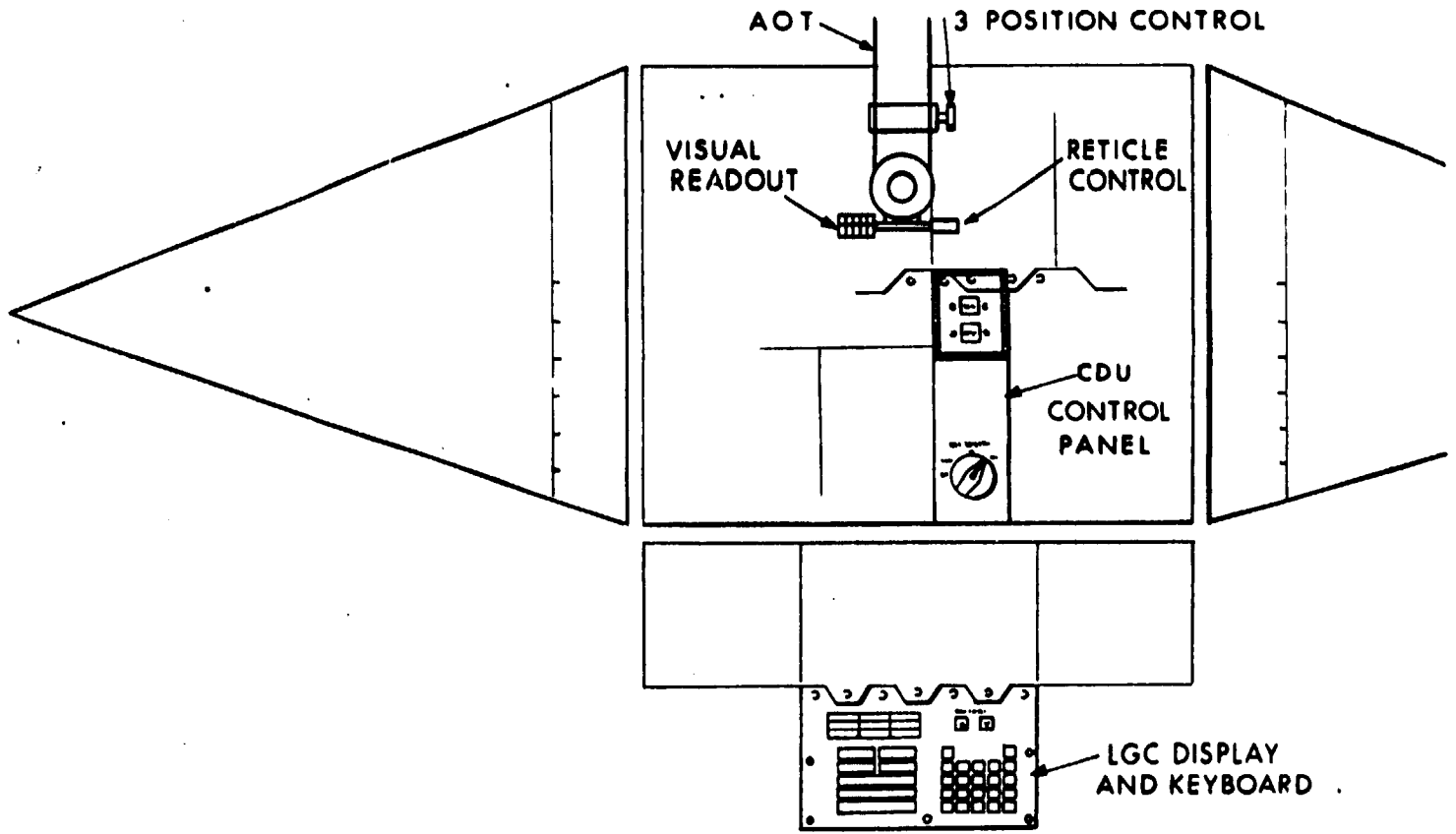


Fig. 1.11 Preliminary LEM D&C installation.

tentative at the present time, and may be changed as more detailed design is completed.

The primary G&N computer display and keyboard (DSKY) are shown below the main display area in Fig. 1.11. The computer display and keyboard are shown in greater detail in Fig. 1.12. The DSKY allows the astronauts to load information into the LGC, to initiate various program functions, and to perform tests on the computer and other portions of the G&N system. In addition, the DSKY indicates failures in the LGC, displays the program functions being executed by the LGC, and can display specific data selected by the keyboard input. The DSKY also functions to route data from the LGC to the IMU and the spacecraft. Commands for switching operation to different modes are supplied to the IMU, and data is supplied to the spacecraft telemetry system. In conjunction with the LGC, the DSKY supplies alarm indications to the spacecraft and the IMU.

The computer display in Fig. 1.12 consists of three two-digit displayed numbers labelled "program," "verb," and "noun" and three five-digit general word read-out displays. The two-digit displays are coded for various modes and instructions. The "program" display indicates the major operation mode of the computer, such as "lunar landing maneuver." The "verb" and "noun" displays are used together and coded to give possibilities of meaningful phrases or instructions. Examples of typical verb and noun combinations are:

<u>Verb</u>	<u>Noun</u>
Display Value	Velocity
Compute	Abort Velocity
Read in	Landmark Angle

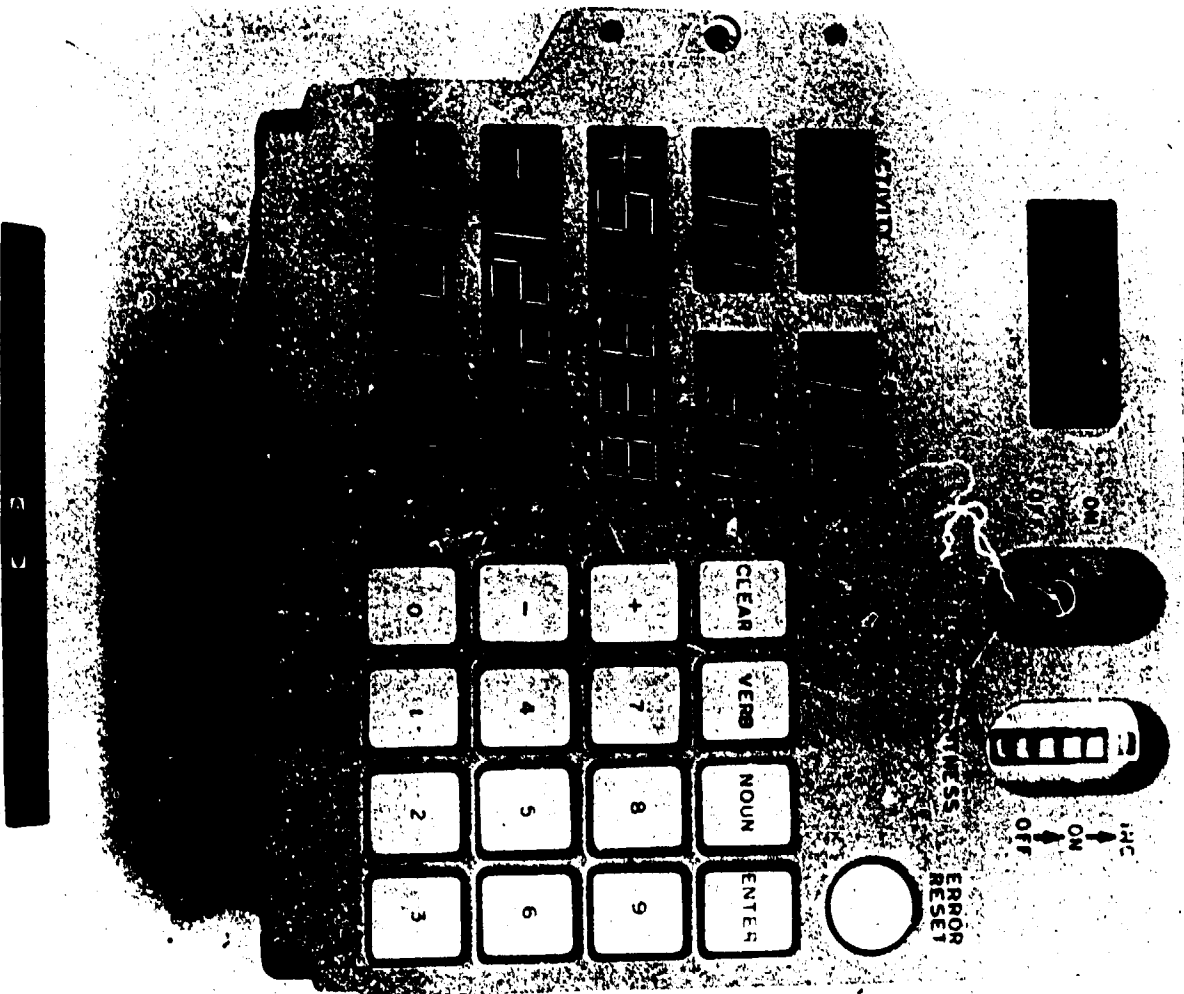


Fig. 1-12 Primary G&N computer display and keyboard.

When the computer wishes to communicate a request for data, or signal an alarm to the astronaut, the "verb" and "noun" numbers flash until the astronaut takes action. The astronaut enters data into the computer through the 12 button keyboard.

#### 1.2.5 Coupling Data Units.

The coupling data units (CDUs) are used to transfer angular information between the guidance computer and the IMU, optics, rendezvous radar and the spacecraft stabilization and control system (SCS). The CDUs in the LEM installation are presently scheduled to be located behind the astronauts in the aft equipment bay, as shown in Fig. 1.5. The CDU is essentially an analog to digital and digital to analog conversion device. There are five identical CDUs in each spacecraft.

Three of the five CDUs are used with the IMU in each spacecraft to provide gimbal angle readout to the computer. They are also used for coarse alignment of the IMU by the computer. In addition, the three IMU CDUs are used by the computer when generating attitude steering error signals for the SCS.

The other two CDUs in the CSM permit the AGC to drive and read the shaft and trunnion angles of the sextant and scanning telescope. Since the rendezvous radar can be slaved to the optics in the CSM, and vice versa, the AGC has essentially the same capability with respect to the radar. In the LEM, the remaining two CDUs are used by the LGC to drive and read the gimbal angles of the rendezvous radar.

A general idea of CDU operation is shown in Fig. 1.13, where the CDU is connected to one of the antenna gimbal servos of the LEM rendezvous radar. The LGC is required to point and possibly generate an angular search command for the radar. To simplify the CDU description, the following operational description will be confined to just one of the two radar CDUs. Assuming

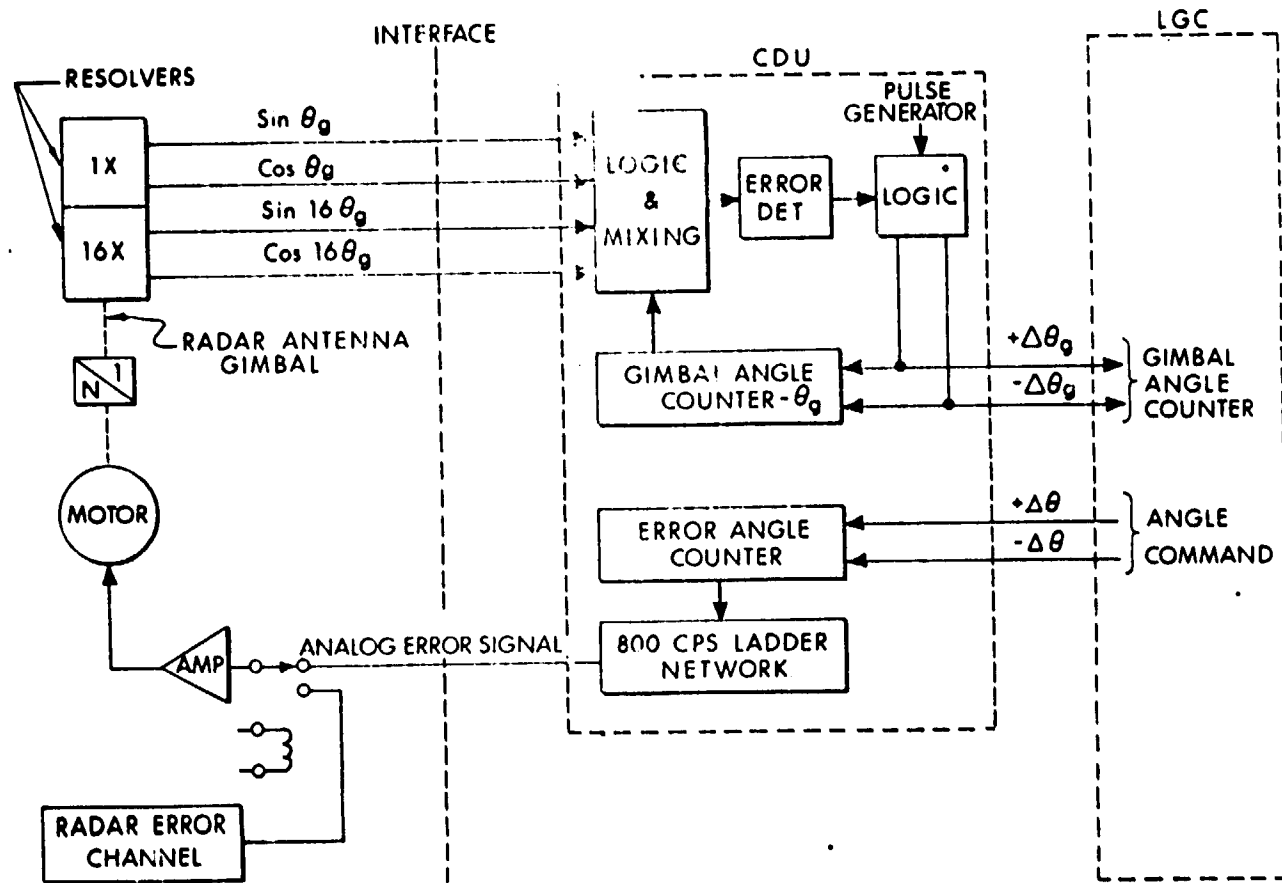


Fig. 1.13 Radar - G&N angle interface on LEM.

that radar power has just been turned on, the LGC first clears its own gimbal angle counter and the two counters in the CDU. The LGC then transmits a serial pulse train to the error angle counter where each pulse corresponds to an increment  $\Delta\theta$  of the total commanded gimbal angle. The error angle counter, in conjunction with a ladder network, converts this digital quantity into an 800 cps amplitude and phase modulated signal which drives the rendezvous radar antenna gimbal servo. Two transmitting resolvers on the antenna gimbal (1 speed and 16 speed) return signals to the CDU logic network, which is essentially an analog to digital converter. Any difference between the angle, represented by the resolver signals and the digital angle in the gimbal angle counter, causes pulses to be generated which update the gimbal angle counter and the LGC counter. When the radar detects the target, it transfers control of the gimbal servos to its own microwave error channels for automatic tracking. The LGC is notified by a discrete radar signal that "lock-on" has been achieved, and there is no further need for angle commands. After automatic radar tracking has been achieved, the gimbal angle counter in the LGC is continuously updated.

#### 1.2.6 Power and Servo Assembly.

The power and servo assembly is a support item and is used in all operations involving the IMU and LGC. It provides various levels and types of d-c and a-c power to the rest of the G&N system. In addition, it serves as a location for various other support electronics, such as the servo control amplifiers for the IMU. The LEM installation of the PSA is shown just above the LGC in the aft equipment bay of Fig. 1.5. The LEM and CSM PSA units are essentially identical, except for installation. A Block II mock-up of the PSA in the CSM is shown in Fig. 1.14.

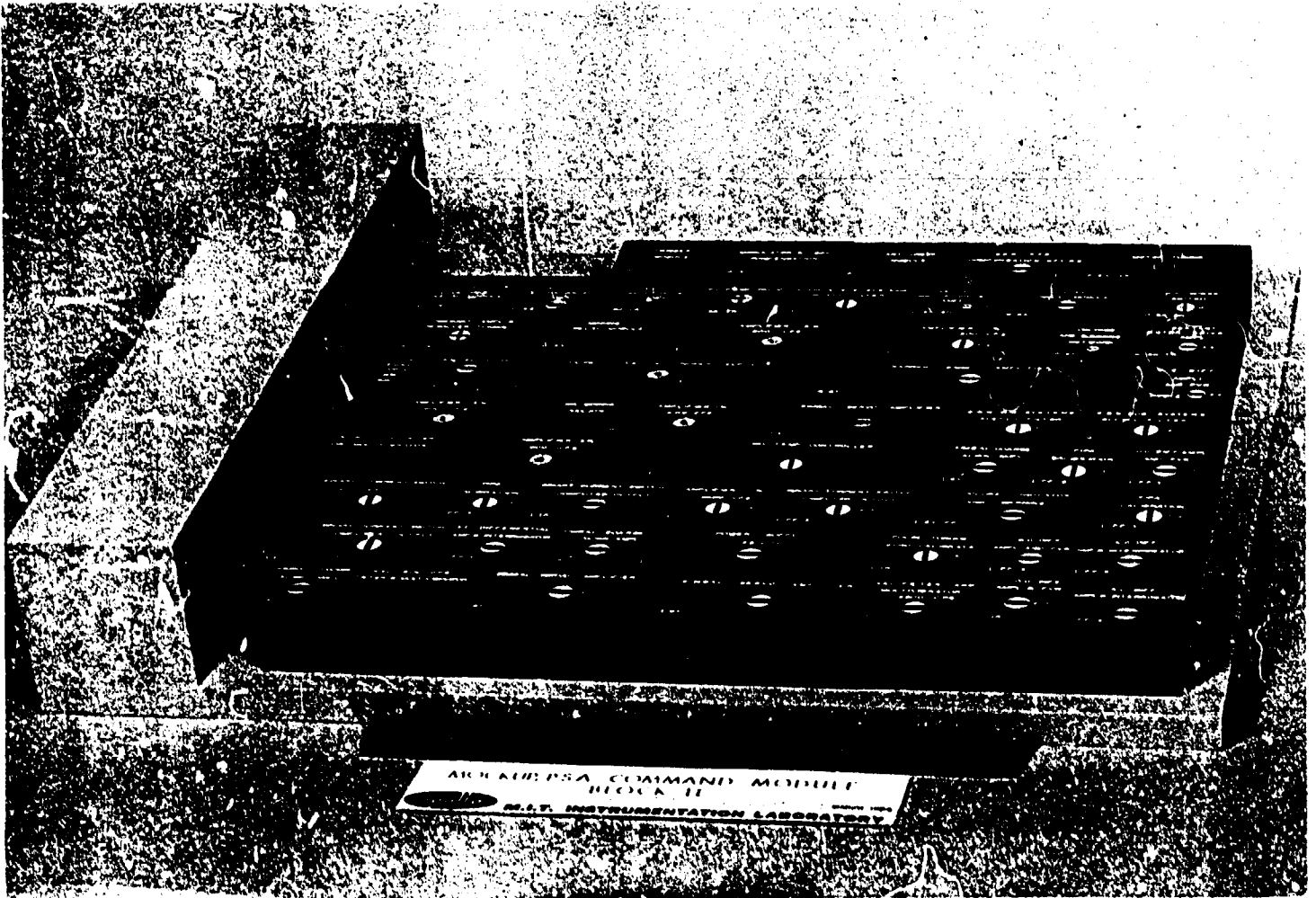


Fig. 1-14

### 1.2.7 Alignment Optical Telescope.

The primary purpose of the alignment optical telescope (AOT) is alignment of the IMU in the LEM during free-fall and prior to launch from the lunar surface. It may also be used during free-fall to determine the direction of the CSM if it is visible. Location of the AOT is shown in Fig. 1.5 directly ahead of the IMU.

The AOT is a unity power periscope with a 60 degree field of view. The shaft axis of the telescope will be parallel to the

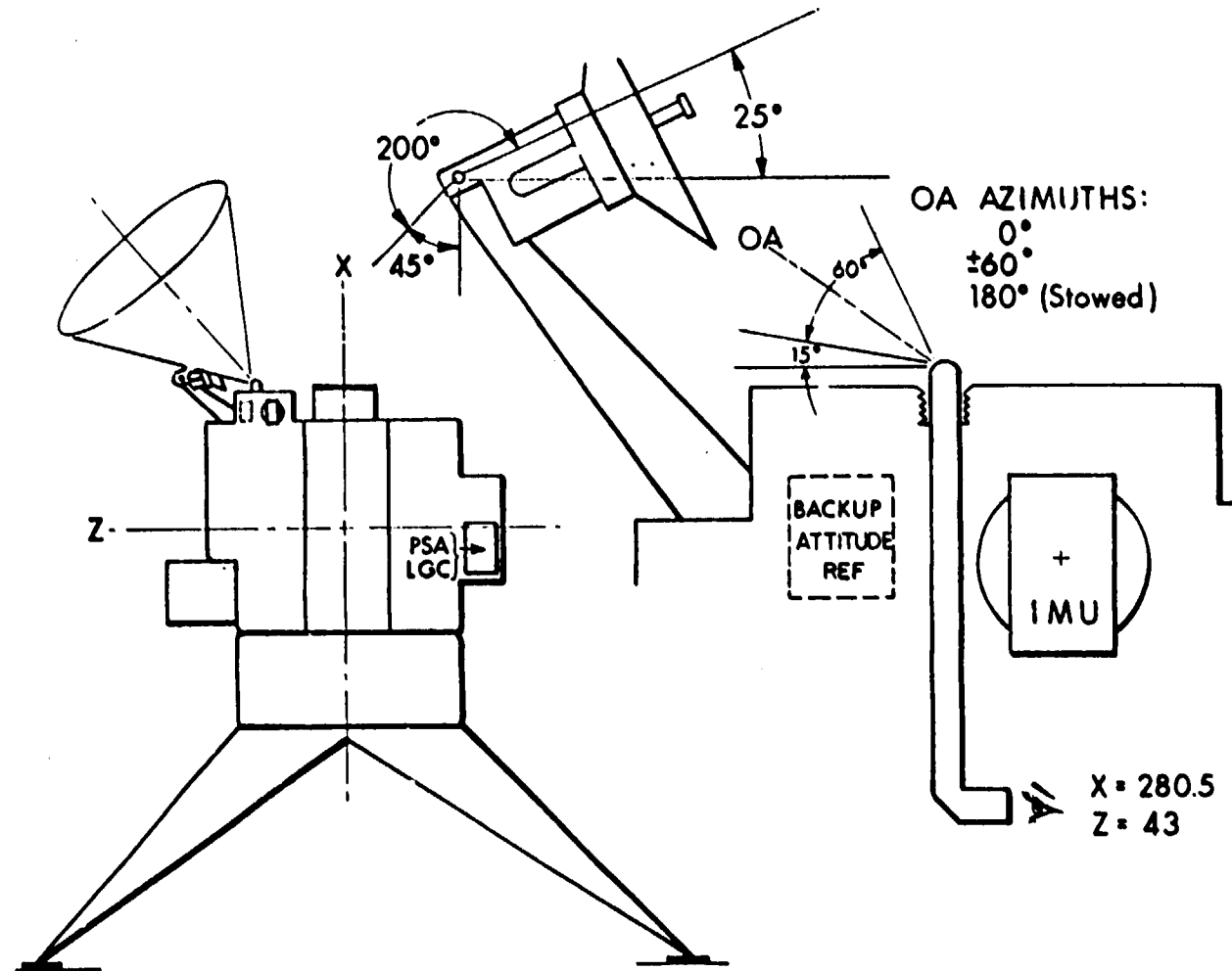


Fig. 1.15 G&amp;N installation.

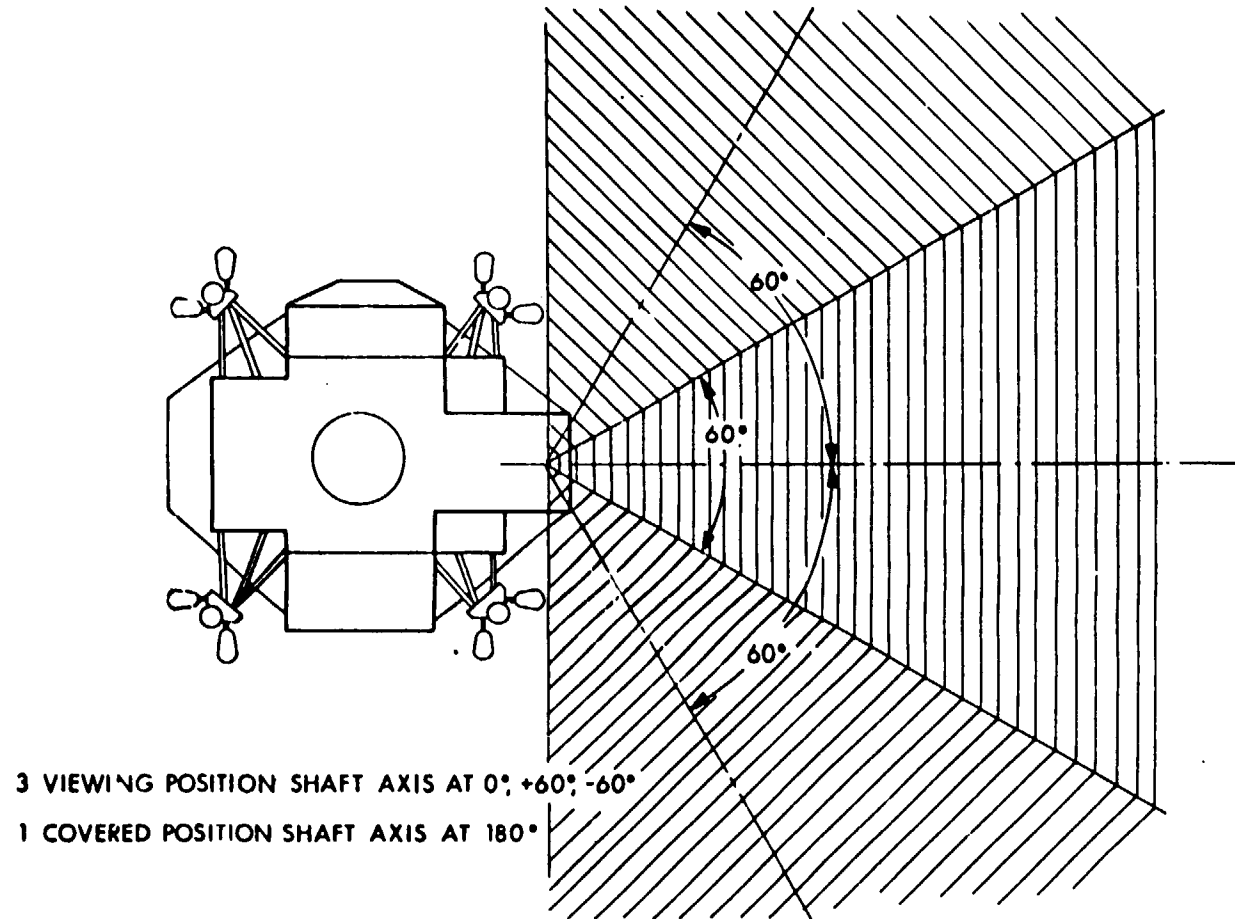


Fig. 1.16 LEM AOT azimuth positions.

- 1) There is very little difference in complexity or weight between two and three positions.
- 2) The addition of a third viewing position increases the number of reasonably bright stars available for measurements.
- 3) The addition of a third viewing position also increases the likelihood of finding two reasonably bright stars separated by an angle approaching 90 degrees, which is optimum for IMU alignment.

The AOT reticle pattern presently considered for the AOT is shown in Fig. 1. 17 along with the manner in which it is used for IMU alignment on the lunar surface. Basically, the pattern consists of two straight lines (arbitrarily called X and Y) and a spiral. The spiral is so constructed as to depart radially from the center as a linear function of rotation about the center. By turning a knob near the eyepiece (see Fig. 1. 11), the astronaut can rotate the entire reticle pattern about the center of the field of view. A micrometer type readout is provided near the knob to indicate the amount of reticle rotation. The operation of the AOT for IMU alignment will be described in more detail in Section 1. 3.

#### 1. 2. 8 Rendezvous Radar.

The current rendezvous radar design (Ref 1. 11 through 1. 13) is an X-band, interrupted-continuous-wave, amplitude comparison, mor. pulse radar that can acquire and accurately track a transponder (on the other vehicle) at any range between 400 nm and 50 feet. Essentially identical radars will be installed on the CSM and LEM. The location of the rendezvous radar in the LEM is shown in Fig. 1. 5. Both CSM and LEM radar systems will usually operate simultaneously, and any mutual interference is prevented by using different microwave frequencies. The

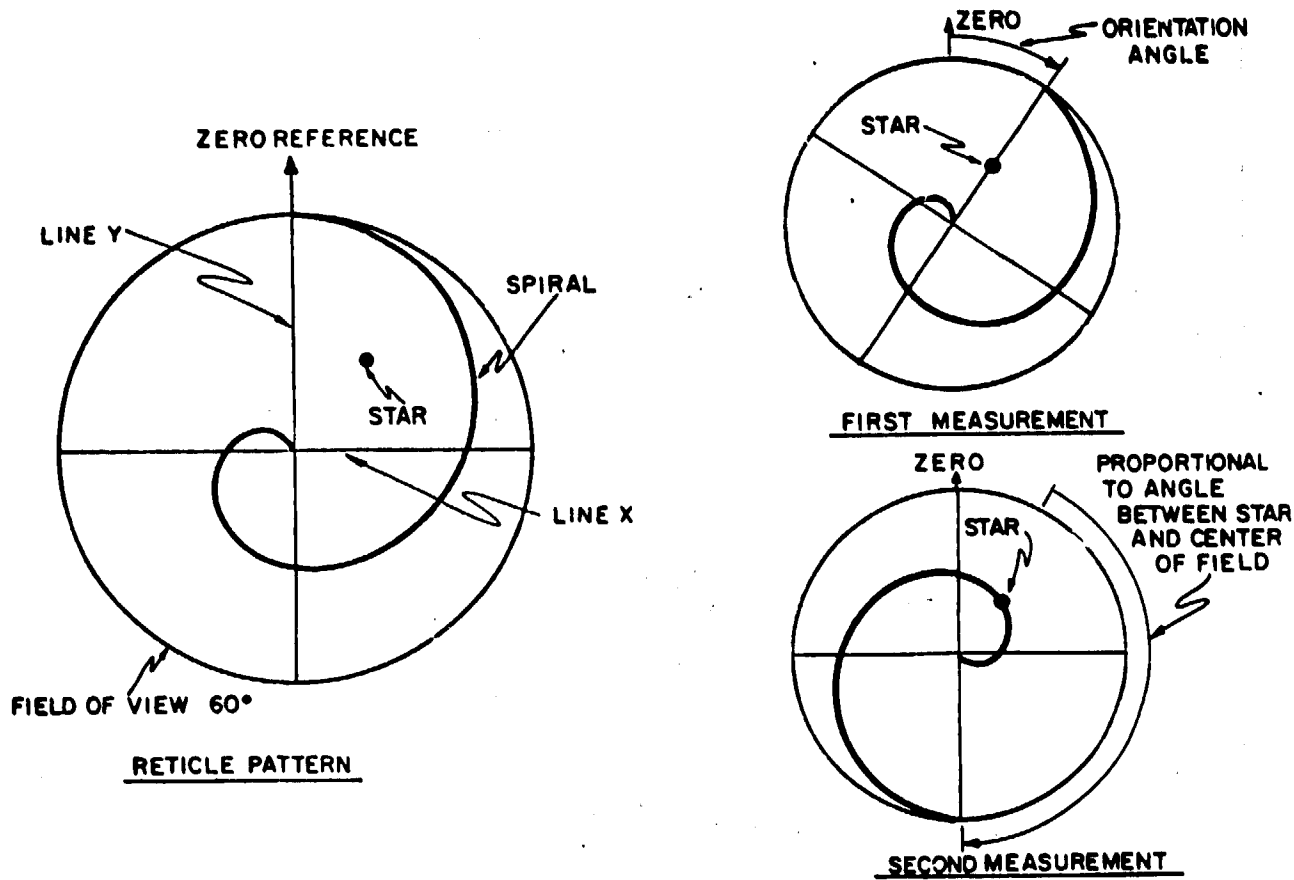


Fig. 1.17 AOT reticle pattern - lunar surface IMU alignment.

parameters measured by the radar for the primary G&N system are range, range rate, and the angle of the line-of-sight.

The current radar design consists of a 2 foot, 4-horn cassegrain antenna which is gyro stabilized and gimballed about two axes. The angular coverage provided by the LEM rendezvous radar is shown in Fig. 1.18. Resolvers are provided on each gimbal for angle readout to the LGC through the CDUs. The angle interface was described in Section 1.2.5.

The rendezvous radar range tracker has two modes of operation: the variable pulse repetition frequency (PRF) mode is used for ranges between 1000 feet and 400 miles, and the fixed PRF mode is used for ranges less than 1000 feet. In the variable PRF mode, the range derived by the range tracker is used to control the PRF. In the fixed PRF mode, the PRF is locked at 250 kilocycles. Range rate is obtained with a frequency tracker which measures the doppler shift of the received signal.

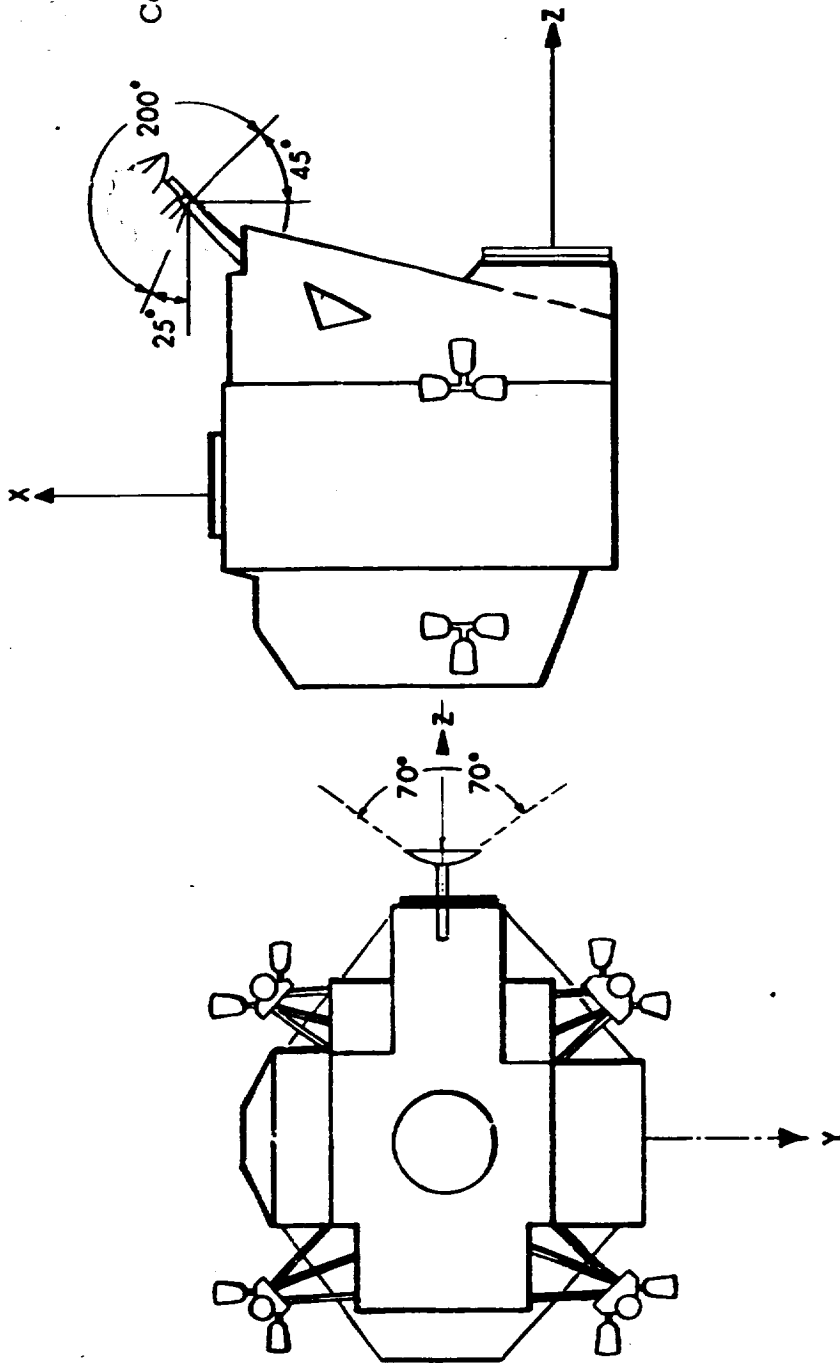
The LGC will be capable of pointing the radar by means of two CDUs for CSM acquisition. If the CSM is not acquired upon initial pointing, the LGC will generate an angular search pattern for the radar.

The LGC is provided with three discrete signals from the radar. One of these discrettes indicates that radar power is on and that the radar is ready to be commanded in angle by the LGC for CSM acquisition. A second discrete indicates when the radar has achieved angle lock-on, so that the LGC may stop angular commands. A third discrete indicates that the radar is working properly and the data is good, and ready to read into the LGC.

The primary G&N system specifications (Ref. 1.12 and 1.13) for the rendezvous radar are given in Table 1.3.

#### 1.2.9 Landing Radar

The Landing Radar (LR) will be an X or K - band 4 beam



Coverage S

Fig. 1.18 LEM rendezvous radar angle limits.

TABLE 1.3  
RENDEZVOUS RADAR SPECIFICATIONS

1. Required Operating Limits	Range (R) nm	Range Rate ( $\dot{R}$ ) fps	Range Accel. ( $\ddot{R}$ ) fps <sup>2</sup>
Maximum	400	$\pm 4900$	50
Minimum	50 ft	1	0
Typical Orbital Conditions Rendezvous Phase	220	$\pm 1000$	1

2. Desired Performance ( $3\sigma$ )

Angle Uncertainty (Random Error)	3 mr
Angle Uncertainty (Max. Fixed Bias WRT IMU Axes)	15 mr
Range Rate Accuracy	1% $\pm$ 1 fps
Range Accuracy	1 % $\pm$ 5 ft.

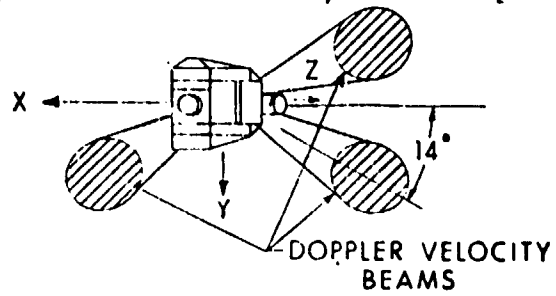
doppler altimeter and velocity radar that provides the LGC with the three components of doppler velocity and the range along the altitude beam during the latter portion of the powered landing maneuver.

The LR antenna assembly will consist of a transmitting antenna and four receiving antennas (Ref. 1.14). The four beams of the transmitting antenna will be generated by two separate mechanically interleaved slotted waveguide arrays: one for the altitude beam, and one for the three velocity beams. The receiving portion of the antenna assembly will consist of three velocity receptors tilted away from the plane of the transmitting antenna, and an altitude receptor in the plane of the transmitting antenna. The beam configuration will probably be that shown in Fig. 1.19.

The landing radar is actually two separate radar systems (doppler velocity and altimeter) which share a common antenna assembly. The radar circuitry is identical for both radar systems through the pre-amplifiers. After the pre-amplifiers there is a slight difference between the two radar systems in the search-acquire-track stages. The doppler velocity radar is a continuous-wave system, meaning there is no modulation of the transmitted signal. The altimeter, however, must use some form of modulation in order to measure altitude. At present, the transmitted signal of the altimeter is frequency modulated by a linear sawtooth waveform. For reliability reasons, both systems use only solid-state components.

During the latter portion of the LEM powered landing maneuver the primary G&N system requires measurements from the landing radar to up-date its knowledge of altitude and velocity. The powered landing maneuver is divided into three major phases (see Section 4.1) which are chronologically the inertial phase (Phase 1), the constant attitude phase (Phase 2), and the hover and touchdown phase (Phase 3). Both altitude and velocity measurements are required of the radar in Phases 2 and 3.

PHASE 2 OF LANDING MANEUVER  
(VISIBILITY PHASE)



PHASE 3 OF LANDING MANEUVER  
(HOVER AND TOUCHDOWN)

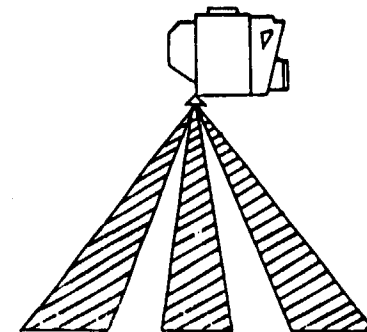
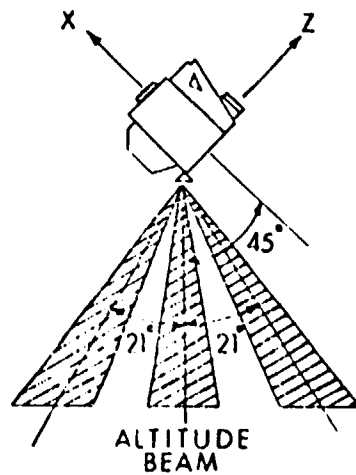
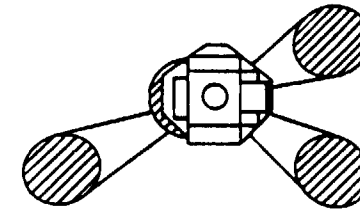


Fig. 1.19 LEM landing radar antenna positions.

TABLE 1.4  
LANDING RADAR SPECIFICATIONS FOR PRIMARY GUIDANCE MODE

Operating Limits:	Altitude	Altitude Rate	Velocity
Maximum	70,000 ft. *	- 500 fps	2200 fps
Minimum	5 ft.	1 fps	1 fps
Typical Maximum Operating Region	20,000 ft.	- 250 fps	2000 fps

\* Potential Requirement for Radar Check-out

PERFORMANCE REQUIREMENTS FOR TYPICAL OPERATING REGION (3 $\sigma$ )

Altitude Accuracy	1% $\pm$ 5 ft.
Velocity Accuracy	1% $\pm$ 1 fps
Boresight Uncertainty Relative to IMU	20 mr *

\* Tentative specification

In addition, radar altitude measurements are used during the latter portion of Phase 1. To insure accurate altitude data, the altitude measuring beam should be directed along or near the vertical to take advantage of lunar specular reflection. It is for this reason that the LR antenna assembly will have two fixed positions with respect to the spacecraft (see Fig. 1.19) which are optimum for the 2nd and 3rd phases of the powered landing maneuver. During the latter portion of Phase 1, the altitude beam will not be vertical; however, the altitude can be obtained in the computer by resolving the range measured by this beam.

The LGC is able to command the LR antenna assembly from the position used in Phase 2 to the position used in Phase 3, and is provided with a discrete signal from the LR indicating which position is present. In addition, the LGC receives two discrete signals from the landing radar indicating when the velocity and altitude data are good and are ready to be read into the LGC.

The specifications (Refs. 1.12 and 1.13) for the landing radar are given in Table 1.4.

### 1.3 IMU Alignment

#### 1.3.1 General Comments

The process of IMU alignment consists of using optical sightings on stars to align the stable member with reference to an inertial frame. The IMU requires alignment each time it is energized or after a prolonged operation during which gyro drift has caused appreciable error in stable member alignment. Star sightings for IMU alignment are made with the sextant in the CSM and with the AOT in the LEM. The alignment procedure is essentially the same in both vehicles except for the manner in which the optics are used to sight the stars.

In order to simplify the interface for alignment of the LEM back-up attitude reference assembly, it has been decided

that the alignment of the stable member axes in the LEM IMU will be as follows for the descent and ascent phases:

1.  $+ X_{SM}$  (stable member X axis) parallel to the vertical at the landing site and directed upward.
2.  $+ Y_{SM}$  normal to CSM orbital plane and parallel to the CSM orbital angular velocity vector.
3.  $+ Z_{SM}$  parallel to the horizontal at the landing site and forming a right handed set with the other two axes.

The alignment procedure for the IMU will consist of both a coarse and fine alignment, depending upon whether the alignment errors are small or large. A coarse alignment will be made prior to the fine alignment whenever the stable member orientation differs from the desired orientation by more than about one degree. Such would be the case if the IMU had just been energized or caged. There are at least two occasions when coarse alignment will be performed on the LEM IMU and these occur when the LEM is first separated from the CSM and prior to launch from the lunar surface.

Other instances requiring coarse alignment are not normally encountered, but would be when gimbal lock occurs (Section 1.2.2) or excessive gyro drift has occurred over a prolonged period.

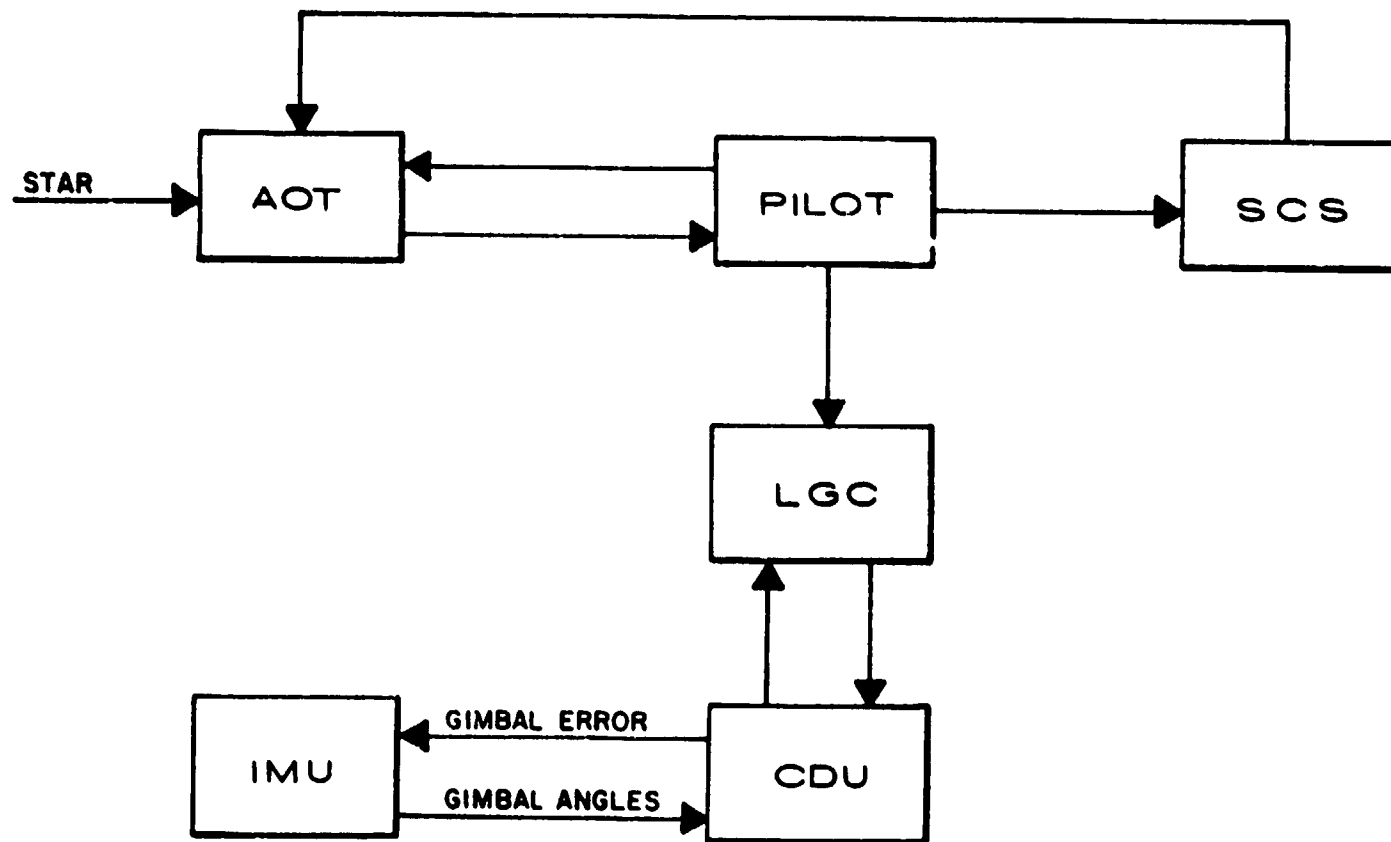
### 1.3.2 Coarse Alignment

There are a number of techniques being considered for providing the LGC with the information necessary for it to perform a coarse alignment of the IMU, depending upon when and where the alignment is to be made. Some of these will be considered in this report.

If coarse alignment is made prior to physically separating the LEM from the CSM (see Fig. 1.3), the required information can be entered into the LGC by star sightings with the AOT or by

duplicating the alignment present in the CSM IMU, which has previously been aligned. Use of the AOT at this time will depend upon whether the telescope's viewing positions are unobstructed by the CSM. It was mentioned in Section 1.2.7 that the AOT viewing positions might be the reverse of those shown in Fig. 1.6 in order to keep the rendezvous radar antenna out of the field of view. However, a reversal of the viewing positions may cause obstruction of the field of view by the CSM when the LEM is attached to the CSM (Fig. 1.3).

The manner in which coarse alignment is performed during free-fall is indicated by the flow diagram in Fig. 1.20. The astronaut takes optical sightings with the AOT on at least two stars, usually by manually controlling the vehicle attitude with the stabilization and control system (SCS). There are a number of techniques for taking star measurements with the AOT and it is possible that the same technique will be used for both coarse and fine alignment. Most of these techniques will be considered later in the fine alignment procedure. However, at the moment, a simple sighting technique shall be assumed for coarse alignment, which requires the astronaut to orient the vehicle so that the desired star is at the center of the telescope's field of view which he indicates (marks) to the LGC when this is accomplished. Each time the LGC receives a mark signal, it reads the IMU gimbal angles via the CDU's. Using the indicated angles of the stars, the LGC transforms the star lines-of-sight into stable member coordinates and compares them with the star lines-of-sight components that would exist if the stable member were properly aligned. The differences are used to compute the angular rotation about each stable member axis which will carry the stable member into the correct orientation. The computer then executes the coarse alignment by sending angular commands to the gimbal servos via the CDU's. It is obvious that the accuracy of the star sighting technique



45

Fig. 1.20 Coarse IMU alignment during free fall.

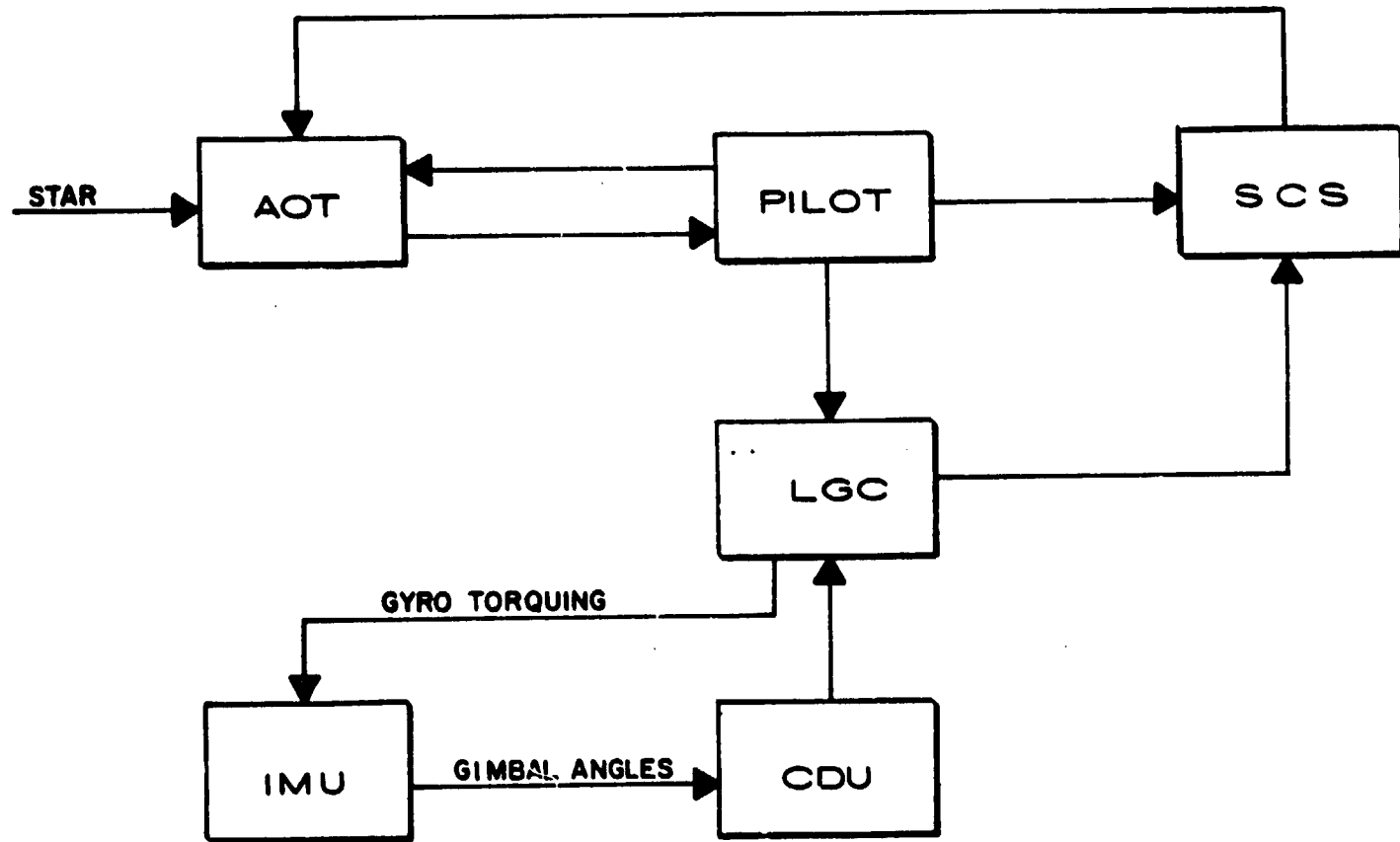
suggested here is limited by the ability of the astronaut to control vehicle attitude, but it is felt that it would suffice for coarse alignment. However, this does not imply that this technique will be used since the type of star sightings used for fine alignment may also be used for coarse alignment as mentioned earlier.

On the lunar surface the same star measurement technique used for fine alignment will be used for coarse alignment. One set of measurements on two stars may be sufficient for both alignments unless additional sets are desired in order to improve accuracy. The manner in which the AOT reticle is used for star measurements while on the lunar surface is shown in Fig. 1. 17. The astronaut first selects the viewing position containing the desired star and indicates the viewing position to the LGC. He then rotates the reticle until the straight line Y coincides with the star and reads the orientation angle into the LGC. Then he continues rotating the reticle until the spiral coincides with the star and reads the second angle into the LGC. This operation is performed on two stars.

Besides star sightings there is one other way in which the LGC might acquire sufficient inertial orientation data for coarse alignment while on the lunar surface. That is to have the LGC store the IMU gimbal angles immediately after LEM touchdown. This approach would, of course, be in error by any LEM attitude changes which occur after the storing operation.

### 1. 3. 3 Fine Alignment

The general flow diagram for fine alignment of the IMU while in free-fall is shown in Fig. 1. 21. This flow diagram is very similar to the one given for coarse alignment (Fig. 1. 20) except that in fine alignment the LGC might be used to control vehicle attitude, and any fine alignment commands from the LGC to the IMU are by means of pulses which torque the gyros. The purpose of showing the control path from the LGC to the



47

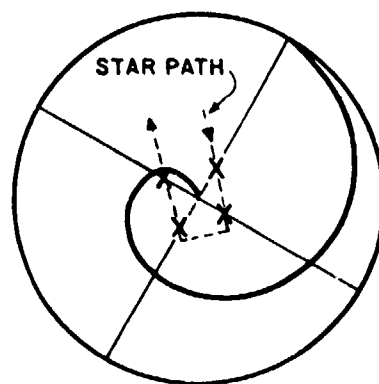
Fig. 1.21 Fine IMU alignment during free fall.

SCS (Fig. 1. 21) was to indicate that the LGC might be used to re-orient the vehicle so that a star, possibly used for coarse alignment, might be conveniently placed in the field of view of the AOT for additional measurements.

During free-fall the astronaut uses only the straight lines of the reticle pattern (Fig. 1. 17). The reticle is rotated to some reference value and the spacecraft attitude is changed so as to produce crossings of the reticle lines by the desired star. The astronaut indicates (marks) to the LGC when a crossing takes place. The crossing of a reticle line by a star defines a plane containing the star. Consequently, the crossing of two different reticle lines, such as the Y and X lines (Fig. 1. 17), by a single star defines the direction of the star.

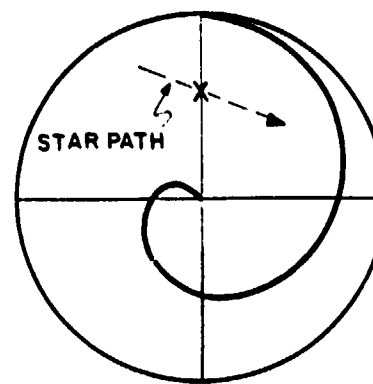
One way of producing star crossings of both lines would be to have the vehicle SCS perform an attitude limit cycle with the star near the center of the reticle as shown on the left in Fig. 1. 22. Multiple crossings for increased accuracy are conveniently obtained with the limit cycle operation. As indicated in Fig. 1. 22, this operation would have to be performed on at least two stars.

A three star method is given on the right of Fig. 1. 22. This method is operationally simpler for the astronaut because it requires him to mark only when the star crosses the Y line. The calculations required in the LGC, however, are more complicated. Another possible advantage of the 3 star method over the previous one is that it does not require the use of the attitude control jets when the sighting is made, thereby, eliminating possible contamination of the front optical surface of the AOT by the jets. The vehicle is simply permitted to drift in attitude for star crossings. The astronaut can select the stars and hasten the process by using the 3 star viewing position selector and by rotating the reticle. Naturally, he would have to indicate to the LGC the viewing position and reticle angle. The possibility of

2 STAR METHOD

1. ATTITUDE LIMIT CYCLE  
OPERATION

2. PILOT MARKS STAR  
CROSSING ON EACH  
AXIS

3 STAR METHOD

1. PILOT MARKS STAR  
CROSSING OF LINE Y

Fig. 1.22 IMU alignment during free fall.

optical surface contamination by the attitude control jets is unresolved at the present time and is under investigation.

It should be pointed out that a two star method is also available which does not require operation of the attitude control jets. The vehicle attitude is permitted to drift so that star crossings are obtained for both the Y and X lines.

## CHAPTER 2

### LUNAR ORBIT NAVIGATION PHASE

#### 2.1 General Objectives

The lunar orbit navigation phase starts immediately after the combined CSM-LEM vehicles have been injected into lunar orbit. The orbital navigation technique is then used to determine or update the orbit parameters with respect to a lunar coordinate system prior to LEM descent injection. The uncertainties in this orbit determination represent the initial condition uncertainties for the LEM descent and landing maneuvers. These, therefore, are important factors contributing to primary G&N system performance in meeting the design goal of a 3000 foot CEP landing capability. Since the lunar orbit ephemeris data are important parameters in the LEM launch, rendezvous, and abort phases of the mission, the CSM continues the orbit navigation mode of operation after LEM separation and descent injection. After a successful rendezvous maneuver phase from either a surface launch or abort trajectory, the orbit navigation procedure is continued until the trans-earth injection phase. During the lunar orbit phases of the Apollo mission, one of the primary objectives of the CSM primary G&N system is to update the orbital parameters. All orbit navigation is carried out by the CSM primary G&N system. The LEM G&N system does not have this capability with the present LEM optics subsystem.

The primary objectives of the G&N system prior to LEM descent injection are as follows:

1. Final determination of the CSM orbital parameters,  $\underline{R}_{CM}$  and  $\underline{V}_{CM}$ , at some reference time.

2. Optical surveillance of the desired landing site.
3. Determination of the landing site position vector  $\underline{R}_L$  relative to the lunar orbit navigation coordinate system.
4. Determination of the required LEM descent maneuver and timing.
5. Determination of abort aim points for the powered LEM landing maneuver.

Items 1 through 3 will be discussed in this chapter. Item 4 is described in section 3.4, and item 5 is presented in Chapter 8.

The general assumptions in the primary G&N analysis concerning the CSM lunar orbit are illustrated in Fig. 2.1. The initial injection point takes place on the far side of the moon relative to the earth at approximately the earth-moon line. The lunar injection maneuver establishes a near circular orbit at an altitude between 80 to 100 nm. Current analysis has restricted this altitude to 80 nm. Under normal operation the CSM G&N system performance during the translunar and lunar injection phases results in maximum lunar orbit eccentricities of 0.0021, or about 3.5 nm maximum variations about the desired 80 nm altitude (Ref. 2.1). The maximum inclination of the CSM orbit relative to the lunar equator is assumed to be  $10^\circ$  as indicated in Fig. 2.1. This value is typical for free return type earth-moon trajectories.

The desired landing site must be on the earth side of the moon, and has been restricted in current analysis to lunar latitudes of no greater than  $\pm 10^\circ$ . Initial studies have further restricted the landing site to earth shine lighting conditions. More current investigations have included either earth shine or sunshine landing site conditions. The phase of the moon, or position of the sun relative to the earth, affects some of the orbit navigation models that will be described in Section 2.3.

2

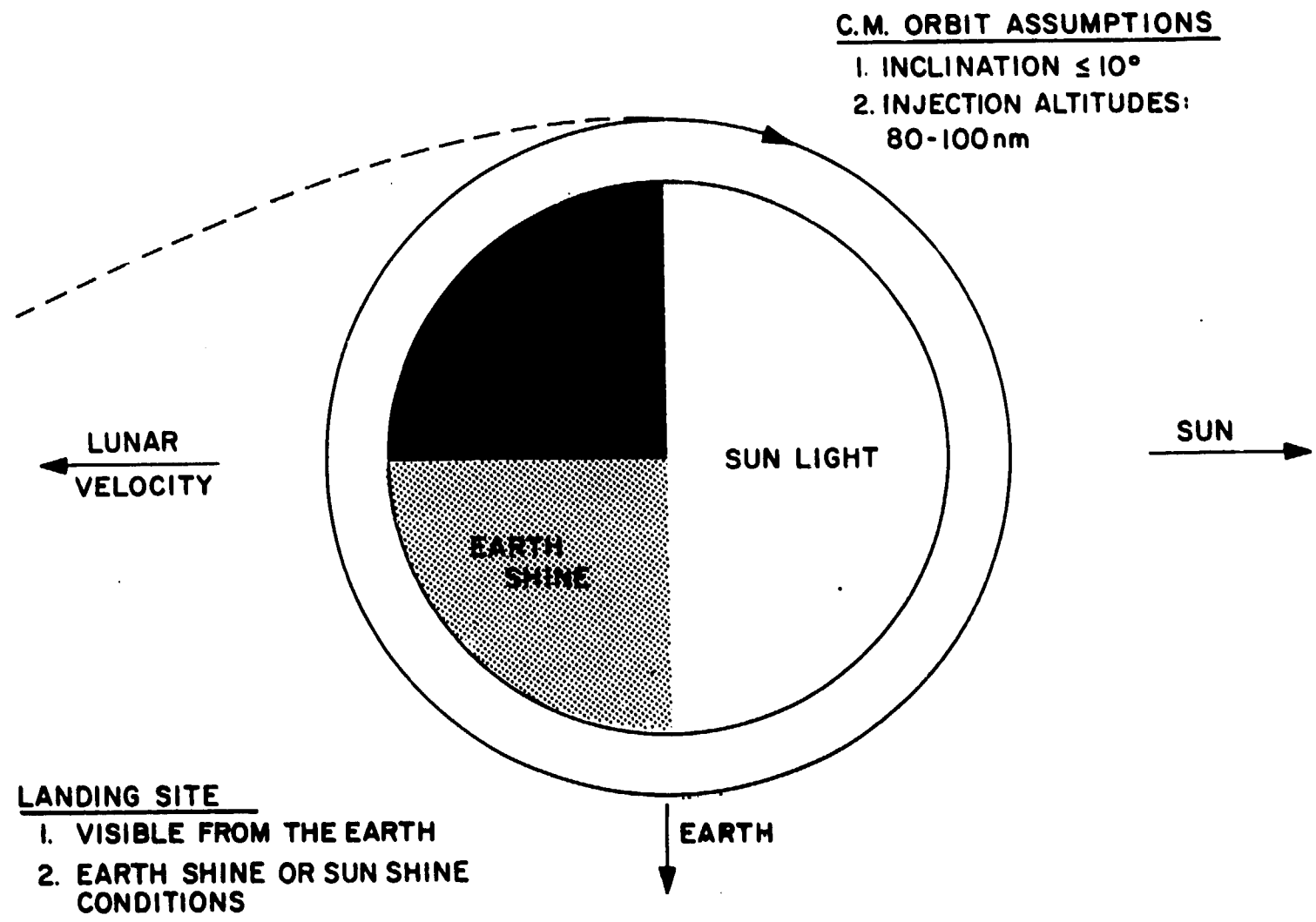


Fig. 2.1 General assumptions.

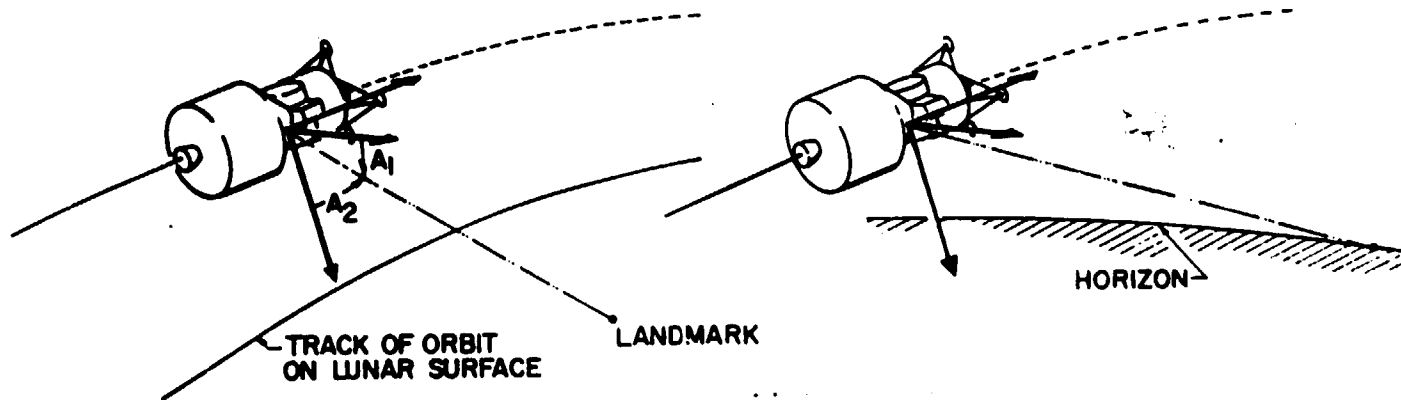
## 2.2 Navigation Concept and G&N System Operation

The lunar orbit navigation phase uses three basic optical measurements as shown in Fig. 2.2. The CSM SCT is used for sighting measurement of mapped lunar landmarks, horizon sightings, and orbital period measurements by timing either successive passages over an identifiable landmark or successive occultations of a star by the lunar horizon. All measurements made with the SCT involve two angles that are referenced to the IMU. The general CSM G&N system operation during lunar orbit navigation is shown in Fig. 2.3. The astronaut positions the SCT reticle in one of the three types of basic measurements by an optics hand controller driving the optics servo by the two CDUs as shown. These commands are monitored by the AGC starting from an initial optics zero or reference position such that SCT tracking angles can be continually determined relative to the initial reference position. When the astronaut has centered the SCT reticle, he "marks" this event by a discrete signal from the AGC keyboard. The AGC then determines the angle between the SCT tracking line and IMU. This angle is the basic input to the orbit navigation computation which then compares it with an estimated or predicted angle.

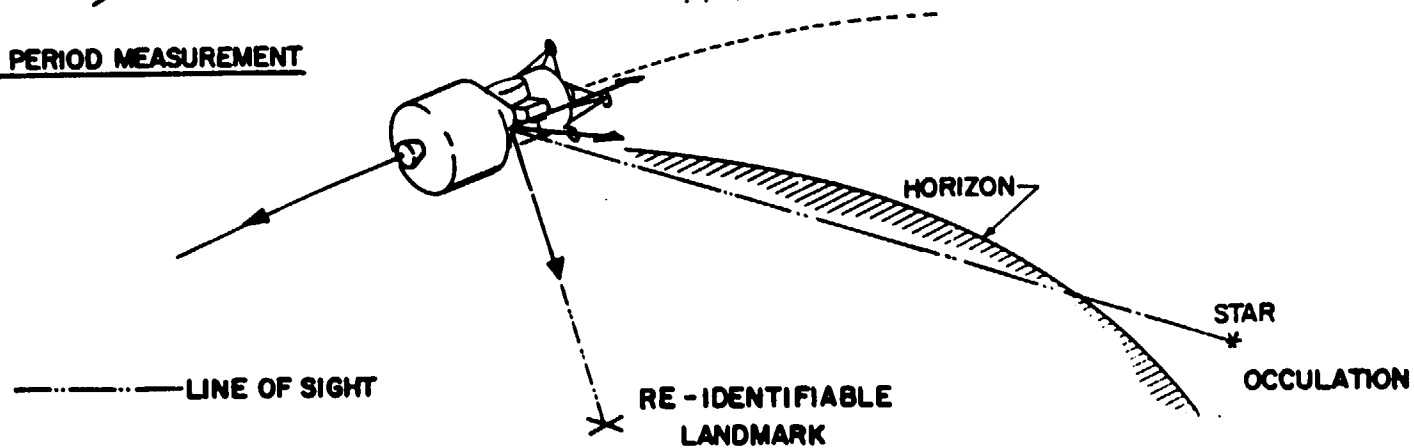
The lunar orbit navigation computation is essentially identical to that of the translunar midcourse navigation technique described in Ref. 2.2. The adaptation of this navigation technique to the orbital navigation problem was presented in Ref. 2.3 and is illustrated in simplified form in Fig. 2.4. The current estimated vehicle position vector ( $\hat{r}$ ) and velocity vector ( $\hat{v}$ ) are determined by integration of the equations of motion for the vehicle. When a navigation measurement such as a landmark sighting is to be made, an estimate of the angle to be measured,  $\hat{A}_{SL}$ , is computed on the basis of current estimated vehicle position and stored landmark coordinates. The actual angle measured,  $\tilde{A}_{SL}$ , is then compared with this estimate to establish the

1. MAPPED LANDMARK SIGHTING

2. HORIZON-IMU SIGHTING



3. PERIOD MEASUREMENT



----- LINE OF SIGHT

RE-IDENTIFIABLE LANDMARK

Fig. 2.2 Basic optical orbital navigation measurements.

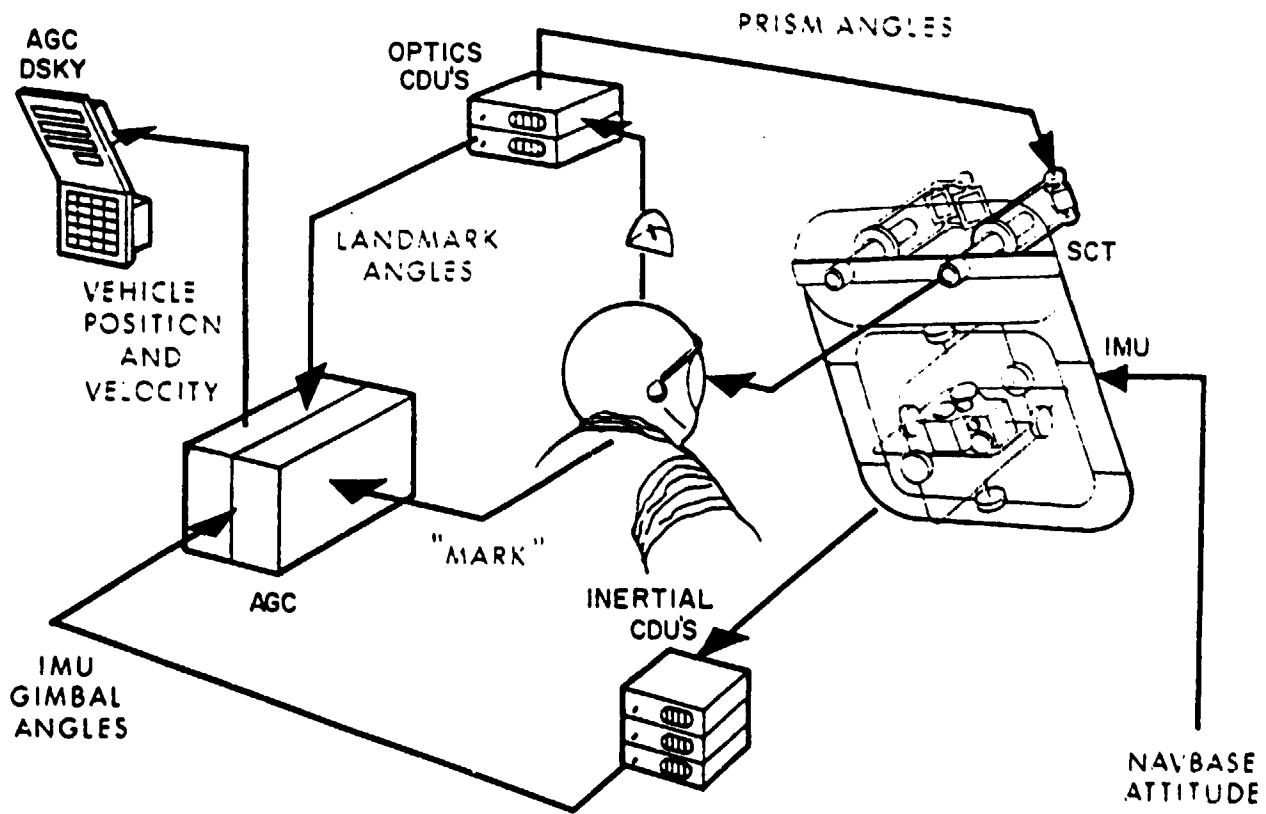


Fig. 2.3 Orbit navigation landmark tracking.

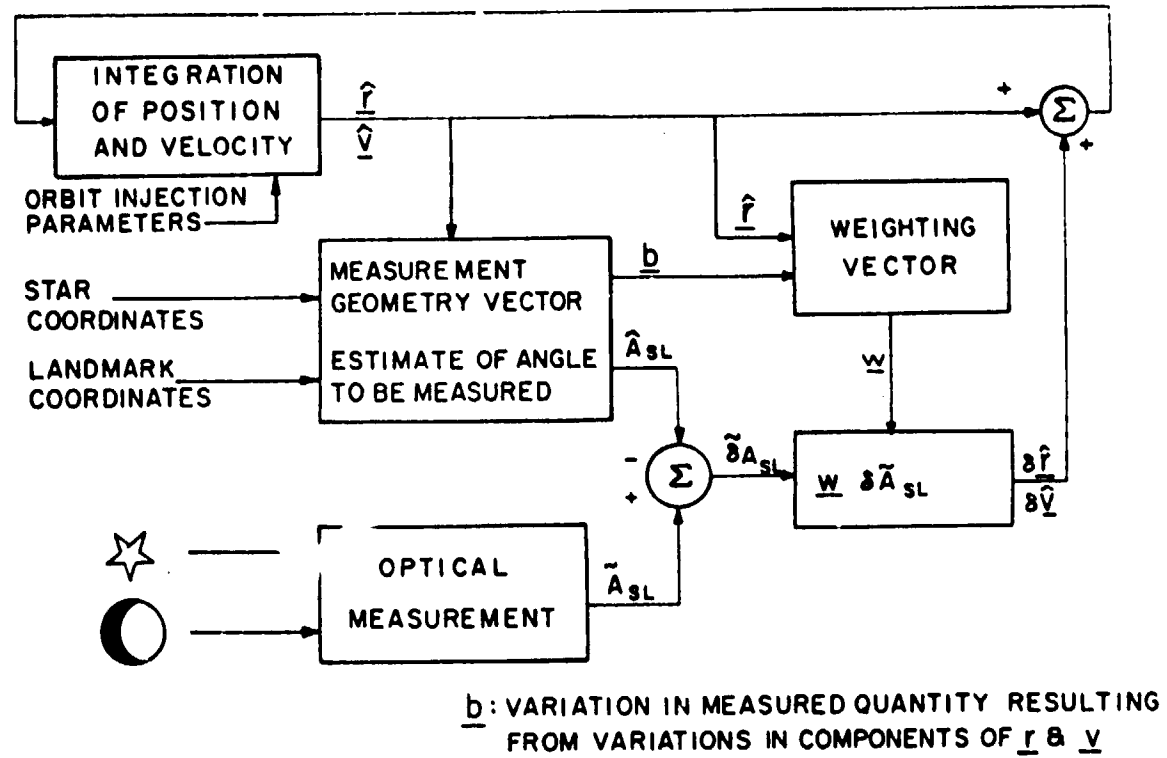


Fig. 2.4 Navigation concept (lunar orbit determination phase).

measurement deviation  $\delta \tilde{A}_{LS}$ . A statistical weighting vector,  $\underline{W}$ , is generated from a priori knowledge of nominal trajectory uncertainties, optical tracking performance, and a geometry vector  $\underline{b}$  based on the type of measurement being made. This weighting vector is defined such that a statistical optimum linear estimate of the deviation of the vehicle position,  $\delta \hat{\underline{r}}$ , and velocity,  $\delta \hat{\underline{v}}$ , from the estimated orbit or trajectory is obtained when the weighting vector is multiplied by the measurement deviation  $\delta \tilde{A}_{SL}$ . The deviations  $\delta \hat{\underline{r}}$  and  $\delta \hat{\underline{v}}$  are then added to the vehicle position and velocity estimates respectively to form a new orbit estimate. This procedure is repeated for each navigation measurement until orbital uncertainties are reduced to an acceptable level.

The general procedure illustrated in Fig. 2.4 is used in all unpowered positions of the CSM and LEM mission phases. Optical measurements are shown in Fig. 2.4, but any type of valid tracking data or measurement can be used such as range, range rate, and optical or radar tracking angles (Chapter 7).

The orbit navigation procedure briefly described above is presented in more detail as follows. At any time  $t$ , there is an actual vehicle position vector,  $\underline{r}$ , and velocity vector,  $\underline{v}$ . The G&N system estimates these state vectors to be  $\hat{\underline{r}}$  and  $\hat{\underline{v}}$  respectively. Since this estimate is never perfect due to injection errors, initial uncertainties, and measurement uncertainties, a position deviation vector is defined as

$$\delta \underline{r} = \underline{r} - \hat{\underline{r}}$$

and a velocity deviation vector as

$$\delta \underline{v} = \underline{v} - \hat{\underline{v}}$$

A geometrical interpretation of these two deviation vectors can be represented in a six-dimensional space, three coordinates for position and three for velocity. The deviation of the vehicle can be expressed as a single six-dimensional vector

$$\delta \underline{x} = \begin{bmatrix} \delta \underline{r} \\ \delta \underline{v} \end{bmatrix}$$

The estimated vehicle trajectory in the G&N system at any time  $t$  can be represented as

$$\hat{\underline{x}} = \begin{bmatrix} \hat{\underline{r}} \\ \hat{\underline{v}} \end{bmatrix}$$

and is propagated in time by means of a transition matrix from time  $t_n$  to time  $t_{n+1}$  where  $t_{n+1} - t_n$  is the integration time step. This  $6 \times 6$  transition matrix,  $\phi$ , satisfies the differential equation

$$\dot{\phi} = F\phi$$

where  $F$ , a  $6 \times 6$  matrix, is a function of the partial derivatives of the gravity vector with respect to the estimated position coordinates.

In order to improve the estimated vehicle position and velocity, a measurement (in this case an optical angle) is estimated and compared with the actual measurement. The measured deviation can be written as

$$\delta \tilde{A}_{SL} = \delta A_{SL} + \alpha$$

where  $\alpha$  is the random error in the measurement and  $\delta A_{SL}$  is the variation due to the deviation vector  $\delta \underline{x}$ . Assuming small deviations,  $\delta A_{SL}$  can be expanded in a Taylor series about  $\underline{x}'$

$$\delta A_{SL} = \frac{\partial A_{SL}}{\partial \underline{x}'} \cdot \delta \underline{x}' + \dots$$

where the prime denotes the value before the measurement and  $\frac{\partial A_{SL}}{\partial \underline{x}'}$  is called the geometry vector  $\underline{b}$  and is a precalculated quantity.

The error in the estimate of the deviation vector at the measurement time is defined as

$$\underline{e} = \delta \underline{x} - \delta \hat{\underline{x}}$$

Immediately after a measurement the reference or estimated trajectory is corrected so that  $\delta \hat{\underline{x}} = 0$ , and  $\delta \underline{x}$  is prevented from becoming too large for valid linear perturbation theory. The six by six correlation matrix of the errors in the estimated trajectory is defined as

$$E = \overline{\underline{e} \underline{e}^T}$$

where the bar represents the average value, and the superscript T indicates the transpose of the vector  $\underline{e}$ .

The objective of the navigation technique is to minimize the error in  $\delta \hat{\underline{x}}$  or the estimate of  $\delta \underline{x}$ . If no correlation between measurements is assumed, the optimum linear estimate can be written as

$$\delta \hat{\underline{x}} = \underline{W} \delta \tilde{\underline{A}}_{LS}$$

where  $\underline{W}$ , the weighting vector, is chosen to minimize the mean squared error in the estimate. It can be shown (Ref. 2.2) that after any measurement:

$$\delta \hat{\underline{x}} = \frac{\underline{E}' \underline{b} \delta \tilde{\underline{A}}_{LS}}{\underline{b}^T \underline{E}' \underline{b} + \alpha^2}$$

$$E = E' - \frac{(\underline{E}' \underline{b}) (\underline{E}' \underline{b})^T}{\underline{b}^T \underline{E}' \underline{b} + \alpha^2}$$

After a measurement, the reference or estimated trajectory is again corrected so that  $\delta \hat{\underline{x}} = 0$ . The effectiveness of a measurement is dependent on both the direction and magnitude of the geometry vector  $\underline{b}$ .

The most effective measurement in lunar orbit navigation is the line of sight angle between a mapped landmark and the IMU reference. An important source of error in such measurements is the uncertainty in landmark position. Reference 2.3 develops a technique for taking such uncertainties into account. A change in the landmark position of  $\delta \underline{L}$  has the same effect on  $\delta A_{SL}$  as a  $-\delta \underline{L}$  change in vehicle position, therefore

$$\delta A_{SL} = \underline{b} \cdot (\delta \underline{r}' - \delta \underline{L})$$

An expression can be developed from this for  $\delta \hat{\underline{x}}$  and E as before. Uncertainties in the landmark position therefore reduce the effectiveness of this type of measurement.

### 2.3 Orbit Navigation Models and G&N Performance

The time sequence, total number and type of orbit navigation measurements will determine the accuracy of the CSM orbit at the LEM descent injection point. The orbit navigation models used in the primary G&N system analysis for determination of the initial condition uncertainties for the LEM phases of the mission are presented in this section.

An orbit navigation model for use prior to an equal period descent to a landing site in the leading lunar quadrant is shown in Fig. 2.5. This will be referred to as Model 1 throughout this report. The landing site for this model is shown in earthshine conditions, but sunlight landing conditions would not change this particular orbit navigation model. It should also be noted that the landing site indicated in Fig. 2.5 need not be one of the mapped landmarks used for orbit navigation and in most cases will not be. Model 1 assumes that the combined vehicles were injected into a near circular orbit at 80 to 100 nm altitudes on the back side of the moon. No orbital navigation measurements are made until the spacecraft passes over the lunar terrain visible to the earth, referred to as the near side, since mapped landmarks on

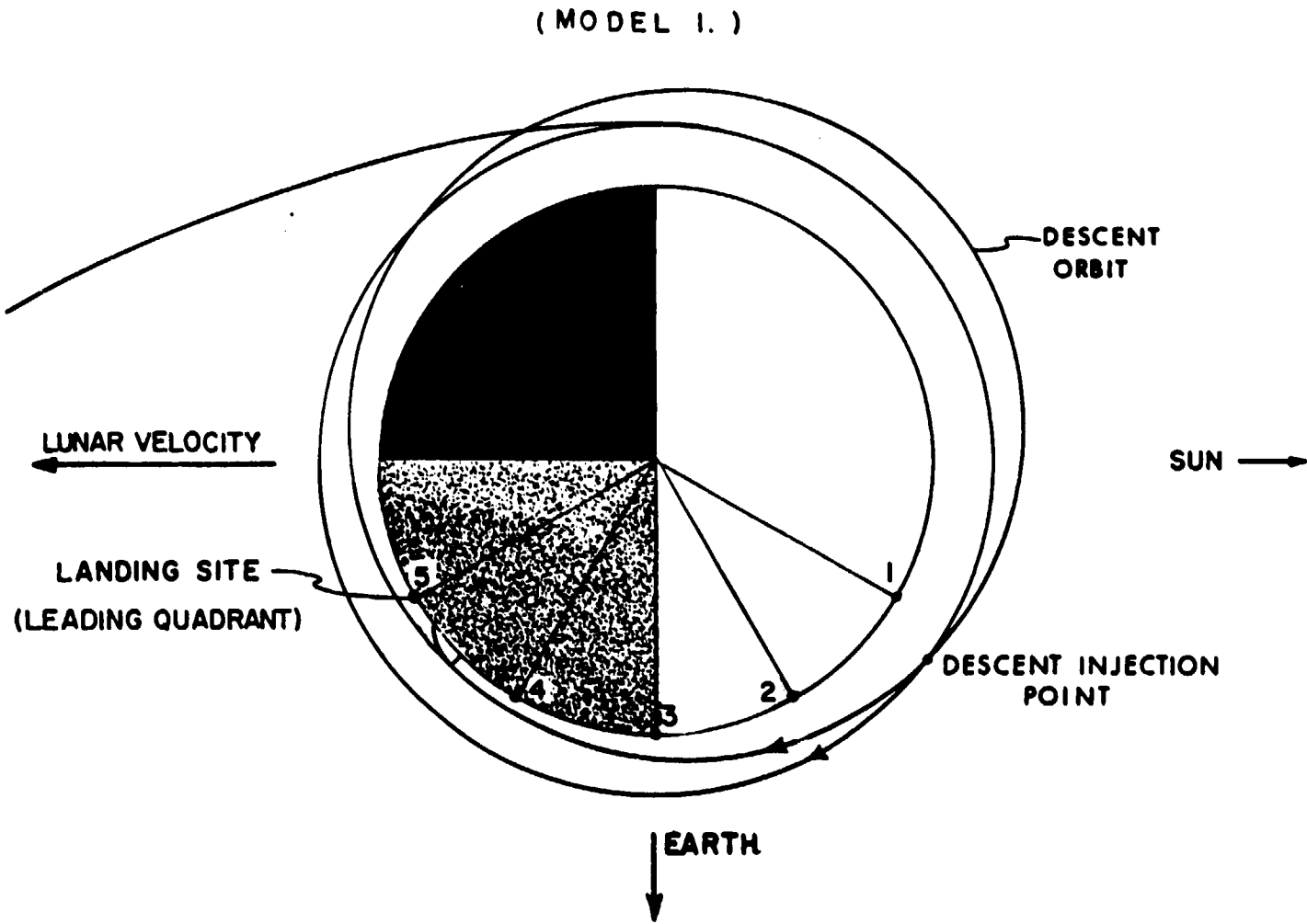


Fig. 2.5 Lunar orbit navigation model 1.

the nonvisible or back side have not been assumed. As the spacecraft passes over the near side, five landmarks are sighted which are approximately equally spaced in central angle ( $\approx 30^\circ$ ) as shown in Fig. 2.5. As the orbiting vehicles pass over each landmark, three sightings are made as the line of sight traverses a  $90^\circ$  sector centered about the local vertical. The SCT sightings are made at the extremes ( $45^\circ$ ,  $-45^\circ$ ) and center ( $0^\circ$ ) of this interval with a 1 mr ( $1\sigma$ ) sighting accuracy in each axis. Three sightings per landmark have proved sufficient over this angle sector, and increasing the number of sightings on a given landmark does not improve the G&N performance significantly. The geometry vector  $\underline{b}$  for a SCT angle measurement is perpendicular to the tracking line or line of sight. Since this line of sight and the geometry vector  $\underline{b}$  traverse a  $90^\circ$  sector during the three sightings in a landmark measurement, the orbital uncertainties are more or less equally decreased in all components. After passing the fifth landmark of Fig. 2.5, the uncertainties in the orbital parameters are allowed to propagate over a period of 1.4 hours until the vehicles again come into view of landmark number one. At this time, three more sightings are made on the first landmark for the final orbit determination. Uncertainties in this determination are allowed to propagate for five more minutes until the LEM descent injection point is reached for the equal period descent.

The CSM primary G&N performance in reducing the lunar orbit uncertainties for Model 1 described above is summarized in Table 2.1. It was assumed that the five landmarks used in this model have been mapped to an accuracy of 1500 feet ( $1\sigma$ ) in both vertical and horizontal directions relative to a lunar centered coordinate system. A CSM 100 nm circular orbital altitude was used for the model summarized in Table 2.1. The initial lunar orbit injection uncertainties at  $t = 0$  of this table are typical for the orbit injection maneuver. The diagonal terms of this initial lunar injection correlation matrix are:

TABLE 2.1  
ORBIT NAVIGATION MODEL 1

Performance Accuracies

1. SCT tracking uncertainty in each axis: 1 mr ( $1\sigma$ )
2. Landmark uncertainty ( $1\sigma$ ): Horizontal = 1500 ft,  
Vertical = 1500 ft.

Measurement	Time (hr)	rms Position Uncertainty		rms Velocity Uncertainty	
		Prior to Meas. (ft)	After Meas. (ft)	Prior to Meas. (fps)	After Meas. (fps)
	0	6710		6.1	
1st Landmark	0.675	33700	2360	28.7	3.5
2nd	0.875	3600	2240	4.3	3.0
3rd	1.05	3200	1920	3.5	2.1
4th	1.25	2830	1710	2.8	1.5
5th	1.4	2020	1510	1.8	1.3
1st Landmark	2.8	6500	1480	5.1	1.3
Descent Injection	2.9	1480		1.3	

Final Uncertainty    One Sigma Components

Position (ft)		
$\delta x$	$\delta y$	$\delta z$
1250	530	580

Velocity (fps)		
$\delta x$	$\delta y$	$\delta z$
0.4	1.1	0.5

$$\begin{aligned} \delta X &= 3040 \text{ ft (range)} \\ \delta Y &= 5160 \text{ ft (altitude)} \\ \delta Z &= 3040 \text{ ft (track)} \\ \delta \dot{X} &= 2.1 \text{ ft/sec} \\ \delta \dot{Y} &= 5.3 \text{ ft/sec} \\ \delta \dot{Z} &= 2.1 \text{ ft/sec} \end{aligned}$$

These rms uncertainties increase to over 5nm and 28 ft/sec until the first landmark sightings are made. The rms position and velocity uncertainties after the three sightings on each landmark are listed in Table 2.1. After the fifth landmark, the orbit uncertainties were reduced to 1510 ft and 1.3 ft/sec. These uncertainties were propagated with no other navigation measurements until three sightings on the first landmark were again made. During the five minute interval between the last sighting and the LEM descent injection point, the uncertainties did not increase over 10 ft or 0.1 ft/sec from the levels at the last sighting. The final orbit uncertainties at LEM descent injection (t = 2.9 hr) are listed by components at the bottom of Table 2.1. These components are the square roots of the diagonal terms of the final correlation matrix for Model 1 presented in Table 2.2.

Since a correlation matrix is symmetrical, only the terms on the diagonal and one side are shown for the Models in Table 2.2. This matrix is in a X, Y, Z,  $\dot{X}$ ,  $\dot{Y}$ ,  $\dot{Z}$  row-column configuration with units of (ft)<sup>2</sup> and (ft/sec)<sup>2</sup> for the diagonal terms. An important correlation exists between the X and  $\dot{Y}$ , and Y and  $\dot{X}$  terms of this correlation matrix. The correlation coefficients for the XY and YX terms of the Model 1 matrix are -0.94 and -0.99 respectively. This indicates that when there is a positive X deviation there is a - $\dot{Y}$  velocity and similarly for Y and - $\dot{X}$ . There is no significant correlation between the other components of the correlation matrix. The correlation matrices of Table 2.2 were used as the initial condition uncertainties for the subsequent LEM phases of the mission, and the error analysis presented later in this report was generated

TABLE 2.2

DESCENT INJECTION INITIAL CORRELATION MATRICES

Model 1 (Fig. 2.5, Table 2.1)

	X	Y	Z	$\dot{X}$	$\dot{Y}$	$\dot{Z}$
X	$1.573 \times 10^6 \text{ (ft)}^2$	$-4.722 \times 10^4$	$4.959 \times 10^4$	$-3.344 \times 10^1 \left(\frac{\text{ft}^2}{\text{sec}}\right)$	$-1.225 \times 10^3$	-6.599
Y		$2.863 \times 10^5$	$-2.133 \times 10^4$	$-2.304 \times 10^2 \left(\frac{\text{ft}^2}{\text{sec}}\right)$	$-7.525 \times 10^1$	-2.25
Z			$3.432 \times 10^5$	$1.493 \times 10^1$	$-3.255 \times 10^1$	$-1.213 \times 10^1$
$\dot{X}$				$1.896 \times 10^{-1} \text{ (fps)}^2$	$1.237 \times 10^{-1}$	$1.889 \times 10^{-3}$
$\dot{Y}$	(Symmetrical)				1.120	$-8.739 \times 10^{-3}$
$\dot{Z}$						$2.868 \times 10^{-1}$

Model 2 (Fig. 2.6, Table 2.4)

	X	Y	Z	$\dot{X}$	$\dot{Y}$	$\dot{Z}$
X	$5.659 \times 10^6 \text{ (ft)}^2$	$-3.642 \times 10^5$	$1.601 \times 10^3$	$8.082 \times 10^1 \left(\frac{\text{ft}^2}{\text{sec}}\right)$	$-4.034 \times 10^3$	$1.154 \times 10^1$
Y		$5.983 \times 10^5$	$-2.163 \times 10^4$	$-4.288 \times 10^2 \left(\frac{\text{ft}^2}{\text{sec}}\right)$	$3.479 \times 10^2$	$-1.153 \times 10^1$
Z			$4.525 \times 10^5$	$1.681 \times 10^1$	6.146	$4.520 \times 10^1$
$\dot{X}$				$3.152 \times 10^{-1} \text{ (fps)}^2$	$-1.149 \times 10^{-1}$	$7.079 \times 10^{-3}$
$\dot{Y}$	(Symmetrical)				2.944	$-1.566 \times 10^{-2}$
$\dot{Z}$						$3.055 \times 10^{-1}$

by propagating these matrices through the required LEM trajectories with the addition of inertial instrument uncertainties when appropriate.

The results of varying some of the important parameters in the orbit navigation technique are summarized in Table 2.3 for Model 1 as illustrated in Fig. 2.5. The first case in Table 2.1 lists the final CSM orbital uncertainties repeated from Table 2.1 and referred to as the standard Model 1 performance. Case 2 in Table 2.3 summarizes the final orbit navigation uncertainties for Model 1 if the CSM were at an 80 nm circular altitude rather than the 100 nm of Case 1. It can be seen from these two cases that there is a very small difference between the two results and either could be used for subsequent error analysis. At lower orbital altitudes, the SCT angle measurements are weighted more heavily in the statistical navigation technique since the distance between the vehicle and the landmark is less, and the  $\underline{b}$  vector is therefore larger in magnitude. (Ref. 2.2) The 1500 ft ( $1\sigma$ ) landmark uncertainties, on the other hand, have a larger effect in the lower altitude case with respect to final uncertainties. The small differences between cases 1 and 2 of Table 2.3 are primarily due to the different effect of landmark uncertainty on the two orbital altitudes.

Case 3 of Table 2.3 represents the effect of larger landmark uncertainties in the vertical direction, 3000 ft vs 1500 ft ( $1\sigma$ ). Final rms position and velocity uncertainties are increased by approximately 70% over the standard case 1. The final case listed in Table 2.3 is the result of degrading the SCT tracking accuracy from 1 mr to 4 mr ( $1\sigma$ ); this has approximately the same effect as the degraded landmark mapping accuracy of Case 3.

The uncertainties listed for the standard Model 1 of Tables 2.3 and 2.1 represent very good orbit determination and approach the performance limit of the primary G&N system. The low

TABLE 2.3

## ORBIT NAVIGATION MODEL 1 PARAMETRIC COMPARISON

Case No.	Model 1 Parametric Variation	Final Position Uncertainty				Final Velocity Uncertainty			
		$\delta x$ (ft)	$\delta y$ (ft)	$\delta z$ (ft)	rms (ft)	$\delta x$ (ft/sec)	$\delta y$ (ft/sec)	$\delta z$ (ft/sec)	rms (ft/sec)
1.	Standard Model 1 - Table 2.1, 1 mr ( $1\sigma$ ) CSM = 100 nm, landmark uncertainty = 1500 ft	1250	530	580	1480	0.4	1.1	0.5	1.3
2.	CSM = 80 nm, 1 mr ( $1\sigma$ ), landmark uncertainty = 1500 ft	1530	570	560	1720	0.5	1.2	0.5	1.4
3.	Landmark uncertainty = 3000 ft ( $1\sigma$ )	2120	840	620	2360	0.7	1.7	0.6	2.0
4.	4 mr ( $1\sigma$ ) SCT tracking accuracy in each axis	2280	720	1060	2610	0.6	2.0	1.0	2.3

orbital uncertainties in this model are due to the fact that the G&N system can take a sighting on an accurate landmark just before LEM descent injection (5 minutes). More current descent mission profiles will require descent injection on the back side of the moon where mapped landmarks cannot be assumed.

Figure 2.6 illustrates an orbit navigation model in which the descent injection point is on the back side of the moon not visible from the earth. The orbit navigation model of Fig. 2.6 will be referred to as Model 2. The descent trajectory shown in Model 2 is an equal period descent, but the results of this model are equally applicable to Hohmann type descents (as will be illustrated in a later example.)

The navigation procedure for Model 2 is identical to that of Model 1 up to and including the fifth landmark measurement. Since no further mapped landmark measurements can be taken before the descent injection point, five horizon measurements are made with the SCT ( $\sigma = 1$  mr overall accuracy) once the horizon becomes illuminated and prior to the LEM descent injection point.

Measurements referred to as horizon measurements in this report are designated as star horizon measurements in other phases such as the translunar phase. These two are equivalent since the SCT measures the horizon relative to the IMU which then holds a desired orientation relative to the stars.

The SCT rms uncertainty,

$$\sigma = \sqrt{\alpha^2}$$

was assumed to be 1 mr for the landmark and horizon measurements. Since a landmark measurement consists of two independent SCT axis angles, the overall measurement RMS uncertainty is

$$\sqrt{\alpha^2 + \alpha^2} = \sqrt{2} \sigma$$

or 1.41 mr if  $\sigma = 1$  for landmark measurements.

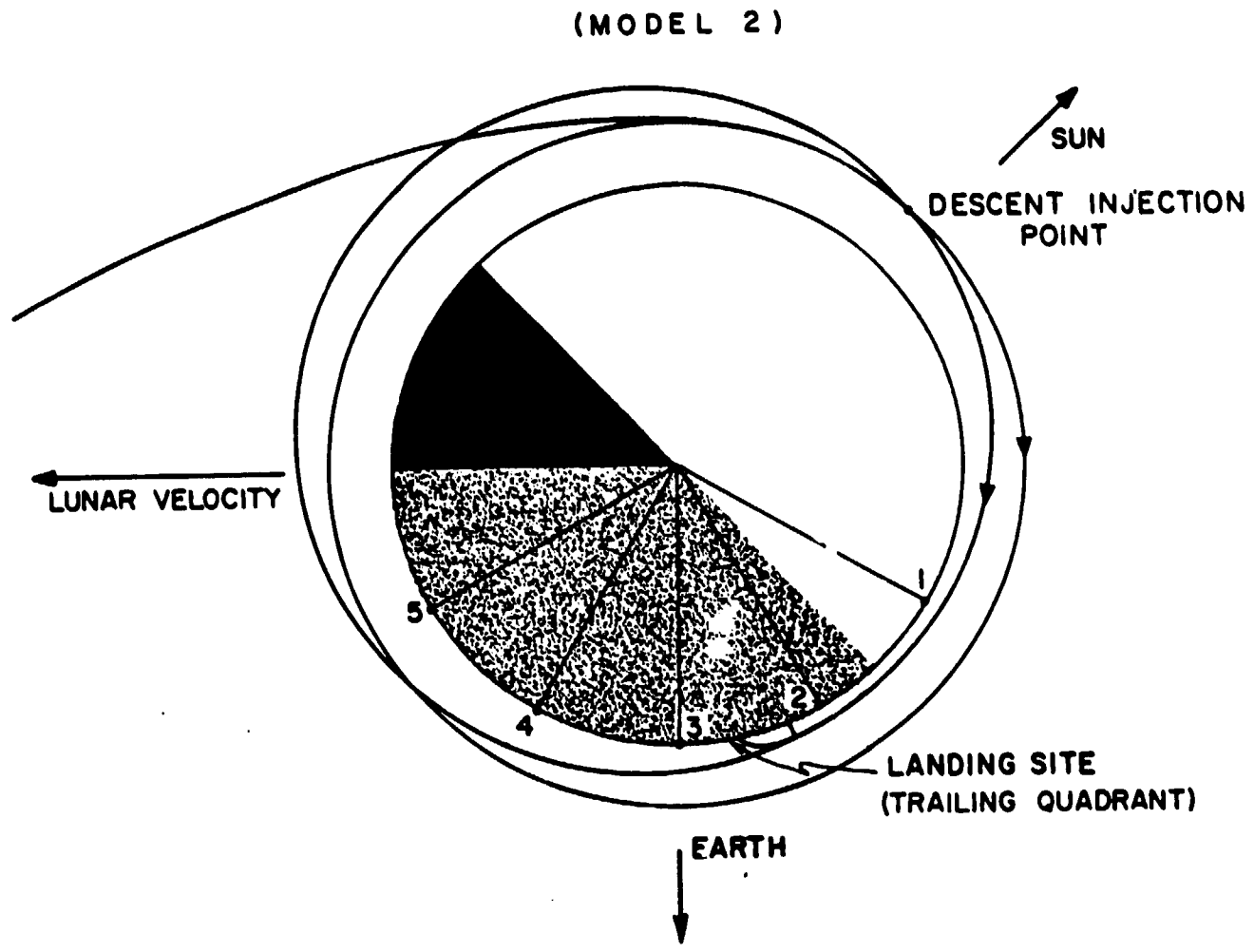


Fig. 2.6 Lunar orbit navigation model 2.

The G&N performance during Model 2 is summarized in Table 2.4. The results of this table are identical to those of Table 2.1 for the first five landmark measurements (1.4 hrs). The first horizon measurement was made 36 minutes later when the CSM passed into the sunlight sector. It can be seen from Table 2.4 that the five horizon measurements are not as effective as the last landmark sighting of Model 1 in reducing the orbital uncertainties. The final uncertainties listed in Table 2.4 are for the LEM descent injection point five minutes after the last horizon measurement. The final uncertainty components listed at the bottom of Table 2.4 are the square roots of the diagonal items of the final Model 2 correlation matrix shown in Table 2.2. The same type of correlation exists between  $\dot{X}\dot{Y}$  and  $\dot{Y}\dot{X}$  as in Model 1. It can be seen by comparing the final uncertainties of Tables 2.1 and 2.4 that all components of Model 2 are larger than those of Model 1, especially the X component (the range component of position).

Orbit navigation Model 3 is illustrated in Fig. 2.7 and is very similar to Model 2 of Fig. 2.6 except that the descent injection point is on the back side of the moon in total darkness. Thus the lunar horizon is not visible for measurements. If the LEM descent injection were made on the second CSM orbit (as in Models 1 and 2), horizon measurements could be made on the back side (where a horizon is still visible) prior to entry into the dark sector. Model 3 is the same as Model 2 in that five landmark and five horizon measurements are made. The major difference is the elapsed time between the last navigation measurement and the descent injection point; this time is 5 minutes for Model 2 and 30 minutes for Model 3. The final orbit uncertainties for Model 3 are listed in Fig. 2.8 along with those of standard and modified Models 1 and 2.

The uncertainties summarized in Fig. 2.8 are the components of the final orbital uncertainties at the LEM descent injection point. The time  $t_1$  is the interval between the last navigation

TABLE 2.4

ORBIT NAVIGATION MODEL 2

Performance Accuracies

1. SCT tracking uncertainties in each axis: 1 m $\sigma$
2. Landmark uncertainties (1 $\sigma$ ): Horizontal = 1500 ft,  
Vertical = 1500 ft
3. Horizon uncertainty included in SCT 1 m $\sigma$  accuracy.

Measurement	Time (hr)	rms Position Uncertainty		rms Velocity Uncertainty	
		Prior to Meas. (ft)	After Meas. (ft)	Prior to Meas. (ft/sec)	After Meas. (ft/sec)
	0	6710		6.1	
1st Landmark	0.675	33700	2360	28.7	3.5
2nd "	0.875	3600	2240	4.3	3.0
3rd "	1.05	3200	1920	3.5	2.1
4th "	1.75	2830	1710	2.8	1.5
5th "	1.4	2020	1510	1.8	1.3
1st Horizon Measurement	2.02	4300	3330	3.2	2.4
2nd "	2.1	3630	3010	2.6	2.2
3rd "	2.17	3210	2800	2.3	2.0
4th "	2.25	2920	2630	2.1	1.9
5th "	2.38	2770	2540	2.0	1.8
Descent Injection	2.45	2590		1.9	

Final Uncertainty One Sigma Components

Position (ft)		
$\delta x$	$\delta y$	$\delta z$
2380	770	670

Velocity (fps)		
$\delta \dot{x}$	$\delta \dot{y}$	$\delta \dot{z}$
0.6	1.7	0.6

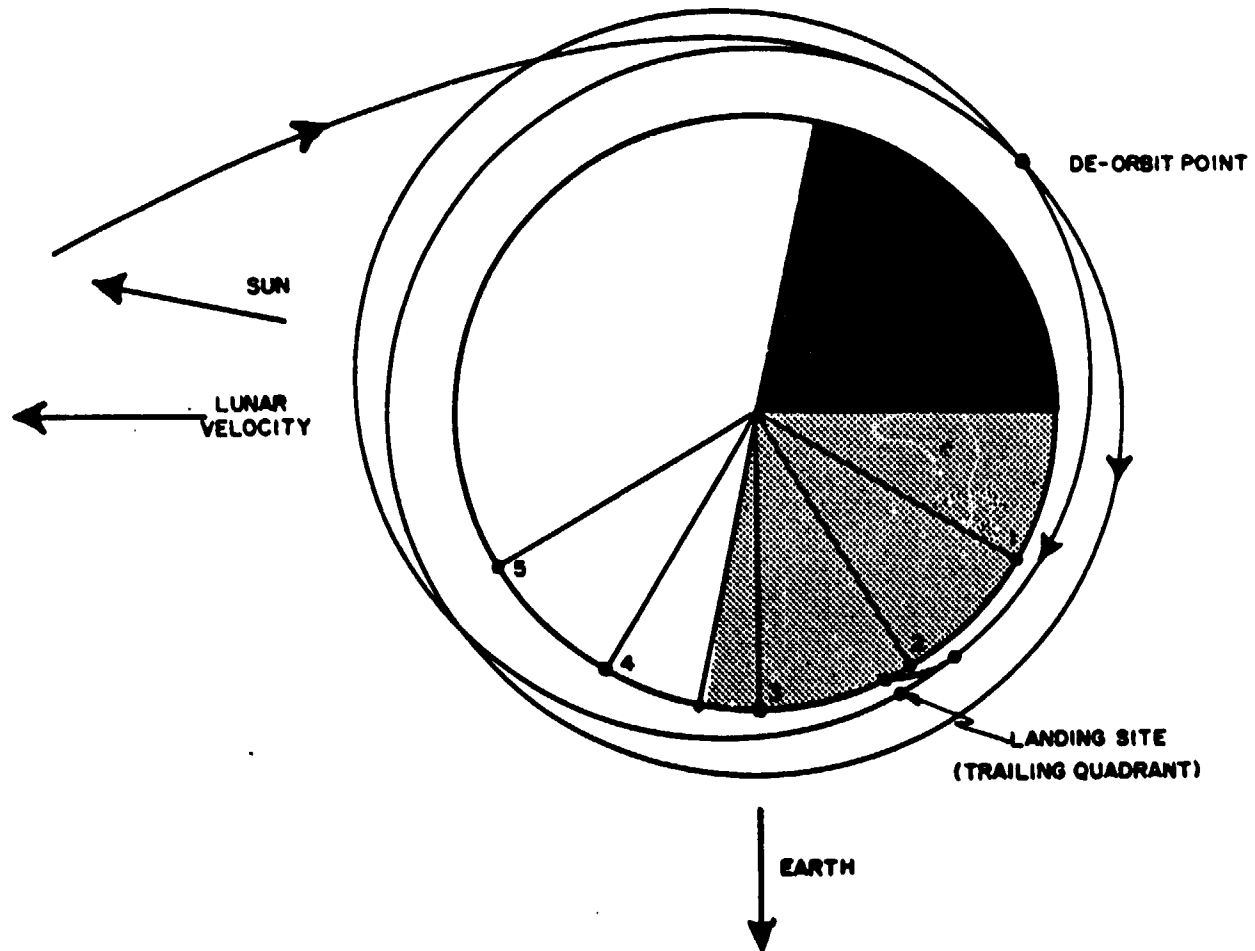


Fig. 2.7 Lunar orbital navigation model 3.

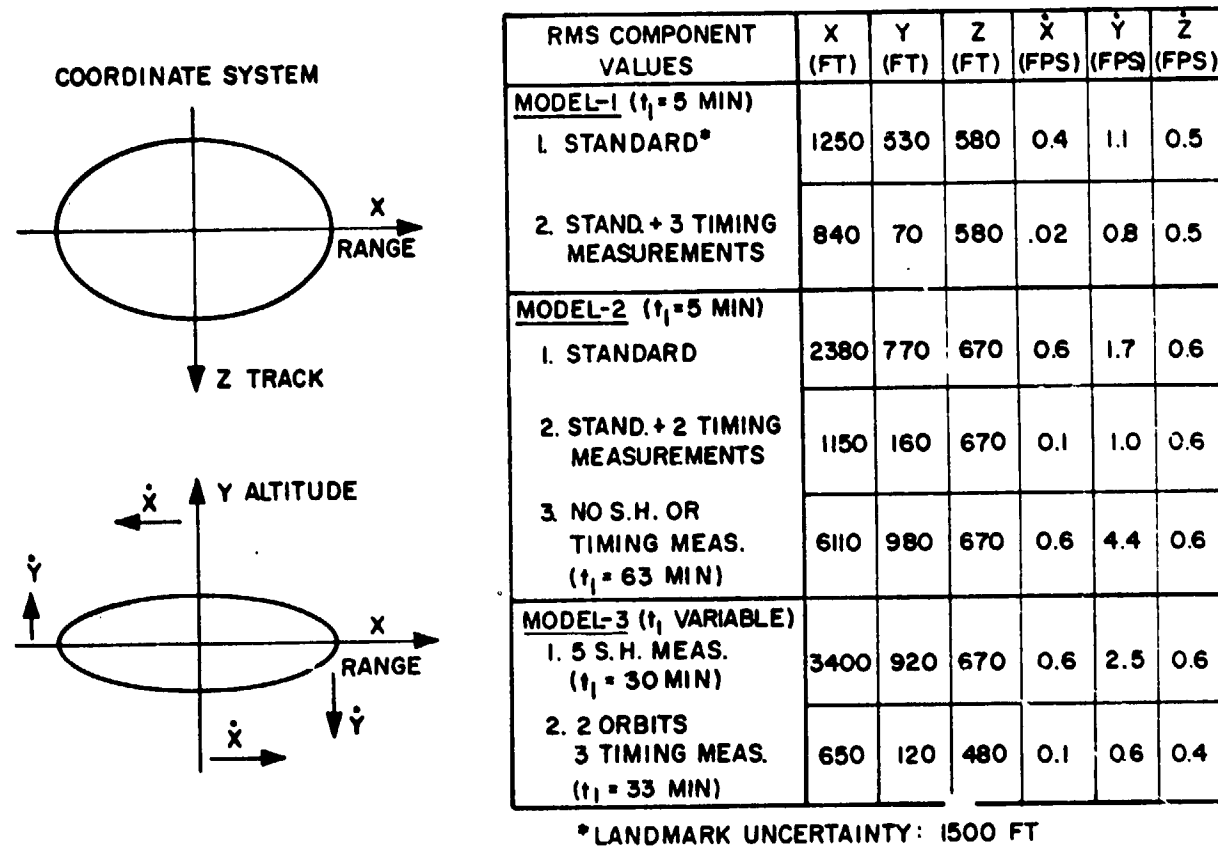


Fig. 2.8 Initial position and velocity conditions at the start of descent orbit injection.

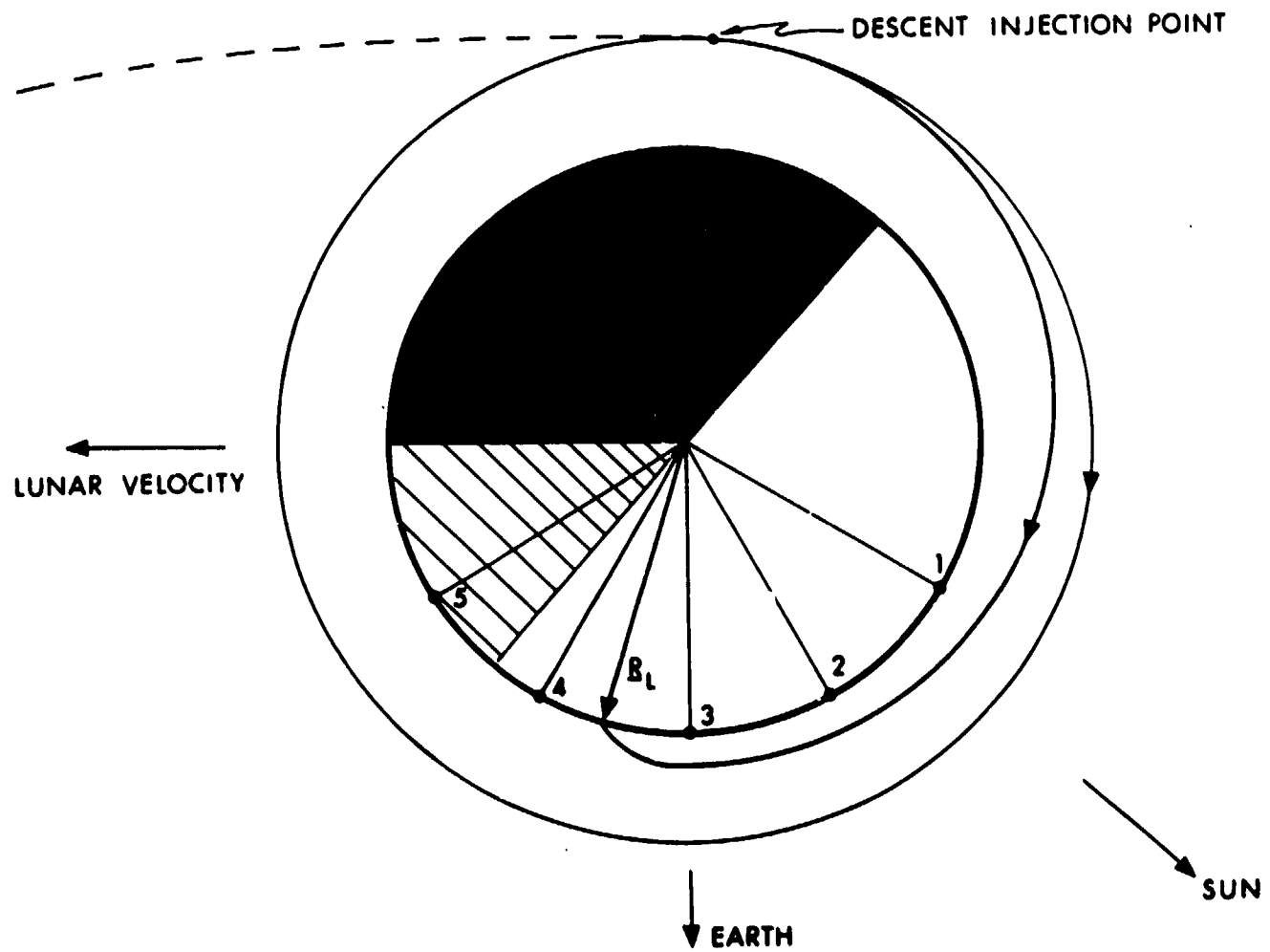
measurement and the descent injection. The standard Model 1 and Model 2 performances listed in this figure are repeated from Tables 2.1 and 2.4, respectively. One modification to Model 1 of Fig. 2.5 incorporates three period or timing measurements on the sunlit back side of the moon when the CSM passed over identifiable, but unmapped landmarks. These three period measurements do not involve three orbital periods, but represent the timing of the CSM period over three separate visible points between the first and second orbital pass. The results for this modified Model 1 are listed in Fig. 2.8 under Model 1-#2 assuming a period measurement accuracy of 0.1 sec ( $1\sigma$ ) in a spherical gravity field. The major effect of including period measurements in this model was to reduce the altitude ( $Y$ ) and forward velocity ( $\dot{X}$ ) uncertainties.

A similar modification was made for Model 2 as listed under Model 2-#2 with the same type of performance improvement. The case listed under Model 2-#3 of Fig. 2.8 was included in order to illustrate the effect of restricting the orbit navigation measurements to only landmark sightings when the descent injection point is on the back side of the moon. The major effect of the horizon measurements of Model 2 was to limit the  $X$  and  $\dot{Y}$  final uncertainties. These two components are highly correlated as described previously (Table 2.2). This correlation holds for all orbit navigation models and is illustrated vectorially in Fig. 2.8.

The results of Model 3 listed in Fig. 2.8 indicate that the major effect of the increased time interval,  $t_1$ , is to again increase the  $X$  and  $\dot{Y}$  uncertainties. Model 3-#2 of Fig. 2.8 is a modification of Model 3 consisting of two full orbits. This involves a total of 10 landmark sightings (5 on each period) plus three timing or period measurements on the back side prior to entering the dark sector and descent injection point. This procedure can reduce the final uncertainties to the level of that for Models 1 and 2.

Current Apollo lunar landing mission profiles restrict the

LEM descent orbit to a Hohmann type trajectory. The LEM descent injection point is restricted to the back side of the moon relatively close to the earth-moon line, because the landing sites under consideration lie within  $\pm 30^\circ$  lunar longitude. The orbit navigation model for this type of operation is illustrated in Fig. 2.9 and will be referred to as Model 4. This navigation model includes two orbital periods during which 10 landmark measurements (5 on each orbit) are taken. The orbital uncertainties for this model are summarized in Table 2.5. Over the first five landmark measurements (1.4 hrs), the results are identical to those of Table 2.1 and 2.4. No horizon or period measurements were taken on the back side of the moon between the 5th and 1st landmark for this particular example. It might be noted that under full moon phase conditions, only period measurements by star occultations could be used on the back side. As indicated in Table 2.5, the navigation system essentially reached an asymptotic level of performance after the first landmark measurement of the second orbital pass. The final uncertainties listed in this table are a result of 42 minutes between the final 5th landmark and descent injection point. A current orbit navigation time-line analysis restricts the orbit navigation landmark measurements to the 1st and 5th landmarks on the second orbit of Model 4. The final position and velocity uncertainties for this modification are 2070 ft and 1.4 ft/sec respectively. These uncertainties are essentially the same as those listed for the 10 landmark case in Table 2.5. The final orbital navigation uncertainties for the Hohmann type LEM descent using Model 4 are less than those uncertainties of Model 2 (Table 2.4) which deorbited on the back side after the first CSM lunar orbit. The error analysis for the landing maneuver phase from the Hohmann type descent used the Model 2 correlation matrix of Fig. 2.2 as the initial uncertainties which are considered to be typical for this type of operation.



77

Fig. 2.9 Lunar orbit navigation model 4  
LEM Hohmann descent.

TABLE 2.5

ORBIT NAVIGATION MODEL 4

Performance Accuracies

1. SCT tracking uncertainty in each axis: 1 mr ( $\sigma$ )
2. Landmark uncertainty ( $1\sigma$ ): Horizontal = 1500 ft,  
Vertical = 1500 ft.

Measurement	Time (hr)	rms Position Uncertainty		rms Velocity Uncertainty	
		Prior to Meas. (ft)	After Meas. (ft)	Prior to Meas. (ft/sec)	After Meas. (ft/sec)
	0	6710		6.1	
1st Landmark		33700	2360	28.7	3.5
2nd "		3600	2240	4.3	3.0
3rd "		3200	1920	3.5	2.1
4th "		2830	1710	2.8	1.5
5th "	1.4	2020	1510	1.8	1.3
1st Landmark	2.78	6540	1400	5.0	1.1
2nd "	2.98	1460	1250	1.1	1.0
3rd "	3.15	1330	1050	1.0	1.0
4th "	3.35	1190	1030	1.0	0.9
5th "	3.50	1140	1010	1.0	0.9
Descent Injection	4.2	1970		1.3	

Final Uncertainty One Sigma Components

Position (ft)		
X	Y	Z
1890	330	450

Velocity (fps)		
$\dot{X}$	$\dot{Y}$	$\dot{Z}$
0.3	1.2	0.4

## 2.4 Landing Site Determination

One of the primary objectives of the CSM G&N system during this phase is to determine the landing site position relative to the lunar coordinate system used for orbit navigation. The landing site position vector  $\underline{R}_L$  of Fig. 2.10 is determined by making SCT sightings on some identifiable surface feature as the CSM passes over the landing area. It must be assumed that some visible feature at or near the desired landing site is available for SCT operation. In this case the landing site determination procedure is very similar to the regular orbit navigation operation of Section 2.2 and is included in the regular landmark sighting procedure as indicated in Fig. 2.10. As the CSM passes over the desired landing site, 3 to 5 SCT angle measurements are made over the regular  $\pm 45$  degree sector about the landing site vertical as shown. The results of this type of procedure are presented later in this section.

If a lunar surface radar transponder is available to mark the desired landing site, the CSM will track the landing site with its rendezvous radar during the overpass. The landing site determination technique would be identical to that using optical SCT angles except that the measurements would be expanded to use range and range rate data also. This type of operation is identical to that prior to LEM launch in which the CSM tracks the LEM on the lunar surface in order to check launch position and aim point calculations. This operation involving CSM radar tracking and its associated performance is described in Section 5.3.1.

In a case in which the desired landing site is neither marked by a clear object visible at or near the site, nor a surface radar transponder, estimated landing site coordinates read from lunar maps must be keyed by the astronaut into the AGC to provide the required vector  $\underline{R}_L$ . These estimated coordinates and their associated uncertainties will be a major factor in G&N performance for the landing maneuver CEP. The primary G&N system objective of a 3000 foot landing CEP assumes that either

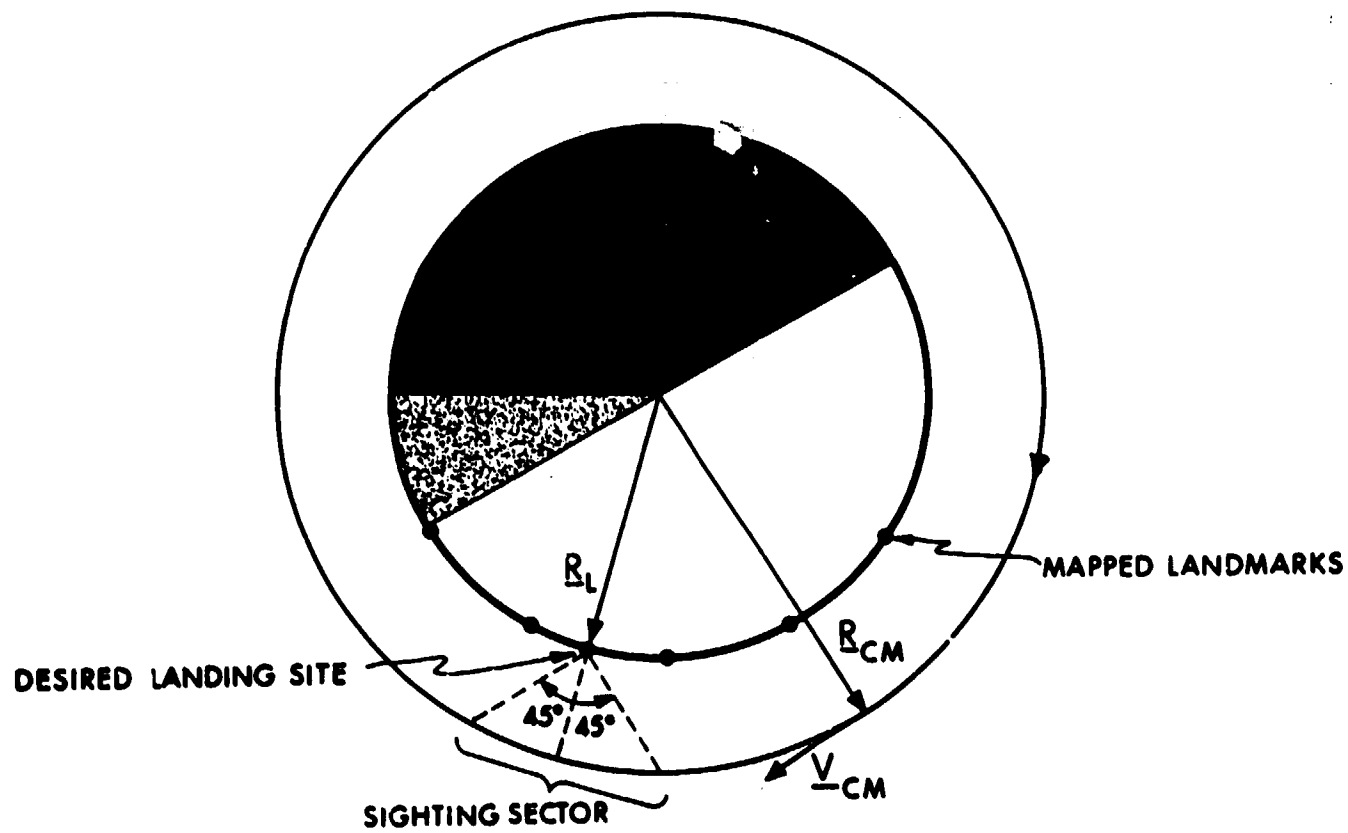


Fig. 2.10 Landing site determination.

optical or radar tracking can be used during the lunar orbit navigation phase for landing site determination.

The landing site determination technique considered for the CSM primary G&N system expands the regular estimating procedure for orbital parameters (6 x 6 matrix) to include the landing site position (9 x 9 matrix). This involves the expansion of the geometric interpretation from six to nine dimensions to include both CSM position and velocity ( $\underline{r}_{CM}$ ,  $\underline{v}_{CM}$ ) and the landing site position,  $\underline{R}_L$  (Ref. 2.4). The deviation vector of Section 2.2 becomes:

$$\delta \underline{x} = \begin{bmatrix} \delta \underline{r}_{CM} \\ \delta \underline{v}_{CM} \\ \delta \underline{r}_L \end{bmatrix}$$

The correlation matrix becomes the 9 x 9 matrix:

$$E = \begin{bmatrix} E_1 & E_2 & E_3 \\ E_4 & E_5 & E_6 \\ E_7 & E_8 & E_9 \end{bmatrix} = \begin{bmatrix} \begin{bmatrix} E \\ 6 \times 6 \end{bmatrix} & \begin{array}{c} E_3 \\ E_6 \end{array} \\ \hline E_7 & E_8 & E_9 \end{bmatrix}$$

where each  $E_n$  is a 3 x 3 submatrix and  $\begin{bmatrix} E \\ 6 \times 6 \end{bmatrix}$  represents the original CMS position and velocity uncertainties of Section 2.2.  $E_9$  is a 3 x 3 matrix which represents the three position uncertainties of the desired landing site. The four off-diagonal matrices represent the correlation, if any, between the landing site and the CSM position ( $E_3$  and  $E_7$ ), and the landing site position and the CSM velocity ( $E_6$  and  $E_8$ ). The geometry vector  $\underline{b}$  also becomes nine dimensional. The first six components are the previous ones used in the six-dimensional analysis and the last three are those required for the landing site position determination. It can be shown that for all types of navigation measurements these

last three components of the nine-dimensional  $b$  vector are the negative values of the first three components.

In simulations involving landing site determination, an initial diagonal matrix,  $E_9$ , was assumed for the landing site position uncertainty. The correlation submatrices  $E_3 = E_7^T$  and  $E_6 = E_8^T$  were initially set to zero. The results for landing site determination after five equally spaced sightings during the tracking sector indicated in Fig. 2.10 are summarized in Table 2.6 for two levels of SCT tracking performance. It was assumed that an initial rms landing site uncertainty of 11,000 ft existed at the start of the tracking interval. The final results listed in Table 2.6 indicate that the landing site can be determined to RMS values of 1600 to 2900 feet depending upon SCT tracking accuracies and the value of the CSM orbital uncertainties. The initial CSM uncertainties used in the examples of Table 2.6 were the results of orbital navigation Model 1, which is typical for CSM positions over accurately mapped landmarks (Fig. 2.10). It might be noted in Table 2.6 that the CSM orbital uncertainties after the five landing site measurements were slightly reduced in the expanded estimating procedure. The  $9 \times 9$  matrix operation is used in the midcourse rendezvous phase of Section 7.2 in order to estimate radar tracking biases, and may also be used for landmark improvement techniques required for the missions in which accurate lunar landmarks are not available (Section 2.5.3)

It might be noted that all components of the landing site uncertainty are important. The horizontal components directly affect the landing CEP performance. The radial uncertainty component of the landing site is an important factor in determining when the LEM landing radar data should be used to update the inertial guidance controlling the powered landing maneuver (Section 4.4.3).

The relative uncertainties between the CSM and the landing site are known to a higher degree than the sum of  $E_1$  and  $E_9$ .

TABLE 2.6  
LANDING SITE DETERMINATION

Performance Accuracies

1. CSM orbital uncertainties:

	Initial	Final (1 mr)	Final (4 mr)
RMS Position Uncertainty:	1484 ft	1340 ft	1410 ft
RMS Velocity Uncertainty:	1.3 fps	1.1 fps	1.2 fps

SCT Sighting	SCT Accuracy = 1 mr ( $1\sigma$ ) each axis RMS Landing Site Position Uncertainty		SCT Accuracy = 4 mr ( $1\sigma$ ) each axis RMS Landing Site Position Uncertainty	
	Prior to Meas. (ft)	After Meas. (ft)	Prior to Meas. (ft)	After Meas. (ft)
1	11000	7770	11000	8305
2	7770	2775	8305	5970
3	2775	1790	5970	3840
4	1790	1610	3840	3135
5	1610	1555	3135	2870

The relative uncertainty matrix between the CSM and landing site positions can be represented as;

$$E_{(rel)} = \overline{(R_{CM} - R_L)(R_{CM} - R_L)} = E_1 - E_3 - E_7 + E_9$$

The final RMS relative uncertainties for the examples of Table 2.6 were 800 feet and 2600 feet for 1 mr and 4 mr tracking cases respectively. The relative radial positional component is important for landing radar updating. In the landing radar operation (Sections 4.4.3 and 4.5.3), it was assumed that the radial uncertainty of the landing site terrain had been determined within an 800 foot rms relative to the CSM orbital altitude.

## 2.5 Lunar Terrain and Gravity Effects

### 2.5.1 Lunar Landmark Bias Effects

The orbital navigation models and results presented in Section 2.3 assumed that there was no fixed bias in either the landmark uncertainty or the estimate of the lunar gravity. The landmark uncertainty of 1500 feet used in these models was a random uncertainty for each landmark. Cases 1 to 3 of Table 2.7 summarize the results of lunar landmark bias effects coupled with these random uncertainties. Case 1 of Table 2.7 is the summary of the final uncertainties for Model 1 (Fig. 2.5) repeated from Table 2.1. In Case 2 of Table 2.7, all five landmarks of Model 1 are assumed to have a radial bias of +1500 feet, which is combined with the standard random uncertainty of 1500 feet in the radial and horizontal directions. This effect is equivalent to assuming that the lunar radius is 1500 feet less than the true radius. The SCT sighting angles are therefore slightly changed since the landmarks are all 1500 feet further from the center of the moon than thought. The estimated lunar orbit is in error due to the combined random and bias errors. The results listed for Case 2 of Table 2.7 are the square roots of the average of the sum of the squares of the

TABLE 2.7  
BIAS EFFECTS ON ORBIT NAVIGATION MODELS

BIAS EFFECTS	FINAL POSITION UNCERTAINTY				FINAL VELOCITY UNCERTAINTY			
	$\delta X$ (ft)	$\delta Y$ (ft)	$\delta Z$ (ft)	RMS (ft)	$\delta X$ (fps)	$\delta Y$ (fps)	$\delta Z$ (fps)	RMS (fps)
1. Standard Model 1 - Table 2.1 No Landmark or Gravity Bias	1250	530	580	1480	0.4	1.1	0.5	1.3
2. Model 1 Landmark Radial Bias = + 1500 ft	1420	600	430	1600	0.5	1.2	0.7	1.5
3. Model 1 Landmark Radial Bias = + 3000 ft	1490	800	530	1770	0.6	1.4	0.7	1.6
4. Model 1 Lunar Gravity = 0.999 $\mu$ (Estimated Gravity)	1330	1840	460	2300	2.1	1.2	0.7	2.4
5. Standard Model 4 - Table 2.5 No Landmark or Gravity Bias	1890	330	450	1970	0.3	1.2	0.4	1.3
6. Model 4 Lunar Gravity = 0.999 $\mu$	2370	2360	695	3420	1.6	1.6	0.5	2.3

85

8-7

final deviation vector components taken over 15 actual trajectory simulations of orbit navigation Model 1. The final deviation for each run was defined as the difference between the true and estimated orbital state vectors. It might be noted that the average of the final deviation vectors is not zero in these simulations. In the landmark bias Case 2 of Table 2.7, the average of the position deviation vectors was -240 feet in X, +360 feet in Y, and 140 feet in the Z direction. The estimated and true trajectories cross at various points around the CSM orbit since the estimated trajectory is shifted after each measurement. After each measurement, the average estimated trajectory is centered about a point other than the true trajectory because the 1500 foot landmark bias has been incorporated into the measurement. Since the final deviation is very dependent on the descent point in the orbit, it is very difficult to draw general conclusions on the maximum and minimum values of the deviation vectors. The results listed in Table 2.7 are for the LEM descent injection point; greater or smaller rms deviations can be found at other points in the orbit navigation model.

It can be seen by comparing Cases 1 and 2 of Table 2.7 that the 1500 foot landmark bias increases the final rms position and velocity uncertainty by 115 feet and 0.2 ft/sec respectively. Case 3 of Table 2.7 is a similar example which represents the results of 15 runs of Model 1 using 3000 foot radial biases for each of the five landmarks.

### 2.5.2 Lunar Gravity Bias Effects

The effects of lunar gravity bias on the orbit navigation results are illustrated in Case 4 of Table 2.7. In this case, it was assumed that the lunar gravity error was one part in a thousand, and the actual lunar gravity was 0.1% less than the gravity constant used in the G&N system computation. Case 4 shows the results of this gravity error for Model 1 resulting

from 15 actual trajectory runs. The true and estimated trajectories again cross each other, as in the landmark bias cases, since the estimated trajectory is shifted after each measurement and the trajectories are propagated differently due to the lunar gravity difference. The final average estimated trajectory at the descent injection point for the particular navigation model of Case 4 was 1650 feet higher, 300 feet ahead and 170 feet to one side of the true trajectory. By comparing Cases 1 and 4 of Table 2.7, it can be seen that the lunar gravity bias had the greatest effect on the Y and  $\dot{X}$  components of the final orbital uncertainties. The gravity effect considered in Case 4 also produced greater final uncertainties than the landmark biases of Cases 2 and 3.

The lunar gravity bias effect was further checked against Model 4 of Fig. 2.9. One of the major differences between this navigation model and Model 1 of Case 4 is the time interval between the last navigation measurement and the LEM descent injection point (42 minutes vs 5 minutes). Case 5 of Table 2.7 summarizes the final uncertainties of Model 4 repeated from Table 2.5 in which no gravity bias was considered. Case 6 of Table 2.7 then lists the final rms deviation of 15 actual trajectories in which the lunar gravity was 0.999 that of the value used in the G&N system. By comparing the results of Cases 5 and 6, it can be seen that the lunar gravity biases increased the final orbital uncertainties by approximately 75% with the major effect again being in the Y and  $\dot{X}$  components. Gravity effects of the magnitude indicated in Case 6 for orbit navigation Model 4 would have to be compensated for in order to achieve the desired 3000 foot landing design objective for the primary G&N system.

### 2.5.3 Lunar Landmark Mapping Accuracy Effects

The 1500 foot one sigma landmark uncertainties used in the orbit navigation models of Section 2.3 were original estimates of possible lunar landmark mapping accuracies by the time the

Apollo lunar landing mission was attempted. More current estimates of present lunar landmark position accuracies (Ref. 2.5) are greater than the three used in Section 2.3. A possible method of using degraded lunar landmarks is currently under investigation and will be presented in a future report. This method improves both landmark and CSM orbital parameters by the expanded estimating technique described in Section 2.4 for lunar landing site determination. If poor lunar landmark accuracies must be accepted, the orbit navigation phase becomes a combined landmark reconnaissance and orbital update phase. The major effect of this operation is expanded G&N computation and increased orbital periods prior to the LEM descent injection maneuver.

## 2.6 CSM Orbit Operations After LEM Descent

The primary objectives of the CSM primary G&N system after LEM descent injection are:

1. Continued orbit navigation.
2. Monitoring of the LEM descent and rendezvous trajectories (Sections 3.6 and 7.7).
3. Final landing site determination (Section 5.3).
4. Provision for LEM back-up guidance commands or active retrieval if required (Chapter 9).

Items 2 through 4 will be described in the sections indicated. The continued orbit navigation procedure is the same technique that has been described in this chapter. The type of navigation measurement will depend upon the length of the LEM lunar mission. The CSM G&N system is normally left in the operating mode for one orbit after LEM descent injection. During this time the orbit navigation operation is continued and the LEM landing site is determined by CSM rendezvous radar tracking (Section 5.3). If the LEM lunar stay time is limited to 6 hours, the CSM primary G&N system will probably be left on and the orbit navigation mode continued with one landmark sighting and IMU alignment per orbit

until the orbital pass prior to LEM launch. At this time one or more landmark sightings will be made so that final orbit parameters can be relayed to the LEM over the communication link.

For lunar landing stay times of greater than six hours, the CSM primary G&N system will be put in a standby mode after the first orbit following LEM descent. Orbit navigation is continued during this standby mode of operation by measuring at least one star occultation per orbit. The computer is the only G&N unit required in this operation which uses the astronaut-observed occultation time. The use of the SXT or SCT is optional, and the IMU is not required. The objective of this standby mode of operation is to limit the increase of orbital uncertainties so that rapid orbit determination can be made prior to LEM ascent in a manner similar to the models described in Section 2.3.



## CHAPTER 3

### DESCENT ORBIT PHASE

#### 3.1 General Description

The LEM descent orbit phase begins with the descent injection maneuver and ends with the landing maneuver ignition point which is nominally the perilune of the descent orbit. The required computation for the timing of the descent injection is naturally done before the injection maneuver and is included in this chapter. The objective of the LEM primary G&N system is to determine the timing and velocity correction needed to effect the desired descent trajectory, and then control the LEM injection maneuver to achieve this trajectory. The desired descent trajectory is one that has a near horizontal velocity at an altitude of 50,000 feet. This trajectory is further restricted in position such that it is a specified ground range or central angle (about 12 degrees for nominal powered landing maneuvers) from the desired landing site. As mentioned in Chapter 2, the primary inputs to the G&N system for the orbit descent phase are the CSM orbital position and velocity vectors at a reference time, and the landing site vector. The guidance concepts used for descent injection are presented in Sections 3.2 and 3.3. Determination of injection timing is described in Section 3.4.

Two basic types of descent orbits are presented in this chapter. The equal period, or synchronous, type descent was first considered as the basic lunar landing mission model. This concept with its associated characteristics is described in Section 3.2. It might be noted that all descent orbit analyses presented in this chapter are based on the assumption that the CSM is in a near circular lunar orbit at an altitude of 80 nm. The

guidance concepts presented in Section 3.2 are general enough, however, to be applied to more elliptical CSM orbits for the equal period type descent. Elliptical CSM orbits, i. e. 80 nm to 30 nm, are a possible method of reducing LEM  $\Delta V$  requirements for the descent and landing maneuvers, while preserving the abort and survey orbit potential of the equal period concept.

More recent mission profiles have restricted the descent orbit to the Hohmann trajectory type, which has an apolune at the 80 nm CSM orbit, and the perilune at the desired 50,000 foot altitude. This type of descent has a substantial  $\Delta V$  advantage over the equal period descent from an 80 nm circular orbit. The guidance concept used for Hohmann type descents is presented in Section 3.3.

It might be noted that both the equal period and Hohmann type descents are considered in this report. The differences in these two types of descent affect the descent phase presented in this chapter, the landing maneuver phase presented in Chapter 4, and finally, the abort requirements presented in Chapter 8.

Coplanar descent orbits, relative to CSM orbital plane, have generally been assumed in most mission profiles. The guidance concepts presented in this chapter are valid for noncoplanar descents if required. Noncoplanar descent operations are described in Section 3.5.

Primary G&N system performance for the combined orbit navigation and injection maneuver instrument uncertainties is presented in Sections 3.7 and 3.8 at the descent injection point and perilune or landing maneuver ignition point.

## 3.2 Equal Period Descent Orbit

### 3.2.1 General Description

The unique property of the equal period descent orbit, as its name implies, is that its period is the same as that of the CSM lunar orbit. This means that if an abort decision is made

prior to perilune, the LEM and CSM will return to the descent injection point on the next period, facilitating a terminal rendezvous maneuver.

This constraint on the descent trajectory period and, therefore, the semimajor axis has the effect of completely specifying the shape of the orbit. Therefore, the question of timing the initiation of thrust for the descent injection maneuver becomes relatively complex. Techniques for timing determination will be discussed in Section 3.4.

The equal period descent orbit is shown schematically in Fig. 3.1. Values of important parameters are shown, under the assumptions of a circular 80 nm CSM orbit and a coplanar descent.

### 3.2.2 Guidance and Steering Equations

Descent injection guidance is defined in this section as the criteria by which the burnout conditions of the powered injection maneuver are determined. Steering equations or concepts, on the other hand, determine the manner in which the thrust vector is controlled to arrive at the desired injection conditions. Two types of guidance concepts have been investigated for the equal period injection maneuver. These two guidance concepts could be used with either of two steering concepts depending upon various requirements or desired operating limits during the injection maneuver. These guidance and steering concepts, with their various characteristics, are described in the following sections.

#### 3.2.2.1 $\underline{V}_G \times \dot{\underline{V}}_G$ Steering

Assume that it is possible to compute a desired velocity vector,  $\underline{v}_d$ , which, if attained, would insure the successful completion of the mission (in this case, arrival at a perilune of 50,000 feet in the proper orientation,  $\underline{i}_p$ ). The unit vector  $\underline{i}_p$  is in the direction of the desired perilune and is determined

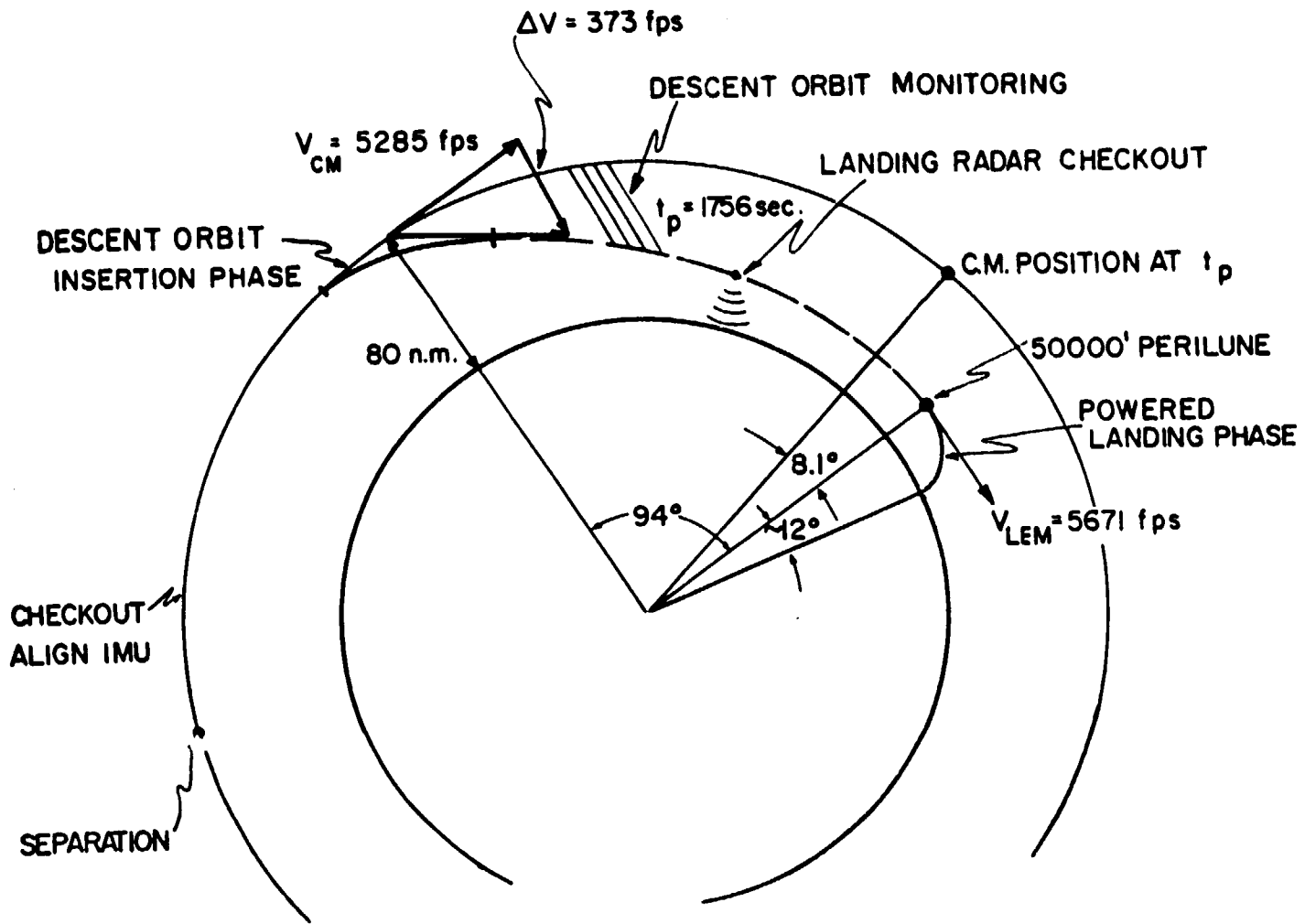


Fig. 3.1 LEM equal period descent orbit.

from an operation of the type

$$\underline{i}_p = \overset{\circ}{R} \underline{i}_L$$

This is a rotation of the landing position unit vector,  $\underline{i}_L$ , in the plane of the descent orbit. The angle of rotation determined by the matrix,  $\overset{\circ}{R}$ , is a function of the nominal powered landing maneuver ground range or central angle ( $\sim 12$  degrees as shown in Fig. 3.1).

The velocity-to-be gained is then defined as

$$\underline{v}_G = \underline{v}_d - \underline{v}$$

where  $\underline{v}$  is the present velocity. Obviously, the burnout conditions are  $\underline{v}_G \equiv 0$ . Now, let

$$\dot{\underline{v}}_G = \dot{\underline{v}}_d - \underline{g} - \underline{a}_T = \underline{b} - \underline{a}_T$$

where  $\underline{a}_T$  = thrust acceleration,  $\underline{g}$  = local gravity, and it is assumed that an analytic expression for  $\dot{\underline{v}}_d$  exists. One reasonable method of insuring efficient control of  $\underline{a}_T$  is to constrain  $\dot{\underline{v}}_G$  to lie along  $\underline{v}_G$ , i. e.  $\underline{v}_G \times \dot{\underline{v}}_G = 0$ . This condition will be met if

$$\underline{a}_T = \underline{b} + (q - \underline{i}_G \cdot \underline{b}) \underline{i}_G$$

where

$$q = \sqrt{a_T^2 - |\underline{i}_G \times \underline{b}|^2}$$

$$\underline{i}_G = \text{unit} \left( \underline{v}_G \right)$$

This is a prescription for thrust direction, as  $|\underline{a}_T|$  is commanded by the LGC and monitored by the IMU accelerometers. Note that the steering law is uniquely characterized by the vector,  $\underline{b}$ .

The  $\underline{v}_G \times \dot{\underline{v}}_G$  steering concept is used in other powered phases of the Apollo mission, such as transearth injection in the CSM primary G&N system. A more thorough description of this

steering concept is presented in Reference 3.1. The major equations for  $\underline{V}_G \times \underline{V}_G$  steering are summarized in Fig. 3.2. The desired velocity,  $\underline{V}_d$ , in this figure is determined by either of two guidance concepts described in Sections 3.2.2.3 and 3.2.2.4. In the equivalent orbit guidance concept (Section 3.2.2.3), the desired velocity at injection is a function of the present position vector,  $\underline{r}$ , the CSM semimajor axis,  $a$ , and the eccentricity,  $e$ , that results in the desired perilune altitude of 50,000 feet. The aim point guidance concept determines a desired injection velocity as a function of present position vector,  $\underline{r}$ , perilune or target position vector,  $\underline{r}_T$ , and time of flight,  $t_f$ .

### 3.2.2.2 W x V Steering

A second steering concept was derived from the basic constraints of the equal period descent orbit. In order to achieve an equal period, or synchronous orbit, with respect to the CSM, it is required on an impulsive thrust criteria that the initial velocity vector be rotated, but not changed in magnitude. This result can be achieved by always thrusting normal to instantaneous vehicle velocity vector until this vector is rotated sufficiently to achieve the desired perilune altitude. This concept can be restated as follows: equal period orbital conditions will be preserved if the time rate change of orbital energy is zero during the injection maneuver. This may be written as

$$E = \frac{1}{2} (\underline{v} \cdot \underline{v}) - \frac{\mu}{r}$$

$$\frac{dE}{dt} = \underline{v} \cdot \left[ \frac{d}{dt} \underline{v} - \mu \nabla \left( \frac{1}{r} \right) \right]$$

But

$$\frac{d}{dt} \underline{v} = \underline{a}_T + \mu \nabla \left( \frac{1}{r} \right)$$

thus

$$\frac{dE}{dt} = \underline{v} \cdot \underline{a}_T$$

DESIRED VELOCITY  $\underline{V}_d ( \underline{r}, a, e )$  EQUIVALENT ORBIT

$\underline{V}_d ( \underline{r}, \underline{r}_T, t_f )$  AIM POINT

DEFINE VELOCITY TO BE GAINED.  $\underline{V}_g = \underline{V}_d - \underline{V}$

$$\dot{\underline{V}}_g = \dot{\underline{V}}_d - \underline{a} - \underline{a}_T = \underline{b} - \underline{a}_T$$

97

THEN:  $\underline{V}_g \times \dot{\underline{V}}_g = 0$  IF,

$$\underline{a}_T = \underline{b} + [q - \underline{i}_g \cdot \underline{b}] \underline{i}_g, \quad \text{WHERE } q^2 = a_T^2 - |\underline{i}_g \times \underline{b}|^2$$

Fig. 3.2  $\underline{V}_g \times \dot{\underline{V}}_g$  steering.

In order to make  $\underline{v} \cdot \underline{a}_T = 0$ , and also acquire a velocity angle down from the horizontal,

$$\underline{a}_T = a_T (\underline{i}_n \times \underline{i}_v)$$

where

$$\underline{i}_n = \text{unit} (\underline{r} \times \underline{v})$$

$$\underline{i}_v = \text{unit} (\underline{v})$$

This may also be written

$$\underline{a}_T = \underline{\omega} \times \underline{v}$$

where

$$\underline{\omega} = \underline{i}_n \left( \frac{a_T}{v} \right)$$

It may further be noted that, for this steering law

$$\begin{aligned} \frac{d}{dt} \underline{h} &= \frac{d}{dt} (\underline{r} \times \underline{v}) \\ &= \underline{r} \times \left[ \mu \nabla \left( \frac{1}{r} \right) + \underline{a}_T \right] \\ &= \underline{r} \times \left[ \frac{a_T}{v} \underline{i}_n \times \underline{v} \right] \end{aligned}$$

or, finally

$$\frac{d}{dt} \underline{h} = \left( \frac{a_T}{v} \right) \underline{i}_n (\underline{r} \cdot \underline{v}) = \underline{\omega} (\underline{r} \cdot \underline{v})$$

Since  $\underline{r} \cdot \underline{v} < 0$ , the orbital angular momentum is decreased if the desired angular momentum is defined as

$$h_d = \sqrt{\mu a (1 - e^2)}$$

where

$$e = 1 - \frac{r_p}{a}$$

a cutoff criterion is then

$$\left[ h_d - |\underline{r} \times \underline{v}| \right] \rightarrow 0$$

It can be shown that this criterion for cutoff is identical with  $\underline{V}_G = \underline{v} - \underline{V}_d = 0$ , where  $\underline{V}_d$  is that defined for an equivalent orbit. The  $\underline{W} \times \underline{V}$  steering concept is summarized in Fig. 3.3. The desired velocity vector,  $\underline{V}_d$ , shown in this figure is determined from the guidance concept described in the following section.

### 3.2.2.3 Equivalent Orbit Insertion Guidance

As an application of  $\underline{V}_G \times \dot{\underline{V}}_G$  steering to the problem, define a desired velocity vector which corresponds to an orbit which is identical to the required descent orbit in shape; i. e. only the orientation of its perilune is unspecified. Assume the following additional precomputed quantities are available:

$$h = \left| \hat{\underline{r}} \times \hat{\underline{v}} \right|$$

and

$$p = h^2 / \mu$$

Then,

$$\underline{v}_d = \underline{i}_h \left( \frac{h}{r} \right) - \underline{i}_r \sqrt{\frac{\mu}{ar^2} (2ar - r^2 - ap)}$$

where

$\underline{i}_r$  = unit radial vector, selenocentric

$\underline{i}_h$  = unit local horizontal vector

$r$  = selenocentric radius

and the other quantities are as previously defined.

If  $\underline{V}_d$  is combined with  $\underline{V}_G \times \dot{\underline{V}}_G$  steering, the thrust vector is specified by

$$\underline{b} = \underline{i}_h \left[ (\underline{i}_h \cdot \underline{v}_G) \sqrt{\frac{\mu}{ar^4} (2ar - r^2 - ap)} + (\underline{i}_r \cdot \underline{v}_G) \left( \frac{h}{r^2} \right) \right]$$

IF  $\underline{v} \cdot \underline{a}_T = 0$  , THEN  $\frac{da}{dt} = 0$

CHOOSE:  $\underline{a}_T = |\underline{a}_T| \underline{i}_N \times \text{UNIT}(\underline{v})$   
 $= w \underline{i}_N \times \underline{v}$

WHERE:  $w = \frac{|\underline{a}_T|}{|\underline{v}|}$  &  $\underline{i}_N = \text{UNIT}(\underline{r} \times \underline{v})$

USED WITH EQUIVALENT ORBIT GUIDANCE:

$$\underline{v}_d = \underline{i}_h \left( \frac{h}{r} \right) - \underline{i}_r \sqrt{\frac{\mu}{ar^2} (2ar - r^2 - ap)}$$

Fig. 3.3  $\underline{w} \times \underline{v}$  steering.

$$+ \underline{i}_r \left[ \left( \underline{i}_h \cdot \underline{v}_G \right) \frac{h}{r^2} + \left( \underline{i}_r \cdot \underline{v}_G \right) \frac{\mu (p - r)}{r^2 \sqrt{2ar - r^2 - ap}} \right]$$

It was noted in Section 3.2.2.1 that the vector  $\underline{b}$  is the main parameter that characterizes  $\underline{V}_G \times \underline{V}_G$  steering concept. The general characteristics of the equivalent orbit concept are listed in Fig. 3.4. As mentioned earlier, application of this guidance concept will produce an orbit equivalent to that desired in every respect except the direction of perilune. The correct perilune direction must be achieved by starting the maneuver at the proper instant in the CSM orbit. Determination of this starting point is described in Section 3.4.

#### 3.2.2.4 Aimpoint Injection Guidance

A second possible approach to descent orbit injection is the requirement that the LEM pass through the perilune or landing maneuver ignition point at a specified time. This is essentially the scheme used for translunar injection (Reference 3.1). The important equations for this concept are listed in Fig. 3.5 and are described as follows. The desired injection velocity is

$$\underline{V}_d = \sqrt{\frac{\mu}{2}} \left[ \sqrt{\frac{1}{s} - \frac{1}{2a}} (\underline{i}_c - \underline{i}_r) + \sqrt{\frac{1}{s - c} - \frac{1}{2a}} (\underline{i}_c + \underline{i}_r) \right]$$

where

$$c = \left| \underline{r} - \underline{r}_p \right|$$

$\underline{r}$  = present position vector

$\underline{r}_p$  = landing maneuver initial position vector (normally perilune)

$$\underline{v}_d = \underline{i}_h \left( \frac{h}{r} \right) - \underline{i}_r \sqrt{\frac{\mu(2ar - r^2 - ap)}{ar^2}}$$

IF  $\underline{v}_g \times \dot{\underline{v}}_g$  STEERING IS USED:

$$\underline{b} = \underline{i}_h \left[ (\underline{i}_h \cdot \underline{v}_g) \sqrt{\frac{\mu(2ar - r^2 - ap)}{ar^2}} + (\underline{i}_r \cdot \underline{v}_g) \left( \frac{h}{r^2} \right) \right]$$

$$+ \underline{i}_r \left[ (\underline{i}_h \cdot \underline{v}_g) \left( \frac{h}{r^2} \right) + (\underline{i}_r \cdot \underline{v}_g) \frac{\mu(p-r)}{\sqrt{r^2(2ar - r^2 - ap)}} \right]$$

Fig. 3.4 Equivalent orbit insertion guidance.

$$c = |r_T - r| \quad , \quad s = \frac{1}{2} (r + r_T + c)$$

$$\sqrt{\mu} \, t_f = \left[ \frac{s}{C(x)} \right]^{\frac{3}{2}} S(x) - \left[ \frac{s-c}{C(y)} \right]^{\frac{3}{2}} S(y)$$

$$a = \frac{s}{x C(x)} = \frac{s-c}{y C(y)}$$

$$\underline{v}_d = \sqrt{\frac{\mu}{2}} \left[ A (i_c - i_r) + B (i_c + i_r) \right]$$

$$\text{where } A = \sqrt{\frac{1}{s} - \frac{1}{2a}} \quad , \quad B = \sqrt{\frac{1}{s-c} - \frac{1}{2a}}$$

$$\underline{b} = \sqrt{\frac{\mu}{2}} \left\{ - \frac{[(i_c - i_r) \cdot \underline{v}_g]}{4 A s^2} (i_c - i_r) + \frac{[(i_c + i_r) \cdot \underline{v}_g]}{4 B (s-c)^2} (i_c + i_r) \right. \\ \left. - \frac{(A+B)}{C} (i_c \cdot \underline{v}_g) i_c - \frac{(A-B)}{r} (i_r \cdot \underline{v}_g) i_r \right\}$$

Fig. 3.5 Aimpoint insertion guidance.

$$s = \frac{1}{2} (r + r_p + c),$$

$$\underline{i}_c = \text{unit}(\underline{r}_p - \underline{r}), \text{ and}$$

$$\underline{i}_r = \text{unit}(\underline{r}).$$

By defining

$$A = \sqrt{\frac{1}{s} - \frac{1}{2a}}$$

$$B = \sqrt{\frac{1}{s - c} - \frac{1}{2a}}$$

the following characteristic vector may be derived for a  $\underline{v}_G \times \dot{\underline{v}}_G$  steering law:

$$\begin{aligned} b = & \sqrt{\frac{\mu}{2}} \left\{ -\frac{1}{4As^2} \left[ (\underline{i}_c - \underline{i}_r) \cdot \underline{v}_G \right] (\underline{i}_c - \underline{i}_r) \right. \\ & + \frac{1}{4B(s-c)^2} \left[ (\underline{i}_c + \underline{i}_r) \cdot \underline{v}_G \right] (\underline{i}_c + \underline{i}_r) \\ & \left. - \left( \frac{A+B}{c} \right) (\underline{i}_c \cdot \underline{v}_G) \underline{i}_c - \left( \frac{A-B}{r} \right) (\underline{i}_r \cdot \underline{v}_G) \underline{i}_r \right\} \end{aligned}$$

Notice that the only quantity in  $\underline{V}_d$  not determined by the geometry is the semimajor axis,  $a$ . It is specified by  $t_f$ , the time of flight, through the equations

$$\sqrt{\mu} t_f = \left[ \frac{s}{C(x)} \right]^{3/2} S(x) - \left[ \frac{s-c}{C(y)} \right]^{3/2} S(y)$$

$$a = \frac{s}{xC(x)} = \frac{s-c}{yC(y)}$$

The parameters  $x$ ,  $y$  and the transcendental functions  $S(x)$ ,  $C(x)$ ,  $S(y)$ ,  $C(y)$ , are made to satisfy the time of flight equation by an iterative procedure, after which  $a$  is computed. The procedure is fully described in Reference 3.2 and is referred to as Lambert's

problem.

This guidance scheme is also sensitive to time of engine ignition, since the value of  $a$  at cutoff must be correct for the descent orbit. This may be achieved as closely as necessary by igniting at the same central angle relative to  $\underline{r}_p$  as in the "equivalent orbit" scheme.

### 3.2.3 Descent Injection Maneuver

An equal period injection maneuver is illustrated in Fig. 3.6. A constant thrust at maximum level (10,500 lbs) for the LEM descent engine was assumed during this maneuver. The equivalent orbit guidance concept (Section 3.2.2.3) and  $\underline{W} \times \underline{V}$  steering concept (Section 3.2.2.2) were used to control the maneuver of Fig. 3.6. Trajectory characteristics of aim point guidance and  $\underline{V}_G \times \underline{V}_G$  steering are not significantly different from that shown in Fig. 3.6. The characteristic velocity,  $\Delta V$ , required for this maneuver is essentially identical to the initial desired velocity magnitude  $|\underline{V}_d|$  of 373 fps. This is an indirect result of the relatively short thrusting time of 29.1 seconds at maximum throttle setting. With reference to Fig. 3.6, it can be seen that the LEM is almost directly below the CSM at injection into the descent orbit. The maneuver starting time of  $t = +14.6$  seconds in Fig. 3.6 is referenced to the time the CSM would intersect the desired descent orbit. It can also be noted from the final injection velocity in this figure, that the guidance concept not only rotates the LEM velocity vector, but also compensates for the altitude change during the maneuver to achieve the desired descent orbit.

The commanded thrust angle profiles for the injection maneuver controlled by various combinations of guidance and steering equations are shown in Fig. 3.7 for constant, maximum thrust maneuvers. The equivalent orbit guidance with the  $\underline{W} \times \underline{V}$  steering case indicated in Fig. 3.7 resulted in the trajectory shown in Fig. 3.6. It can be seen in Fig. 3.7 that the initial

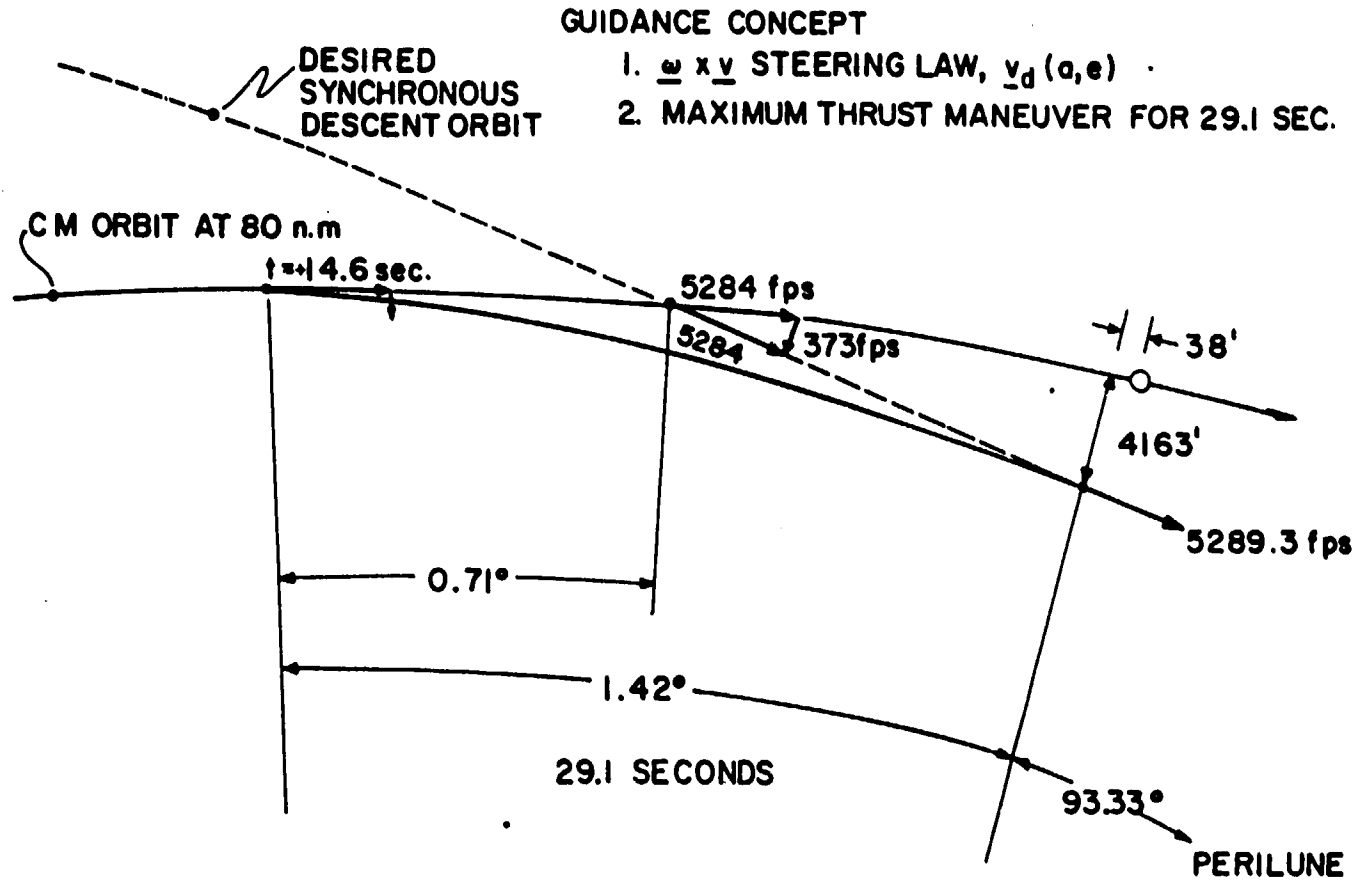
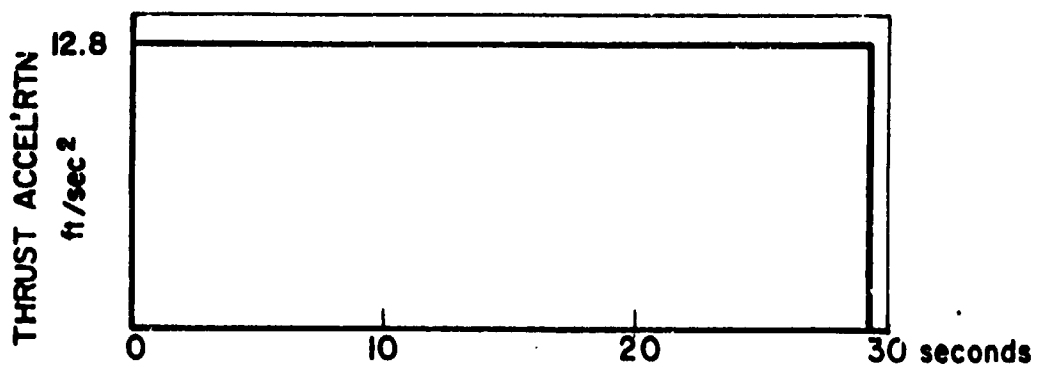
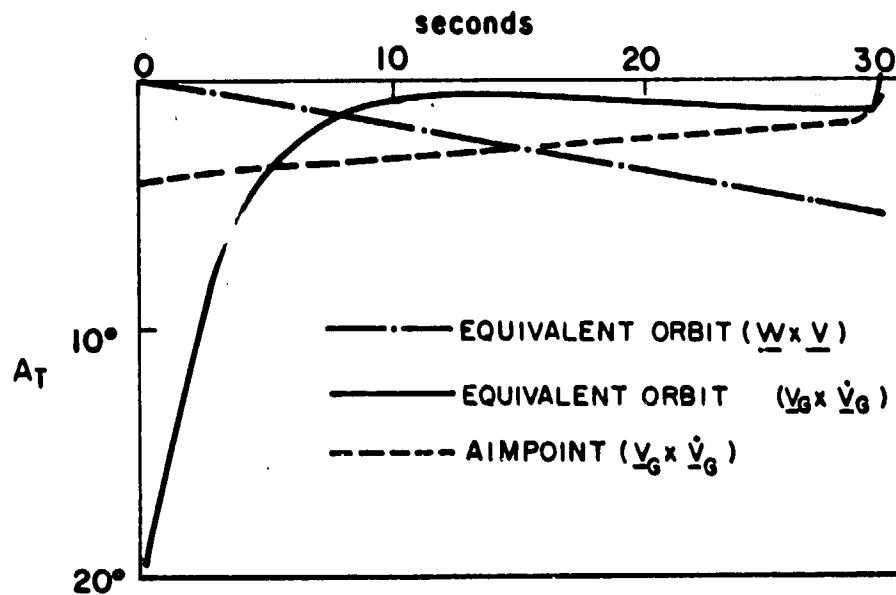
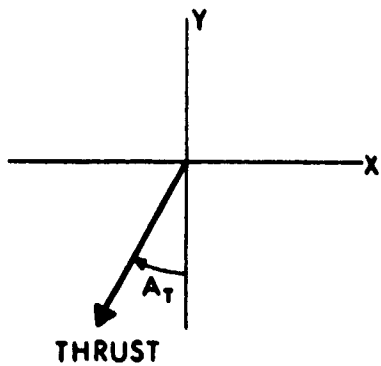


Fig. 3.6 Descent orbit injection.



commanded thrust angle for this case was directed down along the local vertical,  $A_T = 0$  degrees, and rotated approximately 5 degrees during the maneuver as expected, since the LEM velocity vector must be rotated by this same angle for the desired equal period injection (50,000 foot perilune). Aim point guidance and  $\underline{V}_G$   $\underline{V}_G$  steering resulted in thrust angle commands that covered essentially the same range. The most extreme angular limits and rates during injection are commanded by equivalent orbit guidance and  $\underline{V}_G$   $\underline{V}_G$  steering. Maximum angular rates of about 5 degrees per second result in this case, and as a result the other guidance and steering equation combinations of Fig. 3.7 would be preferred.

A desirable operational requirement during the descent injection maneuver is to check the throttle performance of descent engine. This requirement resulted from the check-out philosophy of testing as many of LEM subsystems as possible that are required for a successful landing before initiating the powered landing maneuver at the perilune of the descent orbit. Several variable thrust profiles have been included in the G&N analysis of the descent injection maneuver. The maneuver shown in Fig. 3.8 used a thrust program in which the thrust level was held at maximum for 5 seconds then decreased linearly over the next 40 seconds to a level close to that required for hover conditions. This minimum level was then maintained until thrust cutoff was commanded by equivalent orbit,  $\underline{W} \times \underline{V}$ , concept. As indicated in Fig. 3.8, this maneuver required 50.4 seconds and terminated when the LEM velocity was 5295 fps at a position virtually directly under the CSM, but at a longer range than the case of Fig. 3.6.

The commanded thrust angle profiles for the variable thrust maneuver are shown in Fig. 3.9. These thrust angle profiles are very similar to those of Fig. 3.7 for the various guidance and steering concepts used. The high commanded

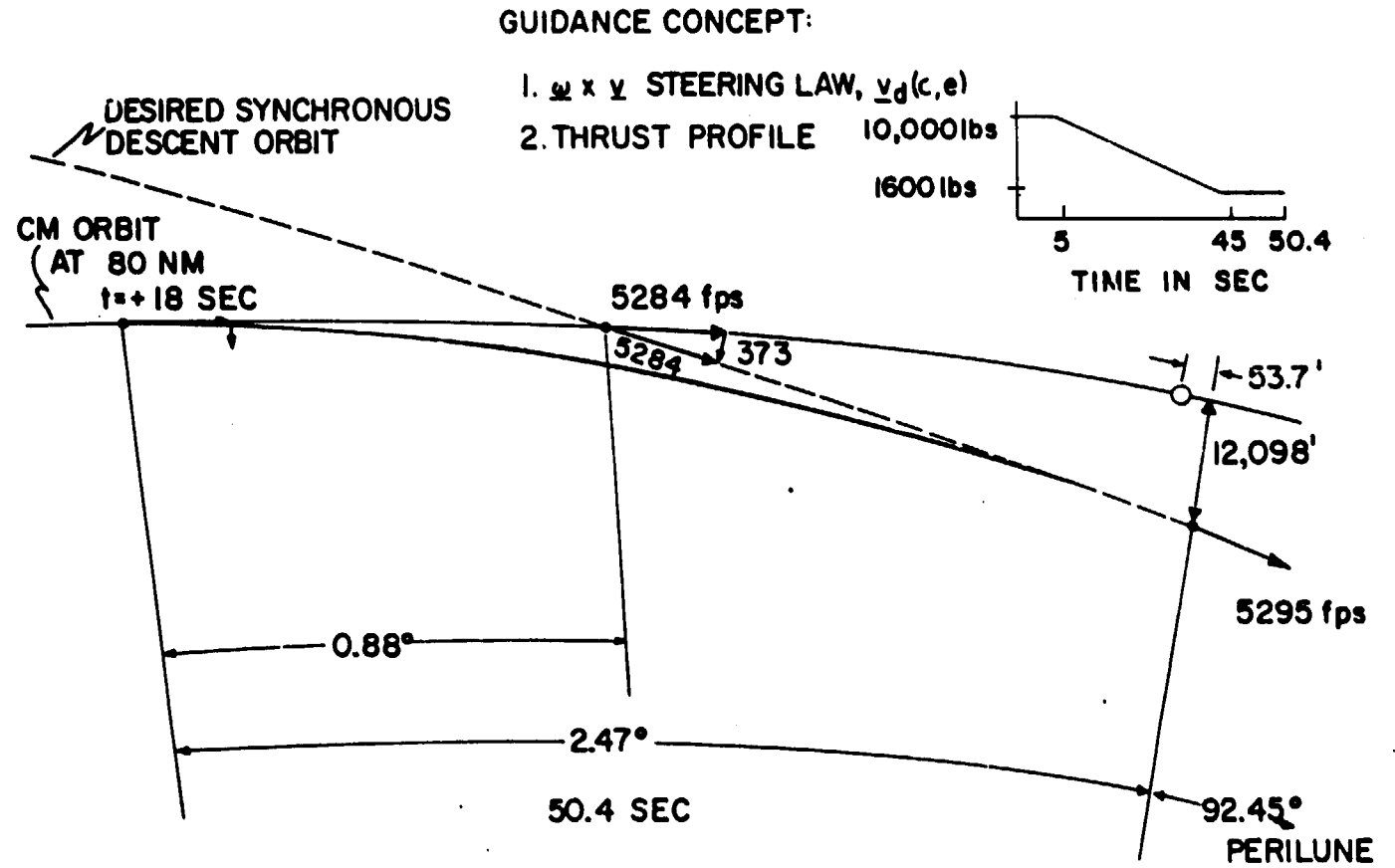


Fig. 3.8 Equal period descent injection maneuver.

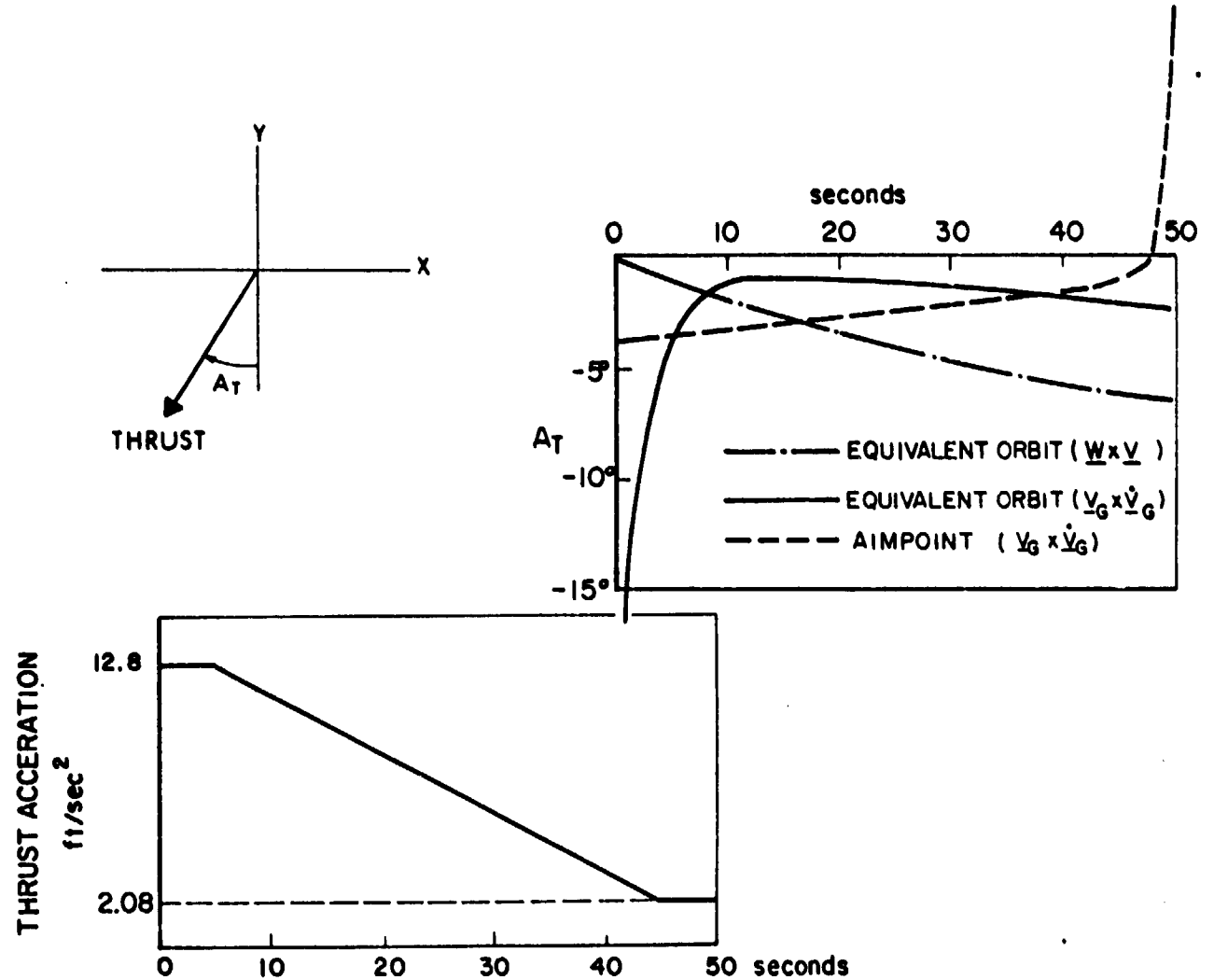


Fig. 3.9 Thrust angle profiles for variable acceleration injection maneuver.

angle rate at the end of the equivalent orbit  $\underline{V}_G \times \dot{\underline{V}}_G$  case resulted from the thrust direction becoming poorly defined as  $|\underline{v}_G| \rightarrow 0$ , and could be restricted with no serious degradation of results. The other combinations shown in Fig. 3.9 are preferred, due to the over-all lower commanded thrust angle range.

It might be noted, that GAEC has suggested a more current thrust profile for throttle check-out during the descent injection maneuver, in which the descent engine is started at minimum thrust and then throttled to maximum thrust after initial descent engine trim gimbals misalignment has been corrected. An example of an injection maneuver using such a thrust program is presented in Section 3.3.3.

The performance of the various guidance and steering equation combinations were evaluated in terms of perilune or landing maneuver initial condition deviations resulting from errors in timing of thrust initiation and thrust magnitude uncertainties of the injection maneuver. It should be noted, that the landing maneuver is always initiated when the LEM reaches a given angle (~12 degrees) from the desired landing site. Nominally, the perilune of the descent orbit lies on this ignition line or vector, but timing and thrust uncertainties will shift the perilune of the actual descent orbit away from this point, thereby changing the altitude and velocity conditions at the start of the landing maneuver. The effects of delayed descent injection are illustrated in Fig. 3.10. Timing errors of 10 seconds were considered and thrust magnitude uncertainties of -5% were assumed in this evaluation. In the case of equivalent orbit guidance with either steering concept, the effect of an initial timing error is a shift in perilune position of the actual descent orbit (Fig. 3.10). The orbital conditions at the desired landing maneuver ignition point are those 10 seconds away from the true perilune. These deviations are -5 fps downward in radial velocity, and a 25 foot

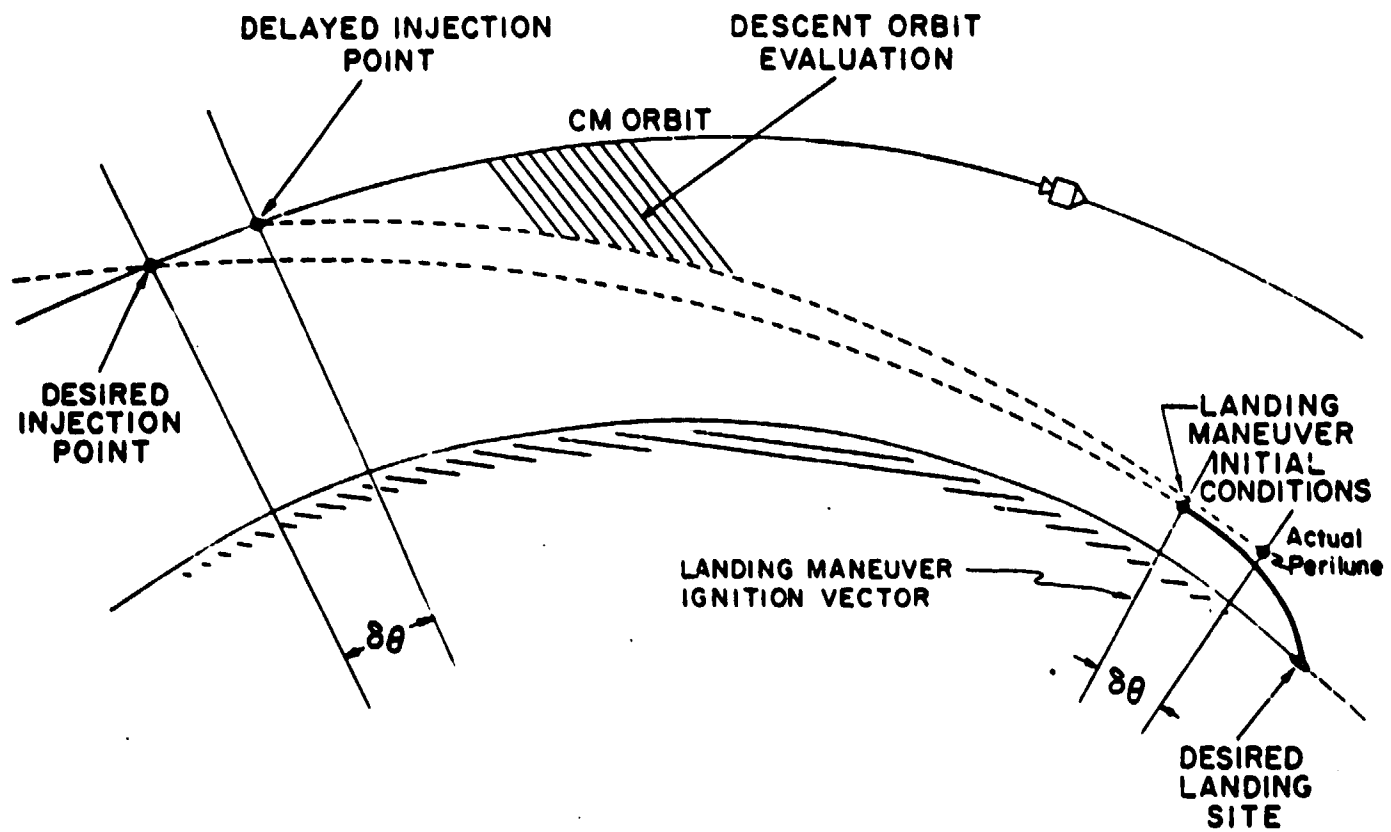


Fig. 3.10 Descent orbit injection timing effects.

higher altitude for a 10 second ignition delay of the injection maneuver. It might be noted that late ignition conditions are known variations as opposed to unknown instrument errors in the LEM G&N system, and these effects could be compensated for in the landing maneuver, as described in Section 4.2. A 5% low thrust condition has the effect of increasing the injection maneuver by about 1.5 seconds for the maximum thrust profile. The effects at the landing maneuver ignition point are roughly those for a timing error of the same magnitude.

The aim point guidance and  $\underline{V}_G \times \dot{\underline{V}}_G$  steering combination will intercept the desired landing ignition vector with negligible error in the event of timing or thrust uncertainties (assuming no G&N instrument errors). Since the time of flight is controlled in this guidance concept, the velocity at the landing ignition point will change as a function of descent injection timing. For the 10 second timing errors considered, the radial velocity, at the landing ignition point, increased to 25 fps downward from the nominal zero value. Variations in horizontal velocity are negligible for timing delays of this magnitude. Five percent thrust variations during descent injection also produced insignificant effects for this type of guidance.

The largest variations in landing maneuver ignition conditions resulted from descent injection timing errors. It is assumed that the 10 second delay, or ignition window, for the LEM descent injection is conservative. This assumption will have to be verified in future investigations as to the specific LEM subsystems which could cause delays in descent injection, and what maximum ignition delay will be tolerated before the descent will be postponed until the next orbital pass. Descent injection delays can be compensated for in the landing maneuver, and delays of 10 seconds are not considered serious for this particular phase of the mission.

Of the guidance and steering concepts presented in

Section 3.2.2, the equivalent orbit  $\underline{W} \times \underline{V}$  concept is tentatively preferred over the aim point concept, due to the abort characteristics described in the following section. It might be noted, however, that current LGC simulations and programming do not include equal period type descents, due to the more recently accepted Hohmann type descents described in Section 3.3.

#### 3.2.4 Aborts During Descent Injection

One of the major advantages of the equal period type descent orbit is that two vehicles theoretically meet at the descent injection point after one period, if a landing maneuver was not initiated. Since impulsive injection is not possible, the guidance and steering concepts used in the descent injection maneuver will determine how well the "free abort" factor is preserved. In the cases in which the descent injection maneuver was completed, all guidance concepts achieved the desired descent orbit with its associated free return characteristics. If the mission was aborted during the injection maneuver, however, the two guidance and steering concepts produced different terminal abort rendezvous conditions. As an example, it was assumed that the injection maneuver was aborted 15 seconds after ignition (constant maximum thrust profile) since this time corresponds to about the greatest variation in orbital period for all guidance concepts considered. The results in terms of LEM orbit perilune and closest approach range to the CSM are summarized in Fig. 3.11.

As expected, the best results are achieved by the  $\underline{W} \times \underline{V}$  steering concept, since it continually holds the orbital period fixed throughout the injection maneuver. In this case, the abort trajectory would normally require only a terminal rendezvous maneuver one period after injection thrust termination. As indicated in Fig. 3.11, any guidance concept with  $\underline{V}_G \times \dot{\underline{V}}_G$  steering, on the other hand, will require one or more midcourse velocity corrections (Section 7.2) to establish an intercept

GUIDANCE TYPE	PERILUNE ALTITUDE	CLOSEST APPROACH	
		RANGE	TIME
FIXED ACCELERATION			
EQUIV. ORBIT ( $\underline{V}_0 \times \dot{\underline{V}}_0$ )	39.2 n.m.	36.5 n.m.	7342.5 sec
AIMPOINT ( $\underline{V}_0 \times \dot{\underline{V}}_0$ )	40.6 "	22.6 "	7343.8 "
EQUIV. ORBIT ( $\underline{W} \times \underline{V}$ )	43.0 "	< 100'	7350.0 "
VARIABLE ACCELERATION			
EQUIV. ORBIT ( $\underline{Q} \times \dot{\underline{V}}_0$ )	41.6 n.m.	38.3 n.m.	7344.1 sec
AIMPOINT ( $\underline{Q}_0 \times \dot{\underline{V}}_0$ )	43.1 "	23.2 "	7344.5 "
EQUIV. ORBIT ( $\underline{W} \times \underline{V}$ )	45.6 "	< 100'	7349.6 "

Fig. 3.11 Rendezvous conditions resulting from an abort initiated 10 seconds after the start of the equal period descent injection maneuver.

trajectory with the CSM so that a terminal rendezvous can be achieved.

### 3.3 Hohmann Descent Orbit

#### 3.3.1 General Description

The LEM descent orbit used in current analysis is a Hohmann type trajectory having its apolune at the descent injection point on the CSM orbit and its perilune at the desired landing maneuver ignition point at 50,000 foot altitude. The primary advantage of the Hohmann descent trajectory is a  $\Delta V$  saving over the equal period descents of previous sections. The general characteristics of the Hohmann type descent are shown in Fig. 3.12. Comparing this figure with Fig. 3.1, it can be seen that the Hohmann descent requires 275 fps less initial injection velocity and arrives at perilune with a velocity 90 fps less than that of the equal period descent. The sum of these two velocity differences is a 35 fps decrease in required  $\Delta V$  of the LEM descent stage. At the time of LEM landing maneuver ignition at perilune, the CSM is behind this point by 9.4 degrees compared with the equal period case of 8.1 degrees. The G&N operations (i. e., monitoring, check out) shown in Fig. 3.12 will be described in Section 3.6.

#### 3.3.2 Guidance and Steering Equations

Two types of guidance concepts for injection into the Hohmann descent trajectory have been considered. Both employ the  $\underline{V}_G = \underline{V}_G$  steering concept and are, therefore, characterized by the previously defined  $\underline{b}$  vector of Section 3.2.2.

##### 3.3.2.1 Hohmann Descent Orbit Guidance

In the first guidance concept, the desired injection velocity, as a function of position, is defined as that velocity at the present position,  $\underline{r}$ , (if  $\underline{r}$  is the apolune of the descent orbit) which will produce a perilune of radius  $r_p$ . This velocity is:

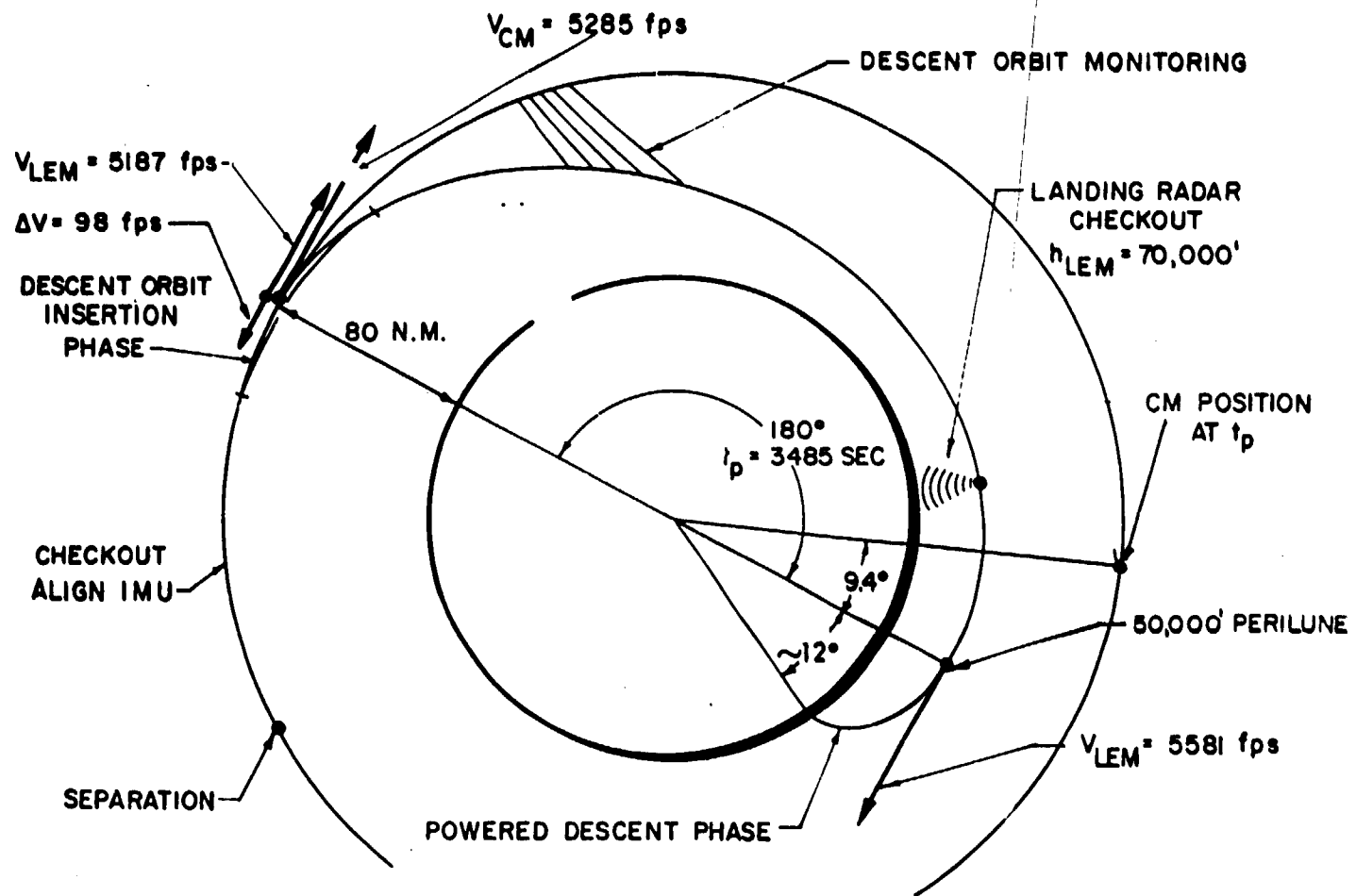


Fig. 3.12 LEM Hohmann descent orbit.

$$\underline{V}_d = \frac{\sqrt{\mu l}}{r} \underline{i}_r \times \underline{i}_z$$

$$l = a(1 - \epsilon^2) = \frac{r_p r}{e}$$

where  $a$  is the semi-major axis of the descent orbit. But

$$a = \frac{1}{2}(r + r_p)$$

so

$$\underline{V}_d = \underline{i}_r \times \underline{i}_z \sqrt{\frac{2\mu r_p}{r^2 + r_p r}}$$

Therefore,

$$\underline{V}_G = \underline{V}_d - \underline{v}$$

and,

$$\underline{b} = \dot{\underline{V}}_d - \underline{g} = \frac{1}{r} \sqrt{\frac{2\mu r_p}{r^2 + r_p r}} \left\{ \frac{1}{2} (\underline{i}_r \times \underline{i}_z) (\underline{i}_r \cdot \underline{V}_G) \left[ \frac{4r + 3r_p}{r + r_p} \right] + \underline{i}_z \times \underline{V}_G \right\}$$

which, as previously explained, completely specified the thrust direction. These equations are summarized in Fig. 3.13.

### 3.3.2.2 Aim Point Guidance for Hohmann Type Descents

The basic form of the aim point guidance concept was presented in Section 3.2.2.4. This concept may be used to reach  $\underline{r}_p$  from any  $\underline{r}$  in the CSM orbit except for transfer angles which are integral multiples of 180 degrees, in which case the descent orbital plane is undefined. Since it is unrealistic to assume that the desired landing ignition point,  $\underline{r}_p$ , will always lie exactly in the CSM orbital plane, a modified descent orbit

STEERING:  $\underline{V}_G \times \dot{\underline{V}}_G = 0$

$$\underline{V}_d = \underline{i}_r \times \underline{i}_z \left[ \frac{2\mu r_p}{r^2 + r_p r} \right]^{\frac{1}{2}}$$

$$\underline{V}_G = \underline{V}_d - \underline{V}$$

$$\underline{b} = \frac{1}{r} \left[ \frac{2\mu r_p}{r^2 + r_p r} \right]^{\frac{1}{2}} \left[ \frac{1}{2}(\underline{i}_r \times \underline{i}_z) \left( \frac{4r + 3r_p}{r + r_p} \right) (\underline{i}_r \cdot \underline{V}_G) + \underline{i}_z \times \underline{V}_G \right]$$

Fig. 3.13 Hohmann descent guidance equations.

is used for the aim point concept. This modification changes the central angle of the descent trajectory from 180 degrees to 175 degrees in order to avoid this singularity condition. Simulations of this concept indicate that the injection maneuver can be performed with essentially the same  $\Delta V$  as the exact 180 degree Hohmann descent trajectory.

### 3.3.3 Descent Injection Maneuvers

A descent injection maneuver using the Hohmann descent guidance concept (Section 3.3.2.1) is illustrated in Fig. 3.14. Maximum thrust was assumed throughout this particular maneuver, which lasted 7.6 seconds. If the LEM and CSM were assumed to start together at the beginning of this maneuver, the LEM was at essentially the same altitude, but behind the CSM by 371 feet at injection. The 500 foot nominal initial separation distance (Section 3.6) should be added to this figure. The thrust angle profiles for the injection maneuver, using both guidance concepts of Section 3.3.2, are shown in Fig. 3.15. Commanded thrust angle limits and rates are modest for either guidance concept. The maximum thrust angle rates occur at the end of the maneuver where  $\underline{V}_G \approx 0$ , and the thrust angle is consequently poorly defined. The  $\underline{V}_G \times \underline{V}_G$  steering concept theoretically forces all three components of the velocity to be gained,  $\underline{V}_G$ , to zero simultaneously. If it is desired to limit commanded thrust angle variation at the end of the maneuver, the thrust angle can be held constant at an earlier time, i. e. 5 seconds in Fig. 3.14, until cut off, which would be controlled by the component of  $\underline{V}_G$  in that thrust direction. This component of  $\underline{V}_G$  is by far the biggest of the three, and negligible error occurs from this modification.

Extrapolation of the injection conditions resulting from the Hohmann guidance concept, assuming no G&N instrument errors through 3485 seconds to perilune, indicated that the desired landing ignition conditions were attained with negligible

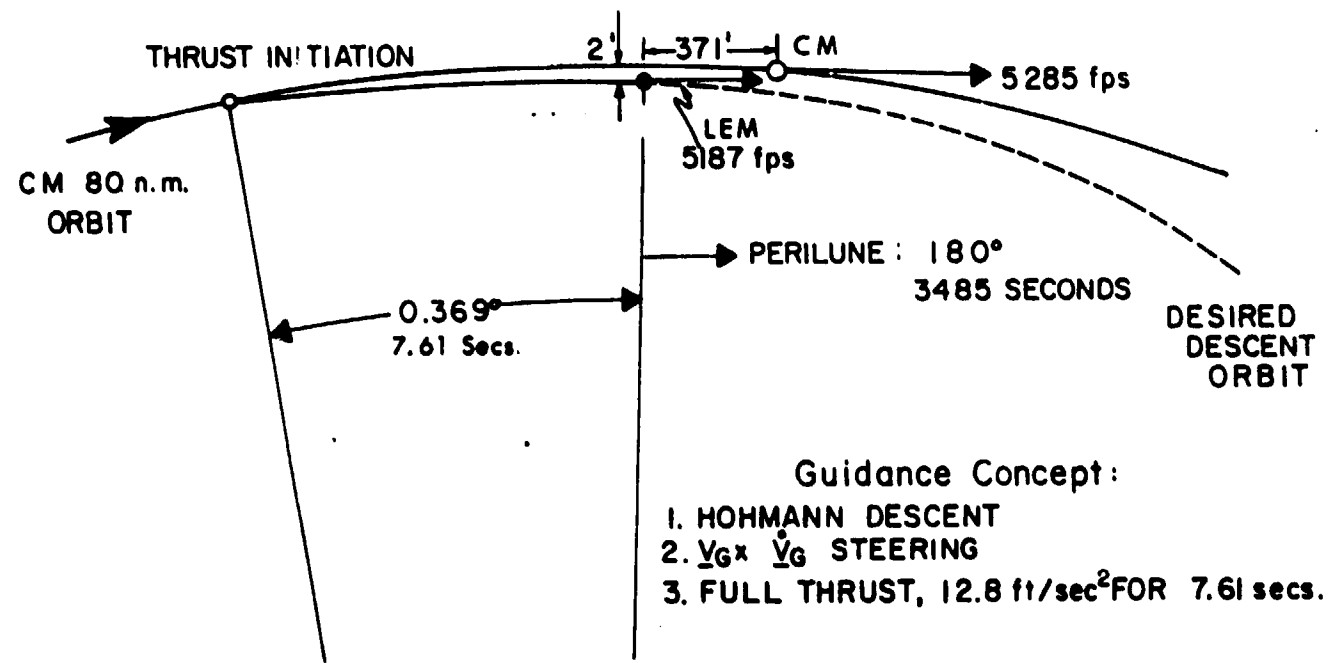


Fig. 3.14 Hohmann descent orbit injection.

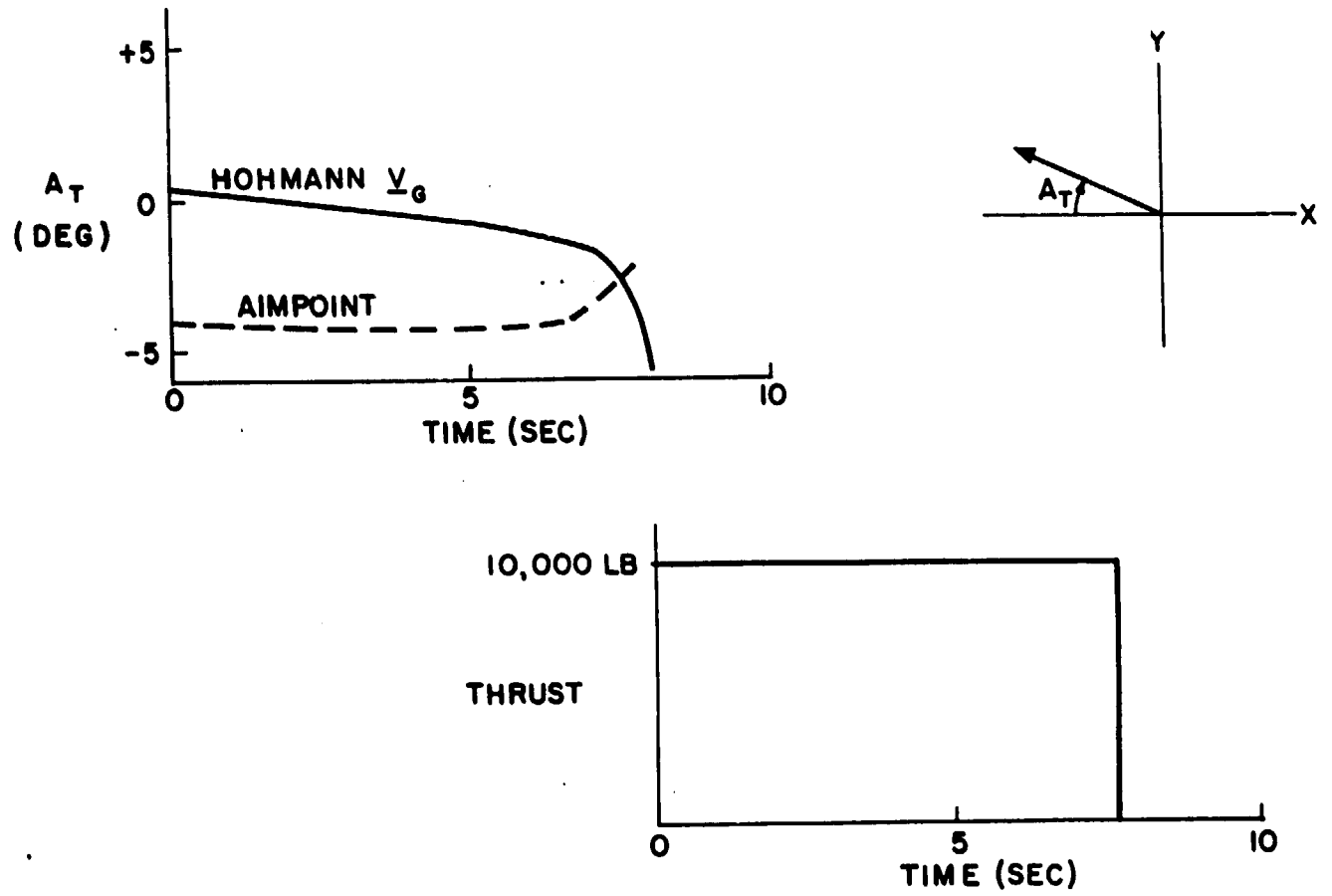


Fig. 3.15 Thrust angle history for Hohmann descent injection.

error due to the guidance equations. Similar results were obtained for the aim point guidance concept using a 175 degree descent trajectory.

As previously mentioned in Section 3.2.3, current thrust profiles for descent engine throttle check-out during the descent injection maneuver start the engine at near minimum thrust, hold this level until the descent engine trim gimbal misalignment has been corrected, then increase the thrust level to maximum until terminated by the G&N system. An injection for Hohmann descent using a thrust profile of this type is shown in Fig. 3.16. The thrust angle profiles for the two guidance concepts considered are shown in Fig. 3.17. Either guidance concept results in powered maneuvers that are essentially identical in Fig. 3.16. As illustrated in this figure, the injection maneuver lasts 22.3 seconds, and results in a LEM position at injection directly behind the CSM. The initial 500 foot separation distance should be added to final range shown in Fig. 3.16.

The examples presented in this section are typical for the two guidance concepts presented in Section 3.3.2. Of these two concepts, the Hohmann descent orbit,  $\underline{V}_G \times \dot{\underline{V}}_G$  concept will be the first programmed in the LGC for more extensive simulations. Final choice will depend upon LGC programming simplicity, storage requirements, and required computation cycle rate for stable operation with the LEM SCS under injection conditions.

Hohmann descent trajectories do not have the abort features of the equal period descents, and any abort initiated during the Hohmann descent will require a separate LEM maneuver to establish a rendezvous trajectory, followed by mid-course velocity corrections as needed. This type of abort operation initiated during the descent phase of Hohmann trajectories is described in Section 8.2.

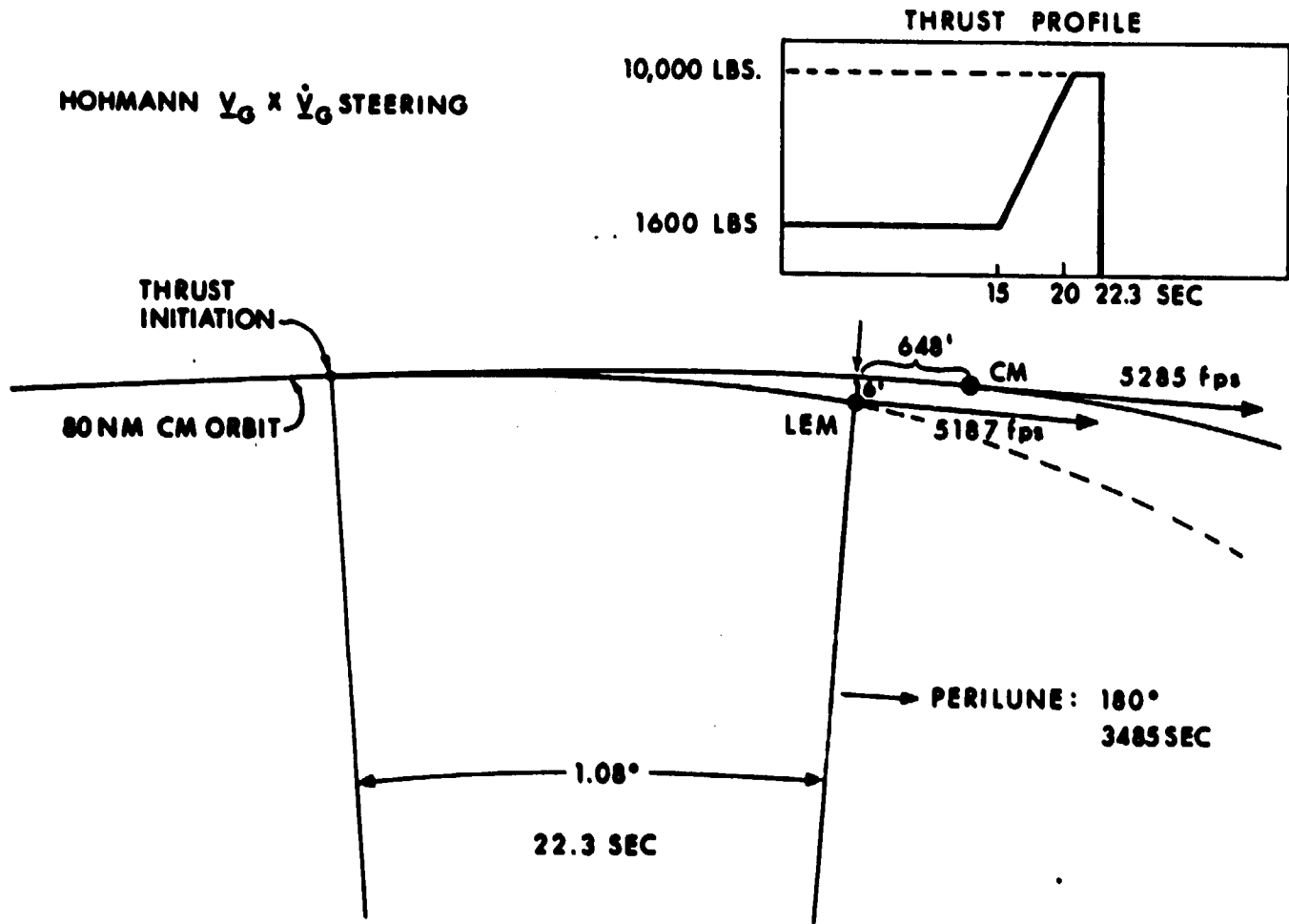


Fig. 3.16 Hohmann descent orbit injection maneuver

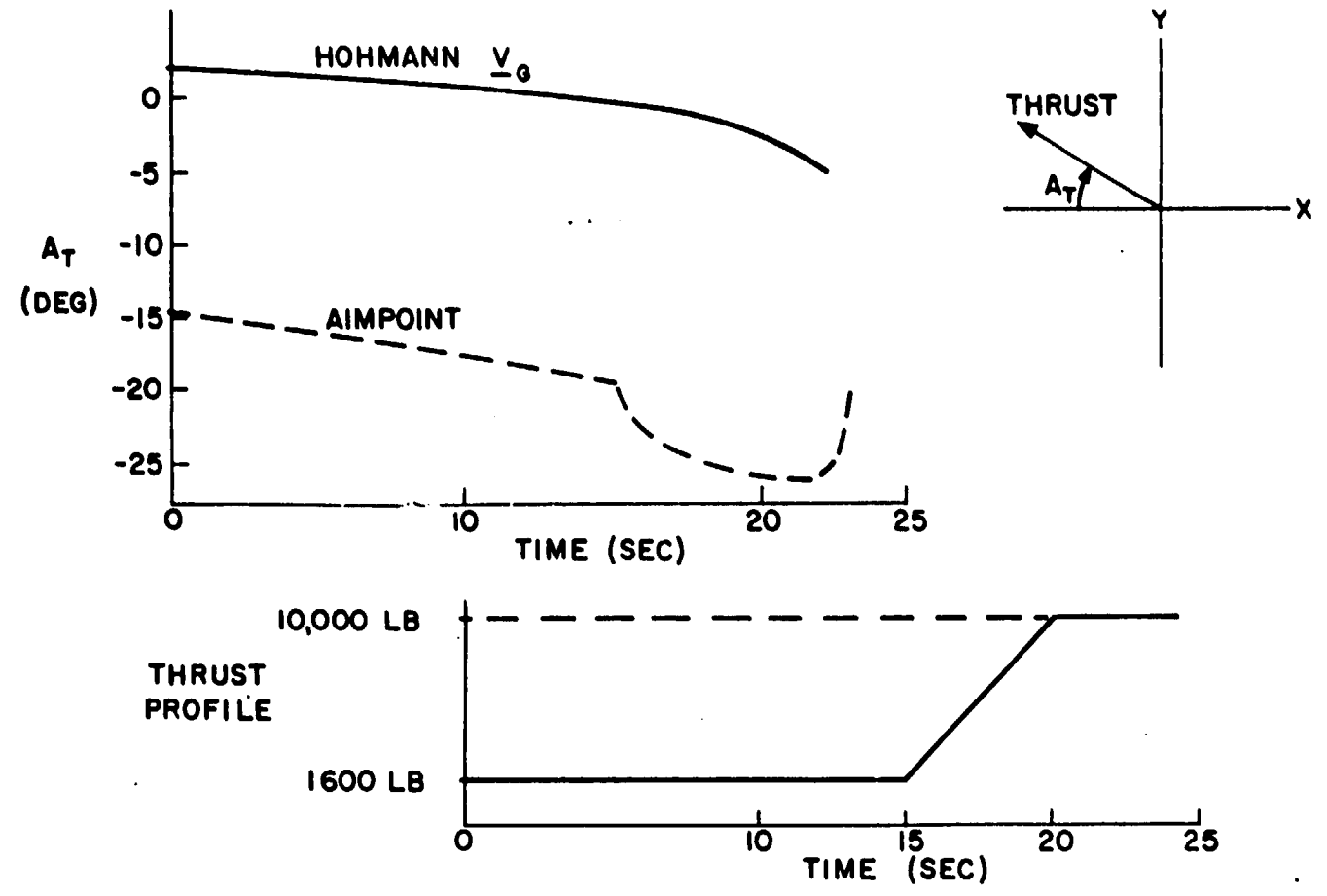


Fig. 3.17 Thrust angle history for Hohmann descent injection.

### 3.4 Injection Timing Determination

It has been previously indicated that all guidance schemes presented are, to some extent, sensitive to the timing of thrust ignition for descent injection. In most schemes, the determination of the orientation of the actual perilune position within the plane of the descent orbit is solely a function of this timing.

Simulation of the guidance schemes has shown that a simple time relationship exists between thrust initiation time and the time at which the vehicles in the LEM CSM orbit reach the intersection with the desired descent orbit. This means that when the intersection point between the CSM and the descent orbits has been established, the position at which thrust initiation should take place is found by simply extrapolating position at intersection back along the CSM orbit for a time which is a function of the injection guidance concept and the desired thrust check-out profile. It might be noted that in the case of a noncircular initial LEM CSM orbit, or an out-of-plane landing point, this time factor is no longer exact. However, for eccentricities and inclinations of expected magnitudes, corrections to this time will result in negligible variations in conditions at perilune.

A simple iterative procedure has been developed for computing the point of intersection of the two orbits, when the shape of the descent orbit is specified. A computation flow diagram of the procedure is shown in Fig. 3.18. It is assumed that the following quantities are available from initial inputs stored in the LGC:

$\phi_L$  = central angle of the landing maneuver

$\phi_D$  = estimated central angle of descent orbit

$\underline{R}_p$  = desired perilune radius



$t_B$  = descent injection thrust ignition time factor based on the desired injection thrust profile and guidance concept.

Estimated CSM position and velocity at any time,  $\hat{R}_{CM}$  and  $\hat{V}_{CM}$ , and a unit vector in the direction of the chosen landing site,  $\underline{i}_L$ , are available from the previous orbital navigation phase. The computational procedure for injection timing determination is as follows. The LGC Kepler routines shown in Fig. 3.18 advance the input vehicle position and velocity vectors by a designated time or angle along its trajectory. An initial trial injection point condition,  $\tilde{R}_{CM}$ , is determined by the landing site vector,  $\underline{i}_L$ , rotated through the desired landing and descent trajectory angles  $\phi_L$  and  $\phi_D$ , respectively. The unit vector,  $\underline{i}_c$ , along  $\tilde{R}_{CM}$ , and the unit vector  $\underline{i}_n$  normal to the CM orbit are computed in Block A of Fig. 3.18 and Item A of Fig. 3.19. The unit vector  $\underline{i}_p$  in the perilune direction is then computed in Block B. The parameters of the descent orbit are next computed in Block C, along with radius  $R_D$ , in the descent orbit at a true anomaly of

$$f_D = \cos^{-1}(\underline{i}_c \cdot \underline{i}_p)$$

This radius,  $R_D$ , is compared with  $|\tilde{R}_{CM}|$ . If they do not agree (within a set tolerance), the parameters of the CM orbit are computed in Block D, as listed in Fig. 3.19. The parameters of the two orbits, and  $\underline{i}_c$ , are then used to compute a new trial value for  $\tilde{R}_{CM}$  in Block E (Fig. 3.20). When the two radii do agree,  $\tilde{R}_{CM}$  is extrapolated back along its orbit to  $\underline{R}_I$ , (Fig. 3.18) which is the position at which thrust ignition is to occur. The equations used in this procedure are summarized in Figs. 3.19 and 3.20.

The effect of errors in descent thrust initiation timing are indicated in Fig. 3.10. This type of result is true for every guidance scheme except aim point. It is seen that the result is

$$A. \quad \underline{i}_C = \text{UNIT}(\tilde{\underline{R}}_{CM}) \cdot \underline{i}_N = \text{UNIT}(\tilde{\underline{V}}_{CM} \times \tilde{\underline{R}}_{CM})$$

$$B. \quad \underline{i}_Z = \text{UNIT}(\underline{i}_L \times \underline{i}_C)$$

$$\underline{i}_P = \underset{(3 \times 3)}{M}(\phi_L, \underline{i}_L, \underline{i}_Z) \cdot \underline{i}_L$$

C. DESCENT ORBIT PARAMETERS (SYNCHRONOUS DESCENT)

$$a_{CM} = a_{LEM} \quad ; \quad e_{LEM} = 1 - R_p / a_{LEM}$$

$$R_D = \frac{a(1-e^2)}{1+e(\underline{i}_C \cdot \underline{i}_P)} \quad ; \quad \underline{R}_p = R_p \underline{i}_P \quad ; \quad \underline{V}_p = \left[ \frac{\mu}{a} \frac{(1+e)}{(1-e)} \right]^{\frac{1}{2}} (\underline{i}_P \times \underline{i}_N)$$

D. CM ORBIT PARAMETERS

$$a_{CM} = \left[ \frac{2}{|\hat{\underline{R}}_{CM}|} - \frac{1}{\mu} \hat{\underline{V}}_{CM} \cdot \hat{\underline{V}}_{CM} \right]^{-1}$$

$$\underline{e}_{CM} = \frac{|\hat{\underline{R}}_{CM} \times \hat{\underline{V}}_{CM}|}{\mu} \hat{\underline{V}}_{CM} \times \underline{i}_N - \underline{i}_C$$

$$e_{CM} = |\underline{e}_{CM}| \quad ; \quad \theta_{CM} = \cos^{-1} \left[ \frac{\underline{i}_C \cdot \underline{e}_{CM}}{e_{CM}} \right]$$

Fig. 3.19 Descent injection timing equations.

$$E. \quad P_{LEM} = \sigma_{LEM} (1 - \sigma_{LEM}^2)$$

$$\delta\theta = \cos^{-1} \left( \frac{P_{LEM} - R_D}{\sigma_{LEM} R_D} \right) - \theta_{CM}$$

$$\underline{i}'_C = \underset{(3 \times 3)}{M} (\delta\theta, \underline{i}'_N, \underline{i}'_C) \cdot \underline{i}'_C$$

$$\underline{\tilde{R}}'_C = R_D \underline{i}'_C$$

F. ENGINE ON AT COINCIDENCE OF  $R_I$  AND  $\hat{R}_{CM}$

$$\frac{R_I}{R_I} \cdot \frac{\hat{R}_{CM}}{\hat{R}_{CM}} = 1 \quad (\text{ENGINE ON})$$

$$< 1 \quad (\text{ENGINE OFF})$$

Fig. 3.20 Descent injection timing equations (cont).

essentially a shift in the orientation of the descent orbit by an angle  $\delta\theta$ . This accounts, in a large part, for the insensitivity of perilune conditions to the timing of the insertion maneuver. With aim point guidance, the desired perilune position will be attained, but with a non-horizontal velocity.

### 3.5 Noncoplanar Descent and Landing Conditions

The descent timing determination procedure summarized in Figs. 3.18 through 3.20 is general in the sense that both coplanar and noncoplanar descent trajectories can be handled. Most mission analysis to date has been based on the assumption of coplanar LEM descent orbits. How closely the CSM orbit must pass over the desired landing site on the particular orbit when descent is initiated has not been determined in detail. It might be noted, that the primary G&N design goal is a 3000 foot CEP landing capability. If exact coplanar descent conditions are required, at least within primary G&N performance levels, the CSM must achieve this condition starting at the lunar sphere of influence in the translunar midcourse phase, further correct the orbital plane at lunar orbit injection, and probably adjust the lunar orbit plane during the orbit navigation phase. The major objective of CSM maneuvers at the sphere of influence and lunar orbit injection will be to achieve the desired lunar orbit relative to the preselected landing site in any case. CSM orbital maneuvers or plane changes prior to LEM descent can be minimized by performing slight noncoplanar LEM descent orbits or landing maneuvers within the  $\Delta V$  capabilities of the LEM descent stage. The primary G&N system in the LEM has the capability of noncoplanar descents which could be accomplished in one of two ways. The LEM descent orbit can be controlled such that it is determined by the injection position vector  $\underline{R}_{CM}$  shown in Fig. 3.18 and landing site vector  $\underline{i}_L$ . This operation results in a noncoplanar LEM descent orbit relative to the CSM, and a landing maneuver that nominally requires no major track or Z correction

(coplanar landing maneuver relative to the LEM descent orbit). In this type of noncoplanar descent orbit operation, the LEM velocity vector  $\underline{V}_p$  at the landing maneuver ignition point,  $\underline{R}_p$ , is coplanar with the plane determined by the vectors  $\underline{R}_p$  and  $\underline{i}_L$  of Fig. 3.18, and the landing maneuver is essentially a two dimensional problem. An alternate approach would restrict the LEM descent orbit to being coplanar with the CSM even though the landing site was not in this plane. The LEM velocity at  $\underline{R}_p$  is then not in the plane determined by  $\underline{R}_p$  and  $\underline{i}_L$ , and a noncoplanar powered landing maneuver is required. This type of operation will be referred to as a coplanar descent-noncoplanar landing. The guidance concept used in the powered landing maneuver (Section 4.2) can handle noncoplanar conditions.

Which of these two noncoplanar approaches would be used will depend upon the type of descent trajectory. A comparison of the two approaches is summarized in Table 3.1 for several noncoplanar landing conditions.

With reference to the  $\Delta V$  requirements summarized in Table 3.1, it can be seen that the coplanar descent-noncoplanar landing maneuver requires the least total descent stage  $\Delta V$  in Hohmann type descents. It should be noted that the landing site out of plane condition listed in this table represents the closest range or central angle between the desired landing site and CSM orbital plane. Noncoplanar descents for the Hohmann trajectories require larger turning angles at descent injection than the landing site out of plane angle (i. e.,  $2.3^\circ$  turning angle at Hohmann descent injection for the  $0.5^\circ$  landing site case). The noncoplanar equal period descents, on the other hand, only require turning angles at descent injection essentially equal to the landing site out of plane angle. For this reason, the noncoplanar descent-coplanar landing maneuver operation requires the least  $\Delta V$  for equal period descent and landing. As indicated in Table 3.1, the noncoplanar landing operation will depend upon the type of descent orbit chosen for the particular

TABLE 3.1

Comparison of  $\Delta V$  requirements for non-coplanar descent trajectories.

Maneuver Concept	Landing Site Out of Place Conditions	Hohmann Descent			Equal Period Descent		
		Descent Injection $\Delta V$ (fps)	Landing Maneuver $\Delta V$ (fps)	Total $\Delta V$ (fps)	Descent Injection $\Delta V$ (fps)	Landing Maneuver $\Delta V$ (fps)	Total $\Delta V$ (fps)
Coplanar Descent, Coplanar Landing	0 <sup>0</sup>	98	6032	6130	373	6111	6484
Non-coplanar Descent, Coplanar Landing	0, 5 <sup>0</sup>	210	6032	6242	376	6111	6487
Coplanar Descent, Non-coplanar Landing	0, 5 <sup>0</sup>	98	6017	6115	373	6131	6504
Non-coplanar Descent, Coplanar Landing	1, 0 <sup>0</sup>	436	6032	6468	384	6111	6495
Coplanar Descent, Non-coplanar Landing	1, 0 <sup>0</sup>	98	6094	6192	373	6106	6569
Non-coplanar Descent, Coplanar Landing	2, 0 <sup>0</sup>	352	6032	6384	415	6111	6526
Coplanar Descent, Non-coplanar Landing	2, 0 <sup>0</sup>	98	6354	6452	373	6507	6880

\*Landing maneuver extended 15 n m over standard 305 n m ground range

mission. For the Hohmann type descent currently considered, the coplanar descent-noncoplanar landing maneuver combination is preferred.

The noncoplanar landing conditions listed in Table 3.1 are useful for comparing descent G&N operations and represent extremes in noncoplanar launch condition restrictions (see Chapter 6). Out of plane launch limits will have to be considered in any noncoplanar descent maneuver along with the CSM orbital inclination, landing site latitude, descent timing and lunar stay time. For moderate out of plane descent conditions (0.5 degree or less) there is little  $\Delta V$  difference in which descent and landing concept is used for Hohmann type descents, but as mentioned above, the coplanar descent-noncoplanar landing maneuver combination is presently preferred.

The descent injection timing determination and guidance-steering concepts presented in this chapter are based on a vector operation which is capable of noncoplanar descents relative to the CSM orbit. A slight modification is required in the case of the  $\underline{W} \times \underline{V}$  steering concept (Section 3.2.2.2). The vector  $\underline{W}$  is normally defined as normal to the CSM orbital plane, as in Fig. 3.3. In the case of non-coplanar descents the  $\underline{W}$  vector should lie along a vector normal to the present velocity,  $\underline{v}$ , and the estimated cutoff velocity, a convenient approximation to which is  $\tilde{\underline{v}}_{CM}$  of Figs. 3.18 and 3.19.

As previously mentioned, the alternative to noncoplanar LEM descents is CSM orbital plane changes during the orbit navigation phase, if required. Current CSM translunar mid-course and lunar injection performance studies indicate maximum noncoplanar conditions of up to 3 nm may exist at LEM descent injection if perturbation effects are combined in the worst manner (Ref 3.3). These noncoplanar conditions are small enough for either of the descent maneuver concepts compared in Table 3.1 to be used.

### 3.6 Descent Phase G&N Operations

The CSM primary G&N system supplies the following inputs to LEM G&N system during the orbit navigation phase (Chapter 2):

1. CSM position and velocity vectors  $\underline{R}_{CM}$  and  $\underline{V}_{CM}$  at some reference time at which the CSM and LEM computer master clocks are synchronized.
2. The landing site position vector.  $\underline{R}_L$ .
3. Possibly an abort aim point, time of arrival polynomial described in Section 8.3.

Both CSM and LEM computers would then determine the injection timing requirement (Section 3.4), and the desired injection velocity (Section 3.2 or 3.3) and compare these results as a G&N check out procedure.

After manually controlled separation, the LEM IMU alignment is made as described in Section 1.3. Whether initial LEM IMU alignment is made prior to, or after separation has not been finally decided, but an IMU fine alignment will be made after separation within 15 minutes of descent injection time. The time of this final alignment check, prior to injection is important in primary G&N performance during the landing maneuver, and will be described in the following sections and in Chapter 4.

The separation and alignment operations are shown schematically in Figs. 3.1 and 3.11. It has been assumed in the primary G&N analysis that the LEM is separated from the CSM about 30 minutes before descent injection, and that final CSM orbital parameter updating is relayed to the LEM prior to injection over the intervehicle communication or data link. The LEM separation maneuver must be checked relative to the CSM in order to preserve the accuracy of the orbital updating continued by the CSM G&N system. It has been assumed

that the desired LEM separation point over this 30 minute interval is at essentially the CSM altitude and either ahead of or behind the CSM for equal period descents, or behind the CSM for Hohmann type descent orbit injections. The separation distance has been assumed large enough for both CSM and LEM rendezvous radar check out, and avoidance of LEM descent engine exhaust effects on the CSM during the injection maneuver. A 500 foot final separation distance has been assumed, since it is the initial range for docking maneuvers, but it is not known if this distance is sufficient for exhaust effects. The LEM separation maneuver can be checked by the rendezvous radars (range rate forced to zero at the desired range) and also with the LEM IMU if it were at least coarsely aligned prior to separation as previously mentioned. The important G&N condition to be met in the separation phase is that the lunar orbit determined by the CSM is also valid for the LEM prior to injection.

The primary G&N system controls the injection maneuver in a pure inertial mode of operation, as shown in Fig. 3.21. The LGC controls the descent engine ignition and throttle through the LEM SCS, and the commanded thrust direction through the IMU CDUs as shown. The IMU accelerometers outputs are fed directly to the LGC, which monitors the injection maneuver and determines the required thrust vector commands to achieve the desired injection conditions (Sections 3.2 and 3.3).

After the powered injection maneuver is completed, the LEM is oriented so that rendezvous radar tracking can be established with the CSM, as indicated in Fig. 3.11. Both vehicles determine or check the LEM descent trajectory perilune with the navigation technique described in Sections 2.2 and 7.2. Under normal G&N operation, the injection maneuver performance (Sections 3.7 and 3.8) is approximately equal to the accuracy limit of the free fall radar tracking mode described in Section 7.2. This insures descent injection check-out, but does not provide significant improvement or updating of the initial

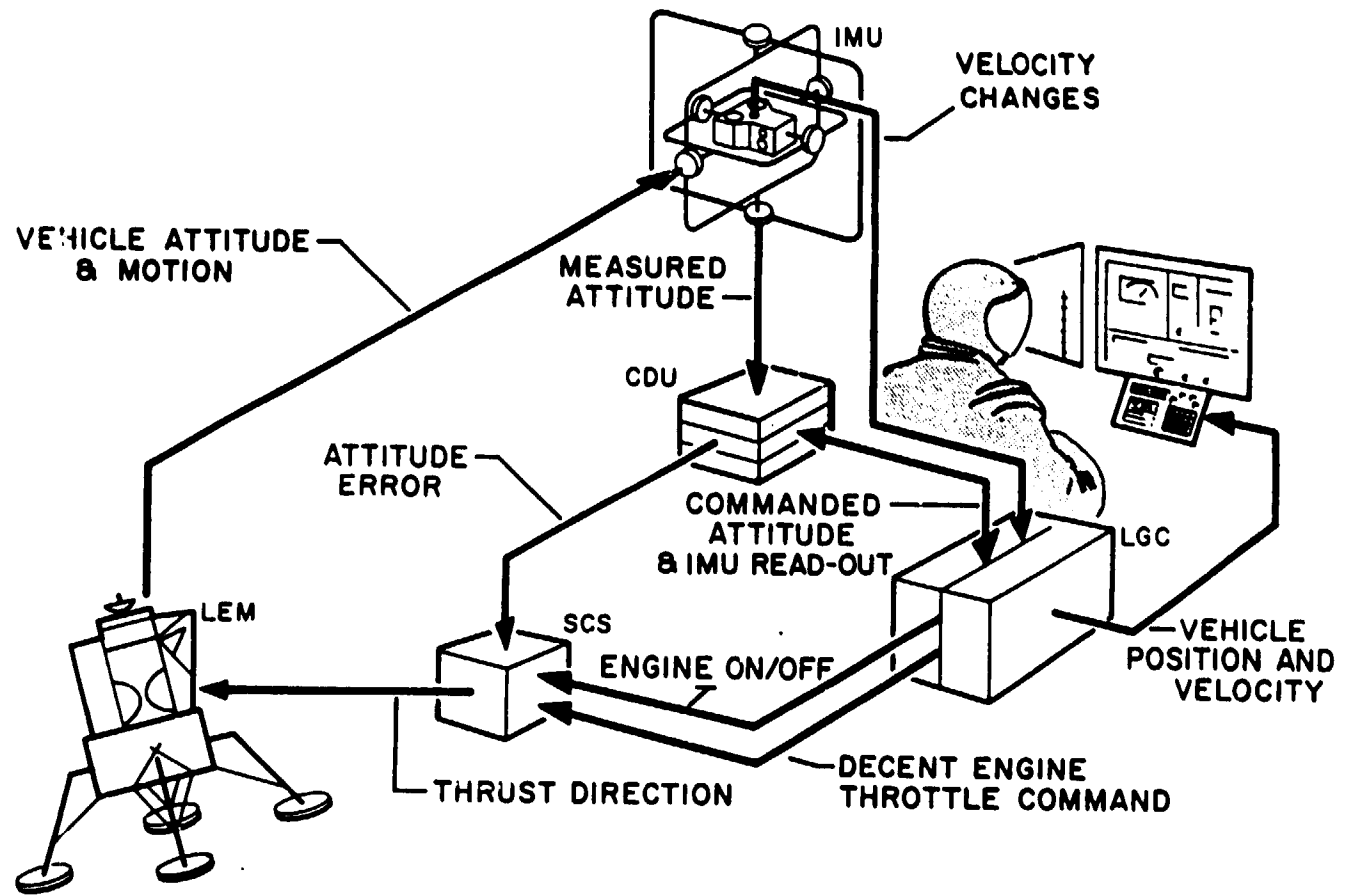


Fig. 3.21 Descent and initial landing phase (inertial control).

landing ignition point velocity and altitude conditions. Under normal G&N system operation in the descent and landing phases, no midcourse velocity corrections are required during the descent orbit. If the descent monitoring indicated such a correction were required, due to a poor injection maneuver, the mission will probably be aborted rather than commit the LEM to landing maneuver with a doubtful primary G&N system.

In Figs. 3.1 and 3.11, a landing radar check out is made against the lunar terrain prior to the landing maneuver. As indicated in these figures, the landing radar check is made at an altitude of 70,000 feet, which occurs about five minutes before perilune or landing maneuver ignition. A check out of this type is consistent with the philosophy of checking all LEM subsystems required for a successful landing maneuver, prior to initiation of such a landing. The original landing radar specification, References 3.4 and 3.5, required operating limits that would allow at least an altitude check-out at 70,000 feet. There may be other methods of checking the landing radar other than lunar terrain tracking, such as internal check-out circuits or CSM skin tracking in the separation phase prior to descent injection.

During equal period descent trajectories, the LEM IMU is not normally realigned after descent injection. During Hohmann descent trajectories, however, a LEM IMU fine alignment is made within 15 minutes of arrival at the perilune or landing ignition point. This alignment is required for the 3,000 foot CEP design objective, and is discussed in Section 4.4.1.

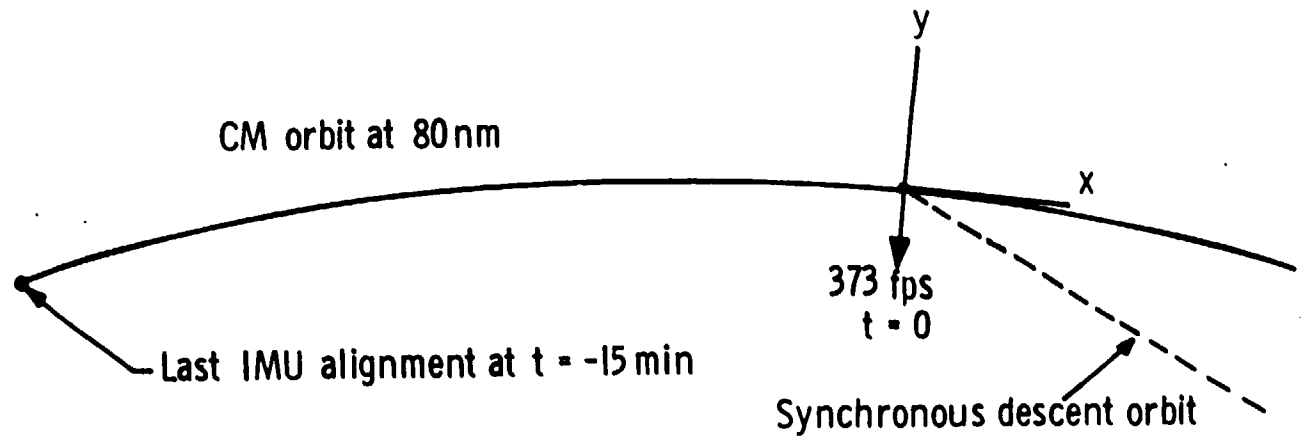
The final G&N operation during the descent phase is to orient the LEM in the proper attitude for thrust initiation of the landing maneuver. This is done by the landing maneuver guidance concept, which is described in Section 4.2.

### 3.7 G&N Performance for Equal Period Descents

The injection maneuver errors for the equal period

descent resulting from LEM primary G&N system instrument uncertainties are summarized in Fig. 3.22. The major factor contributing to these uncertainties is IMU misalignment at the start of the injection maneuver. As shown in Fig. 3.22, the LEM IMU alignment was assumed to be 0.5 mr, one sigma, 15 minutes before the 373 fps descent maneuver. This initial alignment accuracy combined with the following IMU drift during 15 minutes resulted in an rss misalignment of 0.82 mr at injection. This misalignment is the major cause of the X and Z uncertainties for this maneuver. The position uncertainties, X, Y, and Z, are negligible for this maneuver, and were arbitrarily set at 10 feet.

The injection uncertainties due to IMU errors of Fig. 3.22 were combined with the covariance matrix of orbit navigation Model 1 (Section 2.3, Table 2.2) to form a single correlation matrix. From this correlation matrix, two 3-dimensional error ellipsoids were generated: a one sigma position error ellipsoid, and a one sigma velocity error ellipsoid, as shown in Fig. 3.23. The one sigma position error ellipsoid has the property that it contains 68.3% of the position errors. It also has the property that all position errors that lie on its surface have an equal probability of occurrence. The one sigma velocity ellipsoid has the same characteristics, but contains only velocity errors. These 3-dimensional ellipsoids can be considered projections of a 6-dimensional position-velocity ellipsoid having a surface of constant probability density. The probability of a position and velocity error combination lying within this 6-dimensional ellipsoid, or within both ellipsoids of Fig. 3.23 is 26%. The  $\sigma$  values listed at the top of Fig. 3.23 are the square roots of the diagonal terms of the combined correlation matrix, and represent the conventional one sigma values of these components if considered separately. All uncertainty or error conditions presented in this report are in the form of Fig. 3.23. A more complete description of error el-



### 1. IMU ALIGNMENT UNCERTAINTY AT INJECTION

- a. Drift since last alignment (15 min) = .65 mr
- b. IMU alignment accuracy = .5 mr

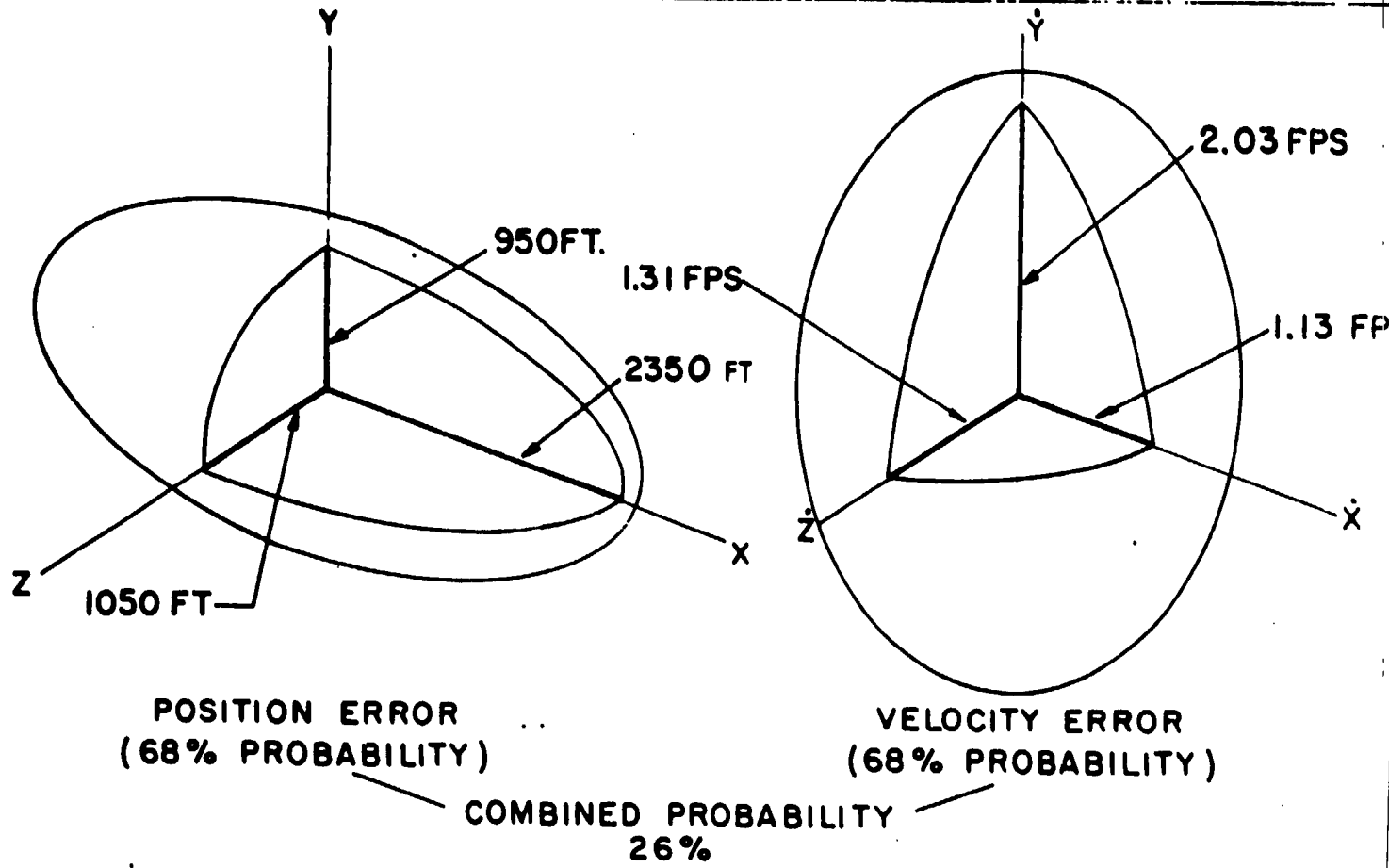
RSS = .82 mr

### 2. INJECTION UNCERTAINTIES DUE TO IMU ERRORS

x	y	z	$\dot{x}$	$\dot{y}$	$\dot{z}$
10 ft	10 ft	10 ft	.45 fps	.25 fps	.45 fps

Fig. 3.22 Equal period descent orbit injection errors.

$\sigma_x = 1250 \text{ ft}$	$\sigma_y = 535 \text{ ft}$	$\sigma_z = 585 \text{ ft}$	$\sigma_{\dot{x}} = 0.626 \text{ fps}$	$\sigma_{\dot{y}} = 1.09 \text{ fps}$	$\sigma_{\dot{z}} = 0.7 \text{ fps}$
------------------------------	-----------------------------	-----------------------------	--	---------------------------------------	--------------------------------------



141

ORIGINAL PAGE IS  
OF POOR QUALITY

Fig. 3.23 Model 1, error volume at descent orbit injection.

142

$\sigma_x = 2375$ ft	$\sigma_y = 775$ ft	$\sigma_z = 675$ ft	$\sigma_{\dot{x}} = 0.72$ fps	$\sigma_{\dot{y}} = 1.73$ fps	$\sigma_{\dot{z}} = 0.71$ fps
----------------------	---------------------	---------------------	-------------------------------	-------------------------------	-------------------------------

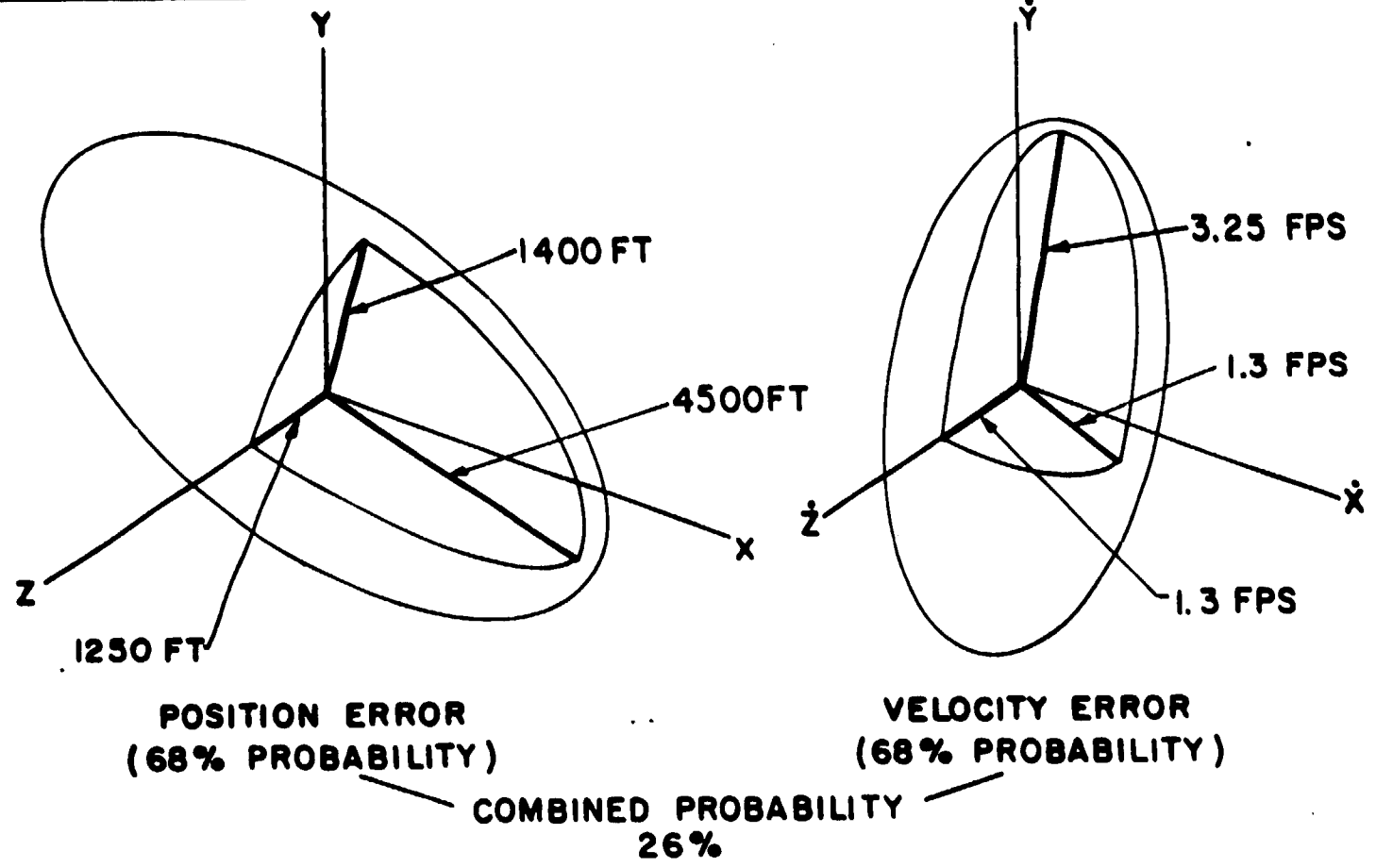


Fig. 3.24 Model 2, error volume at descent orbit injection.

lipsoids is given in Appendix A.

When the injection maneuver uncertainties of Fig. 3.22 were combined with the covariance matrix from orbit navigation Model 2 (Section 2.3, Table 2.2), the resulting uncertainties or error volumes at descent orbit injection are shown in Fig. 3.24. These error volumes are larger than those of Fig. 3.23, due to larger uncertainties of orbit navigation Model 2. The rotation or alignment of the error volumes in Fig. 3.24 about the Z and  $\dot{Z}$  axes indicates a correlation between the X and Y and the  $\dot{X}$  and  $\dot{Y}$  components. This correlation is defined in the combined correlation matrix off diagonal terms which, in turn, cause the rotation of error ellipsoids.

The combined correlation matrices at descent orbit injection were propagated to the perilune of the equal period orbit where new error volumes were generated and plotted in the local vertical coordinate system. The Model 1 error volumes of Fig. 3.23 resulted in those shown in Fig. 3.25, and the Model 2 error volumes of Fig. 3.24 resulted in perilune conditions represented by Fig. 3.26. The error conditions of Figs. 3.25 and 3.26 represent typical uncertainties in the initial conditions for powered landing maneuver from equal period descent trajectories.

### 3.8 G&N Performance for Hohmann Descents

The Hohmann injection maneuver uncertainties are listed in Fig. 3.27 for IMU alignment and performance errors. The IMU alignment schedule and accuracies are the same as those listed in Fig. 3.22. When these injection maneuver uncertainties are combined with orbit navigation uncertainties, the resultant error volumes are slightly smaller, but very similar to those shown in Figs. 3.23 and 3.24.

In the case of Hohmann descents, orbit navigation Model 2 is more realistic since the descent injection point must be on

$\sigma_x = 1600 \text{ ft}$	$\sigma_y = 1150 \text{ ft}$	$\sigma_z = 760 \text{ ft}$	$\sigma_{\dot{x}} = 0.734 \text{ fps}$	$\sigma_{\dot{y}} = 1.875 \text{ fps}$	$\sigma_{\dot{z}} = 0.54 \text{ fps}$
------------------------------	------------------------------	-----------------------------	--	--	---------------------------------------

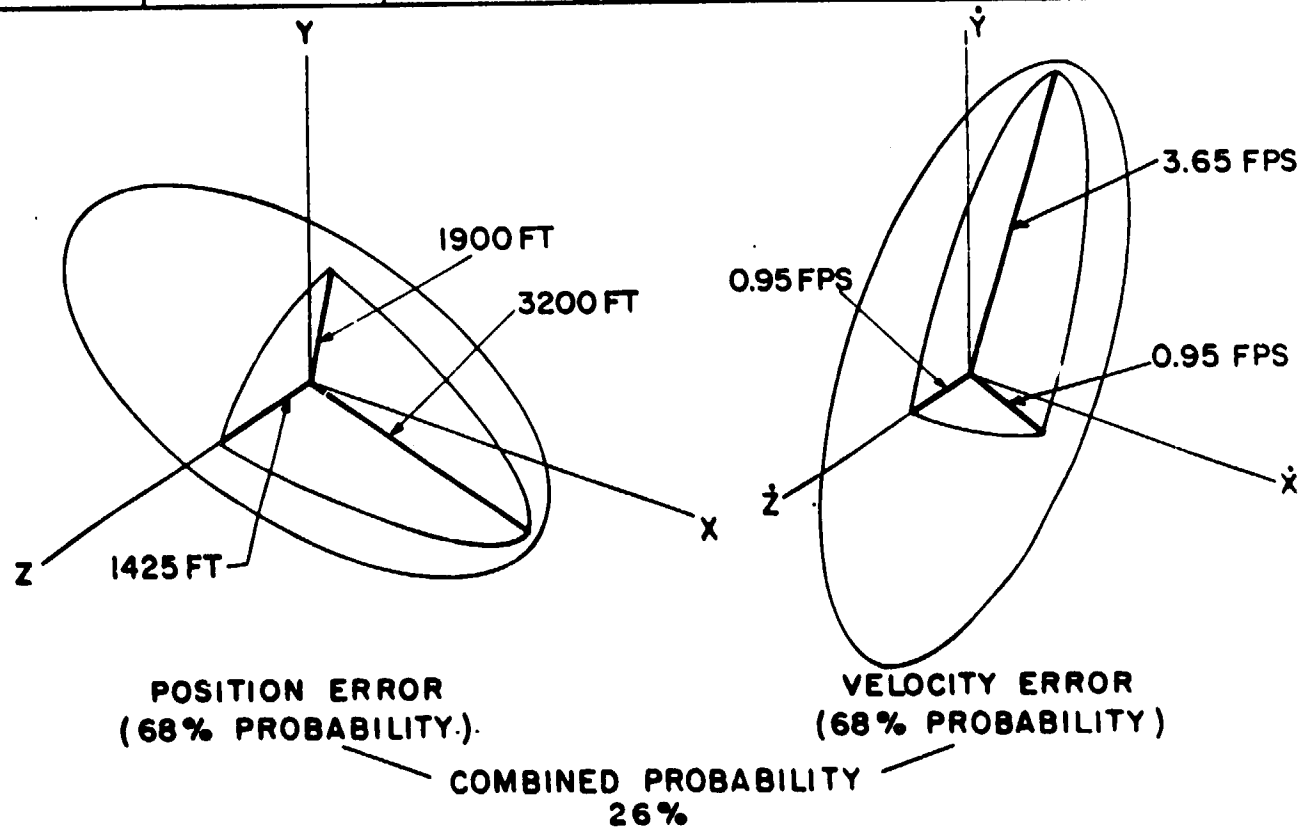
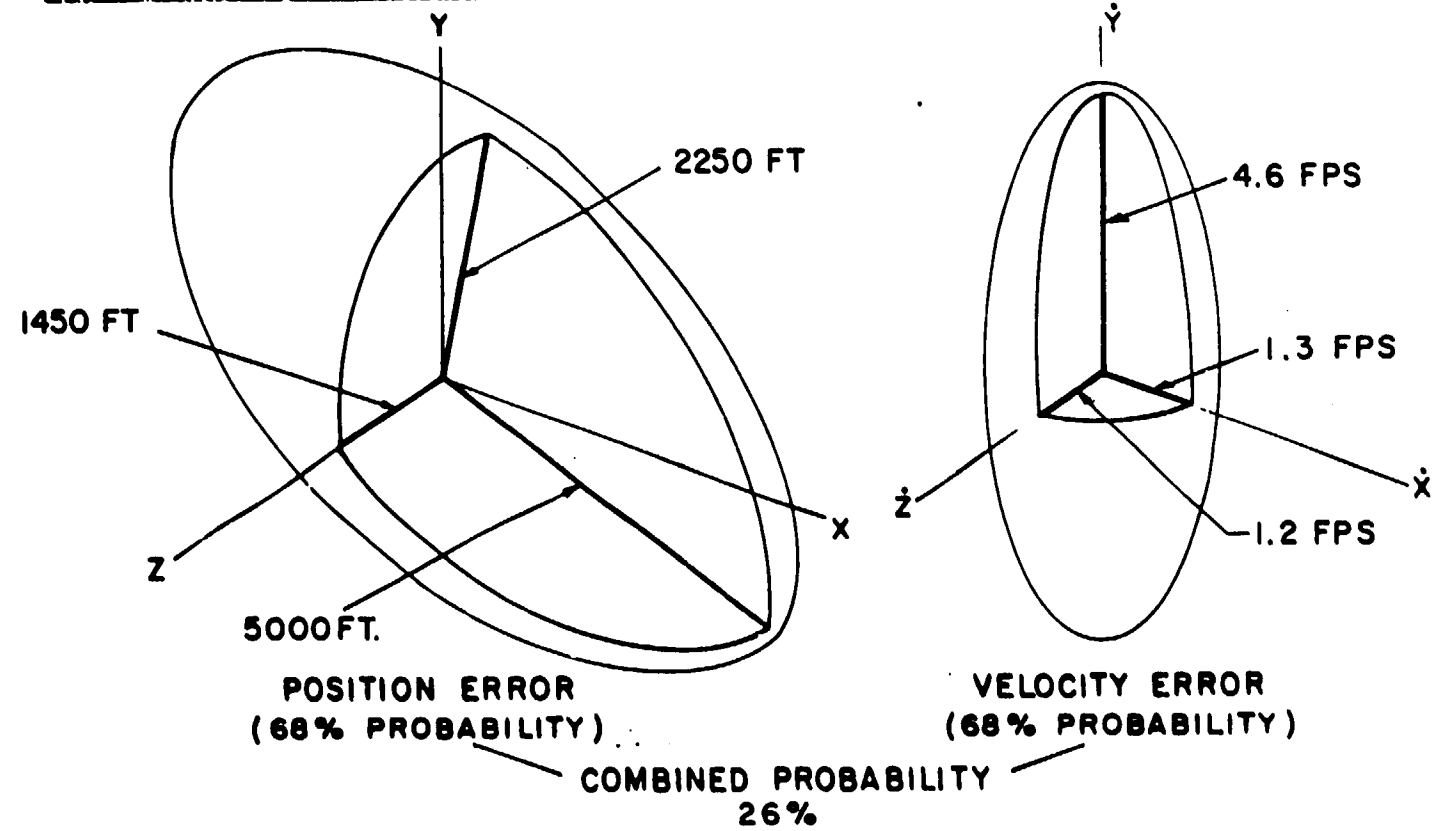


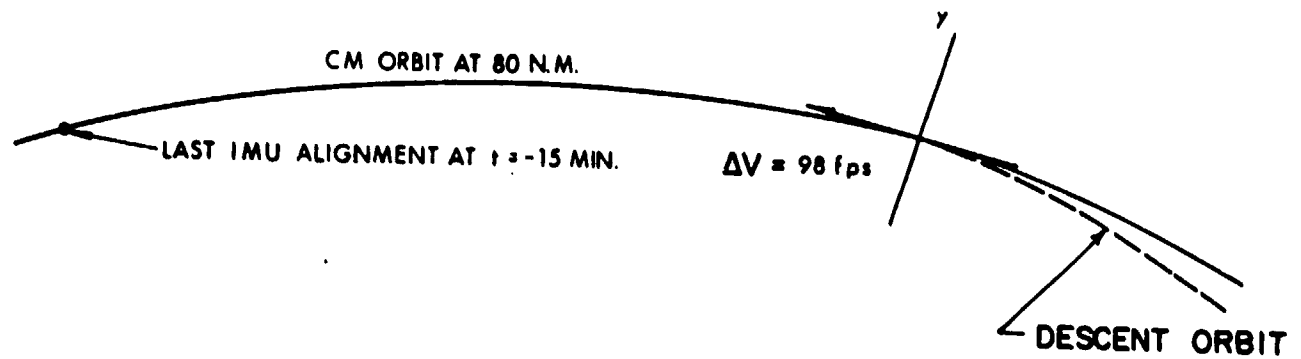
Fig. 3.25 Equal period trajectory error volume at perigee (orbit navigation model 1).

$\sigma_x = 2660 \text{ ft}$	$\sigma_y = 1220 \text{ ft}$	$\sigma_z = 775 \text{ ft}$	$\sigma_{\dot{x}} = 0.77 \text{ fps}$	$\sigma_{\dot{y}} = 2.46 \text{ fps}$	$\sigma_{\dot{z}} = 0.63 \text{ fps}$
------------------------------	------------------------------	-----------------------------	---------------------------------------	---------------------------------------	---------------------------------------



145

Fig. 3.26 Equal period trajectory error volume at perilune (orbit navigation model 2).



### 1. IMU ALIGNMENT UNCERTAINTY AT INJECTION

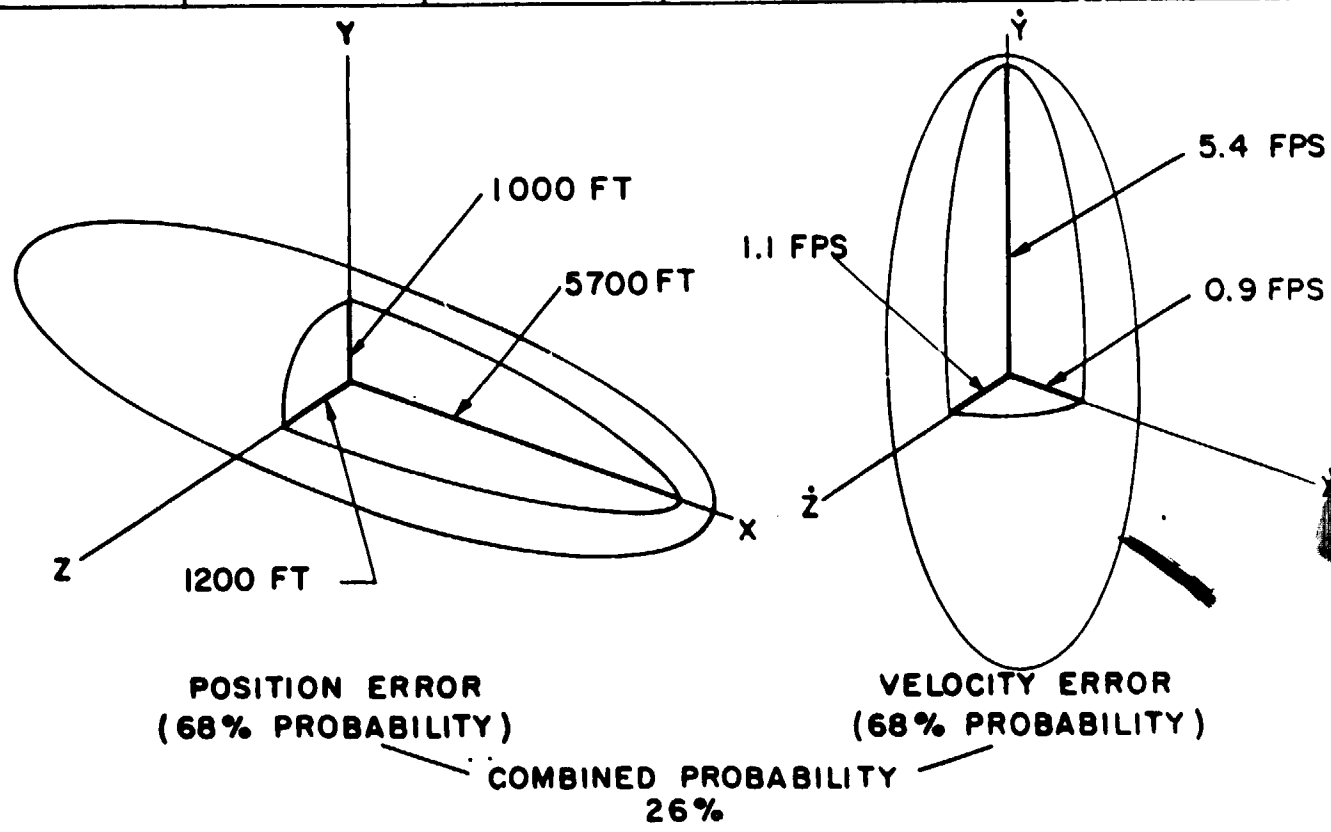
- a. DRIFT SINCE LAST ALIGNMENT = 0.65 mr
  - b. IMU ALIGNMENT ACCURACY = 0.5 mr
- R. S. S. = 0.82 mr

### 2. INJECTION UNCERTAINTIES DUE TO IMU INSTRUMENT ERRORS

x	y	z	$\dot{x}$	$\dot{y}$	$\dot{z}$
10 ft	10 ft	10 ft	0.07 fps	0.12 fps	0.12 fps

Fig. 3.27 Hohmann descent injection errors.

$\sigma_x = 3025$ ft	$\sigma_y = 550$ ft	$\sigma_z = 625$ ft	$\sigma_{\dot{x}} = 0.5$ fps	$\sigma_{\dot{y}} = 2.9$ fps	$\sigma_{\dot{z}} = 0.6$ fps
----------------------	---------------------	---------------------	------------------------------	------------------------------	------------------------------



147

Fig. 3.28 Hohmann descent error volume at perilune (orbit navigation model 2).

[REDACTED]

the far side of the moon relative to the earth where mapped landmarks are not counted on. When the injection maneuver uncertainties of Fig. 3.27 were combined with orbit navigation Model 2 uncertainties (Table 2.2) and propagated 180 degrees to perilune, the resulting error volumes are shown in Fig. 3.28. By comparing this figure with Fig. 3.26, it can be seen that the major difference between perilune uncertainties of equal period and Hohmann descents are in the X (range) and altitude (Y) position components.

## CHAPTER 4

### POWERED LANDING MANEUVER

#### 4.1 General Description

The powered part of the landing maneuver starts at the LEM engine ignition point of the descent orbit and terminates at lunar surface touchdown. The LEM powered landing maneuver has been divided into the three major phases illustrated in Fig. 4.1. The first phase is inertially guided and is the longest with respect to time and ground range. The primary G&N system objective of the first phase, is to achieve a position and velocity condition for the start of the second phase which will allow a near constant vehicle attitude and landing site visibility as the LEM approaches the surface. The scale of Fig. 4.1 is exaggerated in that the landing site is below the lunar horizon relative to the engine ignition point and does not come within view until the LEM is about 125 nm away. For the optimum  $\Delta V$  type landing trajectory, the landing site is not visible with the current LEM window configuration until hover conditions have been achieved. For this reason the landing trajectory is shaped such that a vehicle attitude that permits landing site surveillance is achieved during some phase of the maneuver. The desired vehicle attitude during the second phase is such that the astronauts can visibly check the landing area through the LEM windows. The second phase is guided at approximately half-maximum throttle setting in order to lengthen the maneuver time to about two minutes for visual and landing radar updating of the inertial guidance units. The terminal objective of the second phase is to achieve hover or zero velocity conditions over the desired landing site at some pre-designated altitude. The third phase is the let-down and surface landing from the hover condition.

4.2.1 General Comments

The lunar landing steering equations are a direct, exact solution to the equations of motion. They express the solution thrust vector as an explicit function of the current position and velocity vectors and the desired position and velocity vectors. Figure 4.2 is a simple block representation of the equations. In mathematical parlance, the lunar landing equations are a solution to a two-point boundary-value problem. The first point is the current state (point in state space); the second point is the desired state. Because the equations express the components of the solution thrust acceleration vector as explicit algebraic functions of literal symbols for the current and desired states, any meaningful and physically reasonable numerical values may be substituted for the literal symbols. This flexibility of the landing equations is quite significant because at least two, and probably more than two, different boundary-value problems will be posed to the guidance system during the landing maneuver.

If the first two phases of the landing maneuver (from engine ignition to the hover point) were accomplished in one powered maneuver, the attitude orientation of the vehicle would be such that the astronaut would never see the landing site. The look angle, i. e. the angle between the line-of-sight to the landing site and the vehicle's negative thrust axis, must be greater than  $25^{\circ}$ . Typical vehicle attitudes and phase 2 initial conditions are illustrated in Fig. 4.3. The initial conditions for phase 2, which are also the terminal conditions for phase 1, are chosen so that the phase 2 sink rate (downward vertical rate) is comfortable and the phase 2 look angle is suitable. Figures 4.4 and 4.5 show that at the terminus of phase 1 (the start of phase 2), the vehicle is rotated through approximately  $30^{\circ}$  and the thrust magnitude is reduced.

The thrust vector rotation tips the vehicle to an

ORIGINAL PAGE IS  
OF POOR QUALITY

151

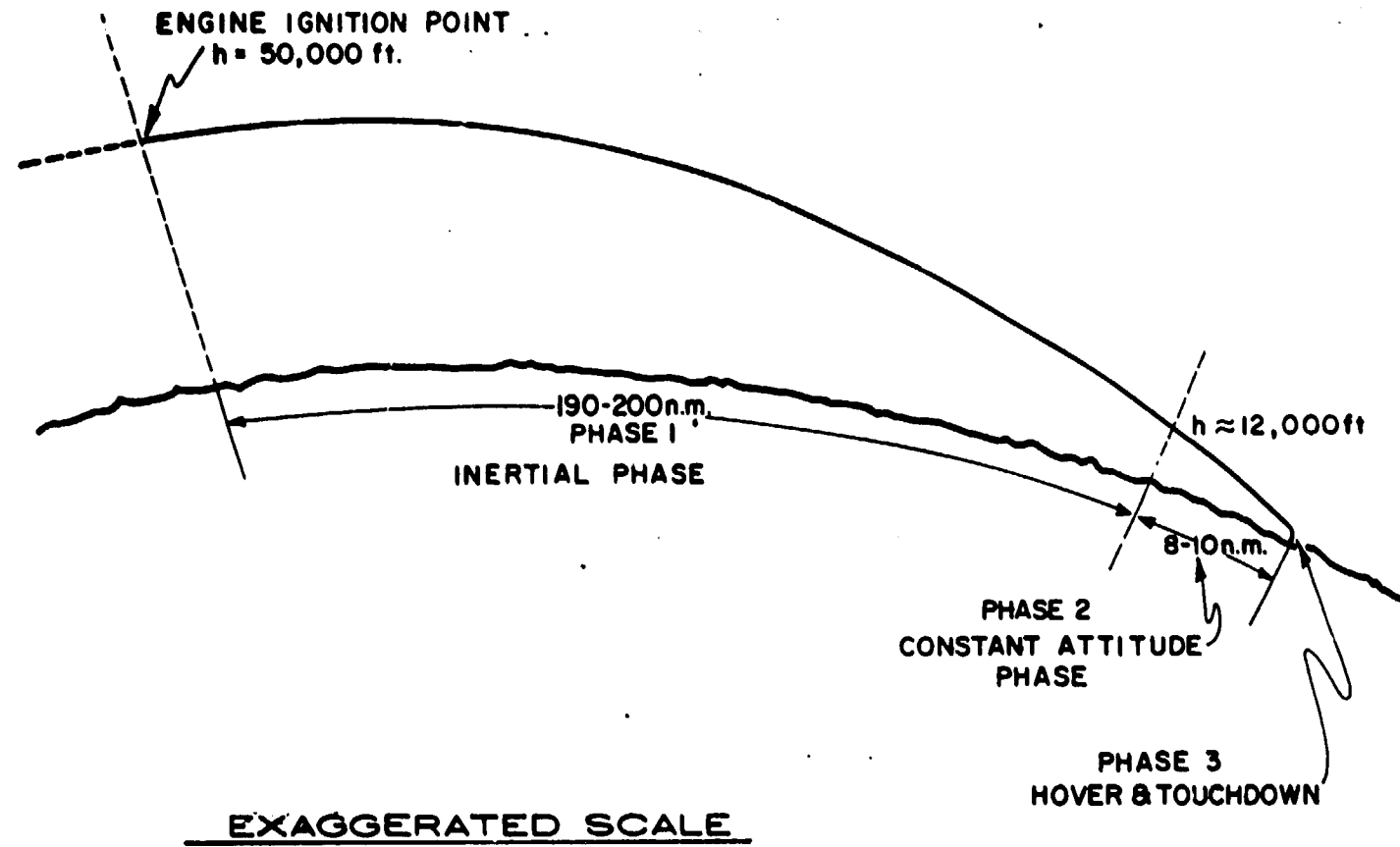


Fig. 4.1 Lunar landing maneuver p

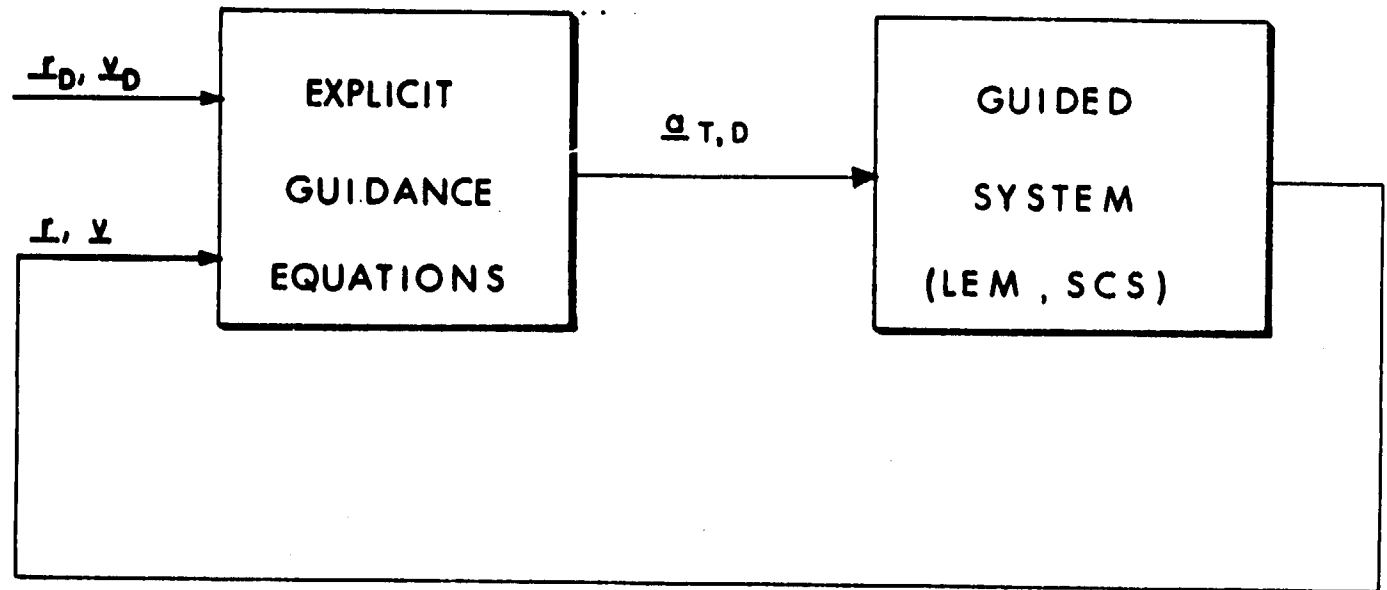


Fig. 4.2 Explicit steering equations.

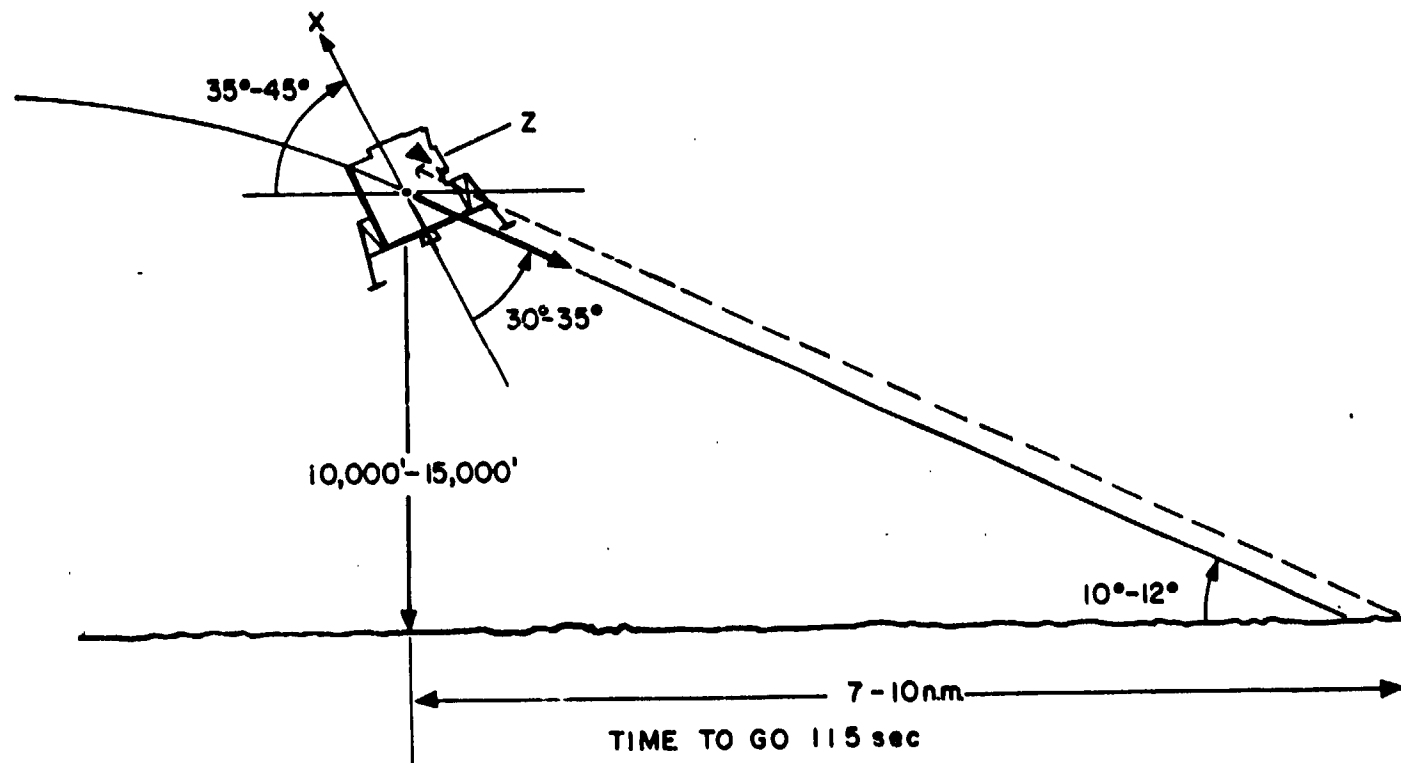


Fig. 4.3 Lunar landing maneuver - phase 2.

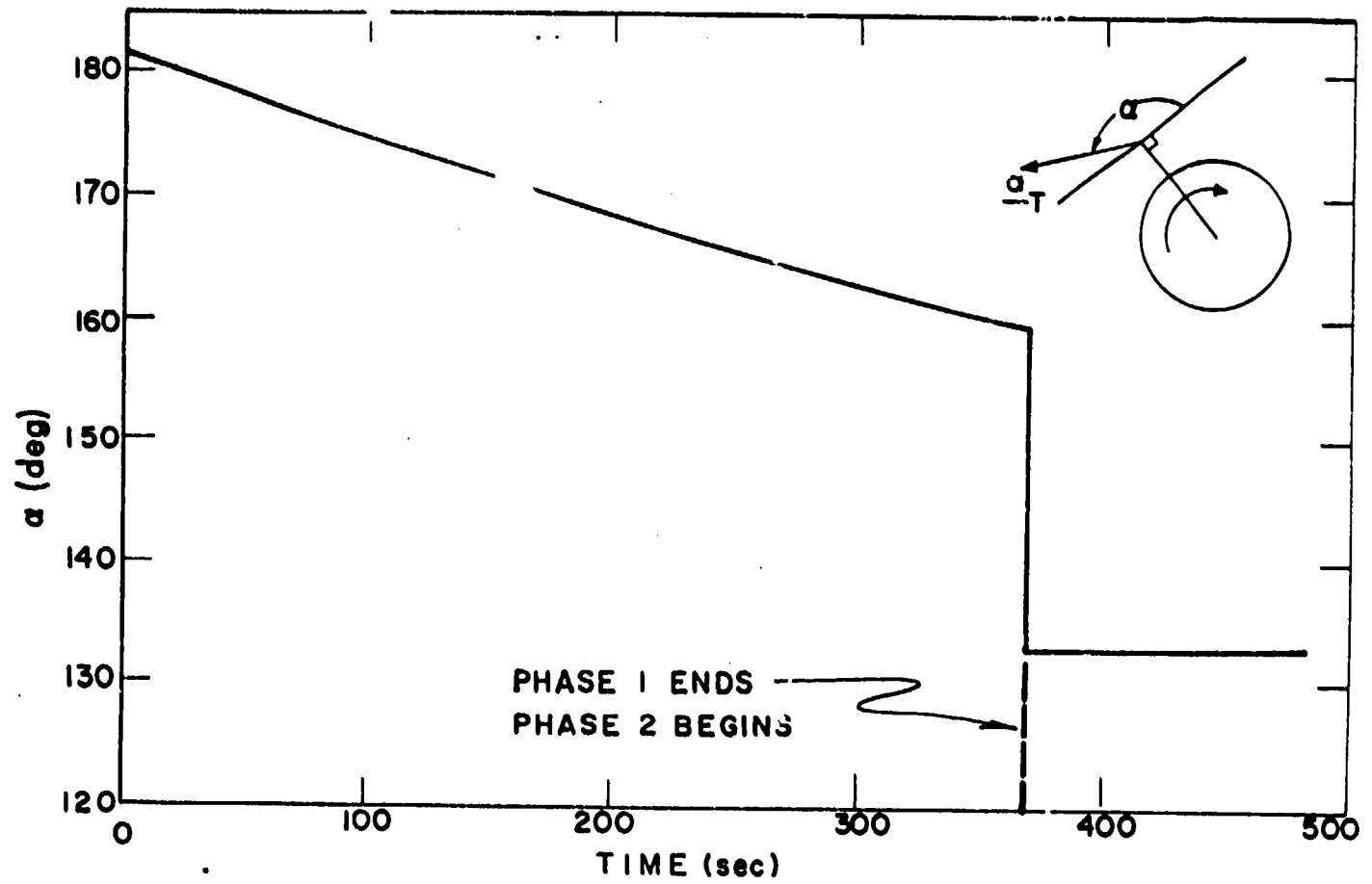


Fig. 4.4 Thrust angle vs. time. (Landing from Hohmann descent).

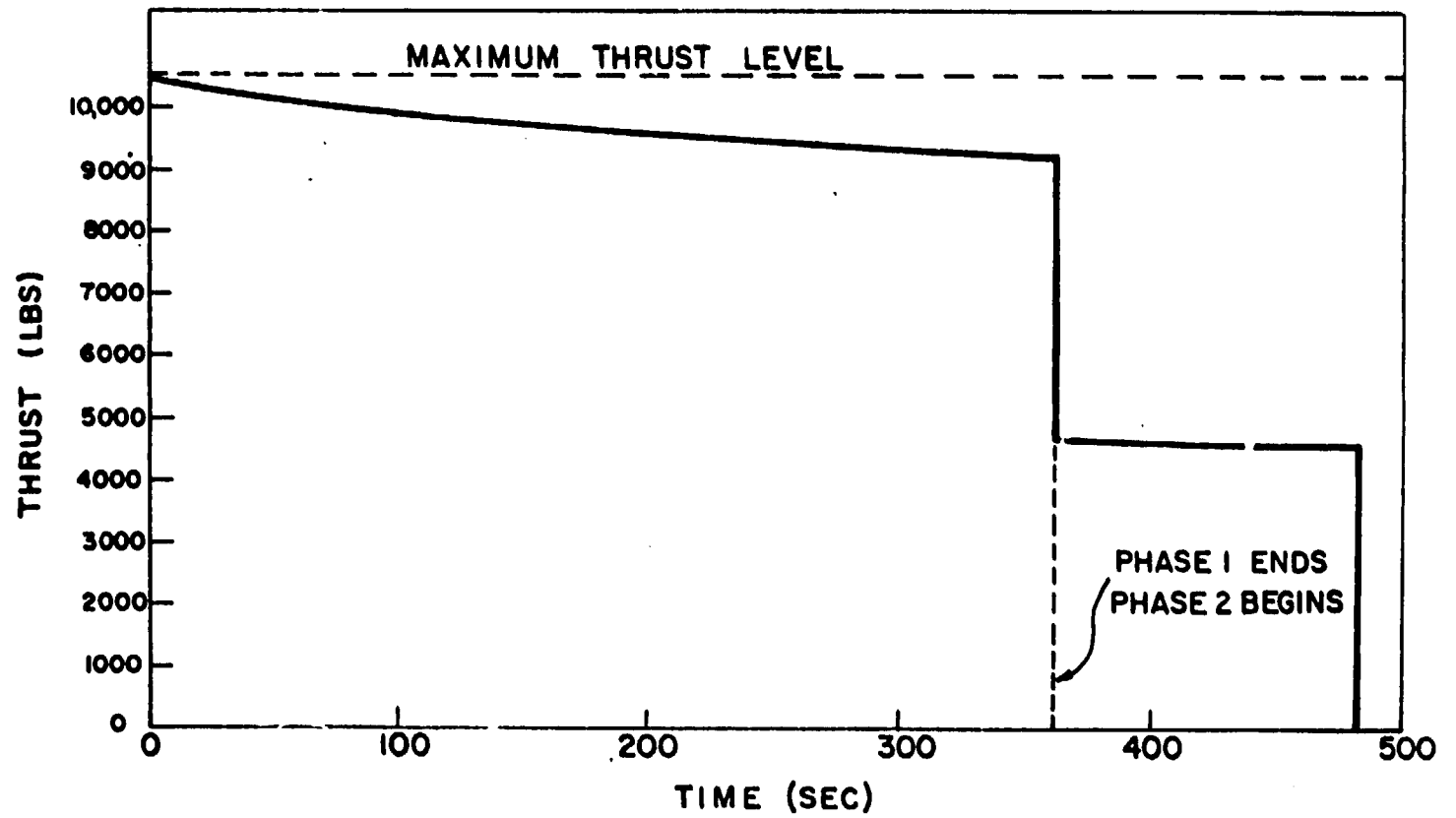


Fig. 4.5 Thrust magnitude vs. time. (Landing for Hohmann decent).

orientation which allows the astronaut to view the proposed landing site.

Several constraints are imposed on phase 2 of the landing maneuver. First of all, both final position and velocity vectors are specified for the terminus of phase 2. It should be emphasized that all components of the terminal position and velocity vectors must be controlled. Next, the spacecraft orientation must be such that the proposed landing site is in the viewing sector of the spacecraft window. The sink rate of the spacecraft must be moderate enough to allow for ascent engine ignitions and descent-stage separation without a lunar contact in case of abort; i. e., the altitude and altitude rate profile must permit aborting the landing maneuver with the ascent engine. Finally, it would be desirable to standardize the duration of phase 2 and the evolution of the state vector during the visibility phase. This would make the astronaut's monitoring problem somewhat easier and decrease the variation of the conditions which he should regard as satisfactory.

Phase 2 is seen to be heavily constrained. The steering equations can be regarded as a "black box". The "input" to the box are the present position and velocity vectors and the desired position and velocity vectors. The "output" from the black box are the required thrust vector orientation and the required thrust acceleration magnitude. The output from the box cannot be constrained, except indirectly, if the desired final position and velocity vectors are to be obtained. Yet it is required that the thrust angle be such that the look angle be suitable. Furthermore, the equations explicitly control only the final position and velocity vectors - the vehicle is not constrained by the equations to a particular trajectory. To obtain all the characteristics required of phase 2, the following procedure is used. The spacecraft is mathematically "flown backwards" from the hover conditions for the number of seconds desired in phase 2. As the vehicle progresses backwards from the hover point the thrust angle is set

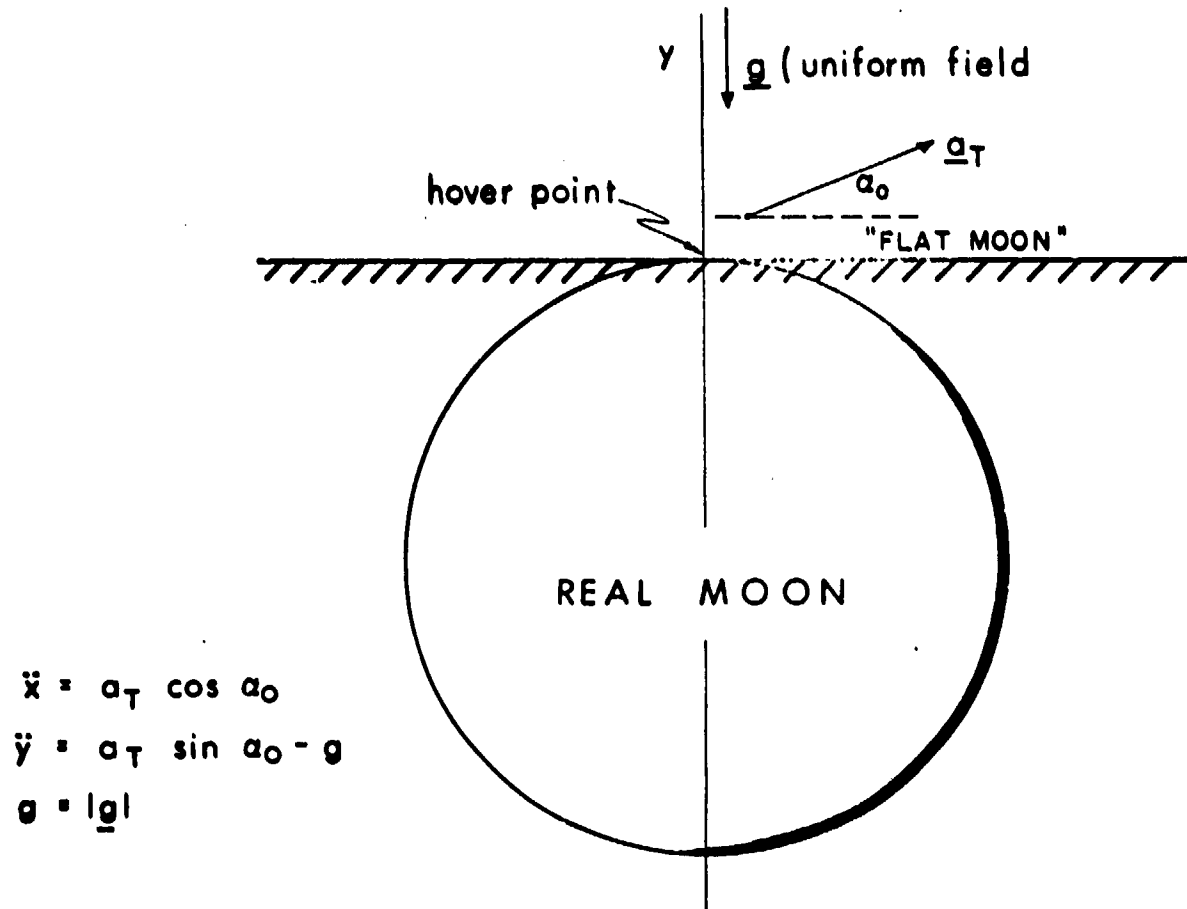
such that the view of the landing site is acceptable. A suitably low altitude rate is also maintained. At the end of this hypothetical backwards flight, the vehicle's position and velocity are observed. This observed position and velocity are specified to be the terminal state for phase 1. Thus the terminal conditions for phase 1 are just those appropriate initial conditions for phase 2 which would produce the desired phase 2 characteristics. It is to be emphasized that during the landing maneuver the thrust vector is not directly constrained to obtain an adequate look angle. The thrust vector is computed as a solution to the two-point boundary-value problem. The phase 2 two-point boundary-value problem is arranged, by the choice of the initial phase 2 boundary point, so that it requires as a solution a suitable thrust angle regime.

To further illustrate the procedure of choosing the terminal conditions for phase 1, a very simple method of finding appropriate initial conditions for phase 2 follows. This method involves a simple solution to a set of simultaneous linear equations. Consider Fig. 4.6 in which a coordinate system and equations of motion satisfactory for phase 2 are given. These equations represent the moon as "flat", a representation which is quite satisfactory for phase 2 since the angular travel of the spacecraft is normally less than  $1^\circ$  during the visibility phase. If the coordinate system in Fig. 4.6 is chosen so that the y-axis passes through the intended hover point, the differential equations of motion are

$$\ddot{x} = a_T \cos \alpha_0 \quad (4.1)$$

$$\ddot{y} = a_T \sin \alpha_0 - g \quad (4.2)$$

Note that  $y$  and  $\dot{y}$  are equivalent to altitude and altitude rate, and  $x$  is equivalent to range-to-go to hover. Equation (4.1) can be integrated between the initiation of phase 2 and the finish of phase 2.



$$\begin{aligned}\ddot{x} &= a_T \cos \alpha_0 \\ \ddot{y} &= a_T \sin \alpha_0 - g \\ g &= |\underline{g}|\end{aligned}$$

Fig. 4.6 Coordinate system and equations for determining phase 1 initial conditions.

$$\dot{x}_f - \dot{x}_i = \cos \alpha_o \int_i^f a_T \quad (4.3)$$

$$x_f - x_i - \dot{x}_i T_{pf} = \cos \alpha_o \int_i^f \int a_T \quad (4.4)$$

where  $T_{pf}$  = time of powered flight for this phase. Similarly, Eq. (4.2) is integrated to give:

$$\dot{y}_f - \dot{y}_i = -g T_{pf} + \sin \alpha_o \int_i^f a_T \quad (4.5)$$

$$y_f - y_i - \dot{y}_i T_{pf} = -g T_{pf}^2 / 2 + \sin \alpha_o \int_i^f \int a_T \quad (4.6)$$

In Eqs (4.3)-(4.6),  $a_T$  can be a constant or a varying thrust acceleration due to a constant thrust engine. Equations (4.3)-(4.6) express a relationship among initial and final vector conditions of phase 2; the duration of phase 2,  $T_{pf}$ ; the assumed constant thrust angle during phase 2,  $\alpha_o$ ; and the thrust acceleration during phase 2,  $a_T$ . Since the hover position and velocity vectors are specified, all the f-subscripted variables are fixed. The thrust angle,  $\alpha_o$ , is chosen to yield a suitable look angle. The phase 2 duration,  $T_{pf}$ , is chosen to allow the astronaut sufficient time to view the proposed landing site. The sink rate at the initiation of phase 2,  $\dot{y}_i$ , must be limited to a moderate value, for the reasons mentioned previously. Since each of the quantities  $\dot{y}_i$ ,  $\dot{y}_f$ ,  $T_{pf}$ , and  $\alpha_o$ , must be chosen to satisfy some operational constraint, the only free variable left in Eq (4.5) is  $a_T$ . Consequently, the value of  $a_T$  is fixed by Eq. (4.5), and this equation is separately satisfied. The remaining equations, Eqs (4.3), (4.4), and (4.6), have only three unknowns, namely,  $x_i$ ,  $y_i$ , and  $\dot{x}_i$ .

The solution for the unknowns is given by the following matrix-vector equation

$$\begin{bmatrix} x_i \\ y_i \\ \dot{x}_i \end{bmatrix} = \begin{bmatrix} 1 & 0 & -T_{pf} \\ 0 & 1 & 0 \\ 0 & 0 & 1 \end{bmatrix} \begin{bmatrix} x_f - \cos \alpha_o \int \int a_T \\ y_f - \dot{y}_i T_{pf} + g T_{pf}^2 / 2 - \sin \alpha_o \int \int a_T \\ \dot{x}_f - \cos \alpha_o \int a_T \end{bmatrix} \quad (4.7)$$

The quantities on the right-hand side of Eq (4.7) are chosen to yield the desired phase 2 trajectory characteristics. The quantities on the left-hand side of Eq (4.7) are the missing phase 2 initial boundary conditions.

The thrust angle required for a suitable look angle can be determined by picturing the spacecraft at the hover point. Figure (4.7) shows the hover point geometry and the equation for the thrust angle,  $\alpha_o$ , in terms of the altitude at hover, the linear distance between the hover sub-point and the landing point, and the required look angle. The shorter the distance  $l$  between the hover sub-point and the landing point, the steeper  $\alpha_o$  must be for an adequate look angle. But, the steeper the thrust angle during phase 2, the greater the  $\Delta V$  requirement for the descent-to-hover maneuver. On the other hand, a greater distance  $l$  requires a longer let-down maneuver after the hover point is reached. A long let-down maneuver from hover uses a large  $\Delta V$  as described in Section 4.6. Thus there is some optimum distance,  $l$ , which is neither very short nor very long. For the examples illustrated in this Section,  $l$  was arbitrarily chosen to be 1000 feet. Many operational considerations, besides  $\Delta V$  optimization, must enter into the final determination of  $l$ . It might be noted that it is advan-

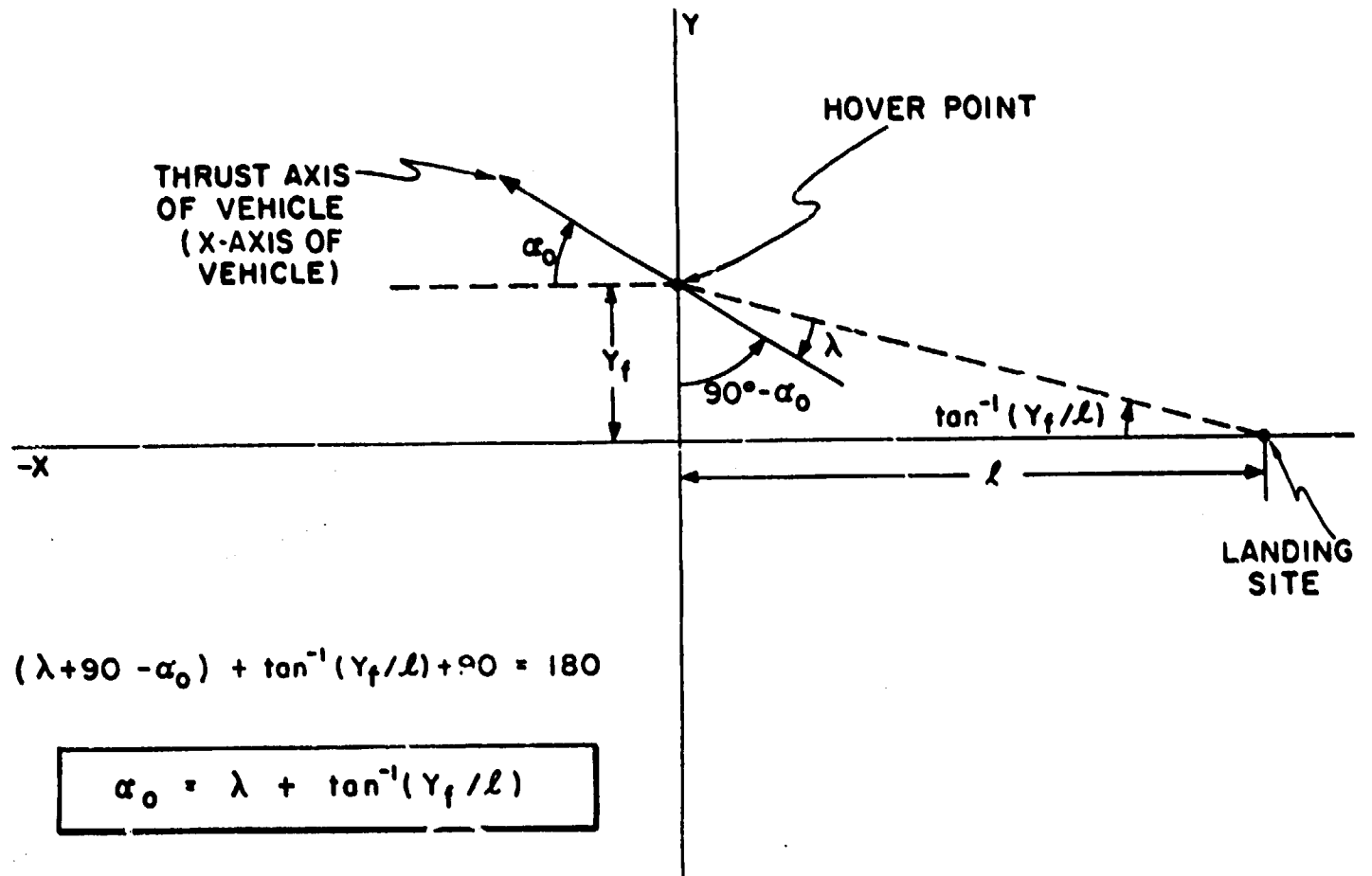


Fig. 4.7 Hover point position viewing geometry.

tageous with respect to  $\Delta V$  requirements to make the hover altitude  $y_f$  as low as possible. The smaller  $y_f$ , the smaller  $\alpha_0$  can be for a given  $l$  and required look angle.

The determination of the phase 2 terminal conditions, either by the method described above or any other method which produces the appropriate initial boundary conditions for phase 1, is done before the landing maneuver is started. In fact, these conditions should be determined and stored prior to Saturn launch. The objective of discussing these intermediate boundary conditions was to show how the desired characteristics of the final part of the descent-to-hover maneuver can be obtained by a two-phase descent with steering equations which solve a two-point boundary-value problem.

#### 4.2.2 Derivation of Landing Maneuver Guidance Equations

The differential equations of a rocket-propelled vehicle subject to gravitational acceleration are:

$$\ddot{x} = g_x + a_{T_x} \quad (4.8)$$

$$\ddot{y} = g_y + a_{T_y} \quad (4.9)$$

$$\ddot{z} = g_z + a_{T_z} \quad (4.10)$$

The gravity vector (row array) is

$$\underline{g} = (g_x \ g_y \ g_z) \quad (4.11)$$

If the gravitational field is spherical, the gravity vector is

$$\underline{g} = \mu \underline{r}/r^3 \quad (4.12)$$

but the steering equations developed in this section can be used with any gravitational field model.

The problem that the steering equations must solve is the following: Given the current position and velocity of the spacecraft:

$$\underline{r}(t_0) = x(t_0)\underline{i} + y(t_0)\underline{j} + z(t_0)\underline{k} \quad (4.13)$$

$$\underline{v}(t_0) = \dot{x}(t_0)\underline{i} + \dot{y}(t_0)\underline{j} + \dot{z}(t_0)\underline{k} ; \quad (4.14)$$

and the desired values of the components of the terminal position and velocity vectors

$$\underline{r}(T) = x_D\underline{i} + y_D\underline{j} + z_D\underline{k} \quad (4.15)$$

$$\underline{v}(T) = \dot{x}_D\underline{i} + \dot{y}_D\underline{j} + \dot{z}_D\underline{k} \quad , \quad (4.16)$$

find a thrust acceleration regime

$$\underline{a}_T(t) = a_{T_x}(t)\underline{i} + a_{T_y}(t)\underline{j} + a_{T_z}(t)\underline{k} \quad (4.17)$$

which satisfies the given boundary conditions and the appropriate differential equations of motion. Note that  $t = t_0$  at the current time and  $t = T$  at the terminal time.

The solution of a single axis boundary-value problem, e.g. the x-axis, is first illustrated. The solution is then expanded for the required 3-dimensional problem.

Without regard for the two component parts of  $\ddot{\underline{x}}(t)$ , the gravitational acceleration and the thrust acceleration, the following requirements concerning  $\ddot{\underline{x}}(t)$  can be noted. The first and second integrals of  $\ddot{\underline{x}}(t)$  must satisfy certain equations of constraint in order for the x-coordinate boundary conditions to be satisfied. Since it is required that:

$$x(T) = x_D \quad (4.18)$$

$$\dot{x}(T) = \dot{x}_D \quad , \quad (4.19)$$

$\ddot{x}(t)$  must satisfy:

$$\dot{x}_D - \dot{x}(t_0) = \int_{t_0}^T \ddot{x}(t) dt \quad (4.20)$$

$$x_D - x(t_0) - \dot{x}(t_0) T_{go} = \int_{t_0}^T \left[ \int_{t_0}^t \ddot{x}(s) ds \right] dt \quad (4.21)$$

where

$$T_{go} = T - t_0 \quad (4.22)$$

Equations (4.20) and (4.21) constitute a pair of simultaneous linear integral equations in  $\ddot{x}(t)$ , i. e., the function to be determined,  $\ddot{x}(t)$ , appears under integral signs in Eqs. (4.20) and (4.21). The solution of Eqs. (4.20) and (4.21) for  $\ddot{x}(t)$  is not simple since they do not even uniquely determine  $\ddot{x}(t)$ . Since  $\ddot{x}(t)$  is a function of time, it has infinitely many degrees of freedom and hence there are an infinite number of  $\ddot{x}(t)$ 's which satisfy Eqs. (4.20) and (4.21). These equations can uniquely determine an  $\ddot{x}(t)$  however, if some other suitable condition is also imposed. The most suitable additional condition to impose is the requirement that

$$\int_{t_0}^T a_T dt = \text{a minimum} \quad (4.23)$$

This condition, however, involves a calculus of variations problem whose solution requires extensive numerical procedures. It is desired to find a solution which is explicit, or analytical. The approach is deliberately to limit the number of degrees of freedom of the  $\ddot{x}(t)$  which can be used for the solution function. Since Eqs. (4.20) and (4.21) regarded as an algebraic system, can only determine two constants, it is appropriate to limit  $\ddot{x}(t)$  to two

degrees of freedom. This is done by specifying that  $\ddot{\mathbf{x}}(t)$  be defined by:

$$\ddot{\mathbf{x}}(t) = c_1 p_1(t) + c_2 p_2(t) \quad (4.24)$$

where  $p_1(t)$  and  $p_2(t)$  are any pre-specified, linearly independent, integrable functions of time, and  $c_1$  and  $c_2$  are quantities which are chosen to satisfy Eqs. (4.20) and (4.21). Then  $\ddot{\mathbf{x}}(t)$  has only two degrees of freedom because two arbitrary coefficients,  $c_1$  and  $c_2$ , are sufficient to determine  $\ddot{\mathbf{x}}(t)$ . Before  $\ddot{\mathbf{x}}(t)$  was limited as in Eq. (4.24), the function  $\ddot{\mathbf{x}}(t)$ , expanded in a general Fourier series, had an infinite number of undetermined Fourier coefficients, and hence an infinite number of degrees of freedom.

Substituting the two-degree-of-freedom definition of  $\ddot{\mathbf{x}}(t)$  into Eqs. (4.20) and (4.21) yields:

$$\dot{\mathbf{x}}_D - \dot{\mathbf{x}}(t_0) = c_1 \int_{t_0}^T p_1(t) dt + c_2 \int_{t_0}^T p_2(t) dt \quad (4.25)$$

$$\mathbf{x}_D - \mathbf{x}(t_0) - \dot{\mathbf{x}}(t_0)^T \mathbf{g}_0 = c_1 \int_{t_0}^T \left[ \int_{t_0}^t p_1(s) ds \right] dt + c_2 \int_{t_0}^T \left[ \int_{t_0}^t p_2(s) ds \right] dt \quad (4.26)$$

The coefficients of  $c_1$  and  $c_2$  in Eqs. (4.25) and (4.26), although written as integrals, are simply algebraic functions of the current time,  $t_0$ , and the terminal time,  $T$ . Equations (4.25) and (4.26) can be solved for  $c_1$  and  $c_2$  and a solution,  $\ddot{\mathbf{x}}(t)$ , determined. It is required that  $p_1(t)$  and  $p_2(t)$  be linearly independent (that is,  $p_1(t)$  must not be a multiple of  $p_2(t)$  or vice versa) in order to ensure that the determinant of the algebraic system (Eqs. (4.25) and (4.26)) exists.

The actual choice made in specifying  $p_1(t)$  and  $p_2(t)$  will determine the propellant economy of the resulting steering law. The derivation is completed by specifying that  $\ddot{x}(t)$  be a linear function of time. It is convenient to define  $p_1(t)$  and  $p_2(t)$  as follows:

$$p_1(t) = 1 \quad (4.27)$$

$$p_2(t) = T - t \quad (4.28)$$

This particular choice for  $p_1(t)$  and  $p_2(t)$  approximately minimizes the integral of the square of the thrust acceleration, and produces a useful steering law. However, this choice of  $p_1(t)$  and  $p_2(t)$  is not necessarily final, and a better choice resulting in better  $\Delta V$  performance may ultimately be made. The data and examples presented in Section (4.2) was obtained with the definitions of  $p_1(t)$  and  $p_2(t)$  given in Eqs. (4.27) and (4.28).

Using the definitions of  $p_1(t)$  and  $p_2(t)$  in Eqs. (4.27) and (4.28), the coefficients of  $c_1$  and  $c_2$  can be determined in the system of equations, Eqs. (4.25) and (4.26). Evaluation of the integrals in Eqs. (4.25) and (4.26) transforms these equations of constraint into

$$\dot{x}_D - \dot{x}(t_0) = T_{go} c_1 + (T_{go}^2/2) c_2 \quad (4.29)$$

$$x_D - x(t_0) - \dot{x}(t_0) T_{go} = (T_{go}^2/2) c_1 + (T_{go}^3/3) c_2 \quad (4.30)$$

The determinant of this pair of linear algebraic equations for  $c_1$  and  $c_2$  is:

$$\text{determinant} = T_{go}^4/12 \quad (4.31)$$

The solution for  $c_1$  and  $c_2$ , in matrix notation, is:

$$\begin{bmatrix} c_1 \\ c_2 \end{bmatrix} = \begin{bmatrix} 4/T_{go} & -6/T_{go}^2 \\ -6/T_{go}^2 & 12/T_{go}^3 \end{bmatrix} \begin{bmatrix} \dot{x}_D - \dot{x}_o \\ x_D - x_o - \dot{x}_o T_{go} \end{bmatrix} \quad (4.32)$$

With  $c_1$  and  $c_2$  determined from Eq. (4.32), a solution to the x-axis boundary value problem is given by:

$$\ddot{x}(t) = c_1 + c_2 (T - t) \quad (4.33)$$

In order to obtain this x-acceleration profile in accordance with differential Eq. (4.8), the following equality is required:

$$g_x + a_{T_x} = c_1 + c_2 (T - t) \quad (4.34)$$

Thus the sum of gravitation and thrust acceleration must be equal to the solution x-acceleration profile, and the solution thrust acceleration program is:

$$a_{T_x} = c_1 + c_2 (T - t) - g_x \quad (4.35)$$

It is obvious that the same kind of treatment can be given to the y and z axes. For example:

$$\begin{bmatrix} c_3 \\ c_4 \end{bmatrix} = \begin{bmatrix} 4/T_{go} & 6/T_{go}^2 \\ -6/T_{go}^2 & -12/T_{go}^3 \end{bmatrix} \begin{bmatrix} \dot{y}_D - \dot{y}_o \\ y_D - y_o - \dot{y}_o T_{go} \end{bmatrix} \quad (4.36)$$

$$a_{T_y} = c_3 + c_4 (T - t) - g_y \quad (4.37)$$

Equations (4.36) and (4.37) yield a solution thrust acceleration program for the y-axis boundary-value problem. A similar set of equations exists for the z-axis problem.

By the method just described, the three components of a solution thrust acceleration program can be computed. This procedure of computing the components of the solution thrust acceleration vector separately is valid because the landing engine is throttleable. The constraint:

$$a_T = \sqrt{a_{T_x}^2 + a_{T_y}^2 + a_{T_z}^2} \quad (4.38)$$

is satisfied by commanding a thrust acceleration magnitude equal to the square root of the sums of the squares of the components of the thrust acceleration. If the engine were not throttleable, this simple procedure could not be implemented.

Because the thrust of the LEM descent engine is bounded between 1050 lbs and 10,500 lbs, the descent engine cannot satisfy Eq. (4.38) under all conditions. The boundary-value problem must be a feasible one; for example, it cannot be expected to decelerate the spacecraft from orbital velocity to zero velocity in 100 miles of range or 200 seconds of burning time. These kinds of boundary conditions require a higher thrust than the LEM descent engine is capable of providing. Note that in the derivation of the steering equations, the method of determining the terminal time  $T$  was not discussed. Determining  $T$  is equivalent to determining  $T_{go}$  since the terminal time minus the current time is the time-to-go. The initial  $T_{go}$ , i. e., the time-to-go at engine ignition, is chosen to make  $a_T$  near the maximum thrust acceleration which the engine is capable of providing. The possibility

currently exists that the descent engine will be required to ignite and run at minimum thrust for about 25 seconds at the start of the landing maneuver. The purpose of the lowered initial thrust setting is to reduce the initial torque on the vehicle for possible initial C.G. offsets until the descent engine trim gimbals can be reoriented. This initial period of lowered thrust is not conceptually important to the development and operation of the guidance scheme and consequently is not dealt with in this section. The actual computation of the initial  $T_{go}$  is discussed in Section 4.2.4. After initial  $T_{go}$ , or equivalently  $T$ , is determined, the time-to-go at any subsequent time can be determined by subtracting the current time from the already established terminal time.

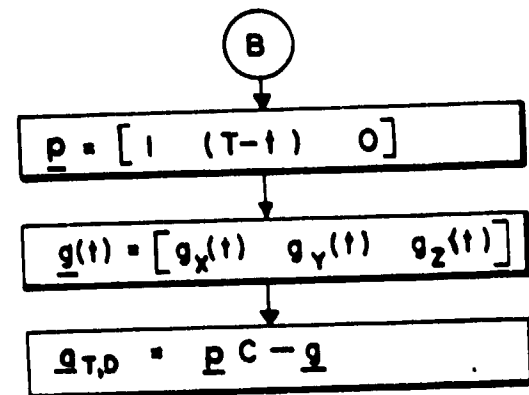
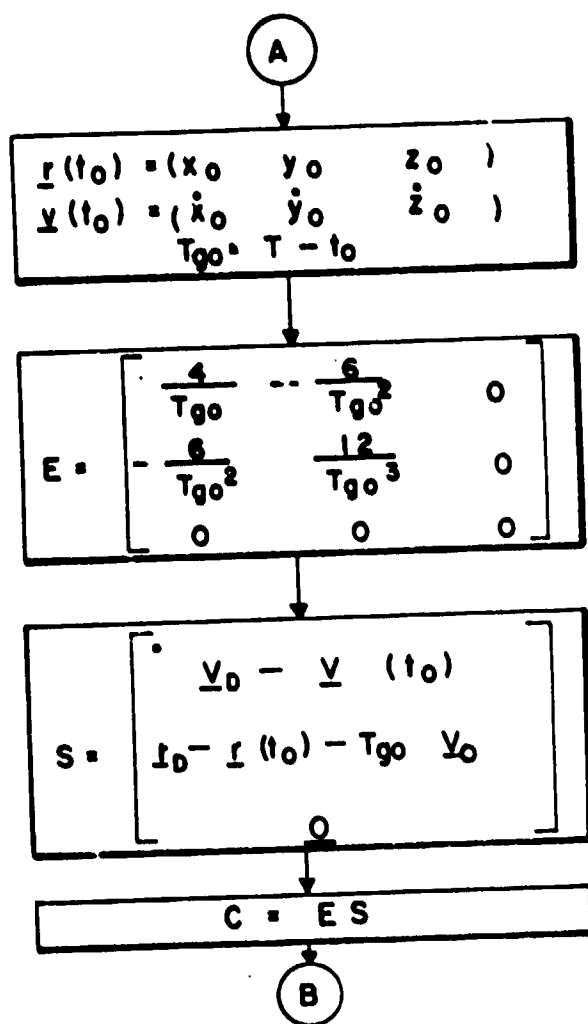
#### 4.2.3 Guidance Equation Summary

A particularly economical statement of the guidance algorithm, which exploits the vector-matrix instructions available in the LGC interpreter, can be developed. A certain matrix, called the E matrix, is fundamental to this statement. The E matrix gives the explicit guidance technique its name, E Guidance.

The following matrices and row vectors are defined:

$$E = \begin{bmatrix} 4/T_{go} & -6/T_{go}^2 & 0 \\ -6/T_{go}^2 & 12/T_{go}^3 & 0 \\ 0 & 0 & 0 \end{bmatrix} \quad (4.39)$$

$$S = \begin{bmatrix} \text{---} (\underline{v}_D - \underline{v}_o) \text{---} \\ \text{---} (\underline{r}_D - \underline{r}_o - T_{go} \underline{v}_o) \text{---} \\ \text{---} \quad 0 \quad \text{---} \end{bmatrix} \quad (4.40)$$



## NOTES

1. ALL VECTORS ARE ROW ARRAYS
2. THE COMPUTATION BETWEEN (A) AND (B) IS NOT PERFORMED FOR  $T_{go} < 5$  or 10
3. THE COMPUTATIONS BEGINNING AT (B) CAN BE USED IN THE INNER CONTROL LOOP IN A MINOR COMPUTATION CYCLE

Fig. 4.8 E guidance steering equations.

In order to clarify the declaration in Eq. (4.40), the first row of the S matrix is the row vector (array)  $\underline{v}_D$  minus the row vector  $\underline{v}_O$ . Furthermore:

$$\underline{C} = \underline{E} \underline{S} \quad (4.41)$$

$$\underline{p} = \begin{bmatrix} 1 & (T-t) & 0 \end{bmatrix} \quad (4.42)$$

$$\underline{g} = (g_x \quad g_y \quad g_z) \quad (4.43)$$

In terms of the foregoing symbols and definitions, the desired or solution thrust acceleration vector is given by:

$$\underline{a}_{T, D} = \underline{p} \underline{C} - \underline{g} \quad (4.44)$$

Figure 4.8 repeats these computational steps in block format. Equation (4.44) can be verified by performing the matrix multiplications and comparing the result with Eqs. (4.32), (4.35), (4.36) and (4.37). In particular:

$$\underline{C} = \begin{bmatrix} C_1 & C_3 & C_5 \\ C_2 & C_4 & C_6 \\ 0 & 0 & 0 \end{bmatrix} \quad (4.45)$$

It might be noted that if the navigation system were perfect, and the LEM's SCS and flight-control system's execution of the guidance commands perfectly implemented, the matrix C would be a constant throughout the entire powered flight phase. Even with physical systems and their associated performance limits the elements of the C matrix change slowly. Thus the C matrix can be computed at a relatively low computation rate. The elements of the  $\underline{g}$  vector, the gravitational acceleration, also evolve slowly. Consequently, the desired thrust acceleration vector can be computed

for many seconds without re-computation of  $C$  and  $\underline{g}$ . A minor computation loop, involving merely the following computation steps, can thus be established:

$$\underline{p} = \begin{bmatrix} 1 & (T-t) & 0 \end{bmatrix} \quad (4.46)$$

$$\underline{a}_{T,D} = \underline{p} C - \underline{g} \quad (4.47)$$

This minor computation loop is particularly important as time-to-go approaches zero, for then the four non-zero elements of  $E$  increase without bound and the  $C$  matrix, which is the product of  $E$  and  $S$ , "blows up". This "blowing up" of the  $E$  and  $C$  matrices is due to the fact that as  $T_{go}$  becomes vanishingly small, the negligible but non-vanishing errors in the boundary conditions require an infinite thrust acceleration for their correction. The wild behaviour of  $C$  is avoided by the simple expedient of not computing  $E$ ,  $S$  and  $C$  during the last few seconds of the powered maneuver.

Figure 4.9 is a block diagram of the landing guidance system. This diagram shows a block in the LGC which operates on the desired thrust acceleration vector in order to produce commands suitable for interpretation by the LEM flight control system. It is in this block, for example, that an increment or decrement in thrust magnitude is computed. The computation of the delta thrust magnitude command requires an estimate of the vehicle mass in order to scale the thrust acceleration magnitude error to thrust change. Thus

$$\Delta \text{ THRUST} = m(a_{T,D} - a_T) \quad (4.48)$$

where

$$a_{T,D} = \left| \underline{a}_{T,D} \right| \quad (4.49)$$

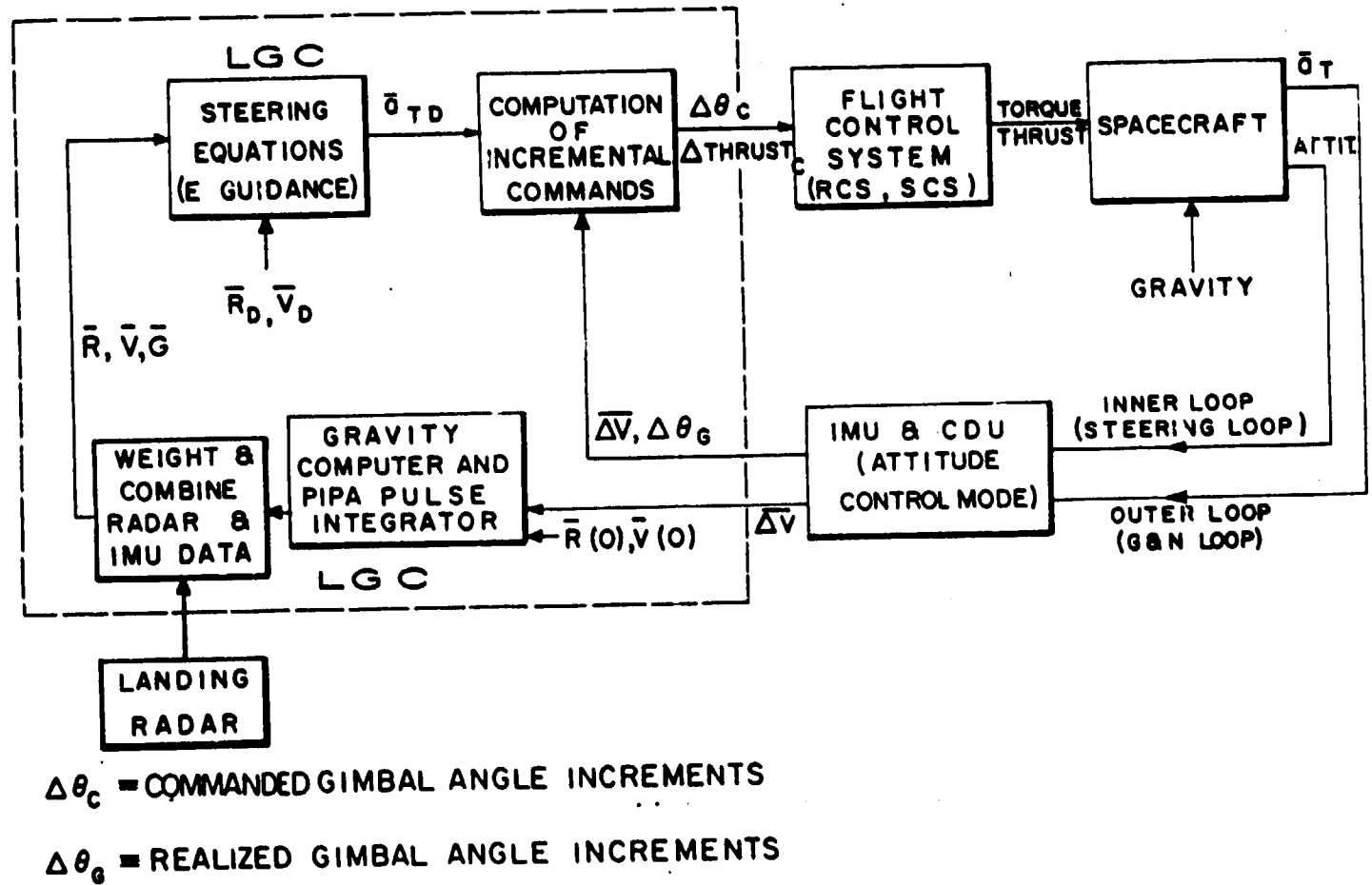


Fig. 4.9 Landing powered flight guidance system.

$$m = m_i / \exp(\Delta V / V_e) \quad (4.50)$$

$$\Delta V = \int_{t_i}^{t_o} a_T(s) ds \quad (4.51)$$

$$V_e = I_{sp} g_e \quad (4.52)$$

$$g_e = 32.174 \cdot \quad (4.52a)$$

The  $i$  subscript refers to the instant of the first engine ignition. Since the IMU accelerometers perform one integration, the computation of  $\Delta V$  can be mechanized by summing the square root of the sum of the squares of the IMU accelerometer (PIPA) outputs. The computation of the vehicle orientation commands can proceed in a manner similar to that used on the CSM. The minor computation loop, Eqs. (4.46) and (4.47), can be used in a relatively fast computation cycle in the inner steering loop in Fig. 4.9. The major computation cycle, Eqs. (4.39) through (4.44), closes the guidance loop through the navigation data. This major cycle, which includes the computation of a new  $C$  matrix, is depicted in Fig. 4.9 as an outer loop.

#### 4.2.4 Determination of $T$ or $T_{go}$

In the discussion of the algorithm for computing the solution thrust acceleration vector, the determination of the choice of  $T_{go}$  was not described. Equations (4.39) through (4.44) produce a thrust acceleration regime for any  $T_{go}$ . While this solution,  $\underline{a}_{T,D}$ , exists mathematically for any given  $T_{go}$ , these solutions are not all physically acceptable or even physically possible. For example, it should be evident that for any given boundary-value problem there exist times-to-go so short that the spacecraft must undergo extreme accelerations in order to

achieve the desired boundary conditions by the terminal time. These accelerations require thrust levels which exceed the maximum thrust capability of the engine. Thus, a very small  $T_{go}$  must be avoided, unless the errors in the boundary conditions are correspondingly small.

There are, of course, many more physically impossible boundary-value problems when the spacecraft is fuel and thrust-limited. There are boundary-value problems for which no appropriate  $T_{go}$  exists. For purely physical reasons, these problems have no useful or practical solution. In order to illustrate the landing maneuver phase 1 boundary-value problem, the following example is described. Consider a fuel-limited, thrust-limited spacecraft which is moving very fast toward point B from point A. Suppose the final boundary conditions are that the vehicle must arrive at point B and possess zero velocity upon its arrival. Because the spacecraft is moving very fast toward B and has only a limited thrust acceleration capability, it is impossible to decelerate the vehicle before its arrival at point B. Thus, the obvious solution is impossible because of the limited thrust. Mathematical solutions requiring very large thrust, nevertheless exist. Now consider a solution in which the spacecraft passes through or past point B and returns. Since the vehicle cannot decelerate to zero speed before its first arrival at point B, application of maximum thrust will only slow it down. The spacecraft will, of course, pass by point B and finally stop. After the vehicle stops, the thrust can be used to start the vehicle moving back toward point B and, at some point in the vehicle's return to B, the thrust can be reversed in order to decelerate the spacecraft before its final arrival at B. While the program just described for bringing the spacecraft to rest at B can be arranged to stay below the engine's maximum thrust level, it should be evident that such thrust vector programs may easily use all the propellant in the fuel-limited vehicle. Thus, both solutions, the one in which the vehicle decelerates and stops at B on its

first approach, and the solution in which the vehicle goes past B, slows down, returns to B and then stops on its second approach, are physically useless although mathematically existent. The first solution is impossible because of the limited thrust; the second solution is impossible because of the limited fuel. There is no choice of  $T_{go}$  which can help with this kind of boundary-value problem.

Now consider how the hypothetical boundary-value problem can be initiated for a practical solution. The problem is to find a physically realizable thrust acceleration regime which will decelerate the vehicle by the time it arrives at B. If the spacecraft goes too fast toward B, the thrust-limited rocket cannot decelerate the spacecraft before its first arrival at B, and thus there is not enough fuel to fly past B, stop, and return to B. It can further be concluded that there is a mathematical solution for this problem for any given  $T_{go}$ , although there is no physically realizable solution for any  $T_{go}$ . The reason that the first obvious mathematical solution is impossible is that point A is so close to B (close with respect to the velocity of the vehicle toward B) that the thrust-limited rocket cannot decelerate the vehicle to zero speed by the time of its arrival at B. If the rocket engine is ignited earlier so that the distance from ignition-point to B is greater, the thrust-limited rocket may be able to decelerate the vehicle to zero speed before its first arrival at B. Assume that an initial distance or range exists which permits a solution to the boundary-value problem of arriving at B the first time with zero velocity for a thrust-limited vehicle. When the landing engine ignition is delayed until the spacecraft is at an A point (too close to B), there are no physical solutions. When the landing engine is ignited at a point A' further away (than the distance AB) there are physically realizable solutions corresponding to an interval of times-to-go. The problem is then to choose from within this interval of feasible times-to-go a  $T_{go}$  which is best. Since there is an interval of feasible A's the best A' also must be determined. A method for

determining the best point for the engine ignition must be developed as well as a best initial  $T_{go}$  (powered flight duration). The determination of a best  $A'$  will lead to the development of an engine ignition algorithm.

The hypothetical boundary-value problem just discussed is quite similar to the phase 1 boundary-value problem. Point  $A'$  is analogous to the point of phase 1 descent engine ignition, which is near the perilune of the descent trajectory and about 12.5 degrees central angle before the hover point. Point B is analogous to the terminal point of phase 1. The phase 1 terminal point speed, however, is not zero. This latter fact does not, of course, invalidate the qualitative conclusions drawn. During the phase 1 maneuver, the spacecraft is decelerated from a velocity of over 5500 ft/sec to a velocity under 1000 ft/sec.

Examination of Eqs. (4.39) through (4.44) shows that the components of the desired thrust acceleration vector are functions of  $T_{go}$ . Thus, if  $T_{go}$  is varied while the boundary conditions are held fixed, all the components of the desired thrust acceleration vector vary. Consequently, the thrust angle and the thrust acceleration magnitude change as  $T_{go}$  is varied. Figure 4.10 shows the variation of thrust magnitude with  $T_{go}$  for ignition of the engine at the perilune point. Note that there are three distinct points for which the thrust magnitude is 10,400 pounds.

For phase 1,  $T_{go}$  is chosen to make the initial thrust nearly maximum. Two reasons exist for choosing time-to-go in this manner. First, good  $\Delta V$  performance can be achieved this way; and second the thrust tends to decay as the vehicle decelerates and approaches the phase 1 terminal boundary conditions. (See Fig. 4.5 for typical thrust magnitude behavior during phase 1.) It is desirable to have the thrust magnitude decay as the spacecraft descends because radar altimeter information becomes available at about 20,000 feet altitude and is used to update the spacecraft's current altitude vector. The updated altitude

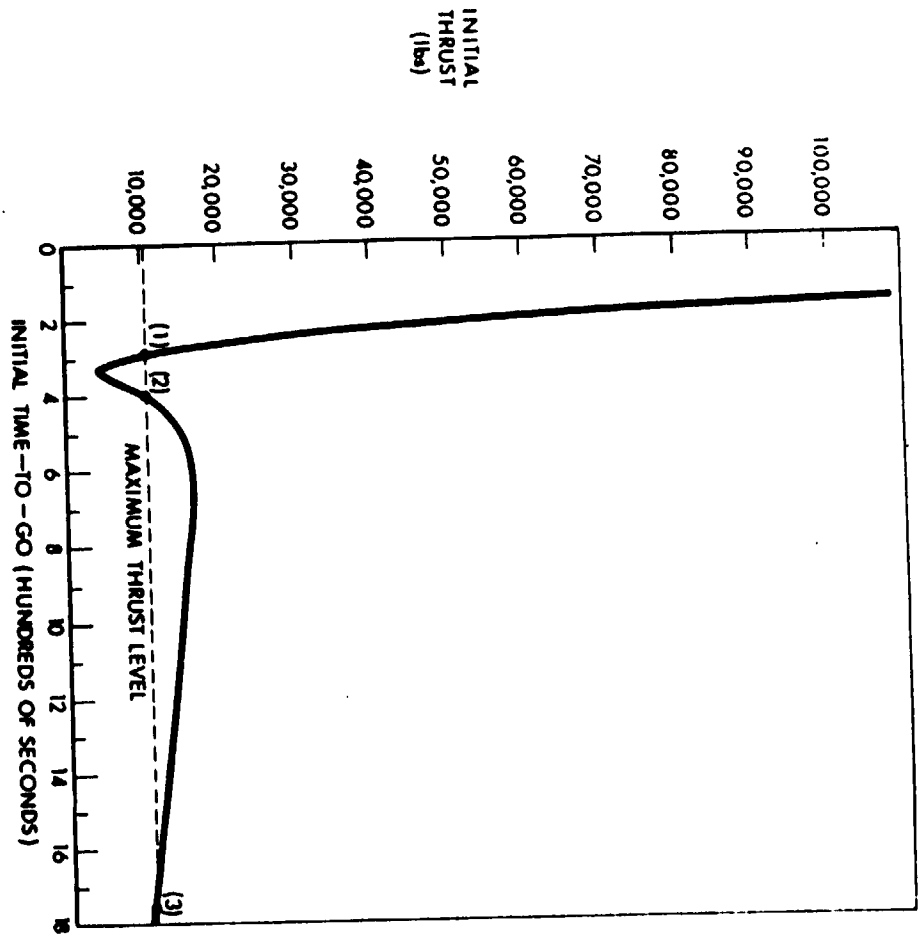


Fig. 4.10 Initial thrust versus initial  $T_{go}$  for lunar landing.

vector modifies the boundary-value problem posed to the guidance system. The new boundary-value problem may require a higher thrust if the terminal boundary conditions are to be achieved. Because the thrust magnitude has decayed from maximum during the first part of the maneuver, a margin exists for increasing the commanded thrust if such an increase is required. It is important to note that if the engine ignition is delayed until the vehicle is too close to the terminal position vector, the required thrust magnitude, which is initially set to nearly maximum, will subsequently increase.

It was stated that  $T_{go}$  is chosen to make the initial thrust magnitude near the maximum thrust level of the engine. Figure 4.10 shows the interesting fact that as  $T_{go}$  is increased from a very small value to a very large value, the initial thrust magnitude passes through the maximum thrust level of the engine three times. Only point (2) of this figure corresponds to the desired thrust vector regime, however. Point (1) on Fig. 4.10 corresponds to such a short  $T_{go}$  that the spacecraft must initially be accelerated toward the terminal point, point B, in order to arrive there at the stipulated time. For very short time-to-go, the acceleration toward point B is immense as shown by the very sharp increase of thrust as  $T_{go}$  is decreased below 300 seconds. The trajectory corresponding to point (1) requires that the thrust vector initially point toward B and finally point away from B in order to decrease the vehicle's speed before its arrival. This speeding up and slowing down of the spacecraft with the thrust vector is, of course, uneconomical. More than that, even if the fuel were available for such wasteful efforts, the thrust magnitude increases as the vehicle proceeds toward B because high thrust is required in order to decelerate the very rapidly moving spacecraft before its arrival at B. Therefore, point (1) is rejected.

Point (2) on Fig. 4.10 corresponds to the desired thrust vector regime. The thrust angle and thrust magnitude plots in

Figs. 4.4 and 4.5 were obtained by choosing the  $T_{go}$  corresponding to point (2) on Fig. 4.10. For this choice of initial time-to-go, the spacecraft is continually and efficiently decelerated while the thrust magnitude gradually decays.

The trajectory corresponding to point (3) of Fig. 4.10 requires a  $T_{go}$  of about 1800 seconds. In order to expend this time, the vehicle must first climb in altitude, pass over the desired terminal point B, decelerate to zero velocity and then finally reapproach point B with the specified velocity vector. This solution is mathematically possible, but obviously impractical.

The actual computation of the initial  $T_{go}$  is performed by a technique which guarantees that point (2) on Fig. 4.10 is chosen. A guess at  $T_{go}$ , call it  $\tilde{T}_{go}$ , which is definitely in excess of the required (but unknown)  $T_{go}$ , is made. A safe and reasonable value would be 450 seconds. The thrust magnitude corresponding to  $\tilde{T}_{go}$  is examined. The first value of the computed thrust will, of course, exceed 10,400 pounds. The initial time-to-go,  $\tilde{T}_{go}$ , is then decremented and the corresponding thrust magnitude computed and examined. A reasonable decrementing step would be 10 seconds. The process of decrementing  $\tilde{T}_{go}$  and computing and examining the corresponding thrust magnitude is continued until a  $\tilde{T}_{go}$  for which the required thrust is less than 10,400 pounds is found. The required value of  $T_{go}$  is known to lie between this  $\tilde{T}_{go}$  and the previous value of  $\tilde{T}_{go}$ . The method of false position (regula falsi, Ref 4.1) is then used to find the exact value of  $T_{go}$  which makes the thrust equal to 10,400 pounds. Examination of Fig. 4.10 will show that this method of computing  $T_{go}$  avoids the mischance of choosing points (1) or (3).

Specifying the initial time-to-go is equivalent to specifying the terminal time,  $T$ . After  $T$  is chosen, the  $T_{go}$  corresponding to any subsequent instant of powered flight,  $t_o$ , can be found as follows:

$$T_{go} = T - t_o$$

The exception to this is during the last part of phase 2 when landing radar information modifies the boundary-value problem. It may be advisable to recompute  $T_{go}$  if a substantial modification of the boundary-value problem occurs.

The duration of phase 2 is not computed in flight. Since the phase 2 boundary-value problem is fairly well standardized by the conduct of the phase 1 boundary-value problem, a standard pre-determined initial  $T_{go}$  can be used for phase 2.

#### 4.2.5 The Engine Ignition Algorithm

It has been concluded in the previous section that the initial  $T_{go}$  should be chosen to maximize the initial thrust level. The implications of requiring an initial period of thrusting at a reduced level will be discussed later. Figure 4.11 is a plot of the total  $\Delta V$  required to achieve the phase 2 terminal conditions versus the initial range-to-go. The phase 2 terminal conditions are desired hover conditions. The examples presented in this section assume phase 2 terminal conditions of 200 feet altitude, 10 ft/sec speed, and  $-10^\circ$  flight path angle. The data for Fig. 4.11 was generated as follows. A simulation was set up which permitted the vehicle to be guided from the perilune of the Hohmann descent orbit through phase 1 and phase 2 to the specified hover conditions. The descent-to-hover was repeatedly simulated. Each simulation was performed with the perilune of the Hohmann descent orbit located at a different angular range-to-go from the specified hover point. The  $\Delta V$  for each case was recorded and Figure 4.11 generated. Each simulation used an initial  $T_{go}$  which set the initial thrust level to 10,400 pounds. If the perilune point (the point at which the engine was always ignited in this simulation) was farther from the hover point than  $11.8^\circ$ , the thrust magnitude decayed from the maximum at which it was initially set. Thus, all the trajectories to the left of  $\theta_{crit}$  in Fig. 4.11 are physically realizable with the LEM's thrust-limited descent engine. But when the perilune point is located closer to the hover

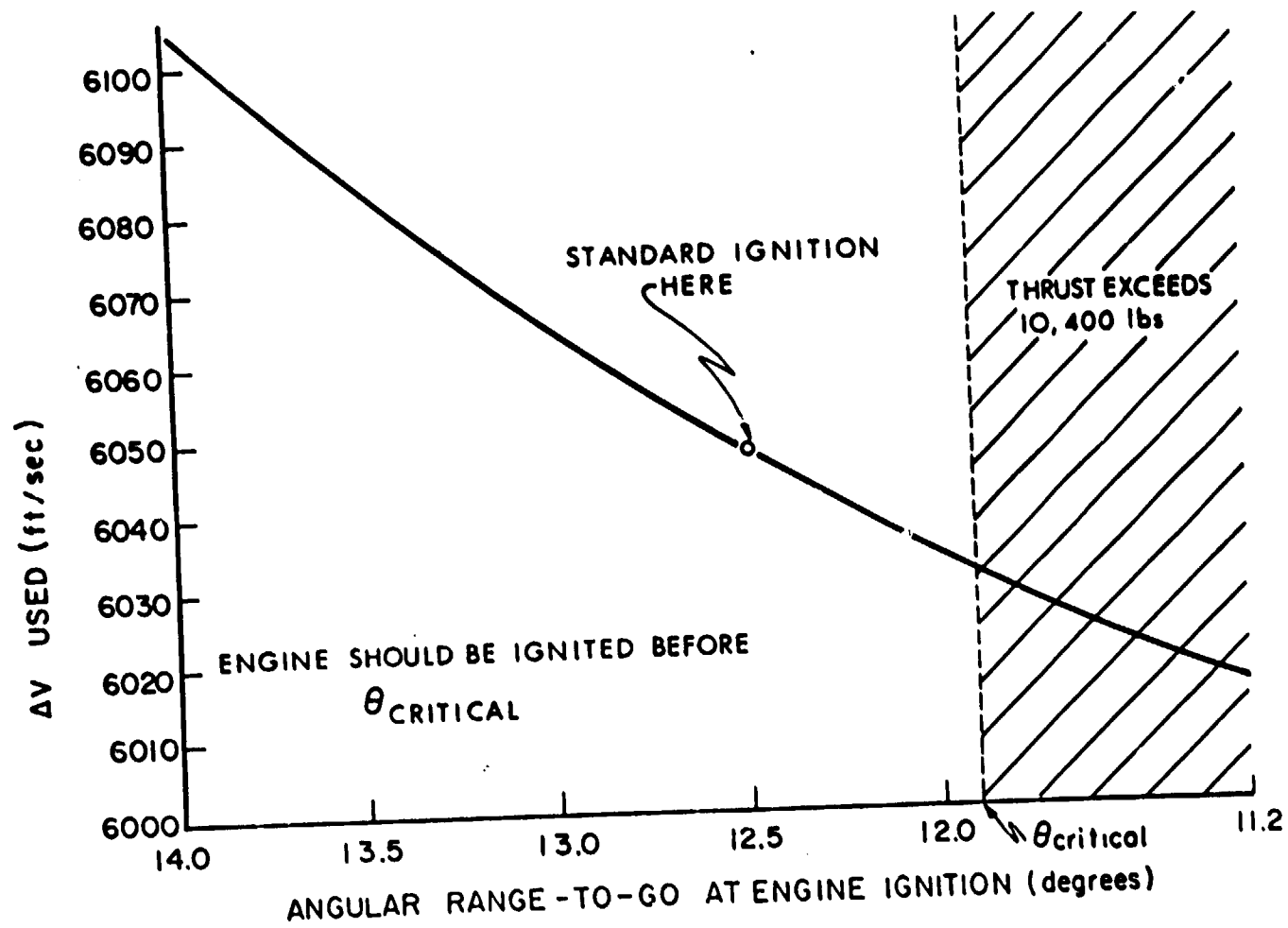


Fig. 4.11  $\Delta V$  versus range - to - go at engine ignition based on 10,400 lbs. initial thrust (landing from Hohmann descent).

point than  $11.8^\circ$ , the commanded thrust subsequently increases. In this simulation, the thrust magnitude was not bounded. The  $\Delta V$  curve's excursion into the shaded region of Fig. 4.11 shows that if the LEM had higher thrust capability, the landing maneuver could be performed more economically. The trajectories corresponding to large initial range-to-go have a long phase 1 which is performed at a lower average thrust level. Such trajectories are less efficient than those corresponding to short initial range-to-go (about  $12^\circ$ ). It appears that the Hohmann descent orbit injection should be so arranged that its perilune is located about  $12^\circ$  before the desired hover point, and so that the LEM engine should be ignited at the perilune position. The objection to specifying the standard engine ignition position at  $\theta_{crit}$  is that if the engine ignition were delayed by even a second or two, the landing could not be performed due to the fact that greater than maximum thrust would be required. The perilune of the Hohmann descent orbit should therefore be located about  $12.5^\circ$  before the hover point, and the perilune point selected as the standard ignition point. This procedure gives an engine ignition window of almost 10 seconds with a  $\Delta V$  penalty, if the engine actually ignites at the standard engine ignition point of about 16 ft/sec.

Figures 4.12 and 4.13 give an engine ignition algorithm for the landing maneuver. Because the engine will probably have to be run at reduced thrust for the first 25 seconds or so of the landing maneuver, the engine ignition (and perilune point) will have to be biased by an angle  $\theta_{COMP}$ . There will be, of course, a small  $\Delta V$  penalty due to this requirement to operate the engine at lowered thrust for the initial seconds of the maneuver. No other difficulty is anticipated from this source.

During the period of thrusting at a reduced level, the thrust vector orientation computation is performed as though maximum thrust were being used. Consequently, no thrust angle discontinuity occurs in the transition from the low thrust setting to the

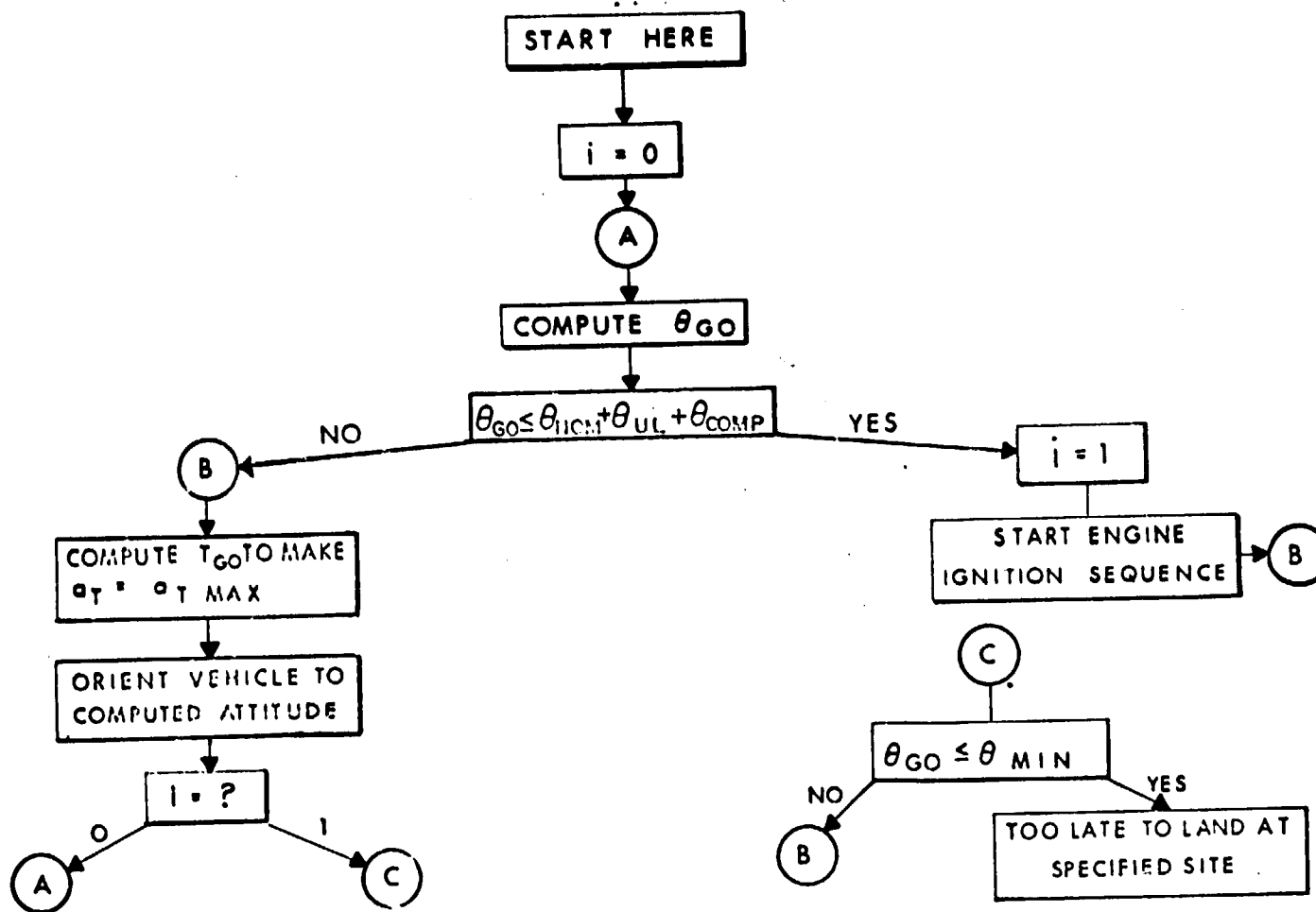


Fig. 4.12 Engine ignition algorithm for specified landing site.

$$i = \begin{cases} 0 & \text{if } \theta_{GO} > \theta_{NOM} + \theta_{UL} + \theta_{COMP} \\ 1 & \text{if } \theta_{GO} \leq \theta_{NOM} + \theta_{UL} + \theta_{COMP} \end{cases}$$

$\theta_{GO}$  = Lunar central angle between LEM and specified landing site

$$\theta_{GO} = \cos^{-1} (\bar{P} \cdot \bar{S} / R)$$

$\bar{S}$  = Unitized site position vector.

$\theta_{NOM}$  = Nominal or standard lunar central angle between LEM and site at engine ignition.

$\theta_{UL}$  = Approximate lunar central angle traveled between decision to ignite engine and actual engine ignition.

$$\theta_{UL} = \frac{V}{R} T_{UL}$$

$T_{UL}$  = Time required for engine ullage, etc.

$\theta_{MIN}$  = The minimum permissible lunar central angle between LEM and specified landing site when the engine is ignited.

$\theta_{Comp}$  = The compensation for initial period of thrusting at reduced thrust.

Fig. 4.13 Definition of symbols for engine ignition algorithm.

## EQUIPERIOD DESCENT

GUIDANCE SCHEME	$\delta y$ (feet)	$\delta \dot{y}$ (ft/sec)	$\delta \dot{x}$ (ft/sec)	$\delta(\Delta V)$ Landing Maneuver
<u>W</u> x <u>V</u>	900	-26	-11	2.5 fps
Aimpoint	0	$\approx 0$	$\approx 0$	Negligible

## HOHMANN DESCENT

$\delta y$ (feet)	$\delta \dot{y}$ (ft/sec)	$\delta \dot{x}$ (ft/sec)	$\delta(\Delta V)$ Landing Maneuver
343	-11	1	$\approx 1.5$ fps

1. THE FINAL CONDITIONS (END OF PHASE I) ARE, OF COURSE, NOT AFFECTED
2. THE THRUST MAGNITUDE FOR THESE PERTURBATIONS DOES NOT DECAY AS RAPIDLY AS FOR THE UNPERTURBED INSERTION; BUT IT REMAINS WITHIN THE ENGINE LIMITS.

Fig. 4.14 Effects of delaying engine ignition for descent orbit insertion maneuver (all data for 60 second delay).

maximum thrust setting. During the period of thrusting at a low level, the C matrix behaves oddly, but no effects of any consequence occur.

Note that if the spacecraft is closer to the hover point than  $\theta_{MIN}$  where:

$$\theta_{MIN} = \theta_{CRIT} + \theta_{UL} + \theta_{COMP}$$

the spacecraft cannot stop at the proposed hover point and landing site. If a landing site further downrange were acceptable, the landing maneuver could still be initiated, assuming that the in-ordinate delay for engine ignition is not due to a cause which necessitates aborting the landing altogether.

Performing the descent orbit injection with the objective of placing the descent orbit perilune at the nominal engine ignition point seems a wise course of action because there are no first order changes in the vehicle's velocity vector due to perturbations in the location of the perilune. Thus, the initial conditions for phase 2 are insensitive (to the first order) to the actual location of the descent orbit perilune. Because of this phenomenon, fairly long delays in the initiation of the descent orbit maneuver are acceptable. Figure 4.14 summarizes the effects which the descent orbit injection delay has on the landing maneuver. Note that a delay of 60 seconds is tolerable. Thus the engine ignition window for the landing maneuver is an order of magnitude smaller than the engine ignition window for the descent orbit injection maneuver.

### 4.3 Landing Maneuvers from Hohmann Descents

The characteristics of a typical landing maneuver trajectory controlled by the E guidance equations of Section 4.2 are summarized in Figs. 4.15 through 4.23. Figure 4.15 illustrates the altitude-range profile for the first two phases of the landing maneuver initiated from a Hohmann descent orbit. Figure 4.16

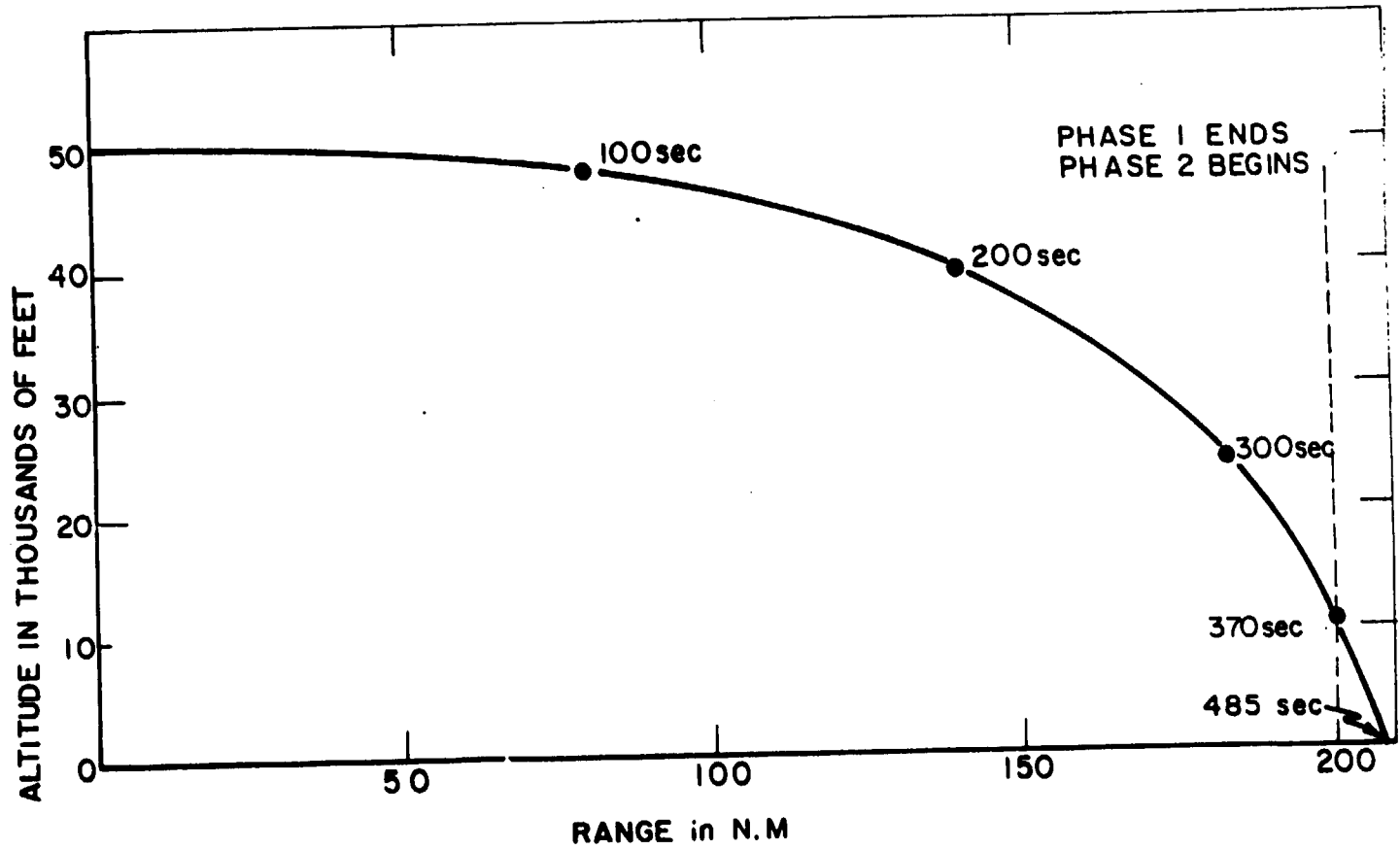


Fig. 4.15 Landing maneuver from Hohmann descent(altitude-range profile).

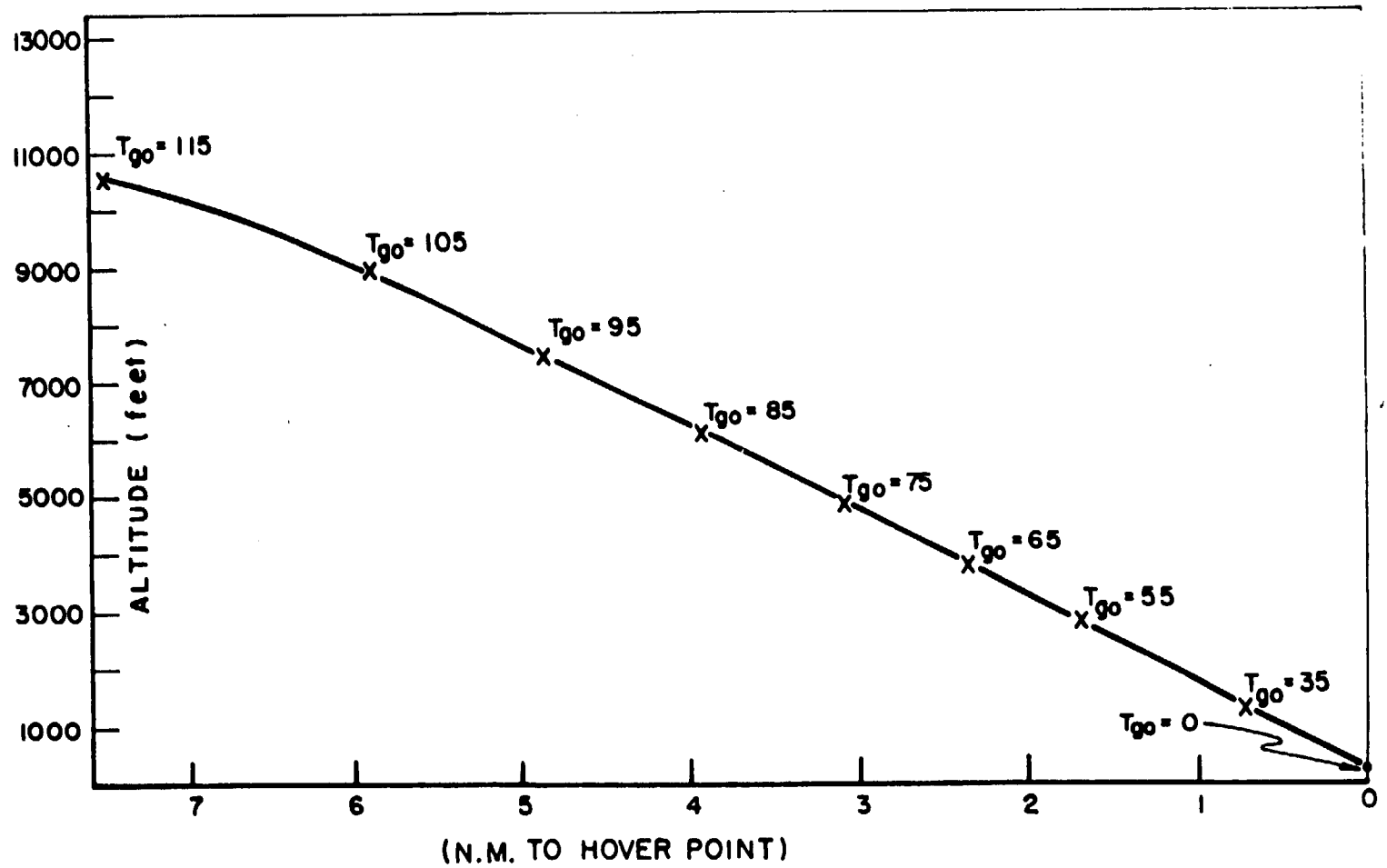


Fig. 4.16 Altitude versus miles-to-go.

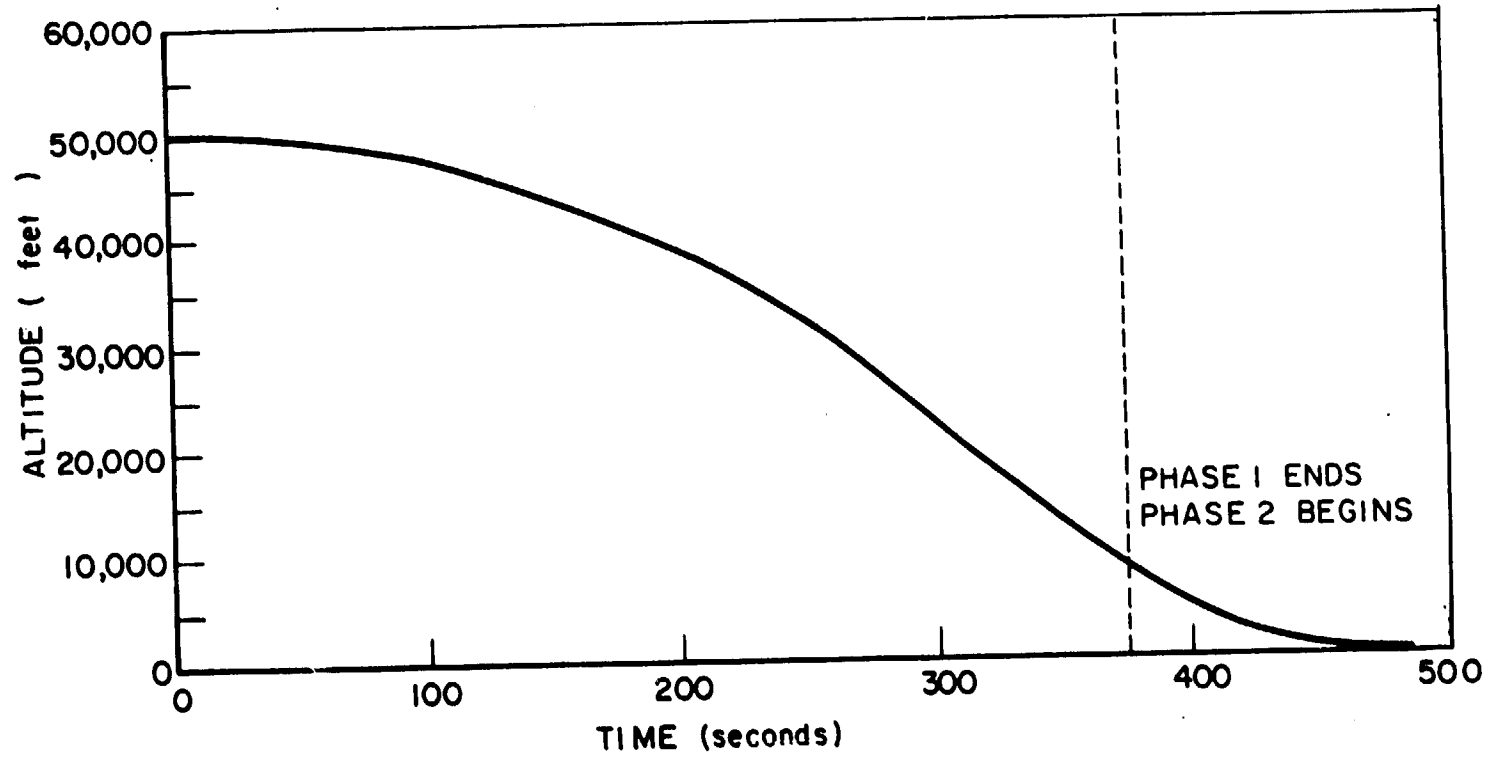


Fig. 4.17 Altitude versus time (landing from Hohmann descent).

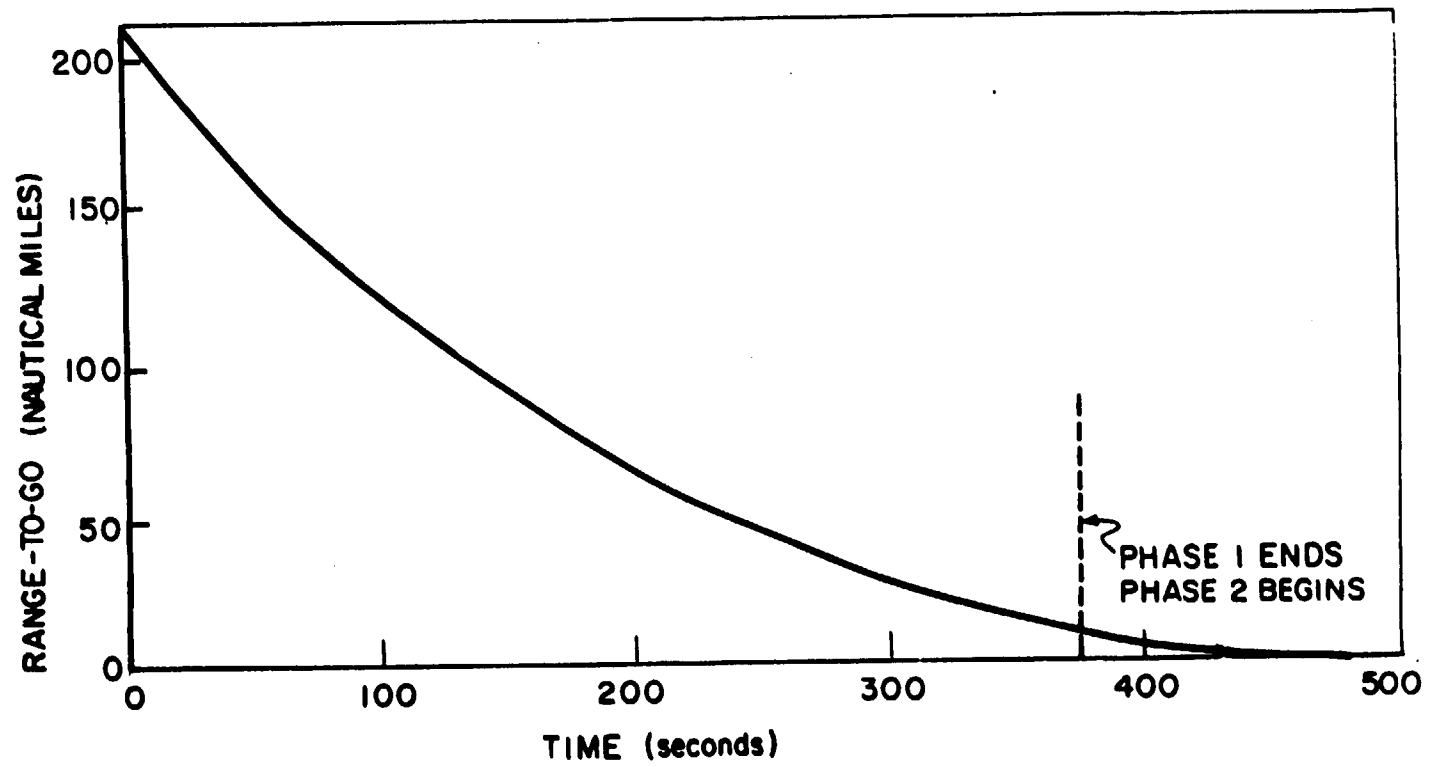


Fig. 4.18 Range-to-go versus time (landing from Hohmann descent).

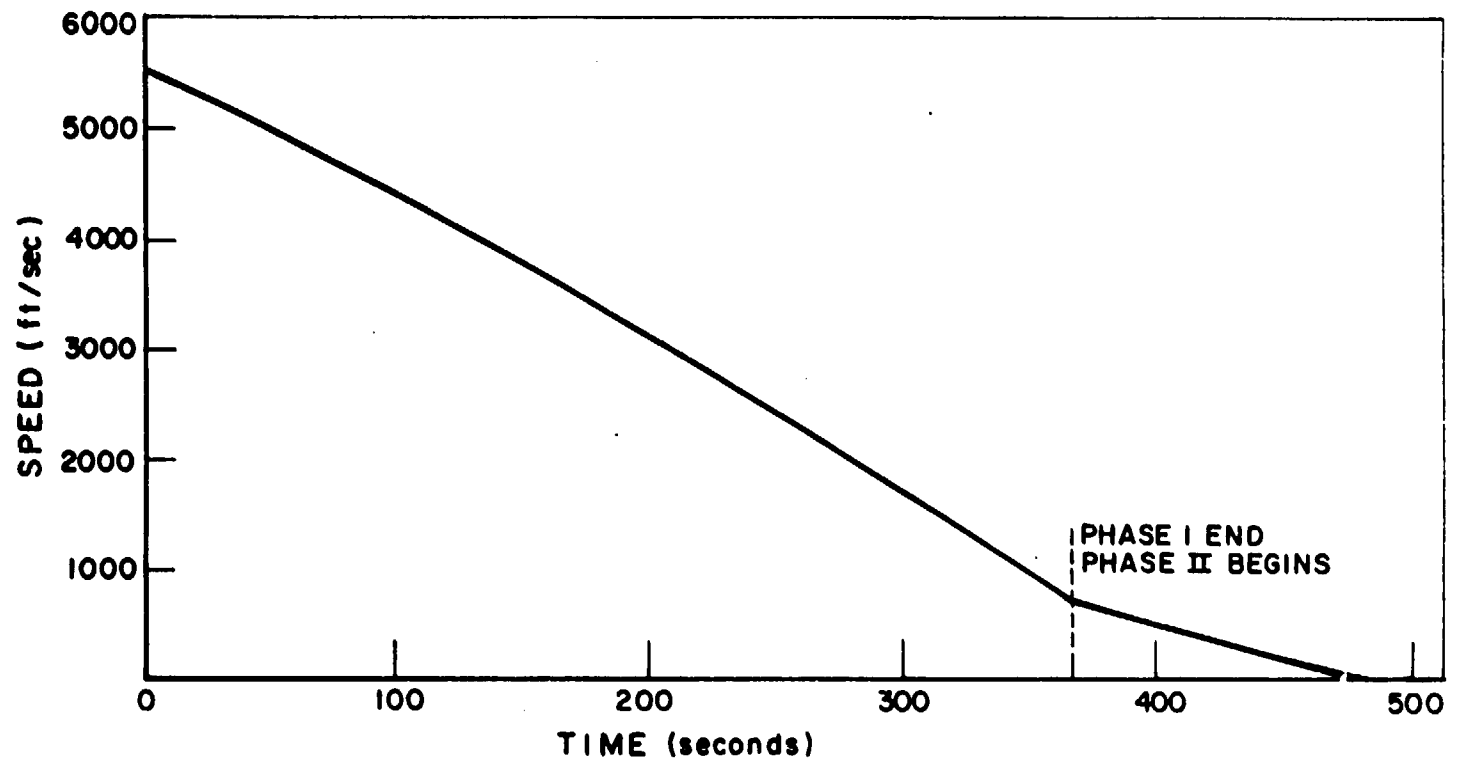


Fig. 4.19 Speed versus time (landing from Hohmann descent).

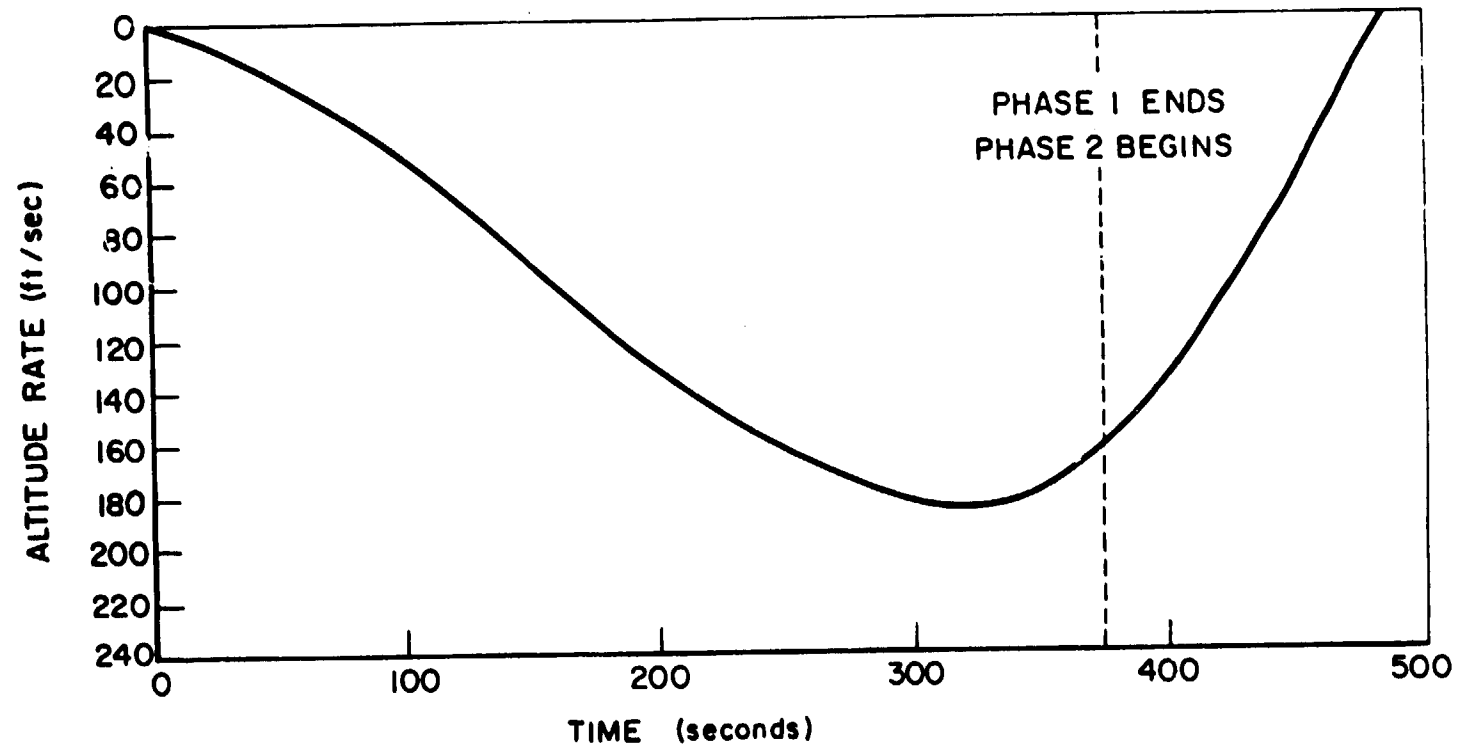


Fig. 4.20 Altitude rate versus time (landing from Hohmann descent).

shows the phase 2 characteristics which were chosen such that acceptable visibility conditions were met. (Figures 4.4 and 4.5 show the thrust magnitude and angle for this trajectory.) Figures 4.17 through 4.20 summarize the general landing maneuver position and velocity conditions as a function of time. With reference to Fig. 4.20, it can be seen that the maximum vertical velocity condition is 180 ft/sec and occurs just prior to the second phase of the landing maneuver.

The  $\Delta V$  requirements for the first two phases of the landing maneuver are summarized at the top of Fig. 4.21. The desired hover conditions at the end of phase 2 are an altitude of 200 feet with a velocity of 10 ft/sec along a  $-10^\circ$  flight path angle relative to the local horizontal. The total  $\Delta V$  requirement of 6048 ft/sec for these two phases controlled by the landing guidance equations is then compared with other types of landing maneuvers and conditions. If a "one piece" descent from engine ignition to hover is controlled by the landing guidance equations, a  $\Delta V$  of 5805 ft/sec is required. This indicates that the two phase maneuver with its associated vehicle altitude and time constraints in phase 2 requires an additional 243 ft/sec  $\Delta V$  requirement compared with the more optimum single phase maneuver in which all visibility would be sacrificed. The optimum  $\Delta V$  trajectory listed in Fig. 4.21 was generated by a numerical steepest descent optimization program and required 10 ft/sec less total  $\Delta V$  than the single phase E guidance case. This indicates that the E guidance concept described in Section 4.2 is very close to optimum  $\Delta V$  conditions for the landing maneuver.

The time history of the look angle during the second phase of the landing maneuver is shown in Fig. 4.22. The look angle,  $\lambda$ , is defined as the angle between the line of sight to the landing site and the thrust or -X LEM vehicle axis. The minimum visibility limit of the present LEM window configuration is  $25^\circ$  as shown. The landing maneuver considered in this section resulted

STANDARD DESCENT (RANGE CONSTRAINT: 12.5° LUNAR CENTRAL ANGLE)	
PHASE 1 -----	4992 ft/sec
PHASE 2 -----	1056 ft/sec
TOTAL (E GUIDANCE) -----	<b>6048 ft/sec</b>
ONE PIECE DESCENT WITH E GUIDANCE (RANGE AS SHORT AS POSSIBLE ) (NO VISIBILITY OR SINK RATE CONSTRAINTS)	<b>5805 ft/sec</b>
ONE PIECE OPTIMUM DESCENT (WITH STEEPEST DESCENT NUMERICAL OPTIMIZATION PROGRAM. NO RANGE, VISIBILITY, OR SINK RATE CONSTRAINTS)	<b>5795 ft/sec</b>
"ΔV PENALTY ATTRIBUTABLE TO E GUIDANCE"-----	<b>"10 ft/sec"</b>
ΔV PENALTY FOR ENGINE IGNITION WINDOW, LOOK ANGLE CONSTRAINT, RANGE CONSTRAINT AND SINK RATE CONSTRAINT.	<b>243 ft/sec</b>
*FOR TERMINAL CONDITIONS OF 200ft. ALTITUDE, 10 ft/sec SPEED, 10° FLIGHT PATH ANGLE.	

Fig. 4.21 ΔV performance summary\* (landing from Hohmann descent).

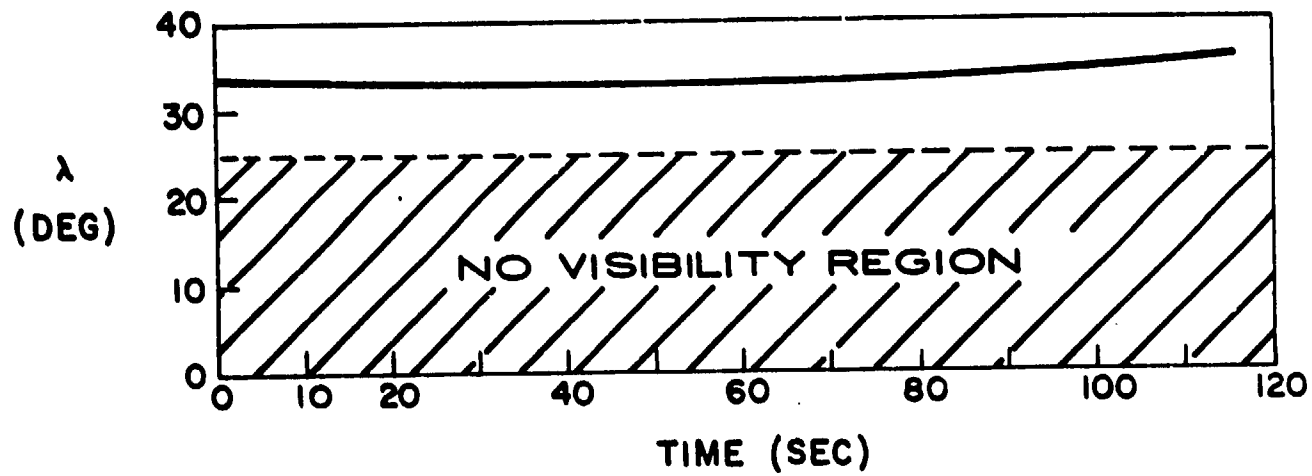
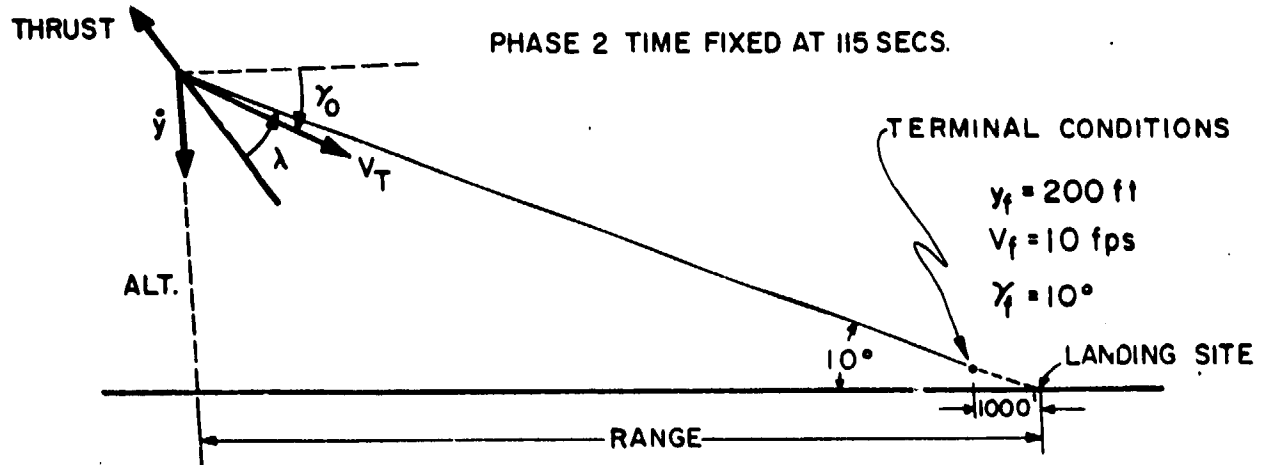


Fig. 4.22 Look angle versus time, for visibility phase.



$\lambda_{min}$ (deg)	$\Delta V$ (fps)	THRUST (lbs)	ALT. (ft)	$\dot{y}$ (fps)	$V_T$ (fps)	RANGE (n.m.)	$\gamma_0$ (deg)
26.5	5978	5887	14,125	-227	1018	9.7	12.9
28.4	6000	5500	12,960	-208	929	8.8	13
30	6019	5165	11,940	-190	851	8.1	13
32	6038	4874	11,040	-175	780	7.4	13
34	6057	4619	10,230	-162	717	6.8	13
36	6076	4395	9,500	-149	659	6.2	13

Fig. 4.23  $\Delta V$  requirements for phase 2 constraints.

in a look angle of  $32^\circ$ , i. e.,  $7^\circ$  above the lower edge of the LEM window. The visibility angle and landing site monitoring during phase 2 are described in detail in Section 4.4.4.

The  $\Delta V$  penalty associated with various values of the minimum look angle,  $\lambda_{\text{MIN}}$ , during the second phase is summarized in Fig. 4.23. Approximately 100 ft/sec additional  $\Delta V$  is required to increase the minimum visibility angle from  $26^\circ$  to  $36^\circ$  if the phase 2 maneuver time is held fixed at 115 seconds. With reference to Fig. 4.23, it can be seen that as the minimum look angle,  $\lambda_{\text{MIN}}$ , is increased, the phase 2 initial altitude, vertical velocity, and range to go all decrease, thus lower thrust levels are commanded. These are desirable effects for astronaut monitoring, but require  $\Delta V$  penalties that make them doubtful.

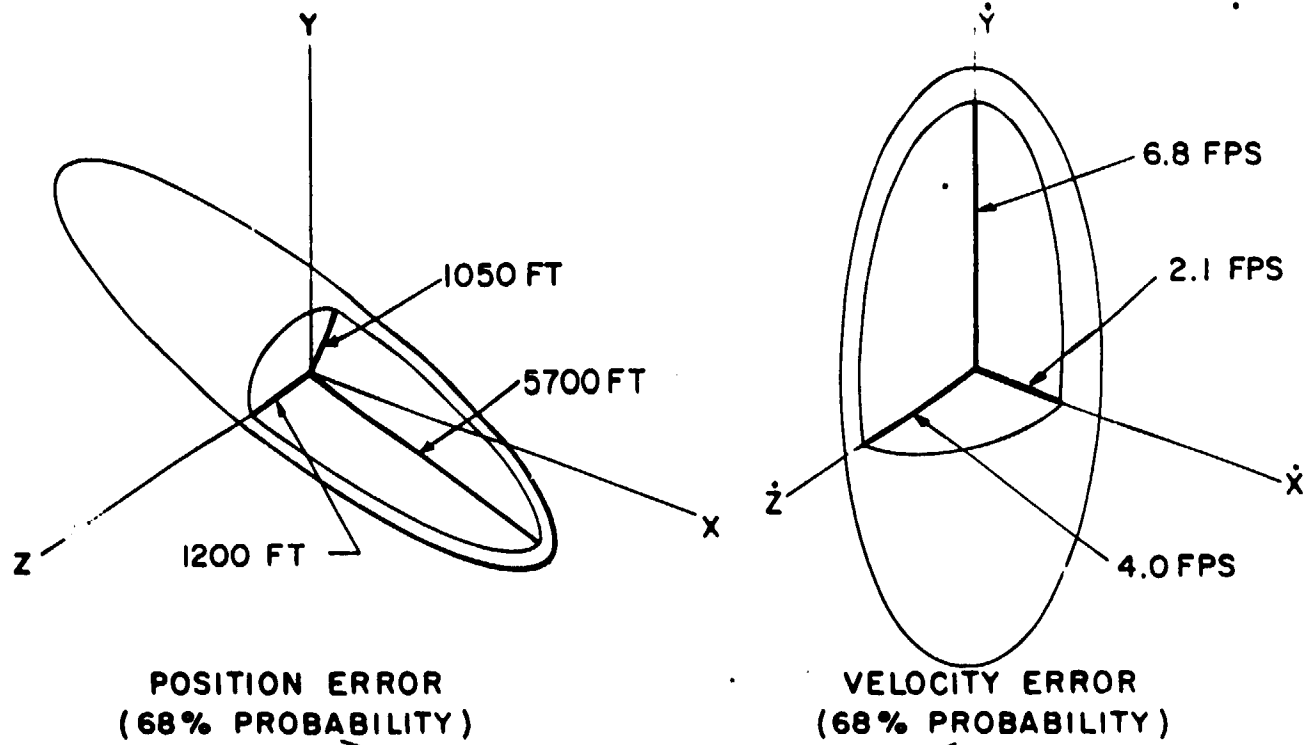
It should be noted that the landing maneuver characteristics presented in this section assumed a point mass LEM vehicle and no LEM attitude or throttle system dynamics were considered. The results of current guidance equation simulations which include the LEM vehicle dynamics will be presented in a future report.

#### 4.4 Primary G&N System Operation and Performance

##### 4.4.1 G&N System Performance for Landing Maneuvers From Hohmann Descents

The combined orbit navigation and descent injection uncertainties at the perilune, or engine ignition point of the landing maneuver, have been summarized in Fig. 3.28. These uncertainties were propagated down a typical powered landing maneuver from the Hohmann descent trajectory, and Figs. 4.24 through 4.26 illustrate the combined uncertainties for various points along the landing trajectory. The error volumes shown in Fig. 4.24 are the result of the propagation of the initial uncertainties at engine ignition, combined with the inertial instrument uncertainties resulting from the powered landing maneuver to this point. Figure 4.24 represents the total uncertainties at a point 150 seconds after the start of the landing maneuver. Figure 4.25

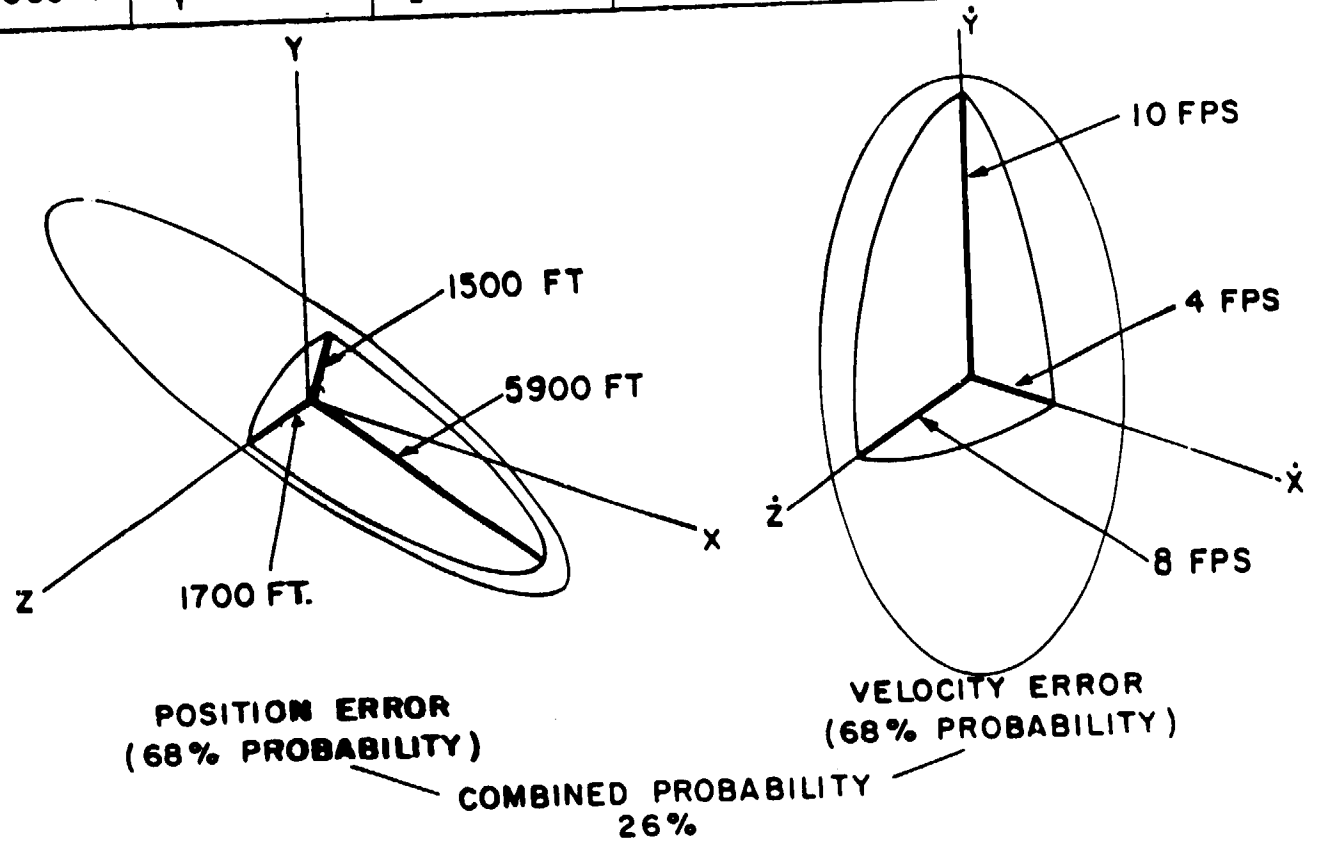
$\sigma_x = 3045$ ft	$\sigma_y = 625$ ft	$\sigma_z = 650$ ft	$\sigma_{\dot{x}} = 1.1$ fps	$\sigma_{\dot{y}} = 3.6$ fps	$\sigma_{\dot{z}} = 2.1$ fps
----------------------	---------------------	---------------------	------------------------------	------------------------------	------------------------------



COMBINED PROBABILITY  
26%

Fig. 4.24 Error volume after 150 seconds in landing trajectory following Hohmann descent.

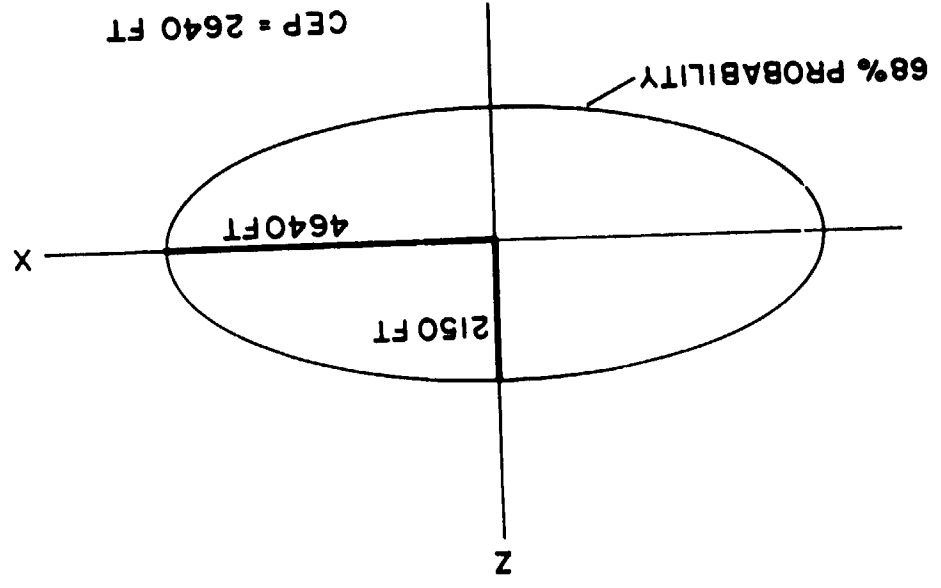
$\sigma_x = 3060$ ft	$\sigma_y = 1000$ ft	$\sigma_z = 895$ ft	$\sigma_{\dot{x}} = 2.1$ fps	$\sigma_{\dot{y}} = 5.4$ fps	$\sigma_{\dot{z}} = 4.3$ fps
----------------------	----------------------	---------------------	------------------------------	------------------------------	------------------------------



200

Fig. 4.25 Error volume after 300 seconds in landing trajectory following Hohmann descent.

$\sigma_x = 3060'$	$\sigma_z = 1420'$
--------------------	--------------------



(MODEL 2)

201

Fig. 4.26 Landing footprint for Hohmann descent trajectory.

illustrates the position and velocity uncertainties at a point 300 seconds after the start of the landing maneuver, and represents the combined uncertainties prior to the pitch-up maneuver initiating the second phase of the landing maneuver. Figure 4.26 illustrates the uncertainties in the horizontal plane (XZ directions) at the hover condition terminating the second phase of the landing maneuver. It is assumed that the landing radar data eliminates the other four uncertainties, i. e., the altitude and the three velocities. The position uncertainties of the hover point illustrated in Fig. 4.26 represent a landing CEP of 2640 feet.

The design objective of the LEM primary G&N system is a 3000 foot CEP landing capability (Chapter 1). In specifying a CEP performance specification, five important factors must be defined. These factors are summarized in Fig. 4.27 and will be described for the performance illustrated in Fig. 4.26. The initial condition uncertainties for the example of Fig. 4.26 were the combined orbital navigation uncertainties of Model 2 (Table 2.4) and the Hohmann descent injection maneuver uncertainties listed in Fig. 3.27. These combined uncertainties at the perilune of the Hohmann descent trajectory are illustrated in Fig. 3.28. The second factor listed in Fig. 4.27 is the type of orbital descent trajectory, the Hohmann descent in this case. The third factor listed in Fig. 4.27 is the G&N operating procedure specifically dealing with the IMU alignment schedule. As stated in Section 3.6, the IMU was aligned 15 minutes before descent injection. In order to achieve a one-half mile CEP, it is necessary to re-align the IMU (through the fine alignment procedure of Section 1.3) within 15 minutes of the perilune or ignition point of the landing maneuver. The IMU performance during the landing maneuver is the fourth factor listed in Fig. 4.27 and will be discussed later. The fifth factor of Fig. 4.27 involves trajectory updating, either during the coast phase of the descent trajectory or during the powered landing maneuver by means of the landing radar or visual updating. The CEP performance illustrated in Fig. 4.26

1. INITIAL CONDITION UNCERTAINTIES
  - CM ORBIT UNCERTAINTY
  - DESCENT ORBIT INJECTION UNCERTAINTIES
2. DESCENT ORBIT TRAJECTORY
  - EQUIPERIOD
  - HOHMANN
3. G & N OPERATING RESTRICTIONS
  - LAST IMU ALIGNMENT TIME
4. IMU PERFORMANCE DURING POWERED LANDING MANEUVER
5. TRAJECTORY UP-DATING
  - MID-COURSE PRIOR TO IGNITION
  - TERMINAL HOVER - RADAR AND VISUAL.

Fig. 4.27 Landing maneuver C.E.P. factors.

UNCERTAINTIES AT LANDING

	ERROR SOURCES	X (ft)	Z (ft)
1	Initial orbit uncertainty (Model 2)	2795	652
2	Injection uncertainties 0.8 mr misalignment 15 min drift interval	1050	60
3	IMU landing man. errors 0.8 mr misalignment 15 min drift interval	622	1260
	R. S. S.	3063	1420

CEP = 2640 ft

POSITION (1000's of feet)

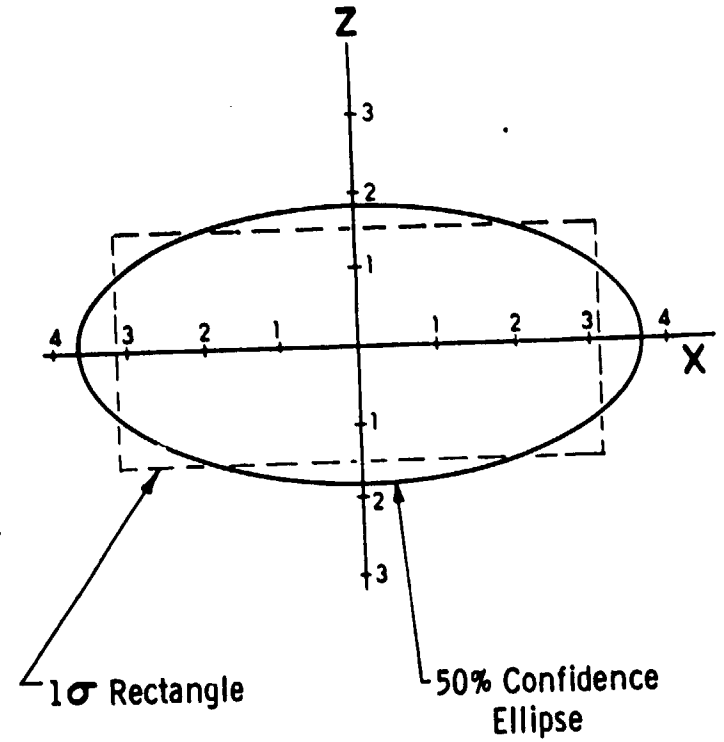


Fig. 4.28 Hover point dispersion for landing from Hohmann descent conditions.

432sec Landing Maneuver No. 100816

IMU ERROR SOURCE	POSITION			VELOCITY		
	Range (ft)	Track (ft)	Alt (ft)	Range (fps)	Track (fps)	Alt (fps)
1. Platform Misalignment (0.82 mr)	61	1100	1142	1.0	4.6	5.0
2. Accelerometer Bias (0.2 cm/sec <sup>2</sup> )	594	605	620	2.8	2.8	2.8
3. Accelerometer Scale Factor (100ppm)	127		133			
4. Accelerometer Misalignment (0.1 mr)	25					
5. Gyro Fixed Drift (0.15 deg/hr)	28	130	142	0.3	0.8	0.8
6. Gyro Mass Unbalance (0.15 deg/hr/g)	13	10	64		0.2	0.3
R. S. S. of All Error Sources	622	1260	1321	3.0	5.4	5.9

Fig. 4.29 IMU lunar landing maneuver uncertainties: Hohmann descent trajectory.

involves no trajectory updating prior to the ignition of the landing maneuver, and assumes no landing radar or visual updating in the XZ directions during the powered landing maneuver. It is assumed that the landing radar was effective in eliminating all uncertainties in the other components (altitude and three velocity components). Through the use of landing radar data, it is possible to improve the knowledge or estimate of the vehicle range and track positions to some degree. Improved or updated capability of this type, however, is not assumed in the CEP performance figures listed.

The final hover point dispersion illustrated in Fig. 4.26 is summarized in more detail in Fig. 4.28. In this figure, the initial orbital uncertainties of orbit navigation Model 2 were propagated independently to the landing point as listed under Item 1. The Hohmann injection maneuver uncertainties were likewise independently propagated to the landing point and listed as Item 2. The IMU landing maneuver performance, assuming that a final alignment was made 15 minutes prior to the engine ignition point, is summarized in Item 3. It can be seen from the three effects listed in Fig. 4.28 that the initial condition uncertainties are the major contributors to the final hover point uncertainty in the range or X direction, while the IMU performance uncertainties during the landing maneuver are the primary source of uncertainty in the track or Z direction. The IMU landing maneuver performance uncertainties are summarized in more detail in Fig. 4.29. In this figure, it can be seen, that the major sources of IMU uncertainties are due to initial misalignment and accelerometer biases. The initial misalignment of 0.82 mr was the result of the 15 minute drift between the alignment during the descent trajectory and the ignition point of the landing maneuver. This initial misalignment is the major contributor for the track and altitude position and velocity uncertainties. The effects of IMU drift during the landing maneuver are illustrated by Items 5 and 6 of Fig. 4.29, and can be seen to be negligible compared to the initial misalignment and accelerometer bias effects. From this

example, it can be seen that the IMU performance contribution to the overall CEP is a direct function of the alignment time prior to the start of the landing maneuver as listed under factor 3 of Fig. 4.27.

#### 4.4.2 G&N System Operation

As previously stated, the primary G&N operation during most of the first phase of the landing maneuver is a pure inertial mode of operation (as illustrated in Fig. 3.30). During the last portion of the first phase and throughout the second phase of the landing maneuver, a radar-inertial mode of operation is used to achieve the desired hover point conditions. This guidance configuration is illustrated in Fig. 4.30. The inertial portion (IMU, LGC, CDU) of this configuration is the same as that shown in Fig. 3.21. Altitude and velocity along the landing trajectory are measured by the landing radar and then compared with similar inertially computed parameters. These four inertial parameters are then updated on the basis of the landing radar data so that the desired terminal conditions can be achieved by explicit guidance commands from the current improved vehicle position and velocity conditions. The analysis and criteria for determining the points in the landing maneuver at which landing radar data is incorporated in the guidance system will be discussed in the following section. The trajectory parameters that are not directly updated by the landing radar are the horizontal position uncertainties relative to the landing site. The astronaut can monitor and change the landing site by some form of window display system and LGC display as indicated in Fig. 4.30. The operation of a landing site display system will be described in Section 4.4.4. The final hover and touch down maneuvers will be discussed in Section 4.6.

#### 4.4.3 Landing Radar Operation

The landing radar data is gradually introduced to the guidance system at some point in the landing trajectory at which it is equal to, or better than, the estimated trajectory parameters in the

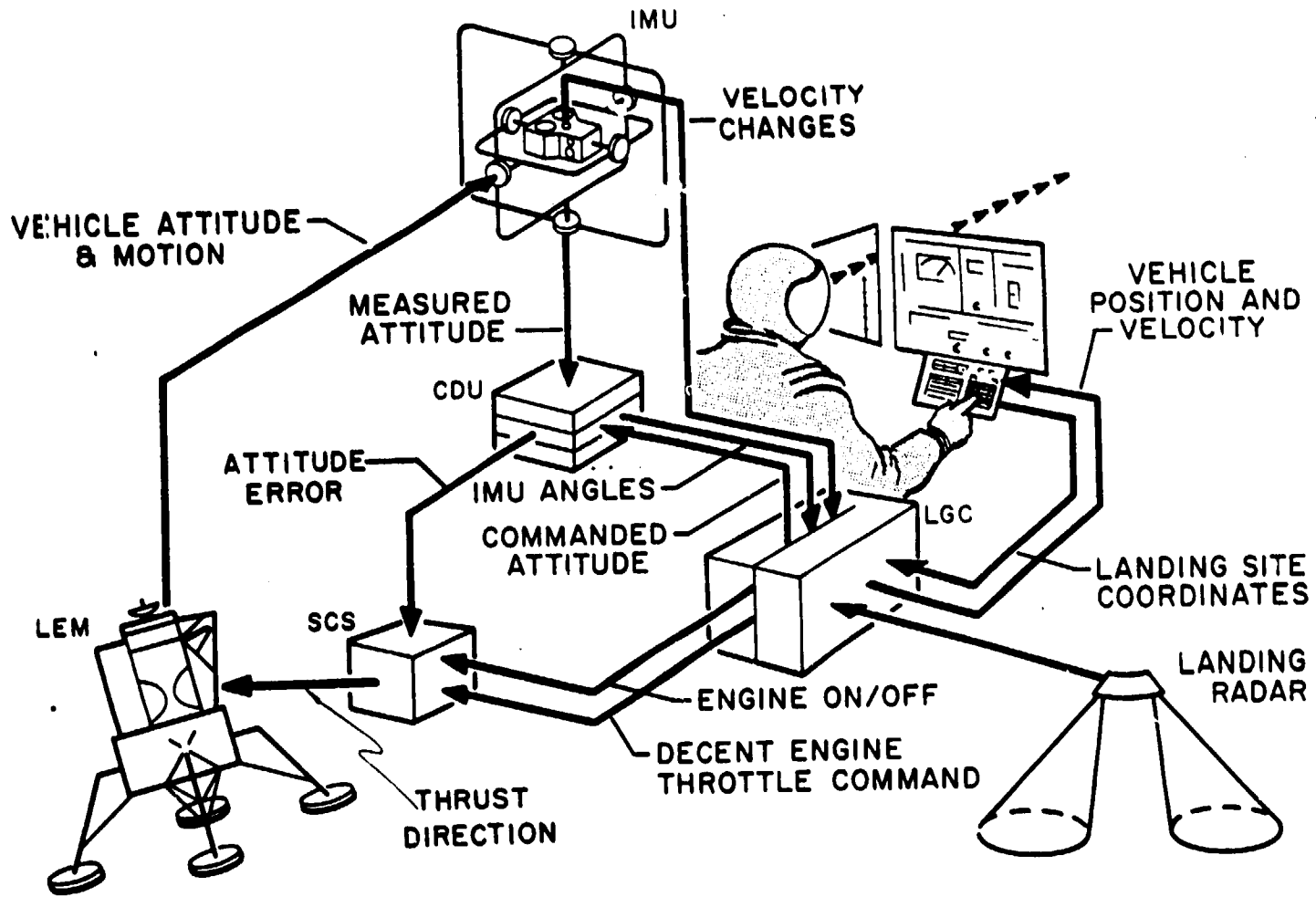


Fig. 4.30 Final landing phase maneuver control.

inertial system. The IMU and landing radar performance during the landing maneuver are compared in Figs. 4.31 through 4.34. The G&N system altitude uncertainty during the landing maneuver is illustrated in Fig. 4.31. From this figure it can be seen that the three sigma IMU uncertainty, resulting from the combined uncertainties of orbit navigation Model 2, injection uncertainties, and IMU landing maneuver performance, increases along the trajectory as illustrated in time from right to left in Fig. 4.31. The IMU performance curve of Fig. 4.31 was determined from the altitude term of the correlation matrix at various points along the landing trajectory, and multiplied by the appropriate factor in order to determine the three sigma condition for this particular parameter. The landing radar performance is also plotted in this figure and improves along the trajectory as the altitude decreases. The major error in landing radar altitude data is due to lunar terrain uncertainties, or slopes, relative to the final landing site. The case illustrated in Fig. 4.31 is the result of an unknown 3 degree terrain slope from present position to the landing site. This was considered to be a three sigma condition, and was the dominant factor in the landing radar uncertainty compared with the radar performance accuracy and antenna direction uncertainties. As indicated in Fig. 4.31, the uncertainties of the radar and IMU cross at a point 305 seconds after the start of the landing maneuver. It can be seen that this point is prior to the initiation of the second phase of the landing maneuver and occurs at the altitude, range and velocity conditions listed in Fig. 4.31. On the basis of the result shown in this figure, the landing radar altitude information would be mixed with inertial data at the crossover point with a weighting factor which is a function of time. This weighting factor would be designed such that the radar data would become more heavily weighted and would reach a maximum value at some point in Phase 2 where the landing radar altitude data is superior to IMU performance. The landing radar updating procedure is incorporated in the

CONFIDENTIAL

explicit guidance technique. This technique accepts landing radar data at any point except within a 10 to 20 second interval prior to the initiation of the second landing maneuver phase.

A comparison of the forward velocity uncertainty ( $\Delta\dot{X}$ ) is shown in Fig. 4.32 for the IMU and landing radar. The IMU velocity uncertainty in this figure was determined from the correlation matrix velocity terms multiplied by the appropriate factor for determining three sigma operation for various points along the landing maneuver (Appendix A). It can be seen in this figure that the IMU and landing radar performance crossover point is during the second phase of the lunar landing maneuver. The radar performance is limited by the terrain fluctuation error for a one second smoothing time of the landing radar doppler networks. Altitude velocity and track velocity uncertainties are illustrated in Figs. 4.33 and 4.34 respectively. The three sigma IMU velocity uncertainties in these two directions are larger than the forward velocity uncertainty of Fig. 4.32 because of the initial misalignment effect as illustrated in Fig. 4.29. The landing radar performance for the Y and Z components is limited by the uncertainty of the landing radar antenna angular alignment relative to the IMU. The alignment accuracy between these two units is unknown at the present time since the landing radar antenna will be mounted on the descent stage and will be used during a powered maneuver that will result in structure misalignment and vibration that has not been fully determined. The landing radar performance illustrated in Figs. 4.33 and 4.34 assumes 20 and 40 mr landing radar antenna misalignments relative to the IMU coordinate frame in which the doppler velocities are resolved into the horizontal, vertical and track directions. The performance crossover points illustrated in these figures indicate that the landing radar velocity data in these two directions will be mixed with the inertial data during the second phase of the landing maneuver at approximately the same time as the forward velocity uncertainty of Fig. 4.32.

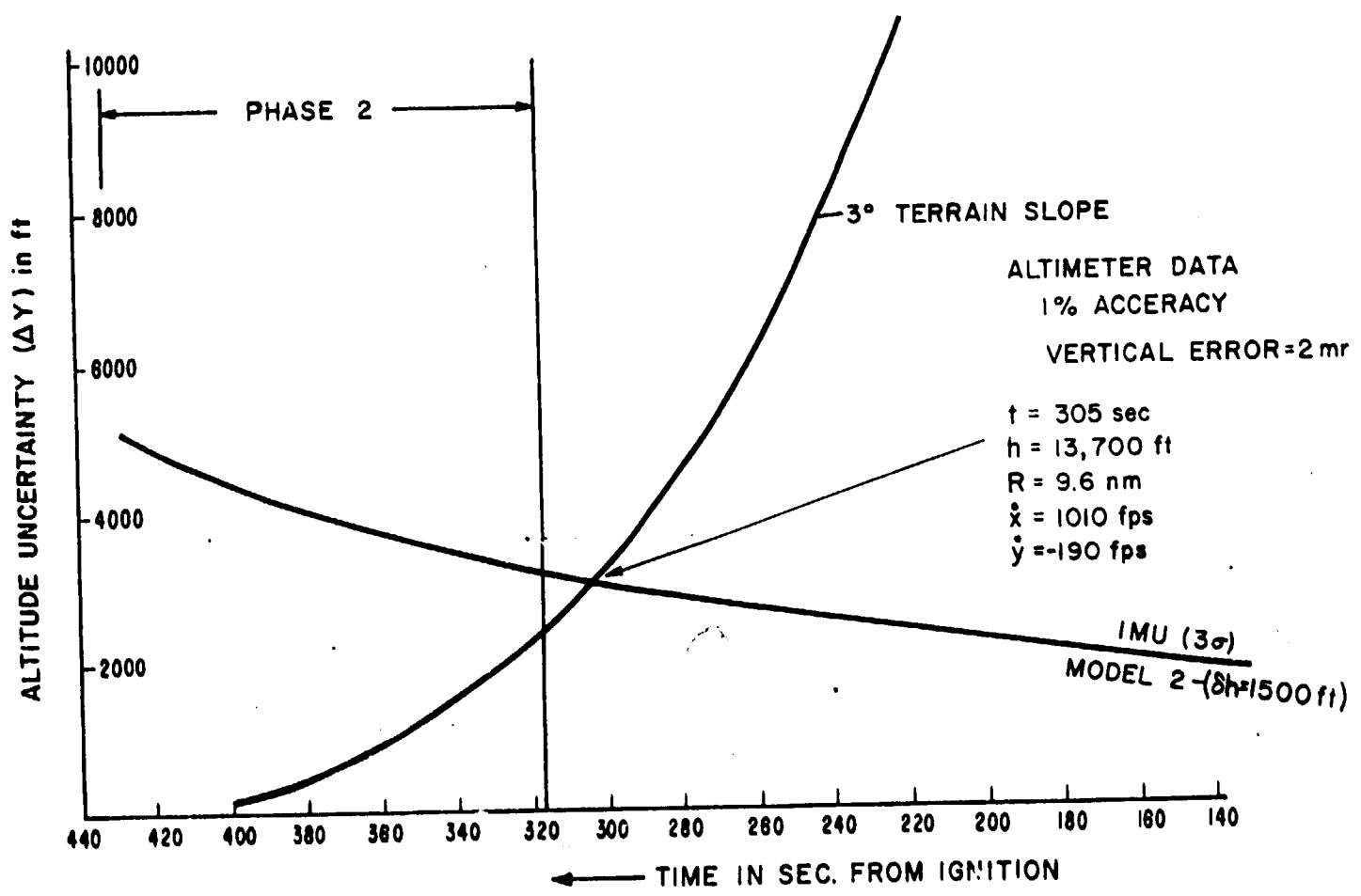


Fig. 4.31 IMU and altimeter error for landing maneuver from Hohmann descent conditions.

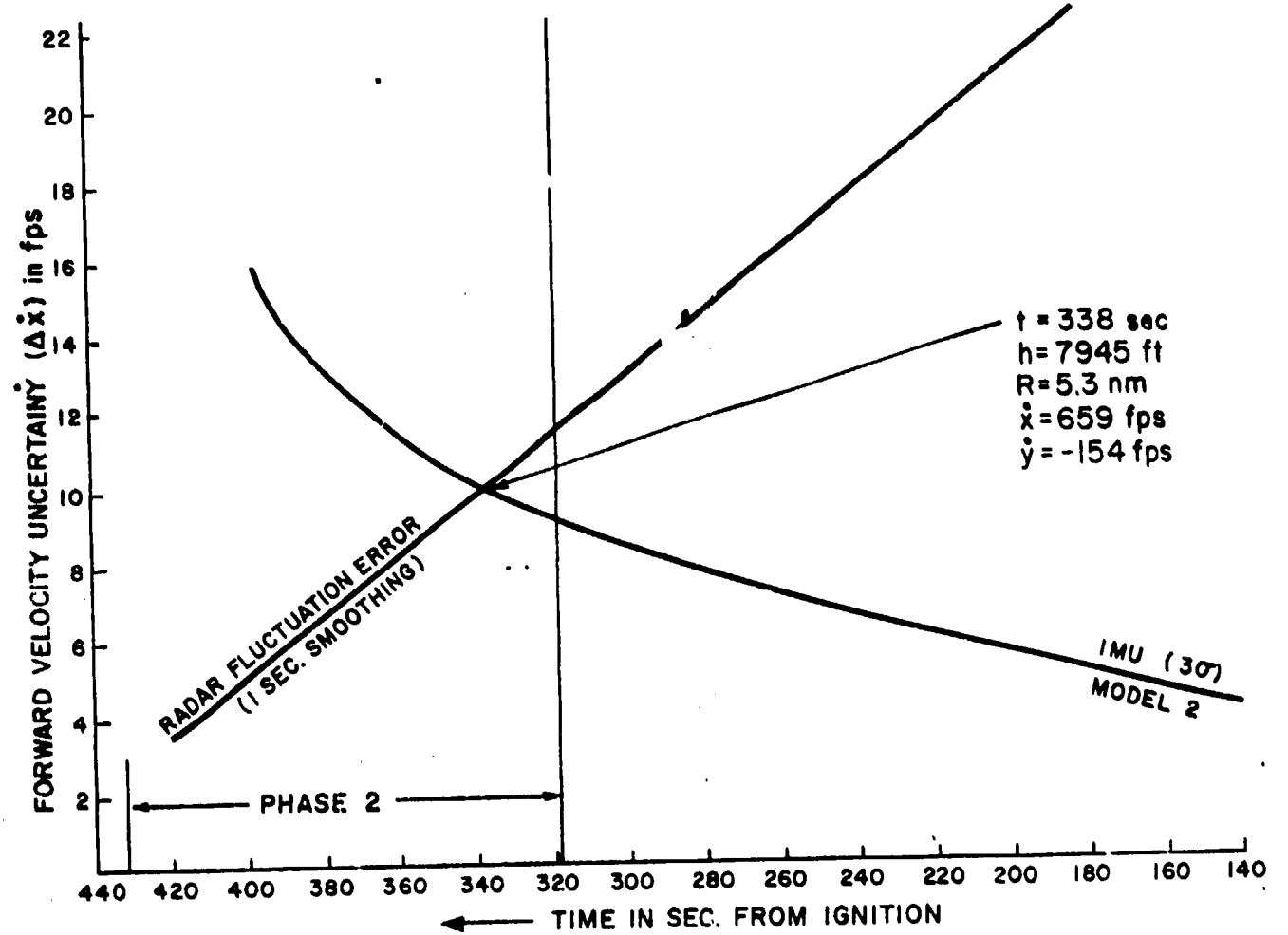


Fig. 4.32 IMU-Doppler  $\dot{X}$  errors for landing maneuver from Hohmann descent conditions.

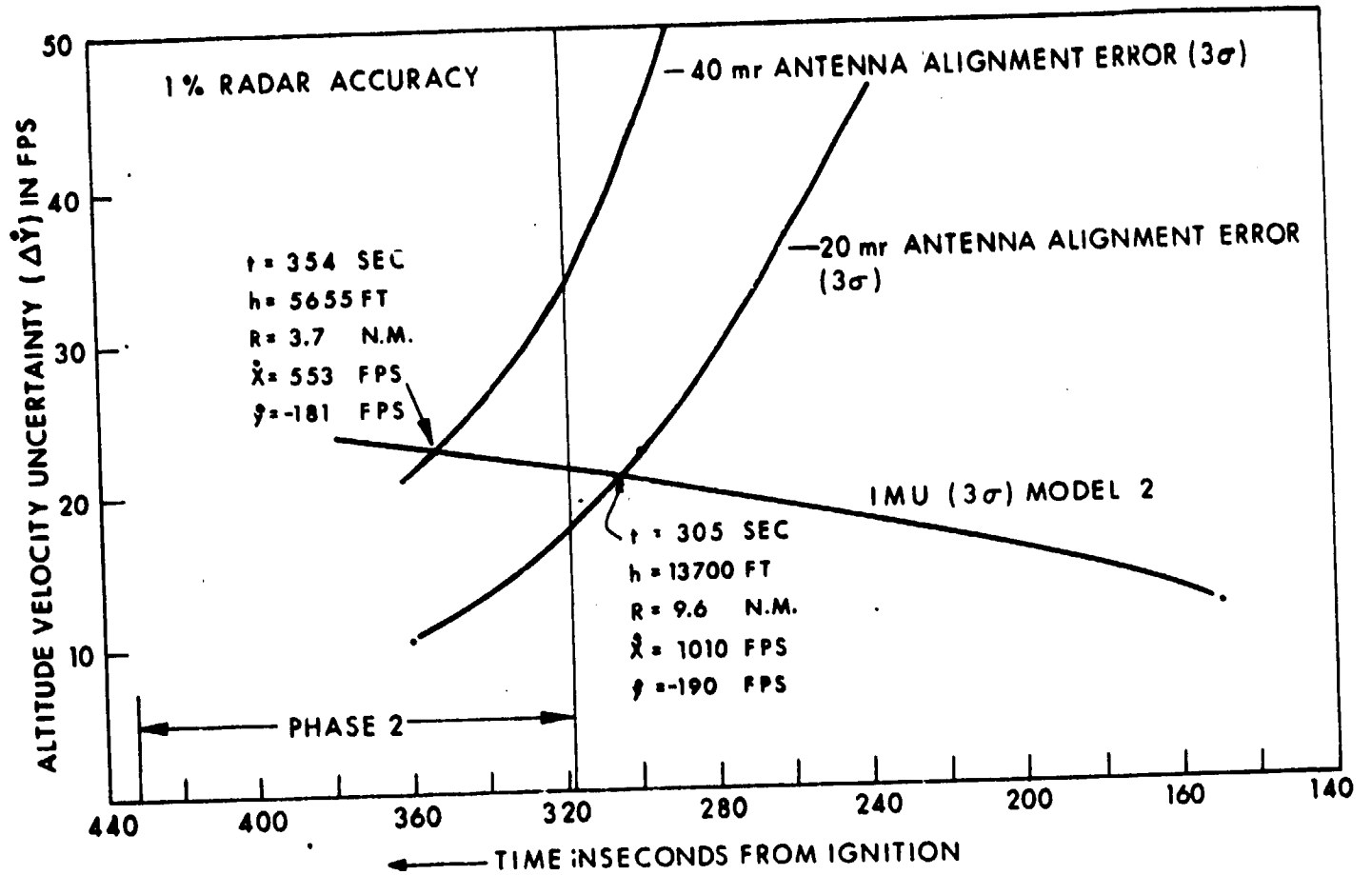


Fig. 4.33 IMU - Doppler radar  $\dot{y}$  errors for landing maneuver from Hohmann descent conditions.

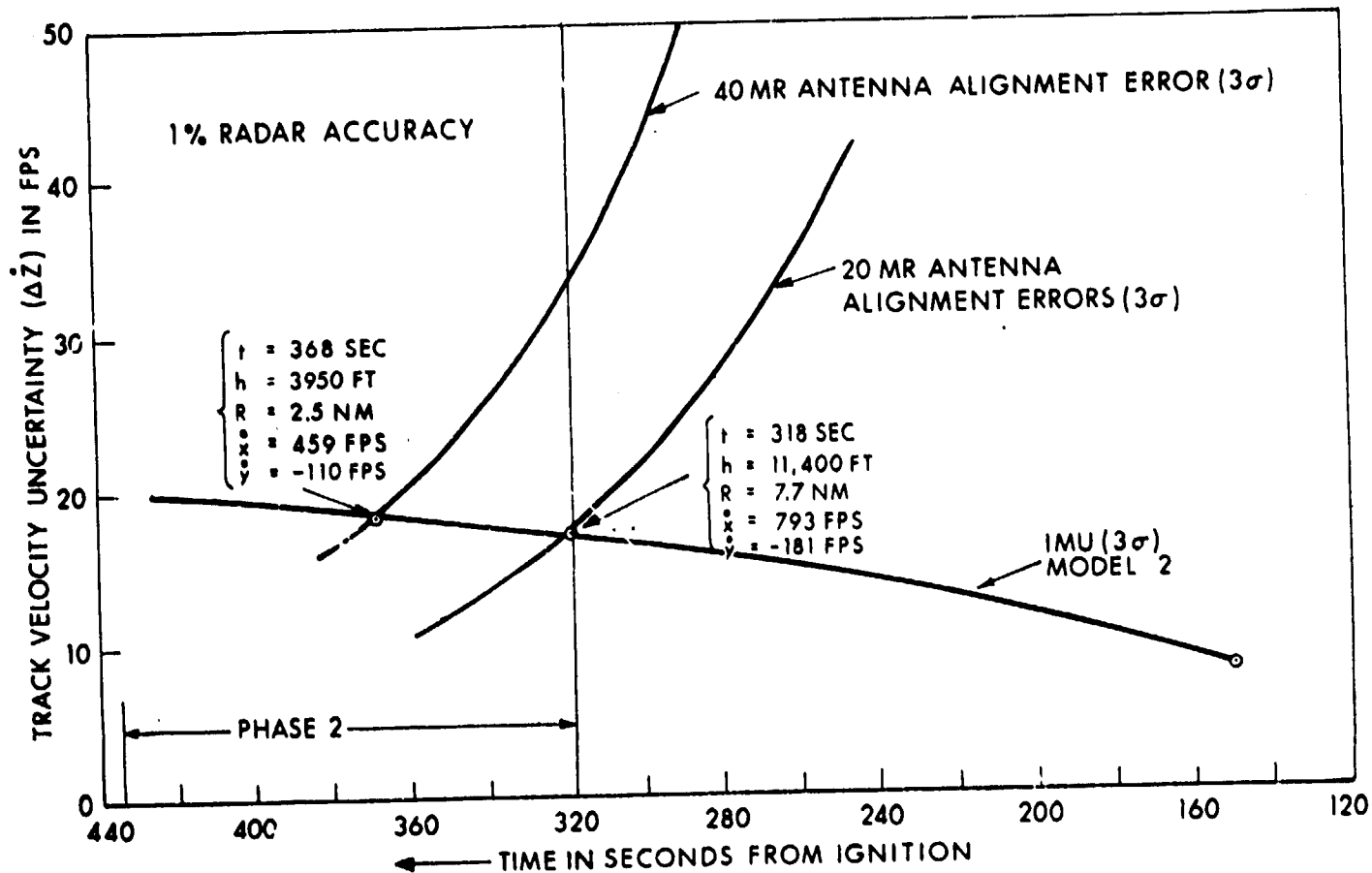


Fig. 4.34 IMU - Doppler radar  $\dot{Z}$  errors for landing maneuver from Hohmann descent conditions.

Error analyses similar to those presented in Figs. 4. 31 to 4. 34 have indicated that the first component used to update the inertial system in the landing radar will be the altitude data starting at altitudes of 15,000 to 20,000 feet, while the velocity components will be updated during the second phase of the maneuver at altitudes ranging from 7000 to 10,000 feet. A simulation involving vehicle and guidance system dynamics is currently in progress for the purpose of determining the most satisfactory manner to phase in the landing radar data with the explicit guidance concept. This simulation will be presented in a future report.

#### 4. 4. 4 Landing Site Display Operation

The primary purpose of the near constant attitude in the second phase of the landing maneuver was to enable the astronaut to visibly check the landing site area. The current LEM visibility limits are illustrated in Fig. 4. 35 in which the center of the coordinate system is the normal eye position of the astronaut, parallel to the vehicle Z axis. The normal positions of the lunar horizon and landing site locations during the constant attitude phase are indicated in this figure. The landing site locations typically appear between 5 and 7 degrees above the lower edge of the LEM window during this maneuver. The astronaut will make a visible check of the landing site area to which the G&N system is controlling the trajectory and will have the capability to change this landing site if it is undesirable. Landing site changes during the near constant attitude phase are of the gross type (involving several thousand feet) compared with the translation type changes made when hovering.

Several landing site display schemes are currently under investigation. One possible way involves a fixed line on the LEM window and is illustrated in Fig. 4. 36. Due to the close proximity of the astronaut's head relative to the window, current LEM window design may require an external reticle fixture for this concept. The basic requirements for the operation of this scheme are:

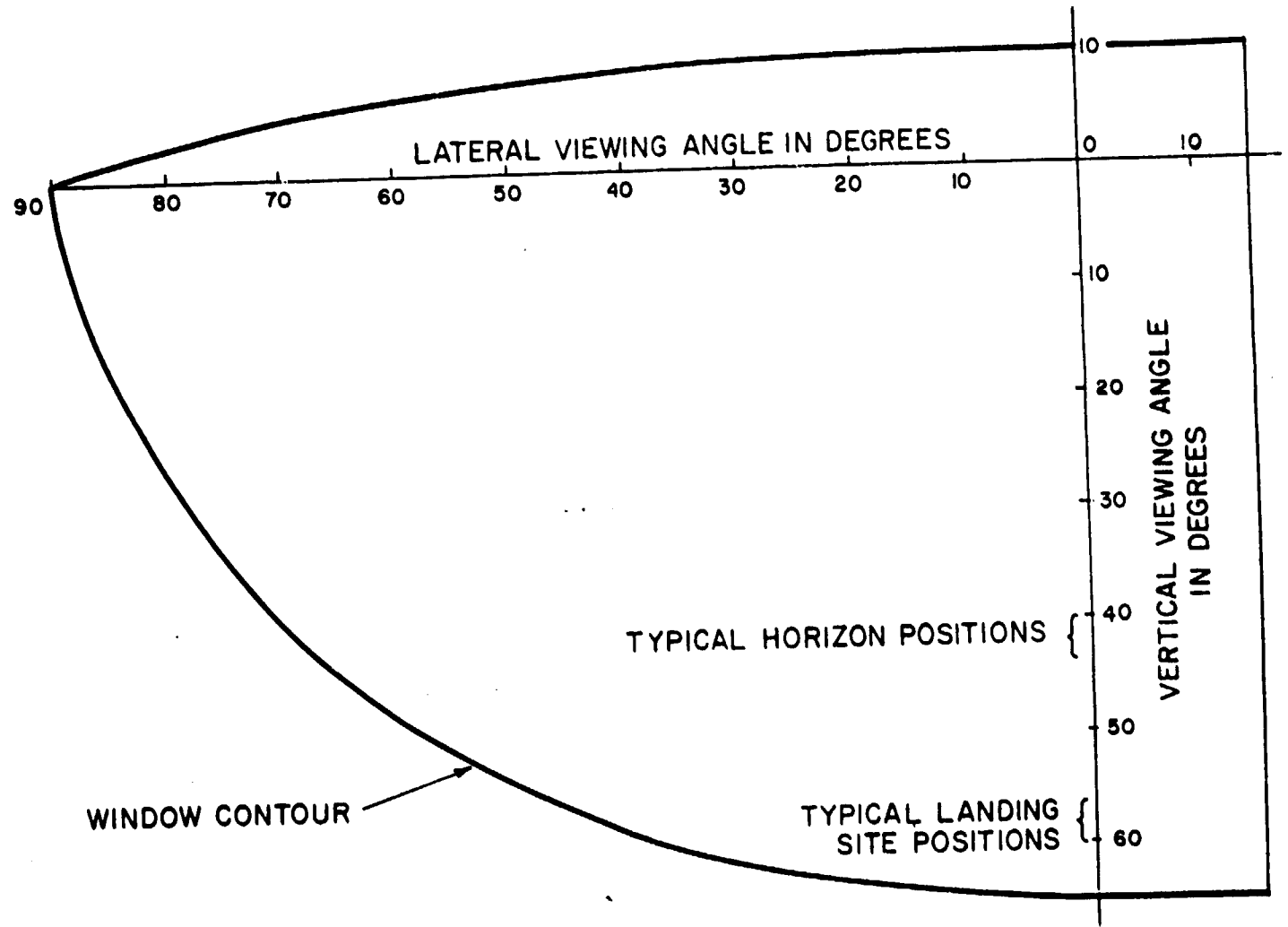
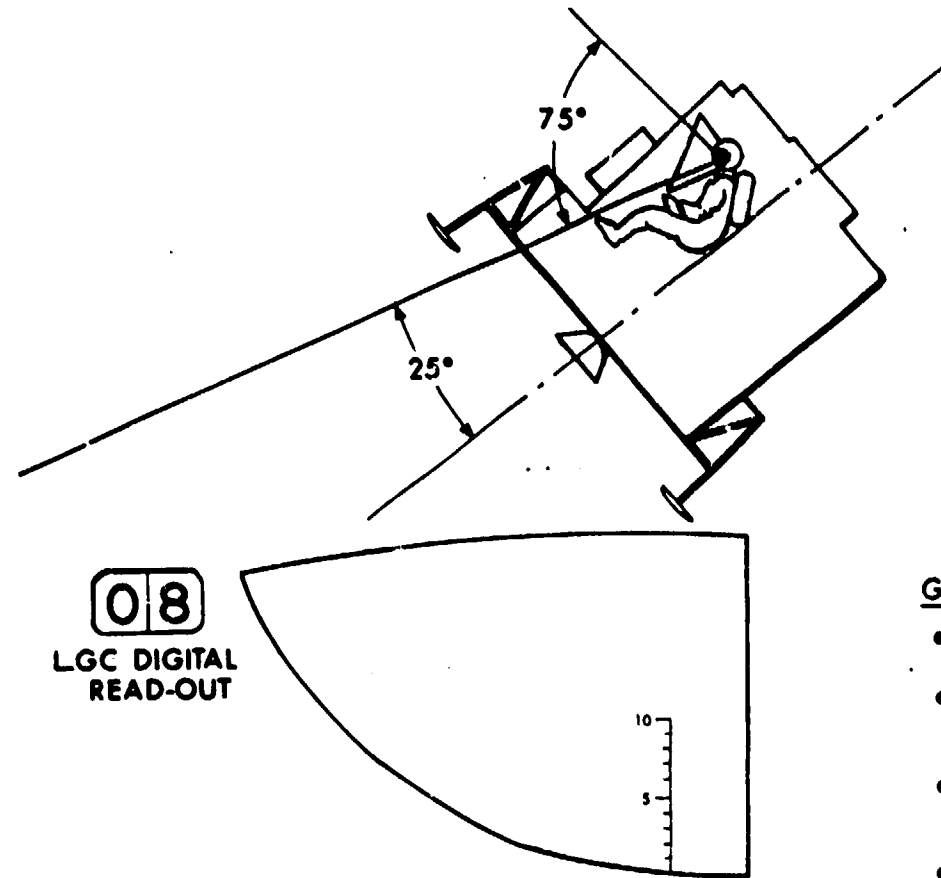


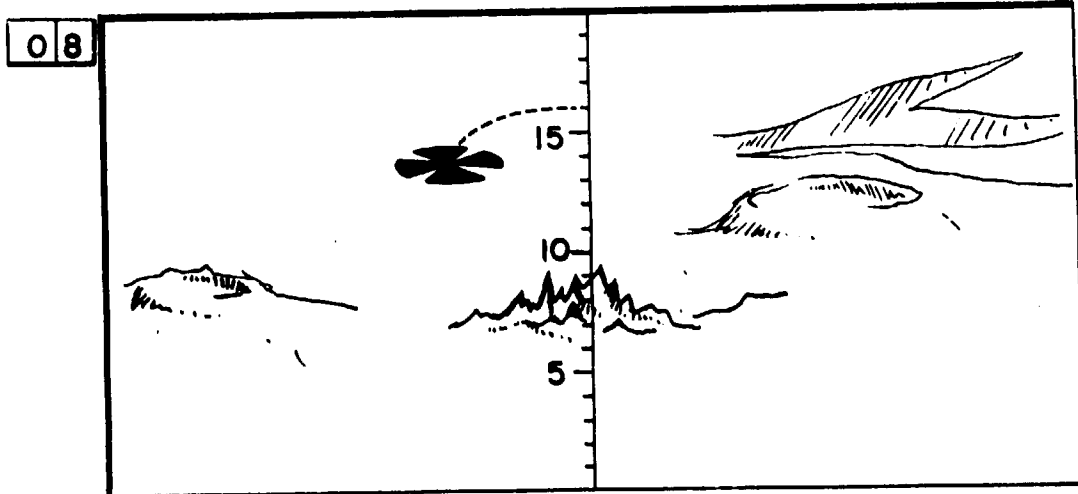
Fig. 4. 35 LEM visibility angle limits.



#### GENERAL REQUIREMENTS

- FIXED RETICLE LINE ON WINDOW
- EYE REGISTER DEVICE
- LGC 2 DIGIT READ-OUT NEAR WINDOW
- READ-OUT SLEWING SWITCH
- X AXIS MANUAL ATTITUDE CONTROL MODE OF SCS.

Fig. 4.36 Fixed reticle concept for terminal lunar landing maneuver.



**PROCEDURE:**

1. CHECK COMPUTED LANDING SITE (08) ON FIXED RETICLE
2. CHOOSE NEW LANDING SITE AND ACTIVATE LGC SITE CHANGE MODE.
3. CHANGE X AXIS ATTITUDE UNTIL NEW SITE IS ON RETICLE
4. SLEW READ-OUT TO CORRESPOND TO RETICLE NUMBER (16)
5. ACTIVATE LGC MARK—RETURNS TO AUTOMATIC MODE
6. MONITOR NEW SITE AND LGC COMPUTED SITE ANGLE
7. REPEAT PROCEDURE IF REQUIRED AS RANGE DECREASES

Fig. 4.37 Fixed reticle concept - procedure for landing site change.

(1) some type of fixed reticle, (2) an eye register device which can position the astronaut's eye within some tolerance, (3) a two digit computer read-out near the window, (4) a read-out slewing switch, and (5) a way of rotating the LEM about its thrust or X axis. The operation of a landing site display scheme of this type is summarized in Fig. 4.37. During the second phase of the landing maneuver, the vehicle attitude about the LEM thrust axis is controlled by the G&N system such that the fixed reticle lies in the landing trajectory plane. The landing site to which the G&N system is controlling the trajectory, therefore, lies on this line, and the LGC displays the coordinates of the site to the astronaut by a two digit read-out which is referenced to markings on the reticle line. This procedure assumes that the astronaut's eye has been positioned by the eye register device. If the astronaut wishes to choose a landing site other than that indicated ("08" of Fig. 4.37), he rotates the vehicle about the thrust axis until the reticle line intersects the desired landing site. He then slews the two digit read-out to correspond to the number on the reticle over the desired landing site. When these conditions are achieved, the astronaut sends a discrete "mark" signal to the LGC from the D&C keyboard which computes a new line of sight angle and range components to the landing site from the knowledge of the two digit read-out setting, the vehicle attitude relative to the IMU, and the knowledge of the altitude and velocity from the updated inertial system. The explicit guidance system then uses these new landing site coordinates as the desired boundary conditions, and alters the trajectory to achieve a hover point condition over the selected landing site. The astronaut repeats the monitoring of the landing site by this same procedure, and can continue making corrections up to a point approximately 20 seconds from the end of the constant attitude maneuver. Other visual monitoring schemes, involving more elaborate reticle patterns and reduced maneuvers about the thrust axis are under consideration. The basic objective of all such schemes, however, is to provide data to the LGC so that a

[REDACTED]

line of sight angle to the landing site relative to the IMU can be computed during the constant attitude phase of the landing maneuver. After achieving hover conditions, a final landing radar updating of the inertial system is made and the terminal descent and touchdown maneuver initiated. This terminal maneuver will be discussed in Section 4.6.

#### 4.5 Landing Maneuvers from Equal Period Descents

##### 4.5.1 Typical Landing Maneuver Trajectories

Landing maneuvers from equal period descent trajectories employ the same guidance concept as outlined in Section 4.2. A typical landing maneuver trajectory and thrust profile is summarized in Figs. 4.38 through 4.41. As illustrated in Chapter 3, the major difference in the initial conditions for the landing maneuver from equal period and Hohmann descent trajectories is in the initial velocity magnitude, the equal period trajectory being about 90 ft/sec greater than that for the Hohmann descent. The landing maneuvers are, therefore, very similar as can be seen by comparing Figs. 4.38 through 4.41 to Figs. 4.15 through 4.23. The first phase of the landing maneuver from equal period descent conditions is illustrated in Fig. 4.38. The second phase of the landing maneuver was chosen to be identical to that of the Hohmann landing maneuver of Fig. 4.16, as illustrated in Fig. 4.39. The boundary conditions for the first phase of the landing maneuver in both cases, therefore, are identical. The thrust magnitude and thrust angle profiles for the equal period landing maneuver are shown in Figs. 4.40 and 4.41, respectively.

##### 4.5.2 Primary G&N Performance

The combined initial condition and IMU instrument uncertainties for the landing maneuver of Section 4.5.1 are illustrated in Figs. 4.42 through 4.50. Figures 4.42 and 4.43 illustrate the position and velocity error volumes at a point 150 seconds after landing maneuver ignition for initial conditions represented by the perilune

ORIGINAL PAGE IS  
OF POOR QUALITY

221

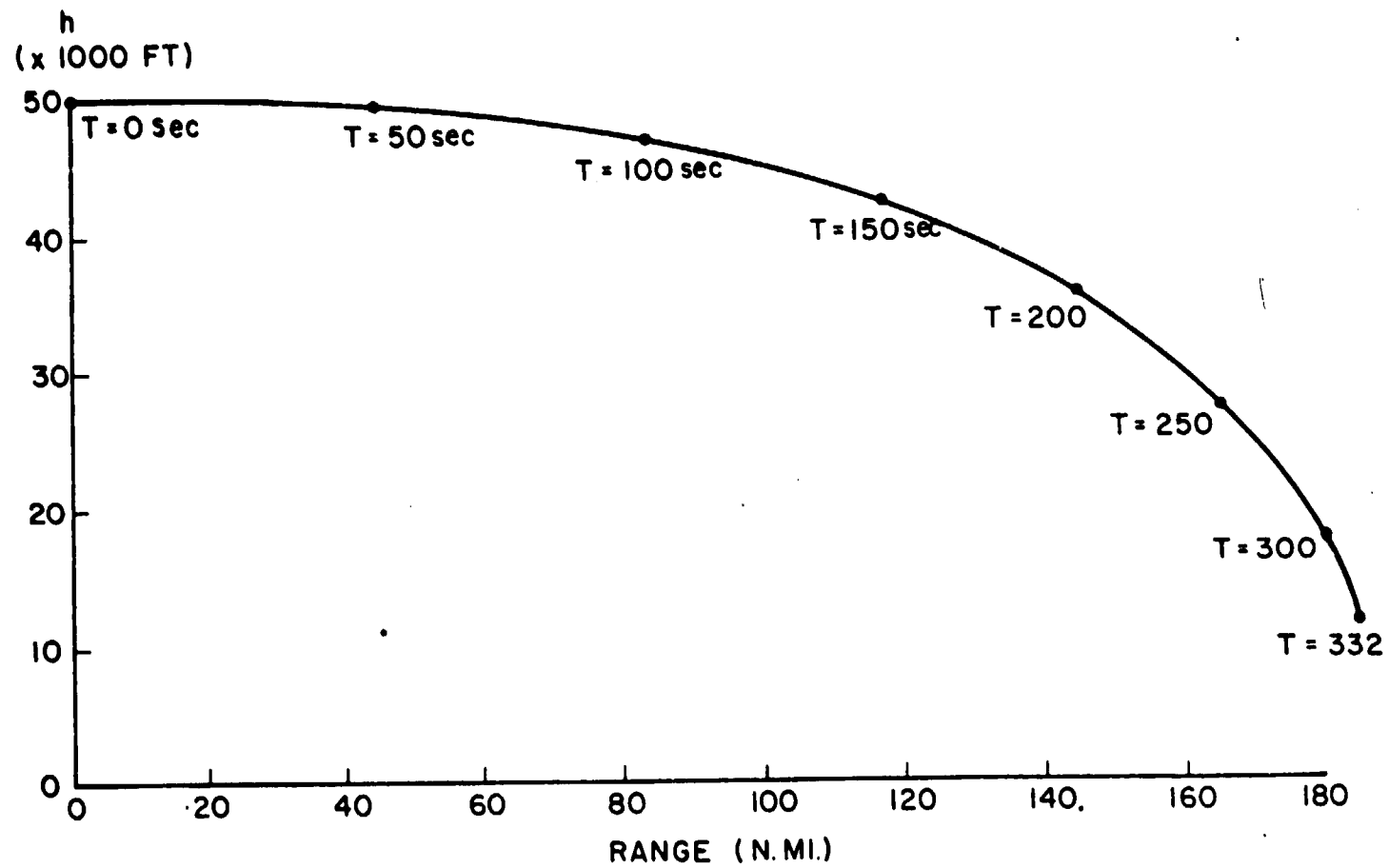


Fig. 4.38 Lunar landing trajectory phase 1.



929

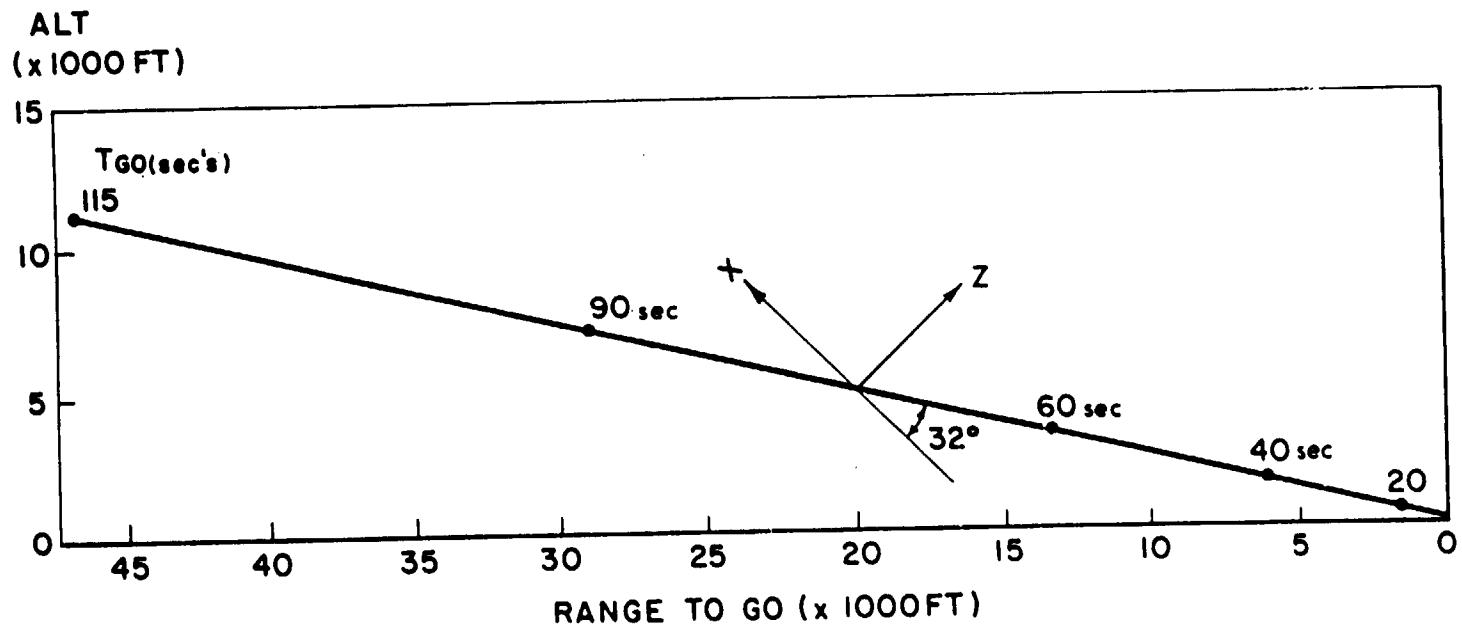


Fig. 4.39 Lunar landing trajectory phase 2.

ORIGINAL PAGE IS  
OF POOR QUALITY

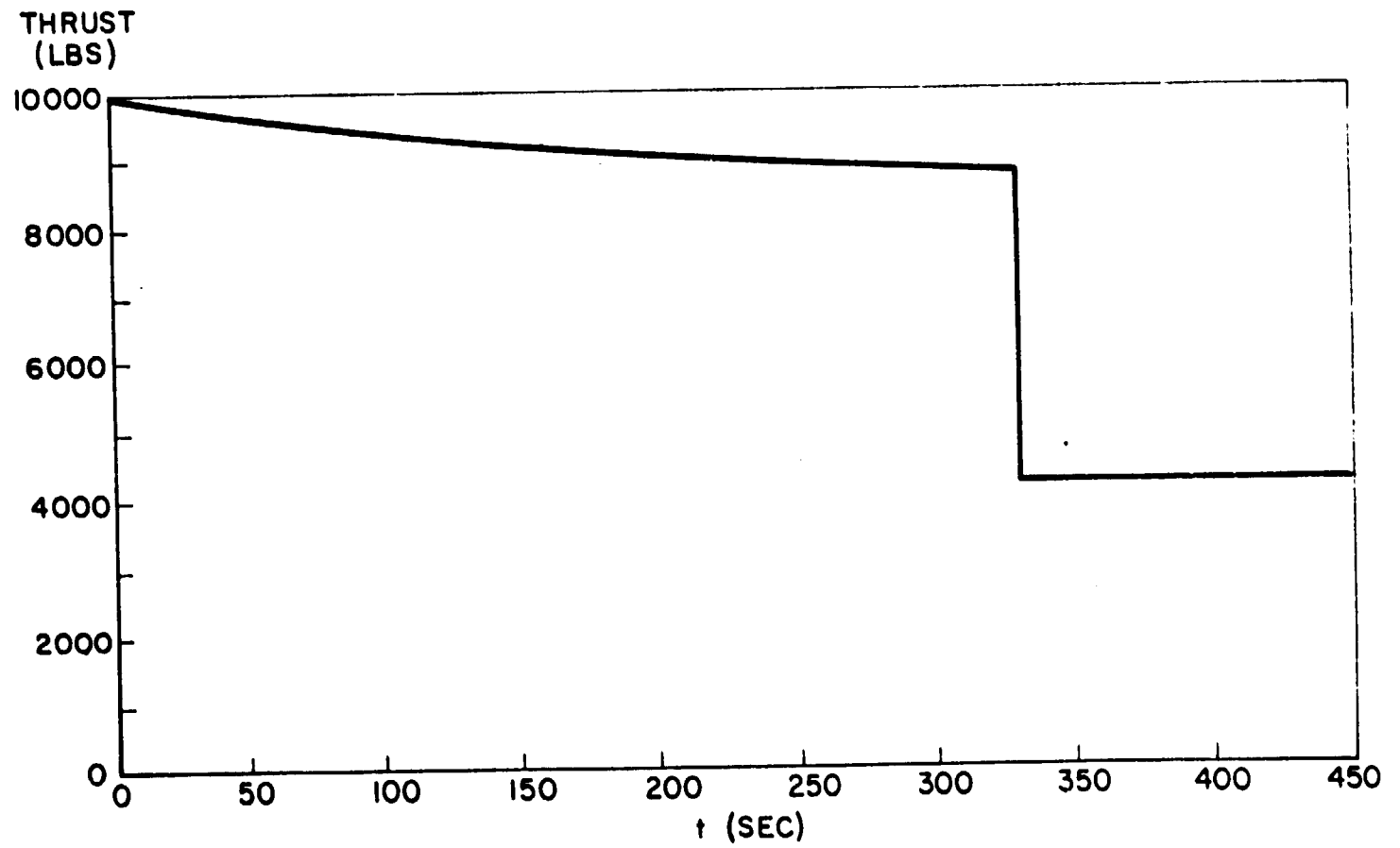


Fig. 4.40 Thrust vs time for landing trajectory.

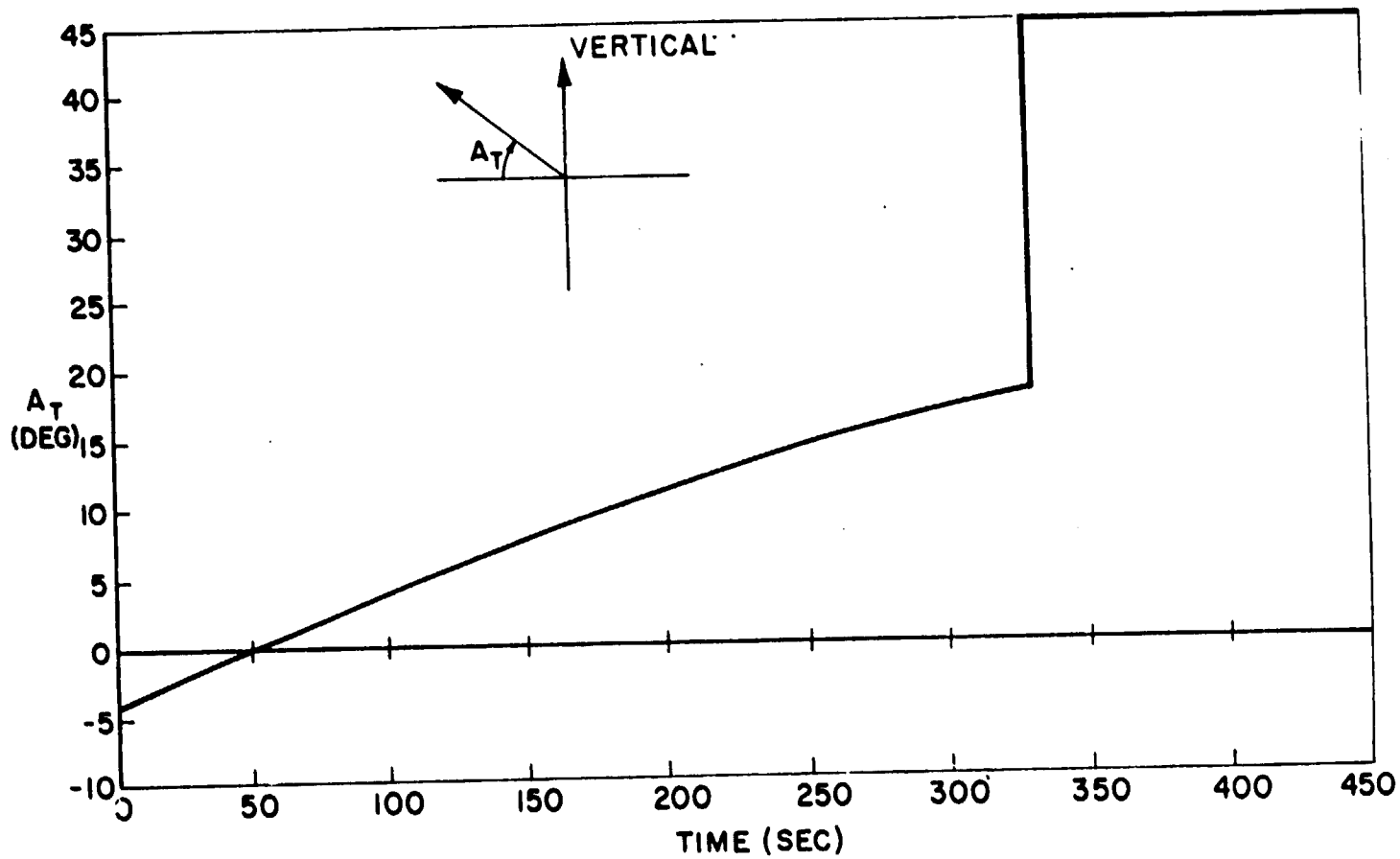


Fig. 4.41 Thrust angle vs time.

uncertainties of Figs. 3.25 and 3.26 for orbital navigation Models 1 and 2 respectively. Figures 4.44 and 4.45 illustrate the position and velocity uncertainties at a point 300 seconds after landing maneuver ignition for the same models. By comparing the equal period landing maneuver of Figs. 4.43 and 4.45 (Model 2 initial conditions), with the Hohmann landing maneuver of Figs. 4.24 and 4.25, it can be seen that the equal period landing maneuver uncertainties are generally larger than those for the Hohmann landing maneuver case. The primary reason for this difference is the fact that the IMU in the equal period landing maneuver case was not realigned after the initial alignment which was made 15 minutes before descent injection. Therefore, at the start of the landing maneuver for the equal period descent, the IMU misalignment had increased over a 45 minute period to a level of 2 mr as compared to the 0.8 mr case of the Hohmann descent described in Section 4.4.2.

The hover point dispersion or landing footprint for the equal period descent from orbit navigation Model 1 initial conditions is shown in Fig. 4.46. The landing CEP performance in this case is below the 3000 foot design objective, and the major contributing factors to this CEP are summarized in Fig. 4.47. The table in this figure illustrates that the orbit initial navigation and descent injection uncertainties are the major contributors to the forward or X direction uncertainty, as in the case of the Hohmann descent and landing maneuver summarized in Fig. 4.28. By comparing Figs. 4.47 and 4.28, it can be seen that the orbit navigation and descent injection uncertainties have a greater effect in the Hohmann descent case, but the IMU performance during the landing maneuver has the greater effect in track or Z direction uncertainties in the equal period descent and landing case of Fig. 4.47. This is primarily the result of the longer interval (45 minutes) of IMU drift for the case of Fig. 4.47 compared with the 15 minute drift prior to landing maneuver ignition in the Hohmann descent and landing case of Fig. 4.28. The IMU performance during the

$\sigma_x = 1720 \text{ ft}$	$\sigma_y = 1330 \text{ ft}$	$\sigma_z = 805 \text{ ft}$	$\sigma_{\dot{x}} = 1.29 \text{ fps}$	$\sigma_{\dot{y}} = 4.52 \text{ fps}$	$\sigma_{\dot{z}} = 4.01 \text{ fps}$
------------------------------	------------------------------	-----------------------------	---------------------------------------	---------------------------------------	---------------------------------------

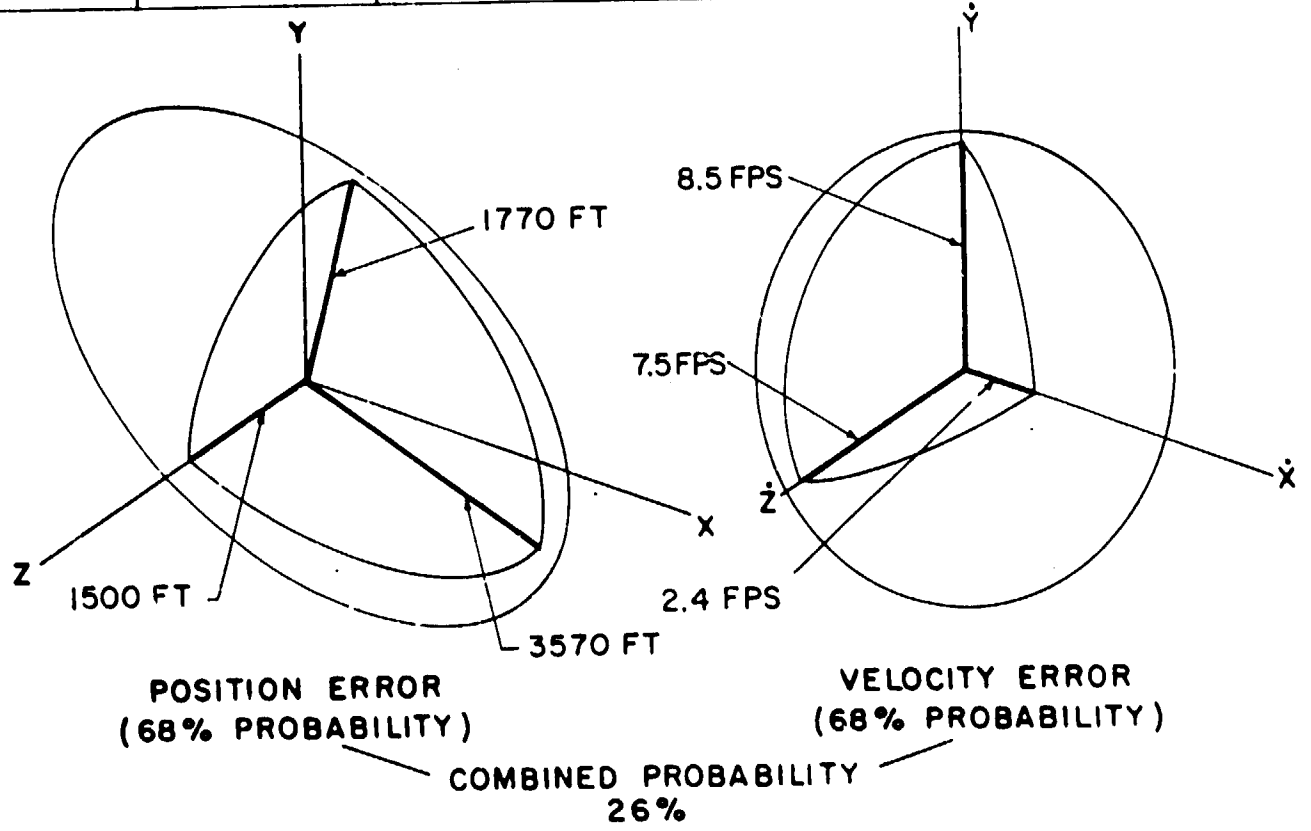


Fig. 4.42 Model 1, landing maneuver error volume at 150 seconds.

$\sigma_x = 2700$ ft	$\sigma_y = 1370$ ft	$\sigma_z = 810$ ft	$\sigma_{\dot{x}} = 1.3$ fps	$\sigma_{\dot{y}} = 4.8$ fps	$\sigma_{\dot{z}} = 4.0$ fps
----------------------	----------------------	---------------------	------------------------------	------------------------------	------------------------------

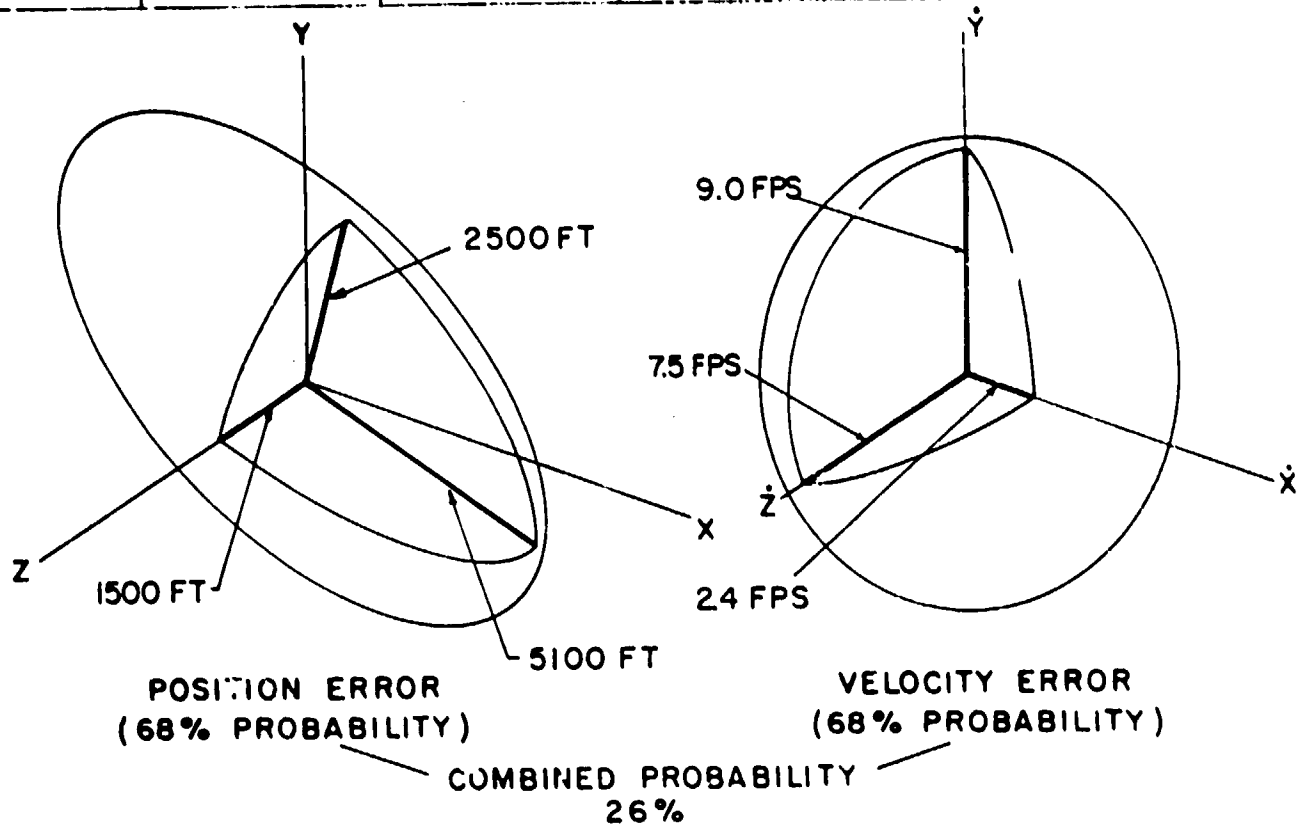
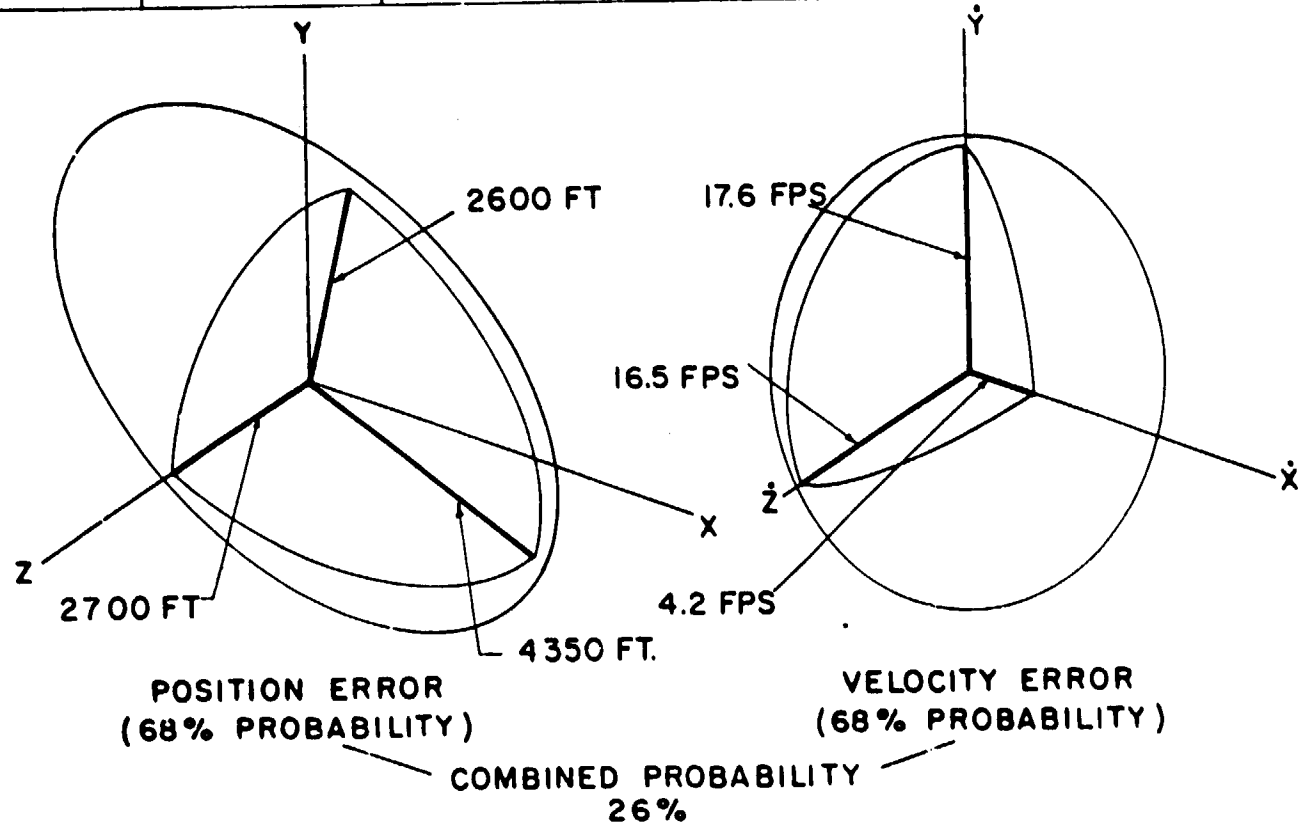


Fig. 4.43 Model 2, landing maneuver error volume at 150 seconds.

227

ORIGINAL PAGE IS  
OF POOR QUALITY

$\sigma_x = 1850 \text{ ft}$	$\sigma_y = 1965 \text{ ft}$	$\sigma_z = 1430 \text{ ft}$	$\sigma_{\dot{x}} = 2.23 \text{ fps}$	$\sigma_{\dot{y}} = 9.4 \text{ fps}$	$\sigma_{\dot{z}} = 8.8 \text{ fps}$
------------------------------	------------------------------	------------------------------	---------------------------------------	--------------------------------------	--------------------------------------



228

Fig. 4.44 Model 1, landing maneuver error volume at 300 seconds.

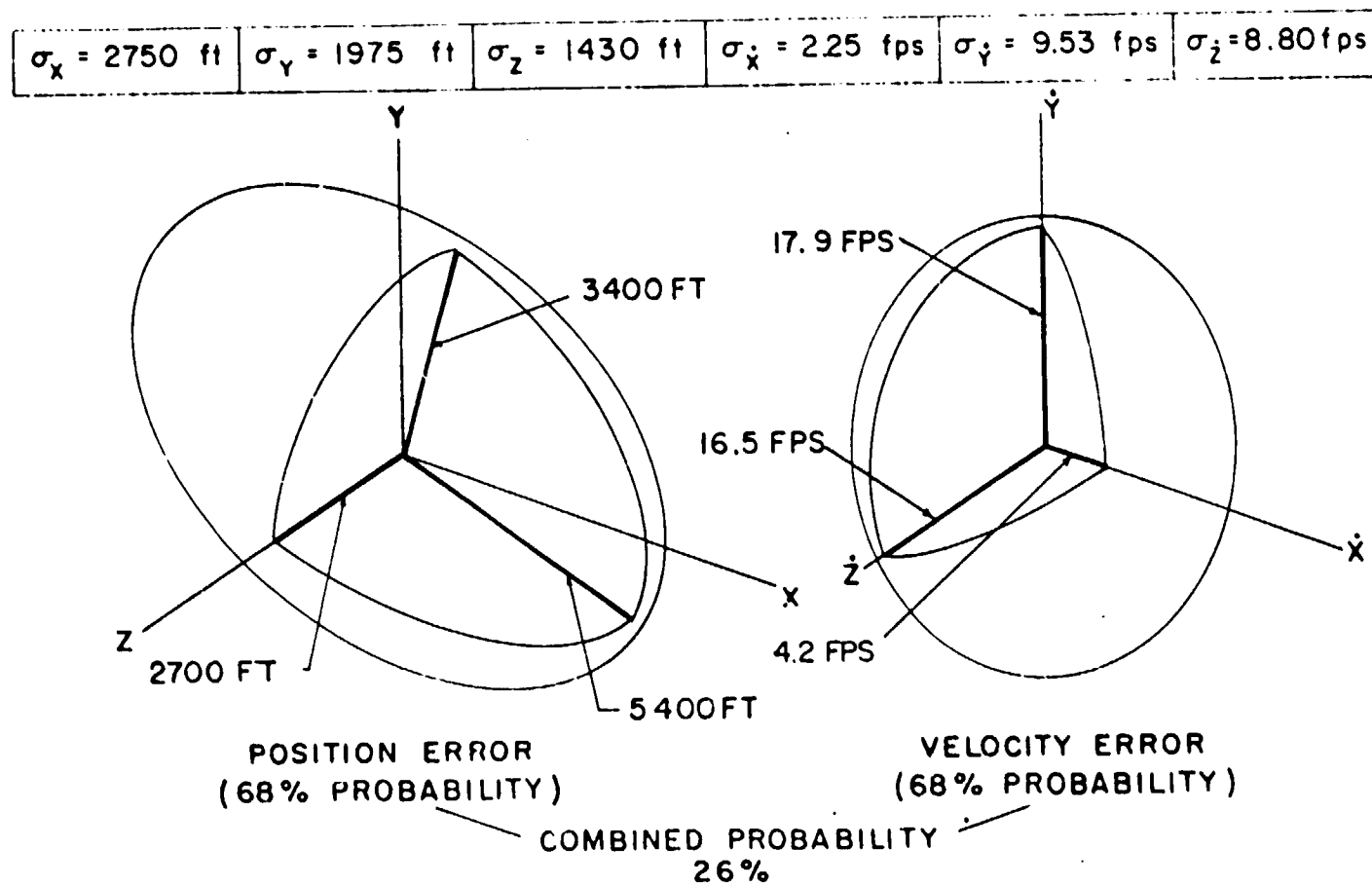


Fig. 4.45 Model 2, landing maneuver error volume at 300 seconds.

$\sigma_x = 2000'$	$\sigma_z = 2850'$
--------------------	--------------------

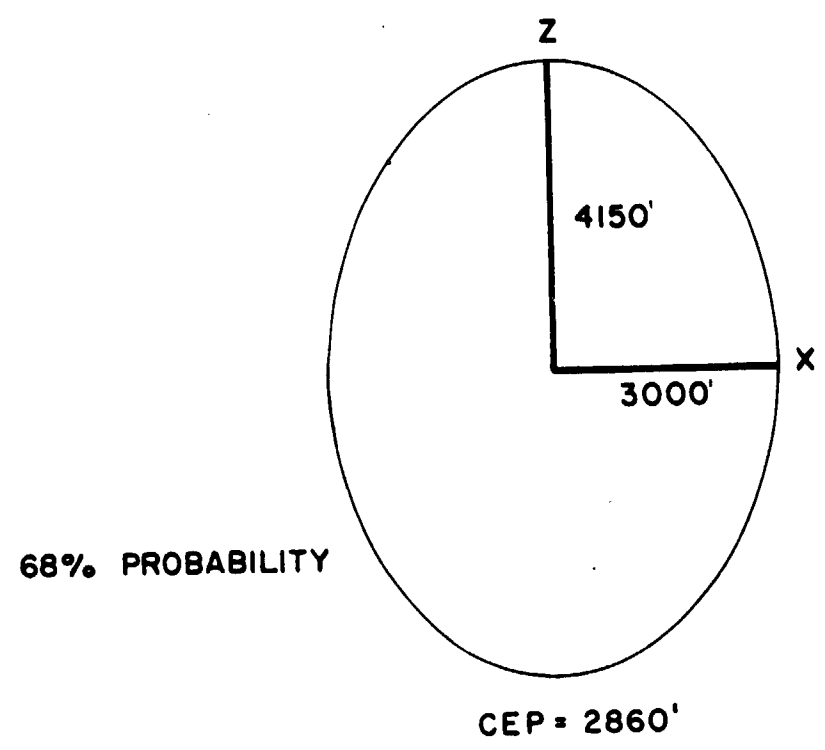


Fig. 4.46 Landing footprint for model 1.

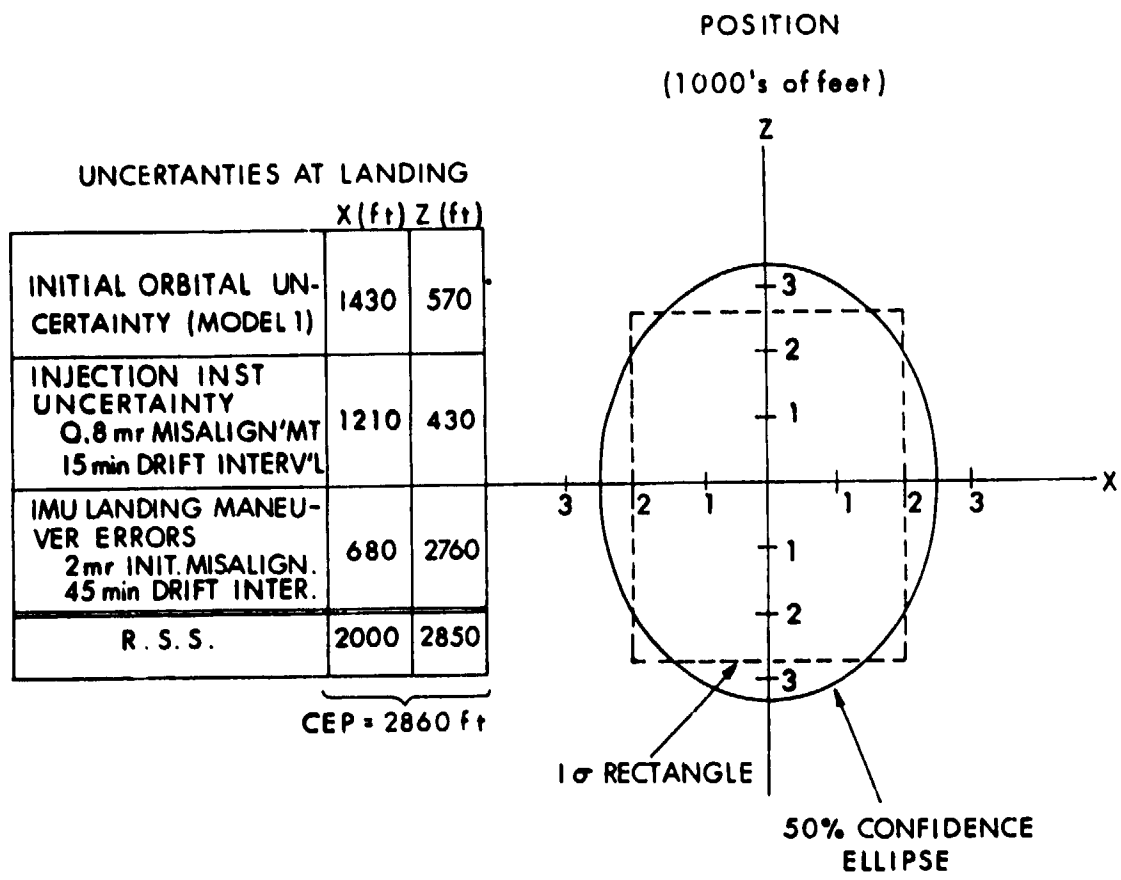


Fig. 4.47 Hover point dispersion (primary G&N performance).

477sec LANDING MANEUVER  
No. 088989

IMU ERROR SOURCE	POSITION			VELOCITY		
	Range (ft)	Track (ft)	Alt (ft)	Range (fps)	Track (fps)	Alt (fps)
1. PLATFORM MISALIGNMENT (2mr)	147	2690	2796	2.4	11.2	12.1
2. ACCELEROMETER BIAS (0.2cm/sec <sup>2</sup> )	677	670	677	2.9	2.9	2.9
3. ACCELEROMETER SCALE FACTOR (100ppm)	127					
4. ACCELEROMETER MISALIGNMENT (0.1mr)	26					
5. GYRO FIXED DRIFT (0.15deg/hr)	30	154	154	0.3	0.9	0.9
6. GYRO MASS UNBAL (0.15deg/hr/g)		25	63		0.2	0.3
RSS OF ALL ERROR SOURCES	680	2761	2886	3.7	11.7	12.6

Fig. 4.48 Lunar landing maneuver uncertainties.

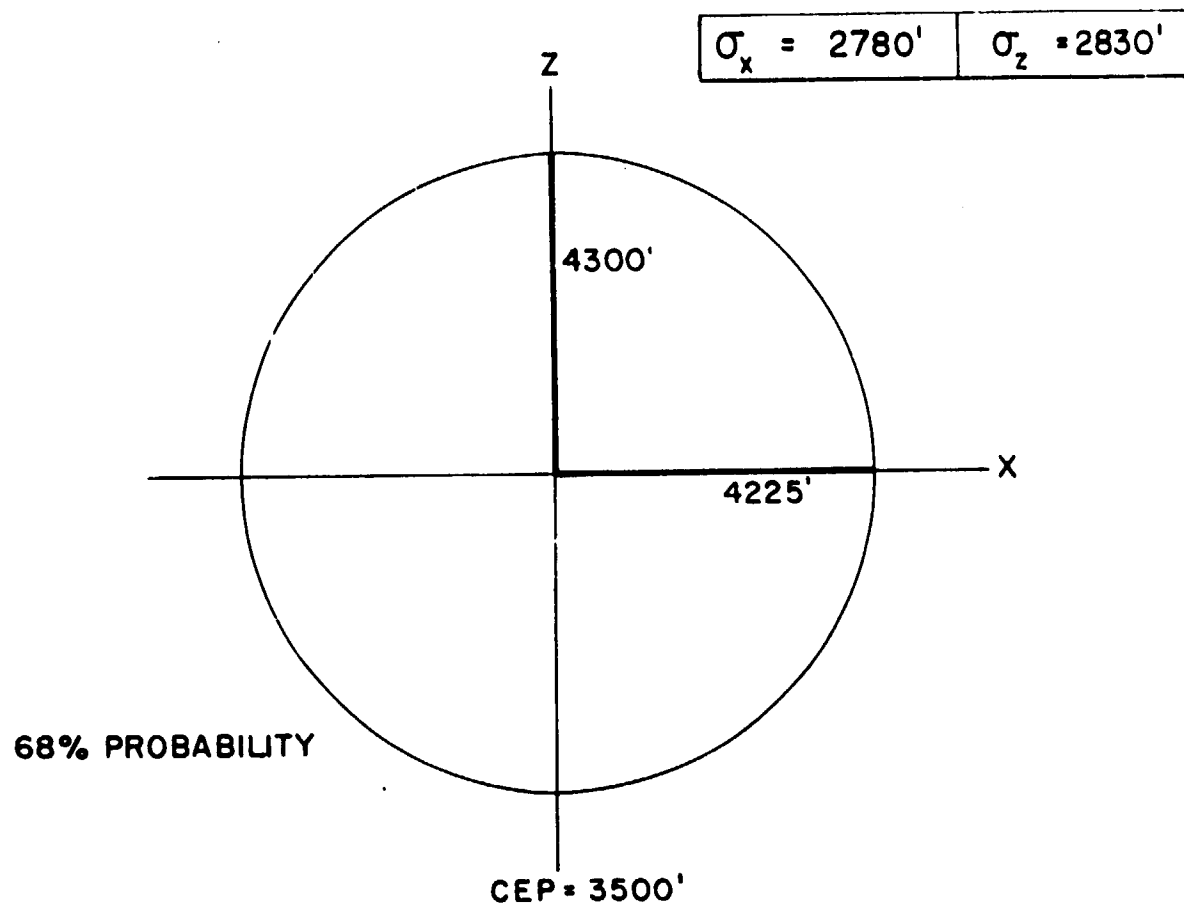
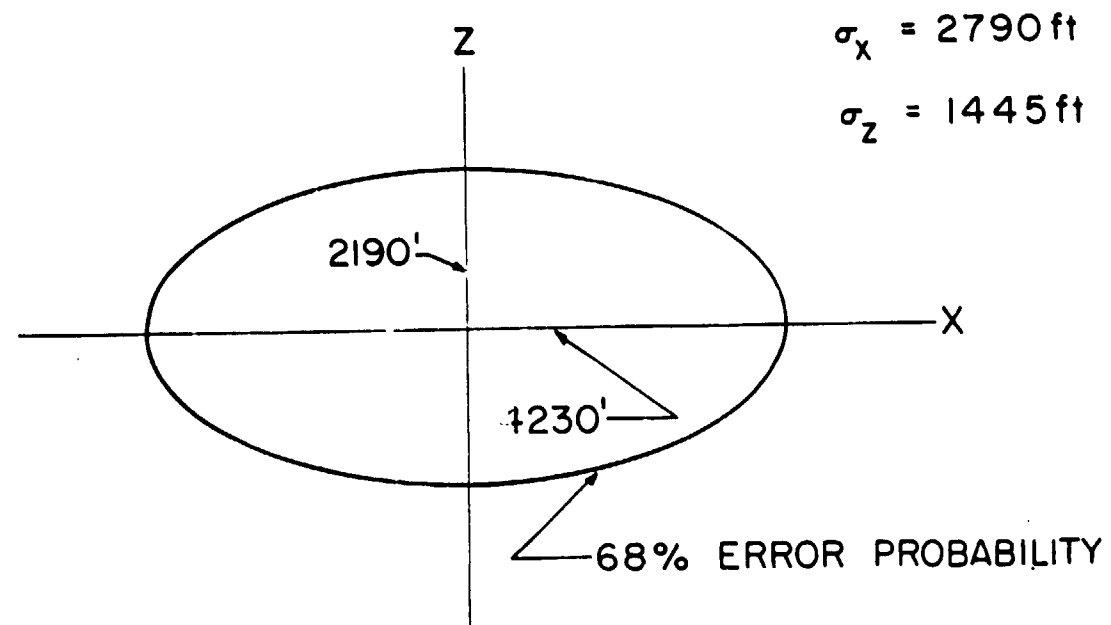


Fig. 4.40 Landing error footprint for model 2.

(IMU REALIGNMENT 15 min BEFORE PERILUNE)



CEP = 2500 ft

Fig. 4.50 Model 2, landing footprint.

[REDACTED]

landing maneuver from equal period descent condition is summarized in Fig. 4.48, and it can be seen that the primary sources of IMU error are from initial platform misalignments and accelerometer bias as in the case of the landing maneuver from Hohmann descent conditions.

The hover point dispersion or landing footprint for the equal period descent and landing maneuver from orbit navigation Model 2 initial conditions is shown in Fig. 4.49. This final hover point uncertainty resulted from the trajectory uncertainties previously illustrated in Figs. 4.43 and 4.45. From Fig. 4.49, it can be seen that the design CEP objective of 3000 feet is not met when the initial condition uncertainties on the level of orbit navigation Model 2 are used with the other factors specified in Fig. 4.27. The 3000 foot CEP objective can be achieved from orbit navigation Model 2 initial uncertainties, if the IMU is realigned 15 minutes prior to engine ignition of the landing maneuver as illustrated by the final hover point results of Fig. 4.50. By comparing the results of Figs. 4.50 and 4.49, it can be seen that the deviation in the X direction is essentially unchanged, but the IMU realignment has a major effect of reducing the track or Z direction deviation, thereby reducing the overall CEP to 2500 feet. These figures illustrate that the alignment schedule of the IMU during the orbit navigation and descent trajectory phases is one of the primary factors effecting the G&N performance for the landing maneuver.

#### 4.5.3 Landing Radar Operation

The landing radar operation during the landing maneuver from equal period descent conditions is very similar to that previously described in Section 4.4.3 for the Hohmann descent and landing case. Similar landing radar and IMU uncertainty profiles are presented in Figs. 4.51 through 4.54. In comparing the altitude uncertainty profile of Fig. 4.51 to that of Fig. 4.31, it can be seen that the three sigma IMU altitude uncertainty is at a higher level for the equal period descent and landing case of Fig. 4.51.

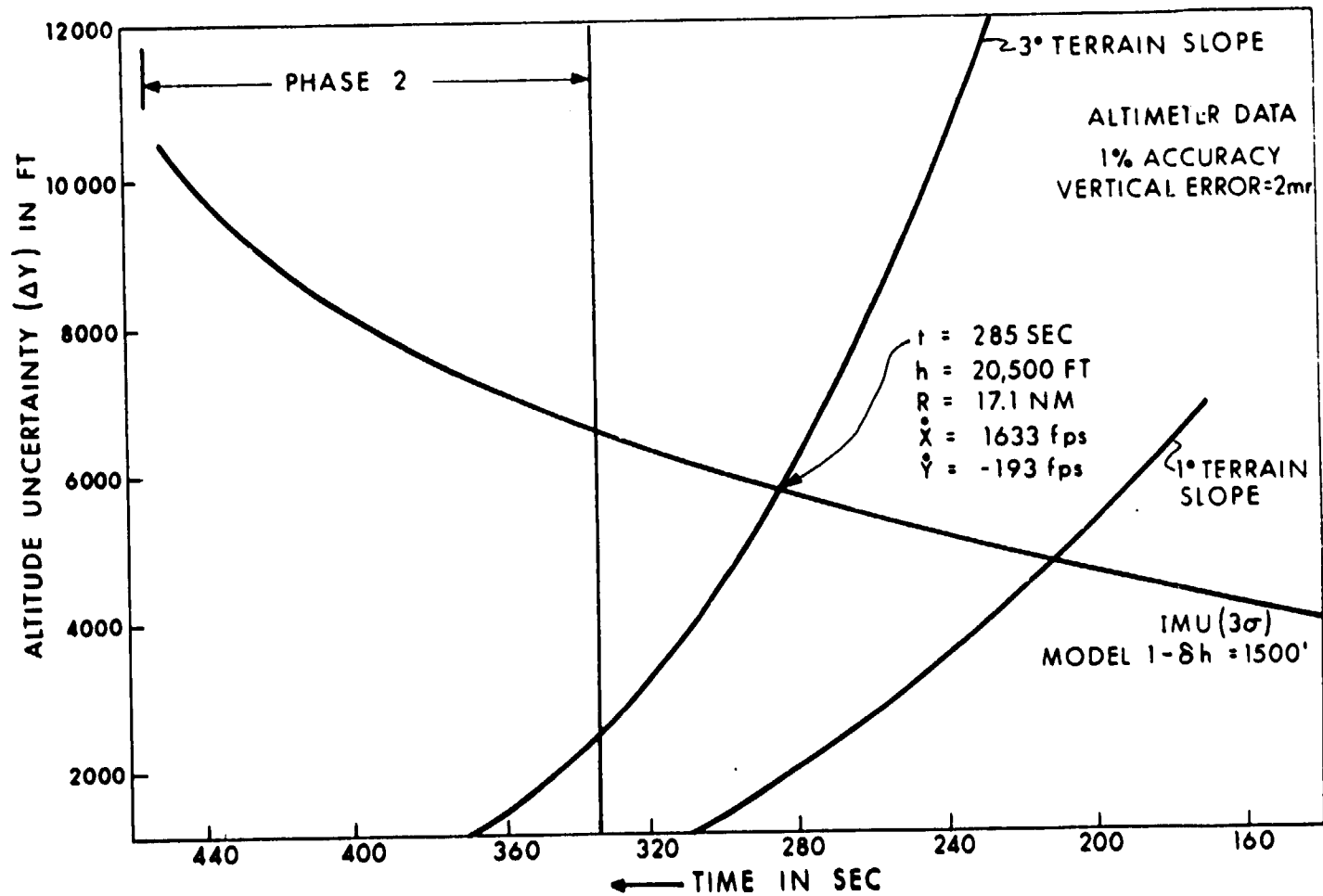


Fig. 4.51 IMU and altimeter errors during 447 sec landing maneuver.

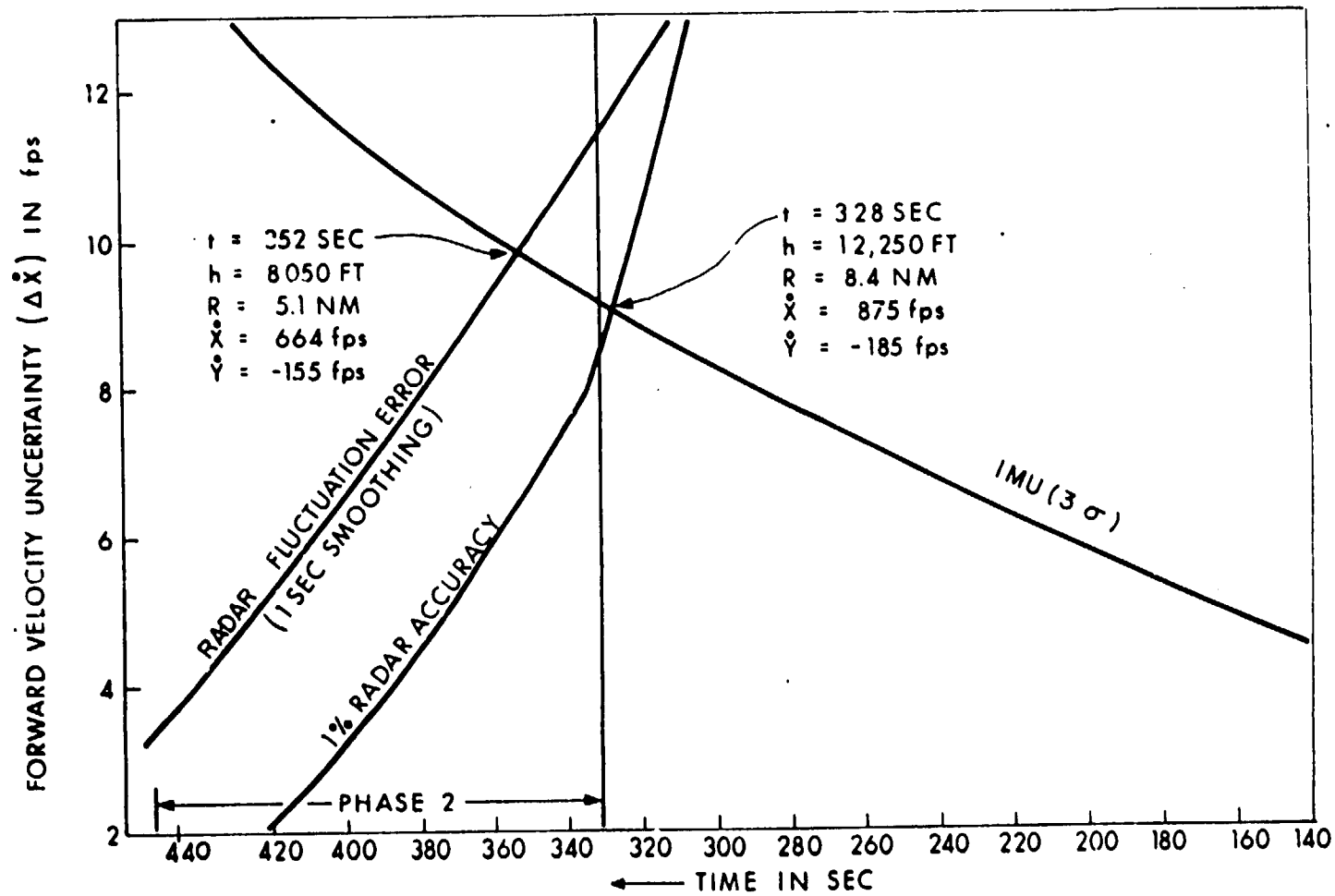


Fig. 4.52 IMU-Doppler radar  $\dot{X}$  errors during 447 sec landing maneuver.

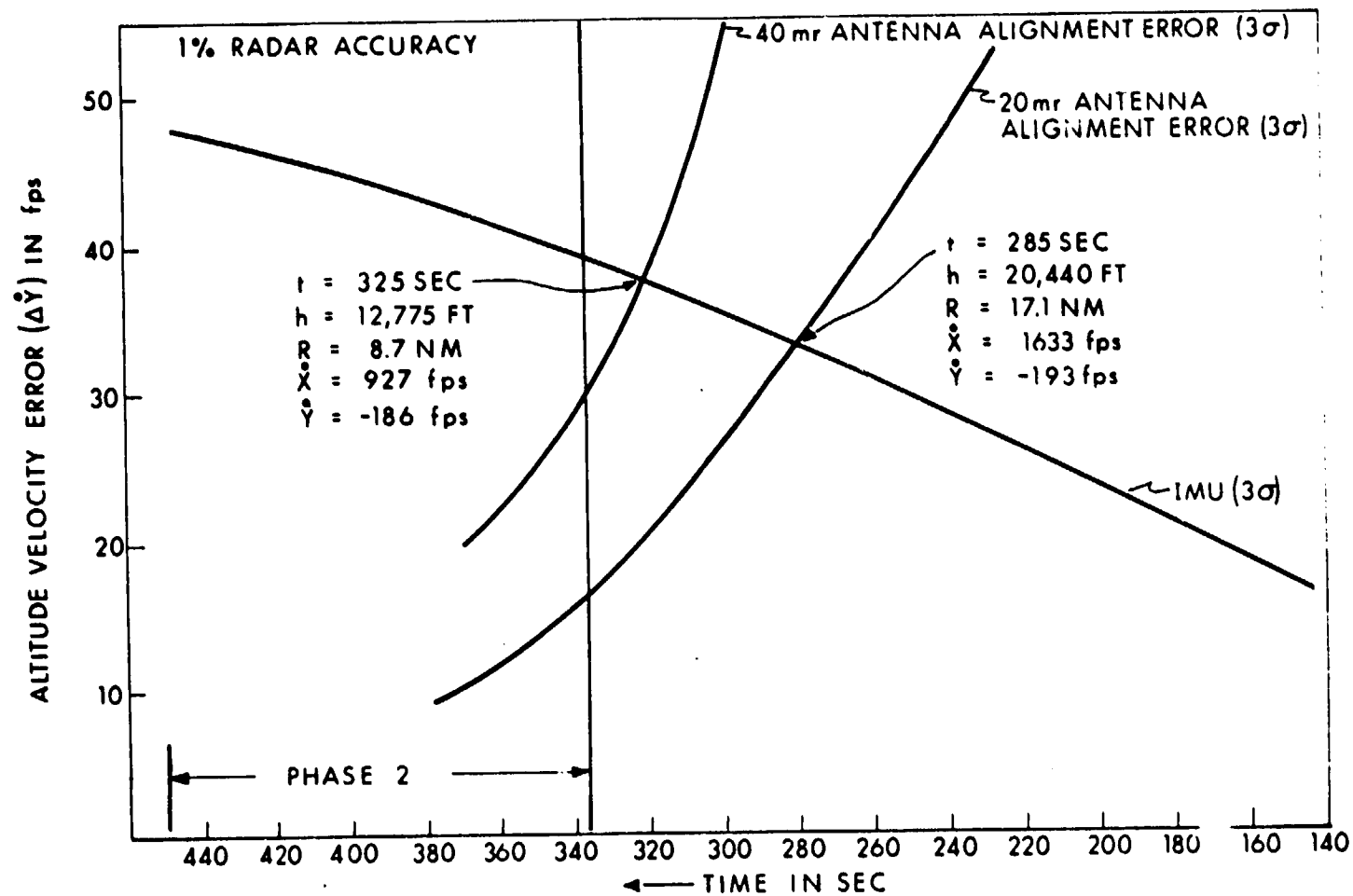


Fig. 4.53 IMU-Doppler radar  $\dot{Y}$  errors during 447 sec landing maneuver.

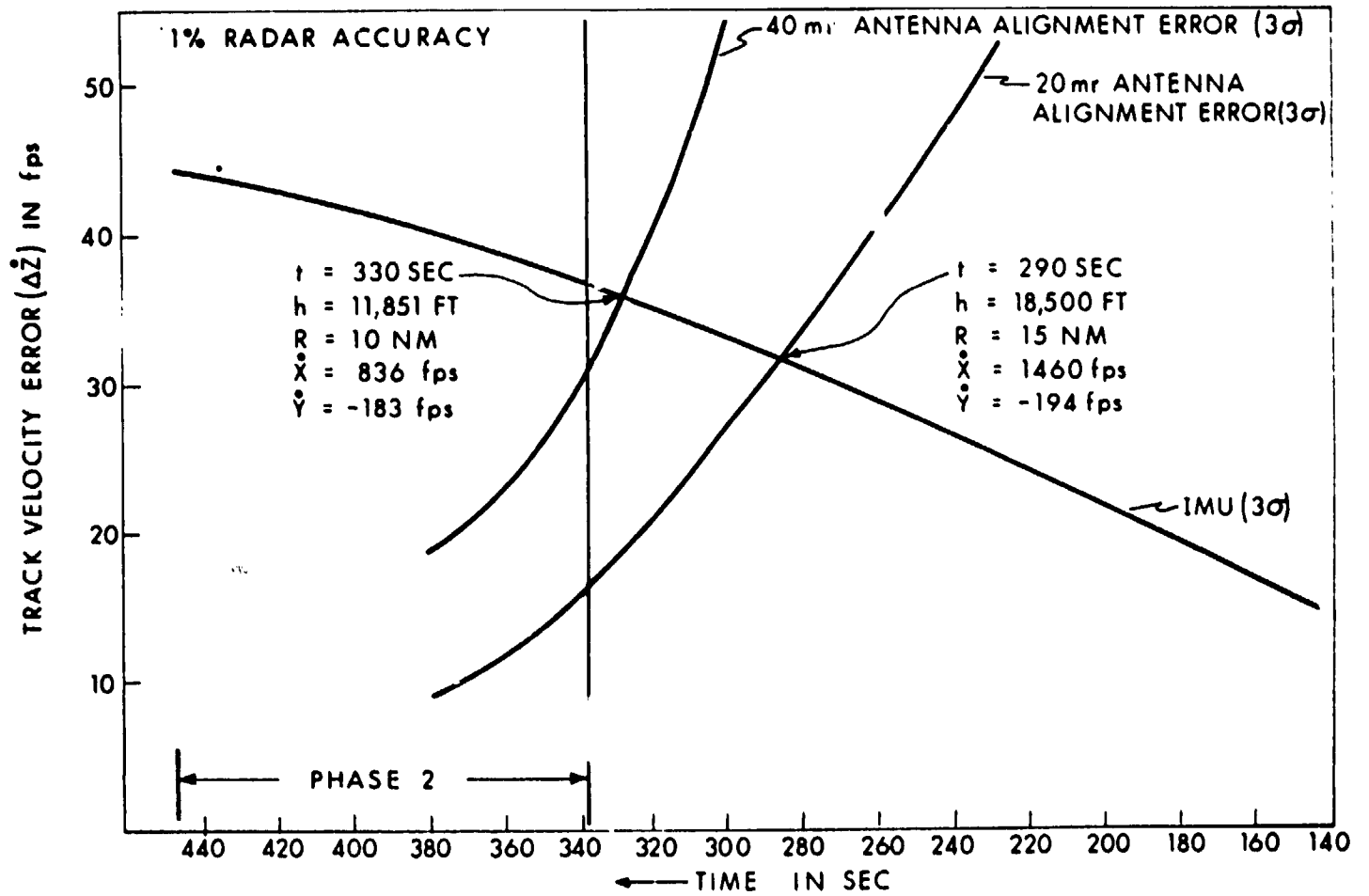


Fig. 4.54 IMU-Doppler radar  $Z$  errors during 447 sec landing maneuver.

[REDACTED]

This again is because of the IMU alignment schedule, and the fact that the IMU initial misalignment for the equal period landing case was more than twice that of the Hohmann landing case. As a result, the IMU and radar uncertainty crossover point occurs at a higher altitude, 20,500 feet, and earlier in the first phase of the landing maneuver.

The forward velocity uncertainty ( $\Delta \dot{X}$ ) for the IMU and landing radar is summarized in Fig. 4.52. By comparing this figure with that of Fig. 4.32, it can be seen that the IMU and radar uncertainty crossover points are essentially the same for the two landing maneuvers. The altitude and track velocity uncertainties for the equal period landing maneuver are illustrated in Figs. 4.53 and 4.54. By comparing these figures with Figs. 4.33 and 4.34, it can be seen that the three sigma IMU uncertainty is higher for the equal period landing case, which is again the result of the IMU difference in alignment schedule, 45 minutes for the equal period case vs 15 minutes for the Hohmann descent. Since the landing maneuver from equal equal period or Hohmann descent trajectories is similar, the IMU and radar uncertainty crossover points will be essentially the same, provided the same IMU alignment schedule is followed in both cases. The landing maneuver uncertainties summarized in Figs. 4.51 through 4.54 resulted from the combination of IMU uncertainties with initial orbit navigation Model 1 uncertainties (Fig. 3.25). If orbital navigation Model 2 uncertainties had been used (Fig. 3.26), it was shown in Figs. 4.49 and 4.50 that an IMU alignment 15 minutes prior to the landing maneuver ignition was required to meet the design objective of a 3000 foot landing CEP. In this case, the same IMU alignment schedule would have been used for both Hohmann and equal period landing maneuvers and the IMU and landing radar crossover points would have been essentially the same.

#### 4.5.4. Lunar Surface Transponder Operation

If the landing maneuver objective is to hover above or near a landing site marked by a lunar surface radar transponder, the LEM rendezvous radar would be used during the landing maneuver to provide the trajectory updating function of the window reticle used for unaided landing maneuvers. Figure 4.55 illustrates the IMU and rendezvous radar altitude uncertainties during the final phases of a landing maneuver from equal period descent conditions. The rendezvous radar would determine the altitude in this case by measuring the tracking line angles and slant range to the lunar surface transponder. It can be seen, by comparing the results of Fig. 4.55 with those of the landing radar case of Fig. 4.51 that the IMU and radar uncertainty crossover point occurs at a much greater range and altitude in the case of the lunar surface transponder landing and radar updating could normally be done at an earlier point in the landing trajectory. The primary error in the rendezvous radar performance is the pointing or angle bias error between the IMU and actual tracking line. It might be noted that this angle bias is normally estimated and compensated for during powered rendezvous maneuver phases, but angular bias estimation is not attempted during powered maneuvers where vibration levels and structural deflections are not known. It should also be noted that even though the uncertainty crossover points illustrated in Fig. 4.55 occur at a relatively high altitude and range from the landing sight, the present LEM rendezvous radar gimbal limits, illustrated in Fig. 1.18, are not sufficient to allow rendezvous radar tracking at ranges of this level in the landing maneuver. With the present rendezvous radar gimbal limits, the first radar updating could be done at the beginning of a modified second phase of the landing maneuver. This should be sufficient to achieve the primary G&N design objective of 100 to 500 foot landing CEPs to a lunar surface transponder. In the case where rendezvous radar updating is first available at the

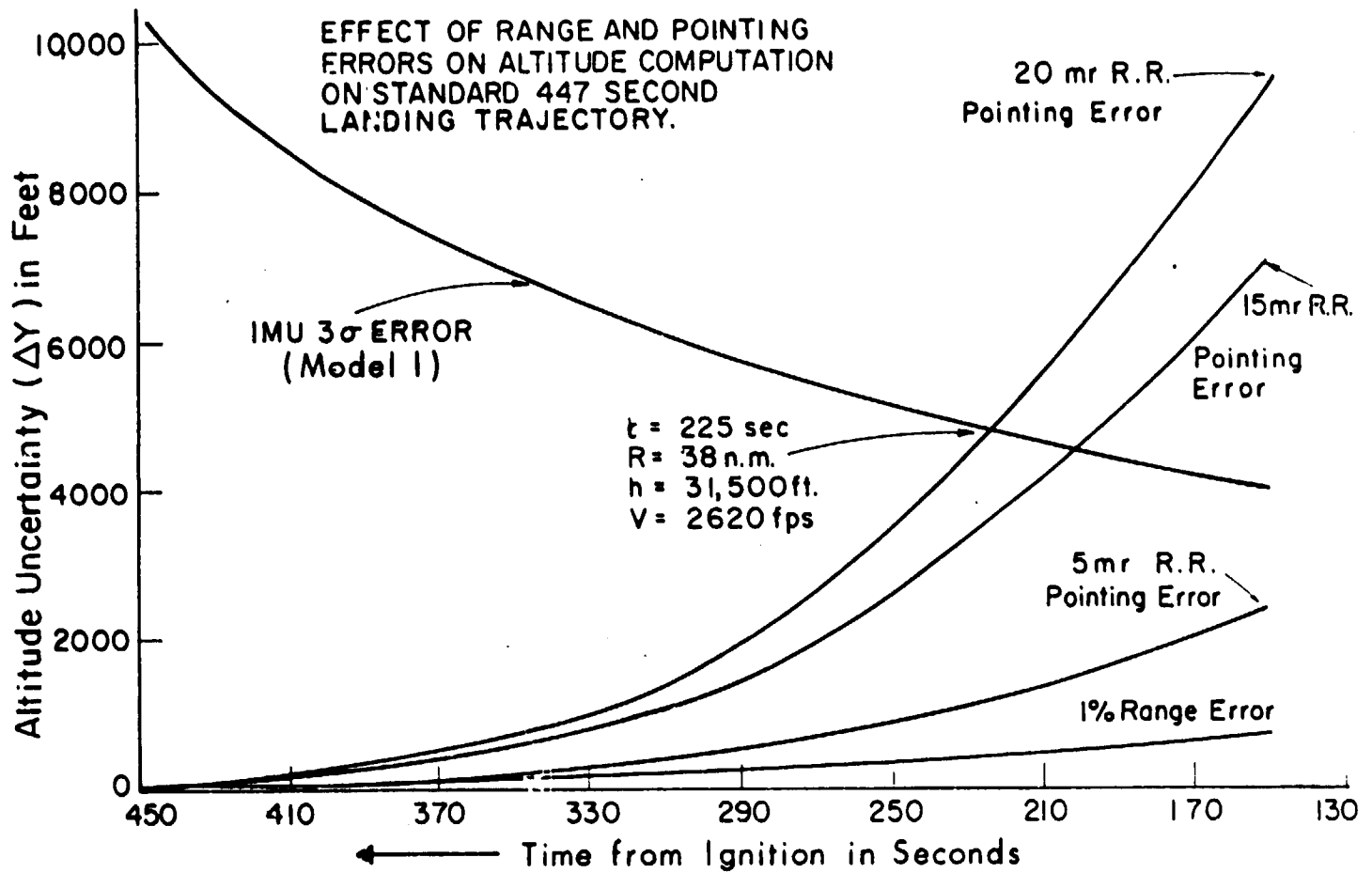


Fig. 4.55 Altitude uncertainties due to IMU and rendezvous radar errors.

initiation of the second phase of the landing maneuver, the radar weighting factor may be relatively high, and radar data would be accepted by the explicit guidance concept as fast as possible.

#### 4.6 Hover and Touchdown Phase.

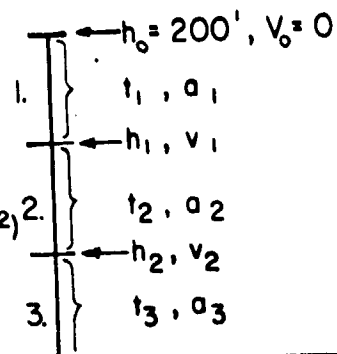
This final phase of the landing maneuver starts from the hover conditions established by the previous second or constant attitude phase of the maneuver. As described in Section 4.2, the boundary conditions for the constant attitude phase are an altitude of 200 feet over the desired landing site with a velocity

The astronaut has the option of

The semi-automatic mode of operation would be similar to the above automatic mode with the exception that the astronaut could interrupt this procedure at any point by an altitude hold mode of operation. When the astronaut selected this mode, the LGC would maintain control of the descent engine throttle servo and maintain a setting that would hold a constant altitude at the time of pilot control initiation. The astronaut would have complete control over the LEM attitude through the attitude controller and by pitching the vehicle in a desired direction he could effect translation maneuvers while the LGC maintained the constant altitude by thrust level control. When the astronaut has performed his desired translation maneuvers, the automatic system is re-engaged, at which time any residual horizontal velocities are nulled and the automatic descent maneuver reestablished.

A hover altitude for the terminal conditions of the second landing maneuver phase were chosen arbitrarily, but are estimated to be the minimum altitude at which potential lunar dust problems would start (Ref. 4.2). The automatic letdown maneuver from these hover conditions will require significant  $\Delta V$ , depending upon various restrictions placed on the terminal letdown maneuver. The important parameters during the terminal letdown and their effects on the overall  $\Delta V$  requirement are summarized in Fig. 4.56. In this figure, the hover condition is assumed to be in an altitude of 200 feet with a zero velocity condition relative to the lunar surface. The first interval of the descent maneuver illustrated in the top of Fig. 4.56 requires reducing the descent engine throttle until a maximum vertical velocity  $V_1$  is achieved. The thrust is then increased so that the desired terminal descent velocity,  $V_2$ , is established at some designated altitude,  $h_2$ , after which the velocity  $V_2$  is maintained until surface contact is made. This operation can be illustrated by the first example of Fig. 4.56 in which the descent engine was throttled to its minimum setting for 5.3 seconds until the maximum desired sink rate  $V_1$  of 15 ft/sec was achieved at an altitude of 160 feet,  $h_1$ . The thrust of the

1. MINIMUM THRUST
2. CONSTANT ACCELERATION
3. CONSTANT VELOCITY ( $a_3 = 5.3 \text{ fps}^2$ )



$$t = t_1 + t_2 + t_3$$

$$\Delta V = a_1 t_1 + a_2 t_2 + a_3 t_3$$

$h_1$ ft	$V_1$ fps	$h_2$ ft	$V_2$ fps	$t_1$ sec	$t_2$ sec	$t_3$ sec	$\Delta v$ fps
159.8	15	40	10	5.3	9.5	4.0	90.6
128.5	20	40	10	7.1	5.9	4.0	80.6
88.4	25	40	10	8.9	2.7	4.0	73.4
88.4	25	20	10	8.9	3.9	2.0	68.8
159.8	15	40	5	5.3	11.9	8.0	129.6
128.5	20	40	5	7.1	7.0	8.0	113.1
88.4	25	40	5	8.9	3.2	8.0	102.1
88.4	25	20	5	8.9	4.2	5.0	91.4

Fig. 4.56 Lunar landing - hover to touchdown (automatic mode).

descent engine was then increased over the next 9.5 seconds such that the desired terminal contact velocity  $V_2$  of 10 ft/sec was established by the time the vehicle reached an altitude  $h_2$  of 40 feet. This terminal velocity of 10 ft/sec was then maintained over the next 4 seconds until lunar surface touchdown was made. The total velocity requirement for this maneuver was 90.6 ft/sec as shown in Fig. 4.56. By comparing the various maneuvers summarized in this figure with their associated maximum vertical velocities,  $V_1$ ; terminal contact velocities,  $V_2$ ; and altitude of the constant velocity phase  $h_2$ ; it can be seen that the  $\Delta V$  requirements range between 70 and 130 ft/sec. The maneuvers summarized in Fig. 4.56 are near optimum type maneuvers for the various descent parameters considered. Actual maneuvers involving semi-automatic or pilot assisted landings will obviously require more  $\Delta V$  than the near optimum descents summarized in this figure.

The primary reason that a hover altitude of 200 feet was chosen for the examples illustrated in this chapter for landing maneuvers was that the  $\Delta V$  requirement increases for hover and terminal letdown maneuvers from higher altitudes. The effect of hover altitude on the  $\Delta V$  requirement for the terminal maneuver is illustrated in Fig. 4.57. The curves illustrated in this figure are for the three velocity and altitude conditions previously considered in Fig. 4.56. These are the maximum allowed vertical velocity during the maneuver,  $V_1$ ; the desired terminal touchdown velocity,  $V_2$ ; and the altitude  $h_2$ , at which the constant velocity must be established. It can be seen from Fig. 4.57, that all the conditions shown require essentially 100 ft/sec for automatic maneuver from 200 foot hover altitudes. As this hover altitude is increased to 1000 feet, the  $\Delta V$  requirements range from approximately 300 to 500 ft/sec, depending upon the terminal descent maneuver characteristics chosen. As previously mentioned, the hover altitude will be chosen on knowledge of the lunar surface or dust conditions that are expected. The

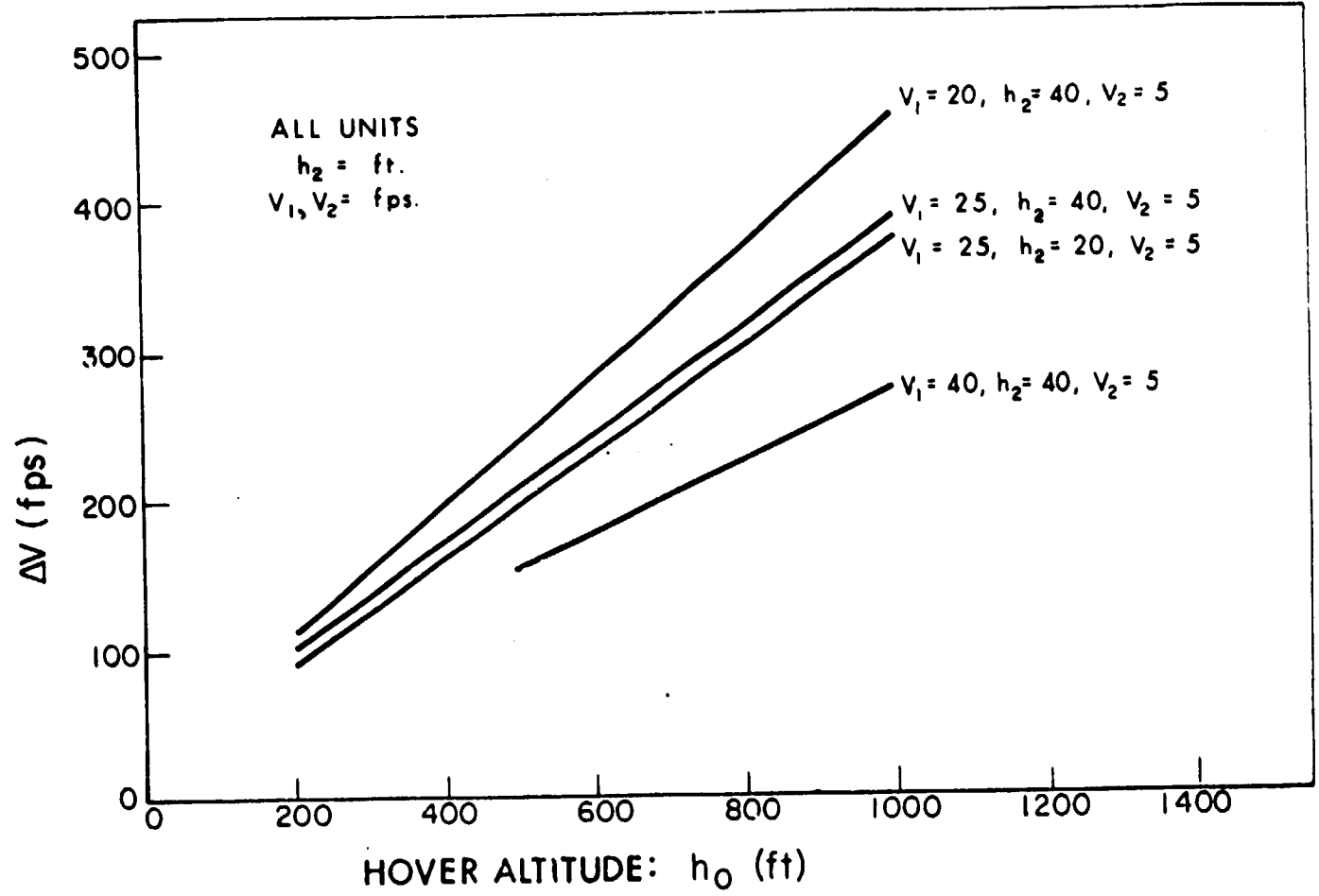


Fig. 4.57 Characteristic velocity vs initial altitude for touchdown maneuver.

primary G&N mode of operation up to the hover point condition requires that all final landing radar updating and astronaut visual monitoring be completed by the time the terminal letdown maneuver is initiated. The astronaut will still have the option of interrupted manual control, pilot assisted landing, if desired after this point.

At the present time, the descent engine cutoff criteria at the end of the terminal letdown has not been completely determined. The lunar surface, or dust conditions, and visibility limitations will be one of the major factors in determining what thrust termination criteria will be used. One of two approaches most often considered is to terminate thrust at an altitude of approximately 5 feet with zero velocity conditions. The uncertainty involved in this technique under heavy dust or no visibility conditions is that knowledge of altitude may not be available from the landing radar and errors would exist if extensive cratering was effected by the exhaust of the descent engine. An alternate approach would maintain the descent engine thrust until lunar contact had been made at the inertially controlled terminal velocity  $V_2$  of Fig. 4.56 at which time the thrust would be terminated. This technique would not depend on landing radar data and would be independent of cratering effects. The major problem with the latter technique is the dynamic effects on the LEM if one landing gear makes contact before the others under a throttle condition that essentially balances lunar gravity. The final engine termination criteria will depend on future simulations and knowledge of the lunar terrain.

An alternate method of third phase operation to touchdown is currently under investigation. This approach uses the same guidance concept as phase 2 to maintain visibility to the landing site as long as possible. The LEM does not come to a hover condition followed by a vertical descent in this approach, but the terminal conditions of phase 2 are chosen so that a near constant attitude can be maintained along a trajectory similar to that of phase 2 from altitudes of 200 feet to near surface contact. The results of this investigation are still preliminary and will be

presented in a future report.

The primary G&N system controls the LEM attitudes about the vehicle Y and Z axes throughout all automatically guided phases of the lunar landing maneuver. The vehicle orientation about the thrust axis (X axis) may or may not be controlled by the primary G&N system during the first and third phases of the landing maneuver, but will be controlled during the second or constant attitude phase of the landing maneuver as described in Section 4.4.4. During the first phase of the landing maneuver, the vehicle Z axis, may be directed downward so that the astronauts will be able to see the lunar surface until an altitude of approximately 30,000 feet is reached. At this time a 180 degree maneuver about the X axis is effected so that the window, or Z axis, is in the up direction prior to the pitch-up or initial point of the second phase of the landing maneuver. It is important for primary G&N operation that the attitude about the Z axis be such that the windows are up when an altitude of 20,000 feet is reached, so that the landing radar can be used for updating altitude. The current landing radar antenna configuration is a two position arrangement such that the altitude measuring beam would be essentially vertical during the constant attitude phase (Fig. 1.19). This altitude beam could be used prior to the constant attitude phase at altitudes of approximately 20,000 feet. The second position of the landing radar antenna would be such that the altitude measuring beam would be vertical when the vehicle is in a vertical orientation at the hover conditions.

There is no primary G&N system requirement for a preferred orientation of the LEM about the X axis at the time of lunar surface contact. The rendezvous radar gimbal axes have sufficient coverage to insure CSM tracking over the desired tracking sector (Section 5.3) under virtually any landing orientation. The three position AOT can achieve IMU alignments if the sun or earth are in the field of view for one fixed AOT position. The primary G&N system places no restriction on the final touchdown

orientation; however, if a choice is available it is preferred to direct the three positions of the AOT away from the sun or illuminated earth.

The primary G&N system is maintained in the operating mode after lunar landing and descent engine cutoff for a period of time that is currently unspecified. This time interval is presently considered to be between 15 and 30 minutes in length, during which time the primary G&N system can control an emergency take-off or abort if desired. This condition is considered in more detail in the following chapters.

